

ISSN 2189-7093  
PRINT ISSN 0919-1038

# KURRI

# Progress Report

# 2016

*The Research Reactor Institute, Kyoto University*

# **KURRI Progress Report** 2016

APRIL 2016 – MARCH 2017

*Published by*  
*The Research Reactor Institute, Kyoto University,*  
*Kumatori-cho, Sennan-gun, Osaka 590-0494 Japan*

## PREFACE

We would like to inform that KUCA and KUR have entered in the final stage to restart after being off for more than 3 years. We changed repeatedly our initial plan to cope with requirements in accordance with the New Regulatory Requirements. I would like to express my special thanks of gratitude to our colleague who made significant contributions to new challenge.

Long shutdown was a big upset in research works and education programs. Unfortunately researchers and students did not have any works with KUR and KUCA in 2016. We lost opportunity of nuclear-educated Human Resources. We are concerned that stopping of nuclear training education would give a significant influence. It is such a shame that patients for a medical treatment with reactor-based BNCT have to wait the restart for years.

It is too bad that KURRI as Joint Usage / Research Center did not provide proper service with users in this year. However we are glad that research activities with the Electron Linear Accelerator, the Co-60 Gamma-ray Irradiation and other facilities have been worked well. BNCT research group makes satisfactory progress with clinical trials with the Accelerator-based BNCT system. We believe their progress would move forward a standard medical treatment with BNCT system in a hospital.

Japan's nationwide nuclear shutdown was imposed in 2011 as a result of the Fukushima-Daiichi accident. Under the new regulation, our staff subsequently discussed with the Nuclear Regulation Authority (NRA) and submitted various amendments to our plans to enhance equipment with KUR and KUCA against extreme events, such as earthquake, forest fire and tornadoes.

After our restart, we would like to stress that research works with Research Reactor are very important. KURRI would like to thank your understanding and patience in our tough period.

Kumatori, June 9, 2017  
Yuji Kawabata  
Director, KURRI

## CONTENTS

<b>I. ANNUAL SUMMARY OF EXPERIMENTAL RESEARCH ACTIVITIES</b> .....	1
<b>I-1. PROJECT RESEARCHES</b> .....	2
<b>Project 2</b> Project Research on the Elucidation of Generating Mechanism of Damaged Protein Induced by Aging and Irradiation N. Fujii (28P2) .....	3
<b>PR2-1</b> Consideration for the Distribution of D-Aspartyl Endopeptidases Activity in Various Living Things T. Kinouchi and N. Fujii (28P2-1) .....	4
<b>PR2-2</b> Damage to Biological Molecules Induced by Ionizing Irradiation and Biological Defense Mechanisms against Ionizing Radiation III T. Saito and N. Fujii (28P2-2) .....	5
<b>PR2-3</b> Separation Condition of the Prion Peptide (106-126) after Treatment of Protein L-Isoaspartyl Methyltransferase (PIMT) Y. Sadakane and N. Fujii (28P2-3) .....	6
<b>PR2-4</b> Analysis of Hearing Impairments in Mice Exposed to Environmental Stress N. Ohgami and N. Fujii (28P2-4) .....	7
<b>PR2-5</b> Identification of Contiguous $\beta$ -aspartyl Residues in Peptide Using MS N. Fujii <i>et al.</i> (28P2-5) .....	8
<b>PR2-6</b> The Stability of D- $\beta$ -Asp :kinetics of the Competitive Reactions of Isomerization and Peptide bond Cleavage K. Aki <i>et al.</i> (28P2-6) .....	9
<b>PR2-7</b> Change of Protein Function by the Replacement of a Single Aspartyl Isomer in a Protein N. Fujii <i>et al.</i> (28P2-7) .....	10
<b>Project 3</b> Studies on Actinides and Fission Products Performed at the KURRI Hot Laboratory T. Fujii (28P3) .....	11
<b>PR3-1</b> Solubility of Tetravalent Metal Hydroxide in the Presence of Isosaccharinic Acid T. Sasaki <i>et al.</i> (28P3-1) .....	12
<b>PR3-2</b> Solubility of $Zr(OH)_4(am)$ in the Presence of Carbonate Ion in Dilute to Concentrated $NaNO_3$ T. Kobayashi <i>et al.</i> (28P3-2) .....	13
<b>PR3-3</b> Electrochemical Analysis for the Redox Reaction of $UO_2^{2+}$ in Calcium Chloride Hydrate Melts A. Uehara <i>et al.</i> (28P3-5) .....	14
<b>PR3-4</b> Electronic Absorption Spectra of Selenium in LiCl-KCl Eutectic Melt Y. Sakamura <i>et al.</i> (28P3-6) .....	15
<b>PR3-5</b> Coordination Structure around $La^{3+}$ Ion in Concentrated Aqueous Solutions of LiCl N. Ohtori <i>et al.</i> (28P3-7) .....	16
<b>PR3-6</b> Study of Isotope Separation of Strontium and Calcium via Chemical Exchange Reaction R. Hazama <i>et al.</i> (28P3-9) .....	17
<b>PR3-7</b> Mutual Separation of Nd and Pr by Molten Salt Electrolysis H. Sekimoto <i>et al.</i> (28P3-10) .....	18
<b>PR3-8</b> Correction of Coincidence Sum Effect by Using $^{134}Cs$ and $^{137}Cs$ Produced through a Photo Nuclear Reaction T. Kubota <i>et al.</i> (28P3-11) .....	19
<b>Project 4</b> Project Research on Nuclear Spectroscopy and Condensed Matter Physics Using Short-Lived Nuclei Y. Ohkubo (28P4) .....	20

<b>PR4-1</b>	Site-to-Site Migration of In Impurity in Fe <sub>3</sub> O <sub>4</sub> W. Sato <i>et al.</i> (28P4-5) .....	21
<b>PR4-2</b>	Atmosphere Dependence of Formation Process of Oxygen Vacancy in Zinc Oxide S. Komatsuda <i>et al.</i> (28P4-5) .....	22
<b>Project 5</b>	Project Research on the Advanced Utilization of Multi-Element Mössbauer Spectroscopy for the Study on Condensed Matter Science M. Seto (28P5) .....	23
<b>PR5-1</b>	Mössbauer Microspectrometer Using Si-PIN Semi-conductor Detector and its Application to Mineral Sciences A. Marutani <i>et al.</i> (28P5-2) .....	24
<b>PR5-2</b>	<sup>57</sup> Fe Mössbauer Spectra of Sr <sub>2</sub> VFeAsO <sub>3-d</sub> (d = 0.232, 0.267, and 0.509) Y. Tojo <i>et al.</i> (28P5-3) .....	25
<b>PR5-3</b>	Relationship between Heme Electronic Structure and Oxygen Affinity of Myoglobin K. Hasegawa <i>et al.</i> (28P5-4) .....	26
<b>PR5-4</b>	Magnetic Property and Local Structures of Functional Irons in Glass by Mössbauer Spectroscopy N. Umesaki <i>et al.</i> (28P5-7) .....	27
<b>PR5-5</b>	Development of Mössbauer Spectroscopy System on <sup>67</sup> Zn M. Saito <i>et al.</i> (28P5-8) .....	28
<b>PR5-6</b>	Mössbauer Study of Ba <sub>0.6</sub> K <sub>0.4</sub> Fe <sub>2</sub> As <sub>2</sub> under High Magnetic Fields S. Kitao <i>et al.</i> (28P5-9) .....	29
<b>Project 6</b>	Translational Research on BNCT for Clinical Application M. Suzuki (28P6) .....	30
<b>PR6-1</b>	Preliminary Formulation of <sup>10</sup> Borono-phenylalanine Entrapped WOW Emulsion for Neutron Capture Therapy to Hepatocellular Carcinoma H. Yanagie <i>et al.</i> (28P6-6) .....	31
<b>PR6-2</b>	Pre-BNCT Biodistribution of <i>p</i> -borono-L-phenylalanine in Metastatic Bone of Human Breast Cancer-bearing Animal Model F. Fujimoto <i>et al.</i> (28P6-14) .....	32
<b>PR6-3</b>	Nanoparticle-assisted Boron Neutron Capture Therapeutics: Design of Novel Boron-Containing Nanoparticle for ROS Scavenging Ability Improving Therapeutic Efficiency with Low Adverse Effect Z. Gao <i>et al.</i> (28P6-15) .....	33
<b>PR6-4</b>	Toxicity Evaluation of <sup>10</sup> BSH Entrapped WOW Emulsion on Intra-arterial Delivery in Rabbits for Neutron Capture Therapy to Hepatocellular Carcinoma H. Yanagie <i>et al.</i> (28P6-17) .....	34
<b>PR6-5</b>	Exfoliation of Hexagonal Boron Nitride Nanosheet with Chlorin e6 and Application of the Composite to Cancer Photodynamic Therapy K. Maruyama and N. Komatsu (28P6-21) .....	35
<b>PR6-6</b>	Establishment of QA/QC Using Ionization Chamber and Bonner Sphere in BNCT Field (III) Y. Sakurai <i>et al.</i> (28P6-22) .....	36
<b>PR6-7</b>	Calculational Survey of Converter Configuration for Quality Assurance of Beam Component Distribution at KUR Using Imaging Plate K. Takata <i>et al.</i> (28P6-23) .....	37
<b>PR6-8</b>	Initial Test Operation of Patient-Position-Error Measuring System for BNCT Irradiation T. Tanaka <i>et al.</i> (28P6-26) .....	38
<b>Project 7</b>	Analyzing Tumor Microenvironment and Exploiting its Characteristics in Search of Optimizing Cancer Therapy Including Neutron Capture Therapy S. Masunaga (28P7) .....	39
<b>PR7-1</b>	Effect of Oxygen Pressure during Incubation with a <sup>10</sup> B-carrier on <sup>10</sup> B uptake Capacity of Cultured <i>p53</i> Wild-type and Mutated Tumor Cells, Referring to Dependency on <i>p53</i> Status of Tumor Cells and Types of <sup>10</sup> B-carriers S. Masunaga <i>et al.</i> (28P7-1) .....	40

<b>PR7-2</b>	Design and Synthesis of Pepducin-BSH Conjugates with Polyamine Linker A. Isono <i>et al.</i> (28P7-2) .....	41
<b>PR7-3</b>	UCHL1-HIF-1 Axis-mediated Antioxidant Property of Cancer Cells as a Therapeutic Target for Radiosensitization H. Harada <i>et al.</i> (28P7-3) .....	42
<b>PR7-4</b>	The Response and Survival of Cancer Cells after BNCR S. Imamichi <i>et al.</i> (28P7-9) .....	43
<b>Project 8</b>	Production Mechanism of Radioactive Aerosols Released from Fukushima Daiichi Nuclear Power Plant K. Takamiya (28P8) .....	44
<b>PR8-1</b>	Solution Concentration Dependence of Production Ratio of Radioactive NaCl Solution Aerosols K. Takamiya <i>et al.</i> (28P8-1) .....	45
<b>PR8-2</b>	Growth of Aerosol Particles in Irradiated Air of an Accelerator Room Y. Oki <i>et al.</i> (28P8-2) .....	46
<b>PR8-3</b>	Interaction of Radioactive Cesium and Suspended Particles in River Water A. Kirishima <i>et al.</i> (28P8-5) .....	47
<b>Project 11</b>	Project Research on a Study on Biological Character and Use of the Particle Induced by the Boron Neutron Capture Reaction Y. Kinashi (28P11) .....	48
<b>PR11-1</b>	Biological Effects of DNA Alkylating Agents on the Cell Lethal Effects of Ionizing Radiation Y. Kinashi <i>et al.</i> (28P11-1) .....	49
<b>Project 12</b>	Improvement of Characterization Techniques in High-Energy-Particle Irradiation Research A. Kinomura (28P12) .....	50
<b>PR12-1</b>	Study on Efficient Use of Positron Moderation Materials A. Kinomura <i>et al.</i> (28P12-1) .....	51
<b>PR12-2</b>	Effects of Electron-irradiation on Cu Solubility and Diffusivity in Fe Studied by Three Dimensional Atom Probe K. Nagumo <i>et al.</i> (28P12-2) .....	52
<b>PR12-3</b>	Irradiation Defects of F82H Irradiated at SINQ Using Positron Annihilation Spectroscopy K. Sato <i>et al.</i> (28P12-3) .....	53
<b>PR12-4</b>	Study on Irradiation Effect and Electrical and Optical Properties of Compound Semiconductors K. Kuriyama <i>et al.</i> (28P12-4) .....	54
<b>PR12-5</b>	Validation of D3×t0.5 TEM Disk Size Miniature Test Specimens for Post-irradiation Thermal Diffusivity Measurement M. Akiyoshi and A. Kinomura (28P12-5) .....	55
<b>PR12-6</b>	Positron Annihilation Study on Fe-Cr binary alloy after Electron Irradiation T. Onitsuka <i>et al.</i> (28P12-6) .....	56
<b>PR12-7</b>	Thermal Stability of Diamond-like Carbon Films S. Nakao <i>et al.</i> (28P12-8) .....	57
<b>Project 13</b>	Development on Neutron Imaging Application Y. Saito (28P13) .....	58
<b>PR13-1</b>	Void Fraction and Heat Transfer Characteristics in Two-Phase Flow across a Horizontal Tube Bundle H. Murakawa <i>et al.</i> (28P13-2) .....	59
<b>PR13-2</b>	Estimation of Frosting Formation on the Heat Exchanger by Using X-ray Radiography R. Matsumoto <i>et al.</i> (28P13-6) .....	60

<b>I-2. COLLABORATION RESEARCHES</b>	61
<b>1. Slow Neutron Physics and Neutron Scattering</b>	
<b>CO1-1</b>	Current Status of B-3 Beam Port of KUR, 2016 K. Mori <i>et al.</i> (28010) ..... 62
<b>CO1-2</b>	Development of an Ellipoidal Supermirror with Metallic Substrate M. Hino <i>et al.</i> (28032) ..... 63
<b>CO1-3</b>	The Correlation between Microstructural Evolution and Mechanical Property Changes in Neutron-irradiated Vanadium Alloys K. Fukumoto <i>et al.</i> (28040) ..... 64
<b>CO1-4</b>	Preliminary Study of Radiation Resistivity of <i>Bacillus Subtilis Natto</i> Y. Yanagisawa <i>et al.</i> (28049) ..... 65
<b>2. Nuclear Physics and Nuclear Data</b>	
<b>CO2-1</b>	High-Precision Mass Analysis of RI Sample for Cross-Section Measurements S. Nakamura <i>et al.</i> (28054) ..... 66
<b>CO2-2</b>	Measurement of Doppler Effect by Small Accelerator Neutron Source (1) T. Sano <i>et al.</i> (28061) ..... 67
<b>CO2-3</b>	Development of Neutron Detectors for Precise Measurement of Epi-thermal Neutrons T. Matsumoto <i>et al.</i> (28062) ..... 68
<b>CO2-4</b>	Research and Development for Accuracy Improvement of Neutron Nuclear Data on Long-lived Radioactive Nuclei at KURRI-Linac J. Hori <i>et al.</i> (28076) ..... 69
<b>4. Material Science and Radiation Effects</b>	
<b>CO4-1</b>	Millimeter Wave Absorption Spectra of Ionic Liquids T. Awano and T. Takahashi (28002) ..... 70
<b>CO4-2</b>	Synthesis of Noble Metal Nanoparticles Supported on Graphene by Irradiation Reduction Method F. Hori <i>et al.</i> (28043) ..... 71
<b>CO4-3</b>	Electron Irradiation Induced Damage Structure in Intermetallic Alloys F. Hori <i>et al.</i> (28044) ..... 72
<b>CO4-4</b>	Observation of Transient Damage States in Materials under Ion Irradiation H. Tsuchida <i>et al.</i> (28047) ..... 73
<b>CO4-5</b>	Trapping of Hydrogen Isotopes at Vacancy-Type Defects in Tungsten Y. Hatano <i>et al.</i> (28048) ..... 74
<b>CO4-6</b>	Preliminary Study of Variation in Current-Voltage Characteristics of Field Emitter Array Structure under Gamma-ray Irradiation Y. Gotoh <i>et al.</i> (28050) ..... 75
<b>CO4-7</b>	Study of the Properties of Water and the Physiological Activation Phenomena by using High-Intensity Pulsed Coherent Radiation S. Okuda <i>et al.</i> (28052) ..... 76
<b>CO4-8</b>	Spectrum of Amino Acid in the Sub-THz region using Coherent TR T. Takahashi (28058) ..... 77
<b>CO4-9</b>	Complex Structure of Ions Coordinated with Hydrophilic Polymer. 17. Inner Precipitation of Inorganic Salt as Fillers and Their Dissolution A. Kawaguchi and Y. Morimoto (28079) ..... 78
<b>CO4-10</b>	Hydrogen Retention on Plasma Facing Material Irradiated by High Energy Particle Beam K. Tokunaga <i>et al.</i> (28082) ..... 79

<b>CO4-11</b>	Presence of Diluted High-valence Fe and Sn Ions in Layered Rock-salt Structure M. Tabuchi and Y. Kobayashi (28084) .....	80
<b>5. Geochemistry and Environmental Science</b>		
<b>CO5-1</b>	Evaluation of Radioactive Cesium Behavior in Natsui River Basin, Fukushima K. Sato <i>et al.</i> (28005) .....	81
<b>CO5-2</b>	Size Distribution of Bromine in the Atmospheric Aerosols N. Ito <i>et al.</i> (28017) .....	82
<b>CO5-3</b>	Characteristics of Synthetic Calcite Thermoluminescence by Gamma and Beta Irradiation N. Hasebe <i>et al.</i> (28039) .....	83
<b>CO5-4</b>	Application of Neutron Activation Analysis to Micro Gram Scale of Solid Samples S. Sekimoto <i>et al.</i> (28066) .....	84
<b>CO5-5</b>	Characteristics of a Hydroxide by Reaction of $M_xO_y$ and $H_zT_{2-z}O$ H. Hashizume <i>et al.</i> (28069) .....	85
<b>CO5-6</b>	Chemical Variations of Miller Range 091010 (CV) Collected in the Ice at Miller Range, Antarctica N. Shirai <i>et al.</i> (28080) .....	86
<b>6. Life Science and Medical Science</b>		
<b>CO6-1</b>	Design and Synthesis of Boron-containing Compounds for Effective Accumulation in Tumor Tissues and Detection by Boron Magnetic Resonance Imaging S. Aoki <i>et al.</i> (28004) .....	87
<b>CO6-2</b>	Study of Localization Estimation of Abasic Sites in DNA Irradiated with Ionizing Radiation K. Akamatsu <i>et al.</i> (28019) .....	88
<b>CO6-3</b>	Age-related Stresses Induce Asp Isomerizations of $\alpha$ A-crystallin in Lens T. Takata and N. Fujii (28024) .....	89
<b>CO6-4</b>	LC-MS/MS Analysis of Post-translational Modifications of Lens Protein in Patients with Retinitis Pigmentosa Y. Ikeda <i>et al.</i> (28045) .....	90
<b>CO6-5</b>	Purification, Crystallization, and X-ray Diffraction Study of Lysozyme in $D_2O$ and $H_2O$ Solution T. Chatake <i>et al.</i> (28046) .....	91
<b>CO6-6</b>	Measurement of Transmittance Spectra of a Cryo-Sectioned Tissue of Brain Tumor C6 Model in the Sub-Terahertz Region-IV T. Takahashi and N. Miyoshi (28059) .....	92
<b>CO6-7</b>	The Study for Development and Application of Tissue Equivalent Neutron Dosimeter T. Oita <i>et al.</i> (28083) .....	93
<b>7. Neutron Capture Therapy</b>		
<b>CO7-1</b>	Gadolinium Accumulation using Gd-DTPA-Incorporated Calcium Phosphate Nanoparticles for Gd-neutron Capture Therapy N. Dewi <i>et al.</i> (28028) .....	94
<b>CO7-2</b>	A Fundamental Experiment for the Measure Against the Activation of the Irradiation-room Concrete at BNCT Facility (III) T. Takata <i>et al.</i> (28056) .....	95
<b>8. Neutron Radiography and Radiation Application</b>		
<b>CO8-1</b>	Research and Development of Diamond dose Rate Detector for Radiation Mapping System in Highly Active Environments Y. Takahashi <i>et al.</i> (28077) .....	96

<b>CO8-2</b>	Development of Non-destructive Methods Adapted for Integrity Test of Next Generation Nuclear Fuels Y. Takahashi <i>et al.</i> (28078) .....	97
<b>9. TRU and Nuclear Chemistry</b>		
<b>CO9-1</b>	Search for the Ultraviolet Photons Emitted from <sup>229m</sup> Th Samples Reacted with HF Gas Y. Yasuda <i>et al.</i> (28006) .....	98
<b>CO9-2</b>	Stability of Triphosphine Trioxide Extractant against $\gamma$ -Ray Irradiation in HNO <sub>3</sub> M. Nogami <i>et al.</i> (28057) .....	99
<b>10. Health Physics and Waste Management</b>		
<b>CO10-1</b>	Possibility of Suppression of Cs Elution from Incineration Fly Ash by Adding Soil M. Yoneda <i>et al.</i> (28033) .....	100
<b>CO10-2</b>	Ethnographic Study on Nuclear Reactor - Safety and Relief in Fukushima, post 3.11. - M. Takagaki <i>et al.</i> (28034) .....	101
<b>CO10-3</b>	Characteristics Measurement in High Gamma Ray dose Environments for a Neutron Detector and Amplifier Used in an Active Neutron Method M. Komeda <i>et al.</i> (28086) .....	102
<b>12. Others</b>		
<b>CO12-1</b>	Preliminary Experiments of Coherent Cherenkov Radiation Matched to the Circular Plane at KURRI-LINAC N. Sei and T. Takahashi (28030) .....	103
<b>CO12-2</b>	Structural Analysis of Solid-Liquid Interface for Tribological Study by Means of Multi-Analytical Methods Involving Neutron Reflectometry T. Hirayama <i>et al.</i> (28060) .....	104
<b>CO12-3</b>	Effective Measures on Safety, Security, Hygiene and Disaster Prevention in Laboratories T. Iimoto <i>et al.</i> (28064) .....	105
<b>CO12-4</b>	Development of a Micro-cell MWPC for a Muon-electron Conversion Search Experiment, DeeMe H. Natori <i>et al.</i> (28067) .....	106
<b>CO12-5</b>	Electron Beam Test of Avaranche Photodiode for Ganymede Laser Altimeter of Jovian Icy Satellite Exploerer M. Kobayashi <i>et al.</i> (28071) .....	107
<b>CO12-6</b>	Single Event Test using <sup>252</sup> Cf for On-board Computer used in Lean Satellite H. Masui <i>et al.</i> (28085) .....	108
<b>II. PUBLICATION LIST (April 2016 – March 2017) .....</b>		<b>109</b>

# **ANNUAL SUMMARY OF EXPERIMENTAL RESEARCH ACTIVITIES**

## **I-1. PROJECT RESEARCHES**

## PR2 Project Research on the Elucidation of Generating Mechanism of Damaged Protein Induced by Aging and Irradiation

N. Fujii

*Research Reactor Institute, Kyoto University*

### Objectives and Allotted Research Subjects:

The aim of this project research is to elucidate the correlation between the change of the protein structure induced by various post-translational modifications with UV irradiation, gamma-irradiation, aging and protein function. We also investigate the repair mechanism for the damaged protein by irradiation. In this year, the 7 research subjects were carried out. The allotted research subjects (ARS) are as follows;

**ARS-1:** Consideration for the distribution of D-aspartyl endopeptidases activity in various living things (T. Kinouchi and N. Fujii)

**ARS-2:** Damage to biological molecules induced by ionizing irradiation and biological defense mechanisms against ionizing radiation III (T. Saito and N. Fujii)

**ARS-3:** Separation condition of the Prion Peptide (106-126) after treatment of protein L-isoaspartyl methyltransferase (PIMT) (Y. Sadakane and N. Fujii)

**ARS-4:** Analysis of hearing impairments in mice exposed to environmental stress (N. Ohgami and N. Fujii)

**ARS-5:** Identification of contiguous  $\beta$ -aspartyl residues in peptide using MS (N. Fujii, S. Kishimoto and N. Fujii)

**ARS-6:** The stability of D- $\beta$ -Asp:kinetics of the competitive reactions of isomerization and peptide bond cleavage (K. Aki, E. Okamura and N. Fujii)

**ARS-7:** Change of protein function by the replacement of a single aspartyl isomer in a protein (N. Fujii, H. Sakaue, T. Kinouchi, N. Fujii and T. Takata).

### Main Results and Contents of This Project

**ARS-1:** Kinouchi and Fujii have been researching an evolutionary origin of D-Aspartyl endopeptidase (DAEP), which stereoselectively degrades D-aspartate-containing protein. As a result of searching for a distribution of DAEP in various living things, the activity could be de-

tected only in the animal reproductive tissue. We therefore supposed that the original and primitive physiological functions of DAEP might be associated with fertilization and/or oocyte maturation.

**ARS-2:** Saito *et al.* determined the 1% survival rate of the E. coli clone to be 271 Gy and generated an E. coli cell population with approximately 3-fold resistance to gamma rays, compared with wild-type E. coli, by a directed evolution experiment.

**ARS-3:** Sadakane *et al.* determined the HPLC condition for separation of the prion peptides (106-126) containing isomerized Asp residues generated after treatment of a repair enzyme for aged protein, PIMT.

**ARS-4:** Ohgami *et al.* suggested that mice exposed to elements including barium and manganese via drinking water accumulates in inner ears resulting in hearing loss with neurodegeneration of auditory neurons. Further study is needed to investigate aggregation of a specific protein in the auditory neurons in inner ears.

**ARS-5:** Fujii *et al.* identified the contiguous  $\beta$ -aspartyl residues in a peptide by the analysis of the 2nd generation product ion spectrum of ion trap MS.

**ARS-6:** Aki *et al.* determined the rate constants of two competitive reactions, isomerization and peptide bond cleavage at Asp residue in  $\alpha$ A-crystallin fragment containing L- $\alpha$ - and D-  $\beta$ -Asp-58 isomers. The results clearly indicate that D-  $\beta$ -Asp is stable in competitive reaction pathway of isomerization and peptide bond cleavage at Asp residue.

**ARS-7:** Fujii *et al.* synthesized the Asp isomer-containing RNase A using expressed protein ligation (EPL). The RNase A variants with different Asp isomers decreased the enzyme activity and solubility.

## PR2-1 Consideration for the Distribution of D-Aspartyl Endopeptidases Activity in Various Living Things

T. Kinouchi and N. Fujii

Research Reactor Institute, Kyoto University

**INTRODUCTION:** D-Aspartyl endopeptidase (DAEP), which was discovered in the liver of mammals, stereoselectively recognizes and degrades D-isomer of aspartate (D-Asp) residue in peptides/proteins [1]. D-Asp residue is often detected in low-turnover proteins, e.g., crystallin, prion protein and  $\beta$ -amyloid protein, and these harmful proteins are mostly causing age-related diseases e.g., cataract, prion disease and Alzheimer's disease, respectively. Therefore, it seemed that DAEP would physiologically serve as a kind of quality-control system against the abnormally aggregated D-Asp-containing protein. However, in searching for a tissue-distribution of DAEP in various living things besides mammals, the high activity of DAEP could not be specifically detected in their livers. For example, in African clawed frog (*Xenopus laevis*), high DAEP activity was detected in its testes, ovaries and unfertilized eggs. As a result of searching the distribution of DAEP in other aquatic animals; Japanese green sea urchin, *Hemicentrotus pulcherrimus*, and the ascidian, *Ciona intestinalis*, high DAEP activity was shown in their reproductive organs as a common feature. On the other hand, the existence and distribution of DAEP in plants are still ambiguous. Because, although we tried to detect the DAEP activity in some plants; radish, tomato and broccoli, it was difficult to distinguish the fluorescence liberated in the measurement of DAEP activity from the auto-fluorescence of pigments in those plant samples. In order to make clear the distribution of DAEP in plants, we searched the DAEP activity in the common duckweed (*Lemna minor*) grown under the low-light condition. Because the common duckweed grows and loses the green pigment even under the relatively dark condition.

**EXPERIMENTS:** Plant Materials and Growth Conditions> Common duckweed (*Lemna minor*) was kindly gifted by Dr. Masaru Kobayashi, Kyoto University, and was cultivated at 23°C in hydroponic media containing major nutrients (1 mM Ca(NO<sub>3</sub>)<sub>2</sub>, 0.5 mM KH<sub>2</sub>PO<sub>4</sub>, 0.5 mM K<sub>2</sub>SO<sub>4</sub>, 1 mM MgSO<sub>4</sub>, and 1.5 mM NH<sub>4</sub>NO<sub>3</sub>) and micronutrients (75  $\mu$ M EDTA-Fe, 46  $\mu$ M H<sub>3</sub>BO<sub>3</sub>, 9  $\mu$ M MnSO<sub>4</sub>, 0.8  $\mu$ M ZnSO<sub>4</sub>, 0.3  $\mu$ M CuSO<sub>4</sub>, and 0.8  $\mu$ M Na<sub>2</sub>MoO<sub>4</sub>) under a 16-h low-light/8-h dark cycle in a 60%-humidified growth chamber.

Extraction of Crude Enzyme> Vegetatively propagated common duckweeds were harvested and immediately homogenized by Polytron<sup>®</sup> PT2100 agitator in ice-cold sodium phosphate buffer (pH 7.5). The suspension was filtered through a double layer of cheesecloth and centrifuged at 600 xg for 10 min at 4°C. Since the supernatant was crude enzyme mixtures that might include not only DAEP but also other proteases, the appropriate dose of protease inhibitor cocktail for plant cell extracts (purchased from Sigma-Aldrich, Inc) was added to it. This final supernatant was applied to the measurement of DAEP activity.

Measurement of DAEP activity> We developed an assay system for DAEP activity using the synthetic D-Asp containing substrate, Succinyl-D-Aspartic acid  $\alpha$ -(4-methyl-coumaryl-7-amide) (Suc-D-Asp-MCA) [1,2]. Supernatant of the above samples was mixed and incubated with 0.1 mM Suc-D-Asp-MCA and the assay buffer (10 mM Tris-HCl (pH 8.5), 200 mM NaCl, 3 mM MgCl<sub>2</sub>) at 25°C. The fluorescence of aminomethyl-coumarin liberated from Suc-D-Asp-MCA by DAEP was measured at  $\lambda_{ex}$  = 380 nm and  $\lambda_{em}$  = 460 nm.

**RESULTS & DISCUSSION:** As had been expected, the extract from the common duckweed grown under the low-light condition did not include a high amount of spontaneous pigments. However, the DAEP activity was not detectable. It was suggested that plants do not have any DAEP activity, or have quite low amounts. On the other hand, in animals, the DAEP activity was distributed in the reproductive organ, regardless of any species of animal. We therefore supposed that DAEP might be developed and associated with fertilization and/or oocyte maturation in the evolution of animals.

### REFERENCES:

- [1] T. Kinouchi *et al.*, Biochem. Biophys. Res. Commun., **314** (2004) 730-736.
- [2] T. Kinouchi *et al.*, Chem. Biodivers., **7** (2010) 1403-1407.

## PR2-2 Damage to Biological Molecules Induced by Ionizing Irradiation and Biological Defense Mechanisms against Ionizing Radiation III

Takeshi Saito and Noriko Fujii

Research Reactor Institute, Kyoto University

**INTRODUCTION:** There are various environments in nature, and organisms have evolved diversely to adapt to most of them. Some organisms can survive in environments that are considered extremely severe by our common sense. Elucidation of the adaptive mechanisms of organisms to severe environments will provide meaningful information regarding the evolution and diversity of whole organisms. Of these organisms, some bacteria have extremely high resistance to ionizing radiation [1]. The extreme resistance mechanisms of these bacteria are an interesting research subject to consider when studying adaptation to the environment. In order to elucidate radioresistance mechanisms, it is important to investigate the molecular mechanisms of the biological defense of organisms with radioresistant activity against external stress and the damage of biological molecules due to the ionizing radiation. Nevertheless, the study of radioresistant organisms in nature is expected to face several challenges, as knowledge on their genetic and biochemical properties is poor. In this study, we attempted to generate radioresistant *Escherichia coli* by a directed evolution experiment in which the following operations were repeated: gamma-ray irradiation of *E. coli*, whose genetic and biochemical properties are well known, growth of surviving cells, and irradiation of the grown cells.

**EXPERIMENTS: Evaluation of the sensitivity of *E. coli* to gamma rays:** *E. coli* K-12 cells were grown to the early log phase in LB medium at 37°C at 200 rpm. One milliliter of culture was centrifuged at  $4000 \times g$  at 20°C for 10 min. The supernatant was discarded and the pellet was suspended in 1 mL of PBS(-). The cell suspension was irradiated with gamma rays at a dose rate of 25 Gy/min at room temperature. Gamma irradiation was carried out at the Co-60 Gamma-ray Irradiation Facility of the Kyoto University Research Reactor Institute. The gamma-irradiated cell suspension was diluted appropriately with PBS(-), plated on LB agar, and incubated at 37°C for 12 hr. Colonies were counted, colony forming units (CFUs) were determined, and survival rates were calculated.

**Selection with gamma rays:** *E. coli* K-12 clone cells obtained by single colony pick-up were grown to the early log phase in LB medium at 37°C at 200 rpm. The cell suspension was prepared as described above. The cell suspension was irradiated with 1% survival dose of

gamma rays at a dose rate of 25 Gy/min at room temperature. One milliliter of gamma-irradiated cell suspension was inoculated in 100 mL LB medium and grown to the early stationary phase at 37°C at 200 rpm. Glycerol stock was prepared and stored at -80°C. This protocol was repeated with cells from the glycerol stock grown to the early log phase.

**RESULTS:** In order to evaluate the sensitivity of *E. coli* to gamma rays, *E. coli* clone cells were irradiated with gamma rays, and CFUs of the irradiated cells were determined by the colony forming method. Fig. 1 shows the relationship between the absorbed dose of gamma rays and the survival rate of *E. coli*. The 1% survival rate of this clone was determined to be 271 Gy.

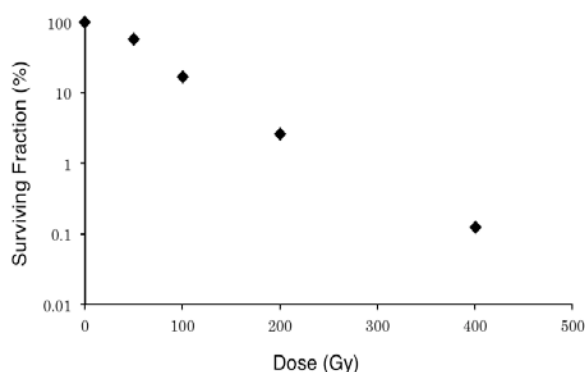


Fig. 1. Relationship between the absorbed dose of gamma rays and the survival rate of *E. coli*.

In order to generate radioresistant *E. coli* by directed evolution using gamma rays as the selection pressure, *E. coli* were irradiated with 1% survival dose of gamma rays, surviving cells were grown, the 1% survival dose of the grown cell population to the same radiation was evaluated, and the cell population was irradiated again with 1% survival dose. By repeating this operation eight times, an *E. coli* cell population with approximately 3-fold resistance to gamma rays compared with *E. coli* without selection, was obtained. Further studies, namely the generation of higher gamma-ray-resistant *E. coli* by employing a higher number of repetitions of the selection cycle and analysis of the genetic and biochemical properties of the resulting *E. coli* strain, will be required to reveal the biological defense mechanisms in response to ionizing radiation.

### REFERENCE:

[1] T. Saito, *Viva Origino*, **30** (2007) 85–92.

## PR2-3 Separation Condition of the Prion Peptide (106-126) after Treatment of Protein L-Isoaspartyl Methyltransferase (PIMT)

Y. Sadakane and N. Fujii<sup>1</sup>

Department of Pharmaceutical Sciences, Suzuka University of Medical Science

<sup>1</sup>Research Reactor Institute, Kyoto University

**INTRODUCTION:** In previous study, we prepared PIMT by *E. coli* expression system, and determined the HPLC condition for separation of the peptides containing isomerized Asp residues generated after treatment of repairing enzyme, PIMT. Using model peptide T10 (HFSPEDLTVK of crystalline), we succeeded in finding the separation condition for the mixture of six T10 peptides bearing L-Asp, L-isoAsp, D-Asp, D-isoAsp, methyl ester Asp and succinimide. The mixture was separated by reversed-phased HPLC with 15 % acetonitrile with pH 3.0 of 15 mM phosphate buffer. The stereoconversion of aspartyl (Asp) residue arise through intramolecular rearrangement, such as *via* a succinimide intermediate. L-isoaspartyl methyltransferase (PIMT) catalyzes repair of L-isoAsp peptide bonds in aged proteins by transferring a methyl group from S-adenosylmethionine to a  $\alpha$ -carboxyl group of L-isoAsp residue (Fig.1). In this study, we determined the separation condition for prion peptide (106-126) containing isomerized Asp residues generated after treatment of repairing enzyme, PIMT because the deamidation of Asn residue in prion peptide has been reported to affect its channel activity in planar lipid bilayer.

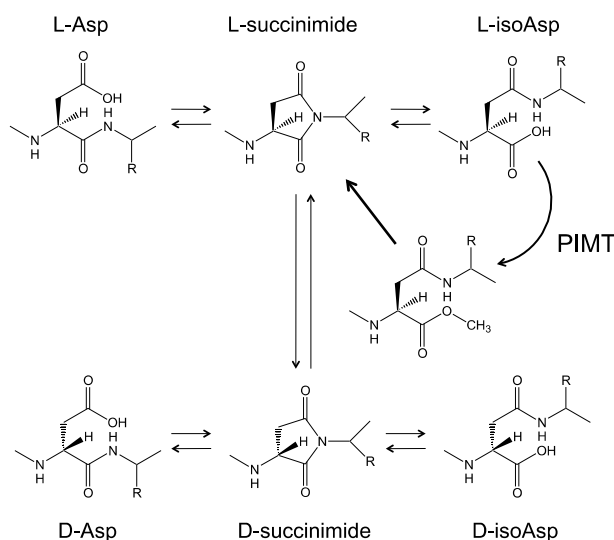


**Fig. 1** The  $\beta$ -linkage isomerization and stereoinversion to D-form of aspartyl residue and PIMT repair system.

**EXPERIMENTS:** The recombinant PIMT protein was prepared by His-tag conjugated *E. coli* expression system, and the four isomerized prion peptides (KTNM-KHMAGAAA AGAVVGGGLG) were synthesized by using Fmoc amino acids. The prion peptide bearing L-isoAsp residue was treated by PIMT for 60 min at 37 °C, and the reaction was stopped by addition of HCl for generating the peptides bearing methyl ester and succinimide. The reacted sample was analyzed by reversed-phase HPLC with acetonitrile/H<sub>2</sub>O containing 15 mM phosphate buffer, detected by absorption at 215 nm.

**RESULTS:** PIMT transfers the methyl group of S-adenosylmethionine onto a  $\alpha$ -carboxyl group of L-isoAsp residue of prion peptide, then resulted in generating the peptide bearing methyl ester. The methyl ester undergoes spontaneously and rapidly demethylation (15 min, half-time) to generate succinimide intermediate. The intermediate was hydrolyzed (1 hr, half-time) to produce the prion peptide bearing L-Asp or L-isoAsp residue. To determine the separate condition the isomerized peptides, we prepared the mixture of the prion peptides bearing L-Asp, L-isoAsp, D-Asp and D-isoAsp, and PIMT-reacted solution, which included the peptide bearing methyl ester and succinimide. (Fig. 2). We became able to determine easily the kinetics of cyclization and de-cyclization of succinimide intermediate.

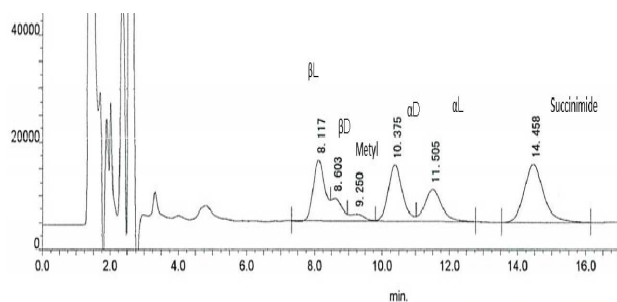


**Fig. 2** Separation of prion peptides containing various isomerized Asp residue by standard HPLC. The mixture of six peptides were separated by reversed-phase HPLC with ODS column using the eluent 20 % acetonitrile with pH 3.0 of 15 mM phosphate buffer and 100 mM NaCl.  $\beta$ L: the peptide containing L-isoAsp residue,  $\beta$  D: D-isoAsp residue,  $\alpha$ D: D-Asp residue, methyl: methyl ester,  $\alpha$ L: L-Asp residue.

## PR2-4 Analysis of Hearing Impairments in Mice Exposed to Environmental Stress

N. Ohgami and N. Fujii<sup>1</sup>

*Units of Environmental Health Sciences, Department of Biomedical Sciences, College of Life and Health Sciences, Chubu University.*

<sup>1</sup>*Research Reactor Institute, Kyoto University*

**INTRODUCTION:** Exposure to elements in occupational and daily environments is known to cause health risks in humans [1,2]. However, there is very limited information that the ingestion of elements from food and water can be a risk to our health. In a previous study, it has been suggested that we are exposed to barium via drinking water and foods [1]. Also, exposure to barium has been shown to affect blood pressure [2], and direct injection of barium to inner ears has been shown to affect physiological functions in inner ears [3]. However, it remains unknown whether ingestion of barium via drinking water affects hearing levels in experimental animals. This study aimed at analyzing whether ingestion of barium affects hearing levels and morphology of inner ears in mice.

**EXPERIMENTS:** Oral exposure to barium chloride (BaCl<sub>2</sub>) to wild-type ICR mice for 2 weeks via drinking water was performed. We measured barium levels in various tissues with inductively coupled plasma mass spectrometry (ICP-MS, Agilent 7500cx). We also performed pathological analyses of inner ears as described previously [4]. After oral exposure to BaCl<sub>2</sub> via drinking water, we performed auditory brain stem responses (ABR) to measure hearing levels in mice [4]. This study was approved by the Institutional Animal Care and Use Committee in Chubu University (approval number: 2510053). This study also followed the Japanese Government Regulations for Animal Experiments. We further performed an epidemiological analysis to determine a correlation between hearing loss and barium levels in biological samples in humans. This study was performed after an approval of Nagoya University International Bioethics Committee following the regulations of the Japanese government (approval number 2013-0070).

**RESULTS:** Mice orally exposed to barium showed hearing loss, especially at higher frequency in mice. Mice orally exposed to barium showed neurodegener-

ation in inner and outer hair cells, stria vascularis and spiral ganglion neurons in the organ of Corti. Correspondingly, mice orally exposed to barium showed higher levels of barium in inner ears than those in control [5]. In a previous study, exposure to manganese has been shown to cause aggregation of proteins resulting in neurodegeneration [6]. Therefore, we further determine hearing loss in mice orally exposed to manganese. After exposure, the exposed group showed hearing loss and neurodegeneration of auditory neurons [7].

**Conclusions:** This study suggests that mice exposed to elements including barium and manganese via drinking water accumulates in inner ears resulting in hearing loss with neurodegeneration of auditory neurons. In our epidemiological study, barium levels in toenails and hair were significantly associated with hearing loss in humans [8]. Thus, it is possible that oral exposure to barium causes hearing loss in humans. On the other hand, our previous study showed that exposure to noise stress caused increased levels of oxidative stress and positive signals stained by anti-D-beta-Asp antibody in inner ears [9]. Therefore, we will pursue a research to elucidate a mechanism of degeneration of auditory neurons, especially to investigate whether exposure to noise or elements causes a protein aggregation in inner ears.

### REFERENCES:

- [1] ATSDR (Agency for Toxic Substances and Disease Registry). 2005.
- [2] NTP (National Toxicology Program), (1994) **432**,1-285.
- [3] S. Takeuchi and M. Ando, *Am. J. Physiol.* (1999) **277**, 91-99.
- [4] N. Ohgami *et al.*, *Proc. Natl. Acad. Sci. USA.*, (2010) **107**, 13051-13056.
- [5] N. Ohgami *et al.*, *NeuroToxicology*, (2012) **33**, 1276-1283.
- [6] T. Verina *et al.*, *Toxicol. Lett.*, (2013) **217**, 177-183.
- [7] N. Ohgami *et al.*, *Sci. Rep.*, (2016) **6**, 36306.
- [8] N. Ohgami *et al.*, *J. Expo. Sci. Environ. Epidemiol.*, (2016) **26**, 488-493.
- [9] H. Tamura, N. Ohgami, N. Fujii *et al.*, *PLoS ONE*, (2012) **7**(6), e39807.

## PR2-5 Identification of Contiguous $\beta$ -aspartyl Residues in Peptide Using MS

N. Fujii, S. Kishimoto<sup>1</sup> and N. Fujii<sup>2</sup>

Radioisotope Research Center, Teikyo University

<sup>1</sup>Faculty of Pharma Sciences, Teikyo University

<sup>2</sup>Research Reactor Institute, Kyoto University

**INTRODUCTION:** We developed a method for four Asp isomers (L $\alpha$ -, L $\beta$ -, D $\alpha$ -, D $\beta$ -Asp) at individual sites in proteins by liquid chromatography - tandem mass spectrometry (LC-MS/MS) system because the four Asp isomers containing peptides were eluted at the different time on the chromatogram [1]. However, to identify the four Asp isomers on the chromatogram, it is necessary to synthesize reference peptides containing the for different Asp isomers as standards. This is time-consuming. Last year, we reported a method for identifying the  $\beta$ -Asp containing peptides by detecting the specific 2nd generation product ions using an ion trap mass spectrometer (MS). In this study, the contiguous Asp residues in peptide couldn't be ever identified an isomer, but it is possible to identify the  $\beta$ -Asp residue by an advanced method using MS.

**EXPERIMENTS:** The peptides containing Asp isomers were made using a fmoc solid-phase chemistry. The synthetic peptides were human  $\alpha$ A-crystallin sequence from residues 89 to 99 peptides ( $\alpha$ AT11 peptide) containing L $\alpha$ - or L $\beta$ -Asp isomers; VQ(L $\alpha$ -D)(L $\alpha$ -D)FVEIHGK ( $\alpha$ AT11  $\alpha$ - $\alpha$ ), VQ(L $\alpha$ -D)(L $\beta$ -D)FVEIHGK ( $\alpha$ AT11  $\alpha$ - $\beta$ ), VQ(L $\beta$ -D)(L $\alpha$ -D)FVEIHGK ( $\alpha$ AT11  $\beta$ - $\alpha$ ), VQ(L $\beta$ -D)(L $\beta$ -D)FVEIHGK ( $\alpha$ AT11  $\beta$ - $\beta$ ).

MS was performed on an ion trap system (LCQ Fleet, Thermo). The 1st and 2nd generation precursor ion of  $\alpha$ AT11 peptides were selected the  $[M+2H]^{2+}$  ion at 643.8 m/z and the  $y_8$  fragment ion at 944.4 m/z or the  $y_9$  fragment ion at 1059.5 m/z.

**RESULTS:** In order to analyze the fourth Asp residues from N-terminal side in peptide, the 1st and 2nd generation precursor ion of  $\alpha$ AT11 peptides were selected the  $[M+2H]^{2+}$  ion at 643.8 m/z and the  $y_8$  fragment ion at 944.4 m/z. Fig. 1 shows the 2nd generation product ion spectrum of  $\alpha$ AT11 peptide containing four types of Asp isomers. The specific fragment ions of 871.4 m/z ( $y_8$ -73) and 853.4 m/z ( $y_8$ -91) were observed in the spectrum of  $\alpha$ AT11  $\alpha$ - $\beta$  and  $\alpha$ AT11  $\beta$ - $\beta$ . The  $y_8$ -91 and  $y_8$ -73 were observed in the 2nd generation product ion spectrum of fourth  $\beta$ -Asp residues from N-terminal side containing  $\alpha$ AT11 peptides (Fig. 1b, d), while these product ions were not observed for fourth  $\alpha$ -Asp residues from N-terminal side containing  $\alpha$ AT11 peptides (Fig 1a, c).

In order to analyze the third Asp residues from N-terminal side, the 1st and 2nd generation precursor ion of  $\alpha$ AT11 peptides were selected the  $[M+2H]^{2+}$  ion at 643.8 m/z and the  $y_9$  fragment ion at 1059.5 m/z. Fig. 2

shows the 2nd generation product ion spectrum of  $\alpha$ AT11 peptide containing four types of Asp isomers. The specific fragment ions of 986.4 m/z ( $y_9$ -73) and 968.4 m/z ( $y_9$ -91) were observed in the spectrum of  $\alpha$ AT11  $\beta$ - $\alpha$  and  $\alpha$ AT11  $\beta$ - $\beta$ . The  $y_9$ -91 and  $y_9$ -73 were observed in the 2nd generation product ion spectrum of third  $\beta$ -Asp residues from N-terminal side containing  $\alpha$ AT11 peptides (Fig 2c, d), while these product ions were not observed for third  $\alpha$ -Asp residues from N-terminal side containing  $\alpha$ AT11 peptides (Fig. 2a, b).

These results indicated that to select the 2nd generation precursor ion of the peptides distinguish the individual contiguous  $\beta$ -aspartyl residues in peptide.

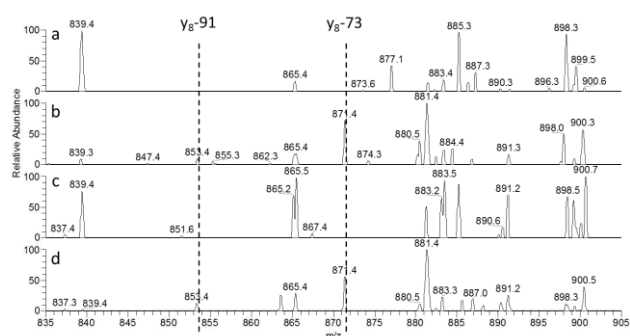


Fig. 1 Second generation product ion spectra of four types of isomeric Asp residues in  $\alpha$ AT11 synthetic peptides; a)  $\alpha$ AT11  $\alpha$ - $\alpha$ , b)  $\alpha$ AT11  $\alpha$ - $\beta$ , c)  $\alpha$ AT11  $\beta$ - $\alpha$  and d)  $\alpha$ AT11  $\beta$ - $\beta$ .

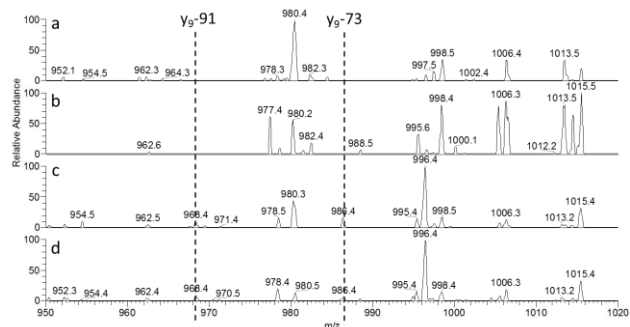


Fig. 2 Second generation product ion spectra of four types of isomeric Asp residues in  $\alpha$ AT11 synthetic peptides; a)  $\alpha$ AT11  $\alpha$ - $\alpha$ , b)  $\alpha$ AT11  $\alpha$ - $\beta$ , c)  $\alpha$ AT11  $\beta$ - $\alpha$  and d)  $\alpha$ AT11  $\beta$ - $\beta$ .

**CONCLUSION:** Identification of contiguous  $\beta$ -aspartyl residues in peptide has been established by the analysis of the 2nd generation product ion spectrum of ion trap MS us.

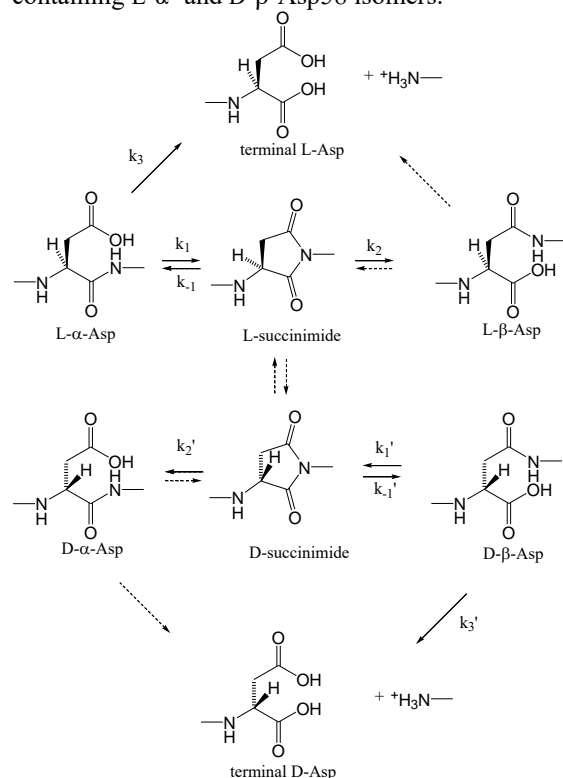
### REFERENCE:

[1] N. Fujii *et al.*, J. Biol. Chem. 287 (2012) 39992 - 40002.

K. Aki, E. Okamura and N. Fujii<sup>1</sup>

*Faculty of Pharmaceutical Sciences Himeji Dokkyo University.* <sup>2</sup>*Research Reactor Institute, Kyoto University*

**INTRODUCTION:** It is well known that L-amino acids are main constituents of peptides and proteins in a living body. D-β-aspartyl (Asp) residue has been found in a living body such as aged lens crystalline [1]. Natural L-α-Asp isomerize to the uncommon D-β-Asp form via a succinimide intermediate. At Asp residue, isomerization and peptide bond cleavage compete with each other as shown Scheme 1. No information has been provided about these competitive processes because each reaction has been studied separately. In this study, the two competitive reactions, isomerization and peptide bond cleavage at Asp residue, were simultaneously observed and compared in αA-crystallin fragment, S<sup>51</sup>LFRTVLD<sup>58</sup>SG<sup>60</sup> containing L-α- and D-β-Asp58 isomers.



**Scheme 1** Competitive reaction pathway of isomerization and peptide bond cleavage next to Asp.

**EXPERIMENTS:** Isomers of αA-crystallin fragment S<sup>51</sup>LFRTVLD<sup>58</sup>SG<sup>60</sup> composed of L-α- and D-β-Asp residues were synthesized by Fmoc solid-phase chemistry using an automated solid-phase peptide synthesizer (Shimadzu PSSM-8). The peptides were dissolved in 50 mM acetate buffer (pH 3.6 – 4.5) and incubated at 60 °C. Each solution was sampled typically after 0–120 h, and subject to RP-HPLC. The loss of reactants and the increase of products were quantified by using HPLC elu-

tion profiles.

**RESULTS:** In Figures 1A and 1B, the increase in the products of isomerization and peptide bond cleavage is quantified as a function of time, together with the decrease of the respective reactants, L-α- and D-β-Asp58. To quantify how each competitive reaction proceeds in L-α- and D-β- isomers, we have determined the rate constants ( $k_{\pm 1}$  ( $k_{\pm 1}'$ ) for succinimide formation,  $k_2$  ( $k_2'$ ) for isomerization,  $k_3$  ( $k_3'$ ) for peptide bond cleavage) for isomerization and bond cleavage reactions at L-α- and D-β-Asp in accordance with the first-ordered reaction model as illustrated in Scheme 1. In Table 1, the obtained rate constants of isomerization and peptide bond cleavage of L-α- and D-β-Asp58 in an αA-crystallin fragment are summarized. The stability of D-β-Asp is because of the suppression of peptide bond cleavage and the enhanced reverse reaction from D-Suc to D-β-Asp after D-β-Asp is converted into D-Suc. Such specific reactivity at D-β-Asp residue is probably the reason for the gradual accumulation of abnormal D-β-Asp in a native αA-crystallin [2].

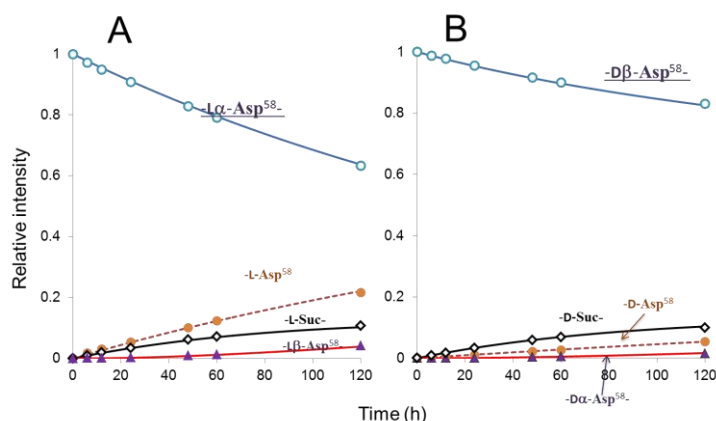


**Figure 1** Change in the HPLC peak intensities accompanied by isomerization and peptide bond cleavage at (A) L-α- and (B) D-β-Asp58 at pH 4.0.

**Table 1** Rate constants of isomerization and peptide bond cleavage.

pH	L-α-Asp58				D-β-Asp58				
	$k_1$	$k_{-1}$	$k_2$	$k_3$	$k_1'$	$k_{-1}'$	$k_2'$	$k_3'$	
3.6	0.7±0.1	n.d.	n.d.	3.6±0.1	3.6	0.8±0.1	n.d.	n.d.	1.2±0.1
4.0	1.8±0.1	2.9±0.9	5.5±0.2	2.3±0.1	4.0	1.6	7.9	2.1	0.5
4.5	1.5±0.1	6.6±1.1	11.0±0.2	1.1±0.1	4.5	1.1±0.1	13.5±1.4	3.8±0.1	0.14±0.01

In  $10^{-3} \text{ h}^{-1}$  unit.

**Acknowledgment:** The authors are grateful to Prof. N. Fujii of Research Reactor Institute, Kyoto University.

### REFERENCES:

- [1] N. Fujii *et al.*, *J. Biochem.* **116** (1994) 663–669.  
 [2] K. Aki and E. Okamura, *J. Pept. Sci.* **23**(1) (2017) 28-37

N. Fujii, H. Sakaue, T. Kinouchi, N. Fujii\* and T. Takata  
*Research Reactor Institute, Kyoto University*  
 \*Radioisotope Research Center, Teikyo University

**INTRODUCTION:** Protein composed of exclusively L-amino acids. However, recent studies have demonstrated the presence of many D-aspartyl (Asp)-containing proteins in various aged tissues such as eye lens, brain, and skin. L $\alpha$ -Asp residues in proteins can be non-enzymatically isomerized to abnormal L $\beta$ -, D $\alpha$ - and D $\beta$ -Asp isomers under physiological conditions via formation of a succinimidyl intermediate over time. Isomerization of Asp is considered to be a trigger of protein denaturation because it induces elongation of the main chain and a different orientation of the side chain within the protein structure. However, previous studies have found no direct evidence of the effects of Asp isomers on protein function. Therefore, the production of Asp isomer-containing proteins is required to verify the effects of Asp isomerization. Here, we describe the process of obtaining an Asp isomer-containing protein using expressed protein ligation (EPL).

**EXPERIMENTS:** As a model protein, bovine pancreatic ribonuclease A (RNase A, 124 amino acid residues, EC 3.1.27.5), which catalyzes the cleavage of phosphodiester bonds in RNA, was used. In this study, L $\alpha$ -Asp at position 121 in RNase A was replaced with L $\beta$ -, D $\alpha$ - and D $\beta$ -Asp because aspartic acid at position 121 is located near the active site and related to RNA cleavage. We synthesize the recombinant RNase A (1-109) with intein at C-terminus by recombinant DNA technology and RNase A (110-124) containing L $\alpha$ -, L $\beta$ -, D $\alpha$ - and D $\beta$ -Asp at position 121 by chemical synthesis. The two segments of RNase A were combined by EPL to create the RNase A which was replaced with L $\beta$ -, D $\alpha$ - and D $\beta$ -Asp at the position 121. The catalytic activity of RNase A toward 2',3'-cCMP was measured by monitoring the increase in absorbance at 284 nm.

**RESULTS:** It is the first time to create a protein containing four different Asp isomers<sup>1</sup>. The short segment of RNase A (110-124) was connected to the large segment of RNase A (1-109). The ligation efficiency did not differ among the different types of Asp isomer. Figure 1 shows the time course of the activity of the RNase A variants with different Asp isomers. The catalytic activity of L $\alpha$ -RNase A was at the same level as commercially available RNase A (Sigma-Aldrich, St. Louis, MO, USA). On the other hand, replacement of the L $\alpha$ -Asp isomer at position 121 with L $\beta$ -, D $\alpha$ - and D $\beta$ -Asp decreased the RNase activity.

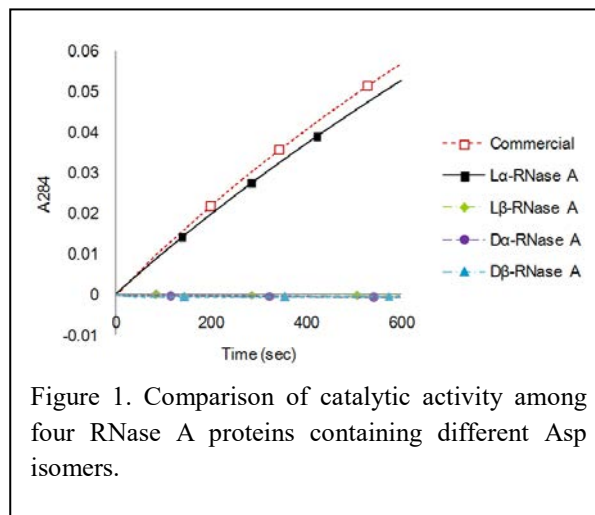


Figure 1. Comparison of catalytic activity among four RNase A proteins containing different Asp isomers.

The solubility of RNase A differed depending on the type of replacement Asp isomer. RNase A containing L $\alpha$ -Asp and D $\alpha$ -Asp was soluble in water at a final concentration of 1 mg/mL. By contrast, RNase A containing L $\beta$ -Asp and D $\beta$ -Asp showed very low solubility in water.

## DISCUSSION

This study clearly indicated that the introduction of Asp isomers into a protein decreases protein function and leads to insolubilization. Our previous study demonstrated that the isomerization of one Asp residue in a partial peptide of  $\alpha$ B-crystallin induced changes in secondary structure, hydrophobicity, and chaperone activity<sup>2</sup>. Molecular dynamics simulation also revealed that inversion of L-leucine to D-leucine at position 2 in the tetrapeptide Leu-Leu-Gly-Asp induced a change in three-dimensional structure<sup>3</sup>. These structural changes may be a trigger of protein dysfunction and insolubilization. Exploring the role of D-amino acids in proteins in an L-amino acid world opens up a new field of protein science and will be useful to understand the mechanism underlying the onset of age-related disease.

## REFERENCES:

- [1] H. Sakaue *et al.*, *ACS Omega* **2**, 260–267 (2017).
- [2] N. Fujii *et al.*, *Amino Acids* **2010**, *39* (5), 1393–1399.
- [3] Gossler-Schofberger *et al.*, *Arch Biochem Biophys* **2012**, *522* (2), 100–106.

## PR3 Studies on Actinides and Fission Products Performed at the KURRI Hot Laboratory

T. Fujii

*Graduate School of Engineering, Osaka University*

### 1. Objectives and Allotted Research Subjects

Studies on actinide and fission product nuclides with careful management are being more important for reprocessing, disposal, partitioning, and transmutation processes in the nuclear fuel cycle. Hot laboratory of KURRI is one of core facilities in Japan, in which various nuclides can be handled. This project enhances utilization of the KURRI hot laboratory by opening for fundamental and application studies related to radiochemistry, nuclear chemistry, environmental chemistry, geochemistry, and so on. Allotted research subjects are;

- ARS-1 Complexation of actinides with organic substances (T. Sasaki *et al.*).
- ARS-2 Solubility of actinide compounds in aqueous media (T. Kobayashi *et al.*).
- ARS-3 Leaching of actinides and FPs from fuel debris (N. Sato *et al.*).
- ARS-4 Neutron irradiation damage of vitrified waste matrices (T. Nagai *et al.*).
- ARS-5 Coordination behavior of actinides in ionic liquids (A. Uehara *et al.*).
- ARS-6 Electrochemical behavior of uranium in pyroprocessing system (Y. Sakamura *et al.*).
- ARS-7 Molecular dynamics simulation of actinide and FP ions in melts (N. Ohtori *et al.*).
- ARS-8 Fundamental study of fission products for trans-actinide chemistry (Y. Kasamatsu *et al.*).
- ARS-9 Isotope fractionation of Sr and Ca by chemical exchange method (R. Hazama *et al.*).
- ARS-10 Thermochemical measurement of rare earth complexes (H. Sekimoto *et al.*).
- ARS-11 Migration behavior of radiocesium in plants (T. Kubota *et al.*).
- ARS-12 Isotopic composition of radionuclides in environmental samples (Y. Shibahara *et al.*).
- ARS-13 Behavior of fission products in soil samples (S. Fukutani *et al.*).
- ARS-14 Noble gas mass spectrometry of neutron irradiated geological samples (H. Sumino *et al.*).
- ARS-15  $^{40}\text{Ar}/^{39}\text{Ar}$  dating of neutron irradiated minerals and glasses (O. Ishizuka *et al.*).

### 2. Main Results and Contents

ARS-1 and -2 were performed in order to deepen the knowledge of nuclear waste management issues. In ARS-1, for further study on actinides, the formation constants of the Zr-isosaccharinic acid (ISA) complexes were determined by the least squares fitting analysis of the solubility data. Deprotonated Zr-ISA complexes were found at high pH region. In ARS-2, Zr solubility in carbonate solutions was measured and discussed based on the thermodynamic constant and existing activity correction model. The results were compared with Th complexes, and it was found that highly negatively charged Zr carbonate complex was not stable at high ionic strength. ARS-5, 6, 7, and 10 were performed with the viewpoint of pyrochemistry. In ARS-5, the redox reactions of uranium ions in hydrate calcium chloride melts were investigated by electrochemical methods. It was found that the disproportionation of U(V) occurs after the reduction of U(VI) via formation of  $\text{UO}_2$ , which is not observed in acidic HCl solutions. In ARS-6, the redox mechanism of Se, a fission product element, in molten salts was studied by UV-Vis spectrometry. The results support the electrochemical data, which indicate the complexation of Se with Cu. In ARS-7, the MD simulation for concentrated aqueous LiCl solutions containing La(III) ion. Specific radial distribution functions of O and Cl around La were found. In ARS-10, mutual separation of Nd and Pr in Ca-Li chloride molten salts using molten metallic tin cathode and graphite anode was performed. Reaction mechanisms of Nd and Pr with Sn were clarified. ARS-9 studied isotope fractionation of Ca. A possible fractionation of  $^{48}\text{Ca}/^{40}\text{Ca}$  was found. In ARS-11, Cs-134 and Cs-137 were produced via photonuclear reactions. The isotopic composition of Cs was measured by mass spectrometry and gamma-spectrometry. The effectiveness of this method for correcting the coincidence sum effect was demonstrated. ARS-3, 4, 8, 12, 13, 14, and, 15, focus on environmental chemistry and geochemistry by using KUR, and hence restart of the KUR operation is needed.

### 3. Summaries of the achievements

New and characteristic chemical, kinetic, structural, and thermodynamic data for actinides and fission products were obtained. These new information encompass aqueous chemistry, pyrochemistry, and isotope chemistry of f-elements and FPs.

T. Sasaki, T. Kobayashi, S. Nishikawa, R. Goto, T. Saito<sup>1</sup> and A. Uehara<sup>1</sup>

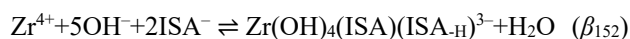
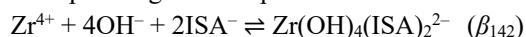
Graduate School of Engineering, Kyoto University

<sup>1</sup>Research Reactor Institute, Kyoto University

**INTRODUCTION:** For the safety assessment of radioactive waste disposal, it is very important to predict the solubility limit of M(IV) under relevant conditions. Isosaccharinic acid (ISA), a degradation product of cellulose found in low- and intermediate-level radioactive waste, is known to form strong complexes with radionuclides [1]. Under repository conditions, in the presence of the aforementioned organic acid, the solubility of radionuclides could potentially be enhanced, which could affect the safety assessment of radioactive waste disposal. Since the solubility and complexation behavior of tetravalent actinide (An(IV)) is primarily controlled by the solubility of the sparingly soluble solid phase amorphous hydroxide (An(OH)<sub>4</sub>(am)) and concentration of complexing agent, respectively, it is necessary to quantify the impact of the complexation ability of the organic acid on the solubility of An(OH)<sub>4</sub>(am). Although several reports have investigated the interaction of ISA with tetravalent actinides, the number of reported values of thermodynamic constants such as complex formation constants were considerably limited [1]. In the present study, we focused on the solubility of zirconium in the presence of ISA at a wide range of hydrogen ion concentrations (pH<sub>c</sub>). As a tetravalent ion, zirconium is considered to be a chemical analog of tetra-valent actinides (such as Pu(IV)), although different chemical characteristics have also been observed. Zirconium is a relevant element in the safety assessment of radioactive waste disposal since it has a high yield in uranium fission products and Zr metal is used as a fuel cladding material in light-water reactors. However, no thermodynamic data on Zr-ISA are available. The formation constants of the Zr-ISA complexes were determined by the least squares fitting analysis of the solubility data.

**EXPERIMENTS:** Calcium isosaccharinate (Ca(ISA)<sub>2</sub>) was synthesized from α-lactose and converted to NaISA stock solution. An aliquot of NaISA stock solution and HCl and/or NaOH solutions were added to polypropylene tubes to prepare sample solutions at specific hydrogen ion concentrations (pH<sub>c</sub>) and ISA concentrations. The ionic strength (*I*) was fixed at *I* = 0.5 mol/dm<sup>3</sup> (M) NaCl. A portion of freshly precipitated Zr(OH)<sub>4</sub>(am) solid phase was then added to the tubes. After aging for several weeks, supernatants were filtered through from 10 kDa to 0.45 μm membranes and Zr concentrations were determined by ICP-MS. The solid phases were investigated by XRD within a range of 2θ = 10°–60°.

**RESULTS:** Zr solubility after 14 weeks in the presence of 10<sup>-3</sup>–10<sup>-1</sup> M ISA was measured in a pH<sub>c</sub> range of 8–12.5 after ultrafiltration through 10 kDa membranes. A steady state was confirmed to be achieved within 10 weeks. In the presence of ISA with a concentration higher than 10<sup>-2.5</sup> M, Zr solubility was found to be higher in comparison with systems with an absence of ISA, depending on the pH<sub>c</sub> and ISA concentration [2]. Zr solubility seemed to be almost independent of pH<sub>c</sub> under weakly alkaline pH conditions between pH<sub>c</sub> 8 and 10, indicating that four OH<sup>-</sup> ions are involved in the Zr-ISA complex, provided that Zr(OH)<sub>4</sub>(am) is in the solid phase. Zr solubility increased with a slope of approximately 1 above pH<sub>c</sub> 10, suggesting that one additional OH<sup>-</sup> was involved in the reaction in this pH region. This may be due to further coordination of one OH<sup>-</sup> to the Zr-ISA complex or to deprotonation of the hydroxyl group on the main chain of ISA. The Zr solubility at pH<sub>c</sub> 9.3 and 12.1 was shown as a function of the total ISA concentration ([ISA]<sub>tot</sub>). The slope against the total ISA concentration was approximately 2, indicating that two ISA molecules were involved in the formation of a Zr-ISA complex. It was noted that no significant peak except that of NaCl(cr) was observed in the XRD patterns of the solid phase aged in the presence of 10<sup>-1</sup> M ISA.



Taking the isosaccharinate complex formation reactions, the deprotonation of the carboxylic group of ISA [3], the lactonization of ISA [3], and the hydrolysis reactions of Zr [4] into account, Zr solubility ([Zr]) and the total ISA concentration ([ISA]<sub>tot</sub>) can be described as

$$[\text{Zr}] = [\text{Zr}^{4+}] + \sum_m [\text{Zr}(\text{OH})_m^{4-m}] + \sum_{x,y} [\text{Zr}(\text{OH})_x(\text{ISA})_y^{4-x-y}]$$

$$[\text{ISA}]_{\text{tot}} = [\text{ISL}] + [\text{HISA}] + [\text{ISA}^-] + \sum_{x,y} y [\text{Zr}(\text{OH})_x(\text{ISA})_y^{4-x-y}]$$

The solubility data in the neutral to alkaline pH range were analyzed to determine the complex formation constants β<sub>142</sub> and β<sub>152</sub>. The parameter values are determined in the least squares fitting analysis. The fixed parameters were corrected by SIT. In the alkaline pH region, one of the hydroxyl groups on the alkyl chain of ISA may be deprotonated to form the Zr(OH)<sub>4</sub>(ISA)(ISA-H)<sup>3-</sup> complexes.

#### REFERENCES:

- [1] Hummel W et al. Chemical Thermodynamics of Compounds and Complexes of U, Np, Pu, Am, Tc, Se, Ni and Zr with Selected Organic Ligands. Elsevier, North-Holland, Amsterdam (2005).
- [2] Sasaki T et al., Radiochim. Acta, **94**, (2006) 489-494.
- [3] Rai D et al., J. Solution Chem., **38**, (2009) 1573-1587.
- [4] Sasaki T et al., J. Nucl. Sci. Technol., **45**, (2008) 735-739.

T. Kobayashi, S. Nakajima, T. Sasaki, A. Uehara<sup>1</sup>

Graduate School of Engineering, Kyoto University

<sup>1</sup>Research Reactor Institute, Kyoto University

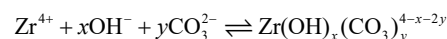
**INTRODUCTION:** For the safety assessment of radioactive waste disposal, it is necessary to predict radionuclide solubility limits under relevant disposal conditions. Actinide elements such as uranium, neptunium and plutonium in the radioactive waste have long half-life and the solubilities are primarily controlled by sparingly soluble hydroxides of tetravalent actinides (An(OH)<sub>4</sub>(am)). In spite of the strong hydrolysis reaction, the complex formation of An(IV) with carbonate is one of the most important reactions for the reliable prediction of the An(IV) solubility. Since part of low-level wastes (TRU waste) generated from Japanese nuclear reprocessing process contain considerable amount of nitrate salt, an impact of dilute to concentrated NaNO<sub>3</sub> on the complex formation of An(IV) carbonate need to be clarified within the context of co-disposal of TRU waste and high level waste. Although a comprehensive literature review has been performed on the thermodynamic constant of actinide including the An(IV) carbonate [1], the literature data on An(IV) carbonate at high ionic strength is still lacking. In the present study, we focus on the complex formation of Zr(IV) carbonate, which is known as an analogue of An(IV). Zirconium is also a relevant element in the safety assessment of radioactive waste disposal, since it has a high yield among the uranium fission products and zirconium metal is used as a fuel-cladding in light water reactors. However, limited thermodynamic data on Zr carbonate at low to high ionic strength is available [2]. Zr solubility in carbonate solution containing 0.1 to 5.0 mol/dm<sup>3</sup> (M) NaNO<sub>3</sub> was measured and discussed based on the thermodynamic constant and existing activity correction model.

**EXPERIMENTS:** Amorphous zirconium hydroxide solid phase (Zr(OH)<sub>4</sub>(am)) was pre-precipitated and washed with purified water. The Zr(OH)<sub>4</sub>(am) was then added into the solutions at certain pH, total carbonate concentration ([C]<sub>tot</sub>), and ionic strength (*I*). The pH was adjusted in the range of p*H*<sub>c</sub> 7 - 12 by HNO<sub>3</sub>/NaOH and the ionic strength was controlled to be 0.1, 0.5, 2.0 and 5.0 mol·dm<sup>-3</sup> (M) by NaNO<sub>3</sub>. The [C]<sub>tot</sub> was adjusted to be 0.015 - 0.1 M by NaHCO<sub>3</sub>. After given aging time, the supernatant of the sample solution was filtrated through ultrafiltration membranes (10 kDa NMWL) and Zr concentration was determined by ICP-MS.

**RESULTS:** In the presence of carbonate, the solubility

of Zr(OH)<sub>4</sub>(am) increased, indicating the formation of Zr p*H*<sub>c</sub> at 8 < p*H*<sub>c</sub> < 9, and, after this point, decreased with carbonate complexes. The solubility was independent of increasing p*H*<sub>c</sub>. The solubility at around p*H*<sub>c</sub> 12 was around 10<sup>-8</sup> M. At p*H*<sub>c</sub> 8.2, the slope of Zr solubility (log [Zr]) against [C]<sub>tot</sub> was determined to be about 4, suggesting that four carbonates were mainly involved in the dominant Zr carbonate complexes. The relationship between Zr solubility and [C]<sub>tot</sub> was similar between p*H*<sub>c</sub> 8.2 to 10.9, while no significant relationship was observed at p*H*<sub>c</sub> 11.7. In the p*H*<sub>c</sub> range of 8–9, the solubility at *I* = 5.0 was about 1.5 orders of magnitude higher than that at *I* = 0.1, while in contrast, little difference was found between different ionic strengths at p*H*<sub>c</sub> > 9. The slope of Zr solubility against [C]<sub>tot</sub> at *I* = 0.1-5.0 was also about 4, suggesting that four carbonate ions were involved. In the case that conditions of high ionic strength and [C]<sub>tot</sub> less than 0.01 M were employed, the slope showed slightly lower values than those at low ionic strength, which suggested the formation of an alternative or additional Zr carbonate complex.

The equilibrium reactions for the formation of the Zr carbonate complexes Zr(OH)<sub>x</sub>(CO<sub>3</sub>)<sub>y</sub><sup>(4-x-2y)+</sup> can be described as:



$$\log \beta_{1,xy} = [\text{Zr(OH)}_x(\text{CO}_3)_y^{4-x-2y}] / [\text{Zr}^{4+}][\text{OH}^{-}]^x[\text{CO}_3^{2-}]^y$$

Under the conditions of the present study, the solubility of Zr(OH)<sub>4</sub>(am) was described as a sum of the concentrations of hydrolysis species and carbonate complexes. The solubility data were analyzed by assuming Zr(CO<sub>3</sub>)<sub>4</sub><sup>4-</sup>, Zr(CO<sub>3</sub>)<sub>5</sub><sup>6-</sup>, and Zr(OH)<sub>2</sub>(CO<sub>3</sub>)<sub>2</sub><sup>2-</sup> from literatures [2]. The β<sub>1,xy</sub> and ion interaction coefficient values for Zr(OH)<sub>x</sub>(CO<sub>3</sub>)<sub>y</sub><sup>(4-x-2y)+</sup> were determined.

The large ion interaction coefficient values for Zr(CO<sub>3</sub>)<sub>4</sub><sup>4-</sup> and Zr(CO<sub>3</sub>)<sub>5</sub><sup>6-</sup> were a consequence of the minor effects of ionic strength on solubility under high carbonate concentration. The results observed in this study indicated that a highly negatively charged Zr carbonate complex was less stable at high ionic strength, compared to the analogous Th complex [3].

#### REFERENCES:

- [1] Guillaumont R. et al., *Update on the Chemical Thermodynamics of Uranium, Neptunium, Plutonium, Americium and Technetium*. Elsevier, Amsterdam (2003).
- [2] Brown P. et al., *Chemical Thermodynamics of Zirconium*. Elsevier, Amsterdam (2005).
- [3] Altmaier M. et al., *Radiochim. Acta* 94, 495-500 (2006).

A. Uehara<sup>1</sup>, T. Nagai<sup>2</sup>, and T. Fujii<sup>3</sup>

<sup>1</sup> *Research Reactor Institute, Kyoto University*

<sup>2</sup> *Nuclear Fuel Cycle Engineering Lab., Japan Atomic Energy Agency*

<sup>3</sup> *Graduate School of Engineering, Osaka University*

### INTRODUCTION:

The calcium chloride hexahydrate,  $\text{CaCl}_2 \cdot 6\text{H}_2\text{O}$ , and similar hydrate melts are of considerable interest as solvents with properties intermediate between those of aqueous solution and molten salts. Activity coefficients, viscosity and structural analyses indicate that the water molecule in  $\text{CaCl}_2 \cdot 6\text{H}_2\text{O}$  melts strongly coordinates to the calcium ion showing that this melt is a liquid with the properties of an ionic melt composed of bulky hydrated calcium cations and chloride anions. Namely, this material has advantages such as inorganic-based melt and low melting point. There are a few studies on the electrochemistry of uranium ions in hydrate melts. Cohen [1] has investigated the formation of  $\text{UO}_2^+$  in concentrated  $\text{CaCl}_2$  and  $\text{LiCl}$  using bulk electrolysis followed by absorption spectrophotometry. Bansal et al. [2] reported that  $\text{UO}_2^{2+}$  was reversibly reduced to  $\text{UO}_2^+$ , which can be further reduced to  $\text{UO}_2$  in  $\text{Ca}(\text{NO}_3)_2 \cdot 4\text{H}_2\text{O}$  melt.

In the present study, redox reactions of uranium ions such as  $\text{U}^{4+}$  and  $\text{UO}_2^{2+}$  in  $\text{CaCl}_2 \cdot n\text{H}_2\text{O}$  hydrate melt ( $n = 6 - 10$ ) were investigated by electrochemical methods. The chemical behavior of uranium ions in the hydrate melt was compared with that in the other solvents such as high temperature [3] or room temperature [4] molten salts, organic solvents [5] and relatively low concentration solution of hydrochloric acid [6].

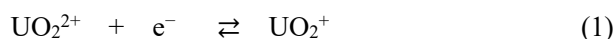
### EXPERIMENTAL:

For the electrochemical measurements, a three-electrode system was used. A pyro-graphite carbon (Toyo Tanso Co. Ltd.) of 3 mm diameter was used as a working electrode, and the silver/silver chloride ( $\text{Ag}|\text{AgCl}$ ) electrode was used as a reference electrode. This reference electrode, in which was put an aqueous solution containing 1 M  $\text{LiCl}$  along with a  $\text{Ag}$  wire of 1 mm diameter coated by  $\text{AgCl}$ . For voltammetric operation, the platinum mesh electrode was employed as a counter electrode. Electrochemical measurement systems, Hz-5000 (Hokuto Denko Co.) were used for the cyclic voltammetry and the linear sweep voltammetry. Controlled-potential electrolysis was carried out in order to identify the electrode reaction. In this experiment, a rotating carbon electrode was employed as a working electrode to enhance the efficiency of the electrolysis. The counter electrode was also a platinum

mesh electrode, and the counter phase was separated by glass membrane filter from the objective phase to avoid cyclic redox reaction. After the electrolysis, absorption spectra were measured. A self-registering spectrophotometer UV-1000 (Shimadzu Co.) was used for the measurements over the wavelength from 400 to 900 nm. These measurements were carried out at  $300 \pm 2$  K.

### RESULTS:

Voltammograms for the redox reaction of 0.05 M  $\text{UO}_2\text{Cl}_2$  in 6.9 M  $\text{CaCl}_2$  were measured by using a platinum working electrode. When the potential scanning rate,  $\nu$ , was from 0.01 to 0.5  $\text{V s}^{-1}$ , a cathodic peak current ( $I_{c,1}$ ) was observed at  $-0.090$  V (vs.  $\text{Ag}|\text{AgCl}$ ) corresponding to the reduction of  $\text{UO}_2^{2+}$  to  $\text{UO}_2^+$  as Eq. (1);



The  $I_{c,1}$  was proportional to the square of  $\nu$  between 0.01 and 0.5  $\text{V s}^{-1}$  and the concentration of  $\text{UO}_2^{2+}$  between  $5 \times 10^{-3}$  and 0.06 M. These results indicated that the  $I_{c,1}$  were controlled by the diffusion of  $\text{UO}_2^{2+}$ . An anodic peak current ( $I_{a,1}$ ) was observed at 0.025 V under the potential sweep rate,  $\nu$ , from 0.1 to 0.5  $\text{V s}^{-1}$ . Mid-point potential between cathodic and anodic peaks was found to be  $-0.058$  V. Assuming that the electrode reaction of the  $\text{UO}_2^{2+}|\text{UO}_2^+$  couple is reversible, the diffusion coefficient of  $\text{UO}_2^{2+}$  at 298 K can be calculated to be  $1.7 \times 10^{-7} \text{ cm}^2 \text{ s}^{-1}$ , which was more 10 times smaller than that in diluted electrolyte solutions such as 0.1 M  $\text{HClO}_4$  ( $7.3 \times 10^{-6} \text{ cm}^2 \text{ s}^{-1}$ ). On the other hand, at  $\nu < 0.1 \text{ V s}^{-1}$ , anodic peak potential shifted positive from 0.025 to 0.165 V. This shift suggests that disproportionation of  $\text{UO}_2^+$  occurs after the reduction of  $\text{UO}_2^{2+}$  as following reaction [2] which is not observed in acidic  $\text{HCl}$  but room and high temperature ionic liquids [3,4];



### REFERENCES:

- [1] D. Cohen, *J. Inorg. Nucl. Chem.* 32 (1970) 3525.
- [2] N.P. Bansal and J.A. Plambeck, *Electrochim. Acta*, 23 (1978) 1053.
- [3] T. Nagai, A. Uehara, T. Fujii, O. Shirai, N. Sato and H. Yamana, *J. Nucl. Sci. Technol.* 42 (2005) 1025.
- [4] P. Giridhar, K.A. Venkatesan, T.G. Srinivasan and P.R. Vasudeva Rao, *Electrochim. Acta*, 52 (2007) 3006.
- [5] L. Martinot, D. Laeckmann, L. Lopes, T. Materne and V. Muller, *J. Alloys Comp.* 185 (1992) 151.
- [6] W.E. Harris and I.M. Kolthoff, *J. Am. Chem. Soc.* 69 (1947) 446.

Y. Sakamura<sup>1</sup>, T. Murakami<sup>1</sup>, K. Uozumi<sup>1</sup>, A. Uehara<sup>2</sup>  
and T. Fujii<sup>3</sup>

<sup>1</sup>Central Research Institute of Electric Power Industry

<sup>2</sup>Research Reactor Institute, Kyoto University

<sup>3</sup>Graduate School of Engineering, Osaka University

**INTRODUCTION:** The electrolytic reduction technique in LiCl-Li<sub>2</sub>O melts has been developed for pyrochemical reprocessing of spent oxide fuels [1]. At the cathode, actinide oxides are reduced to their metals:



where M denotes actinides such as U and Pu. Similar to oxygen, chalcogen fission products such as Se and Te are dissolved into the melt in the form of divalent anion.

Recently, the authors have been studied electrochemical behavior of Na<sub>2</sub>Se in LiCl-KCl eutectic melt to extract Se from molten salts [2]. The cyclic voltammograms of glassy carbon electrode indicated that the deposition of Se proceeded in two steps at the anode: the oxidation of Se<sup>2-</sup> to Se<sub>2</sub><sup>2-</sup> occurred followed by the oxidation of Se<sub>2</sub><sup>2-</sup> to Se, which was similar to the electrochemical behavior of sulfur [3]. When Cu was used as the anode, Cu<sub>2</sub>Se was deposited at the potentials more negative than the potential of Se deposition. To verify the redox mechanism of Se, a spectroscopic study was conducted.

**EXPERIMENTS:** LiCl-KCl-Na<sub>2</sub>Se mixture was prepared by heating a quartz tube containing LiCl-KCl eutectic (59:41 mole ratio, Aldrich-APL) and Na<sub>2</sub>Se (99.8% purity, Alfa Aesar) at 723 K. The Se concentration was determined to be 0.123 wt% by ICP-AES analysis.

LiCl-KCl eutectic (3.075 g) was loaded in a rectangular cylinder quartz cell (10 x 10 mm) used for absorption spectrometry and heated to 723 K in an electric furnace. The experimental apparatus was previously described in detail by Nagai *et al.* [4] The following steps were carried out and then the absorption spectrum of the melt was measured by using an UV/Vis/NIR spectrophotometer (V-570, JASCO).

- (1) 0.278 g of the LiCl-KCl-Na<sub>2</sub>Se mixture was added.
- (2) 0.235 g of the LiCl-KCl-Na<sub>2</sub>Se mixture was added.
- (3) 0.252 g of the LiCl-KCl-Na<sub>2</sub>Se mixture was added.
- (4) 0.015 g of Se on a mullite tube was immersed in the melt.
- (5) The Se was removed from the melt.
- (6) A Cu rod ( $\phi$ 2 mm) was immersed in the melt.

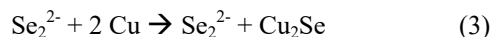
**RESULTS:** Fig. 1 shows absorption spectra of the LiCl-KCl-Na<sub>2</sub>Se melt measured during the steps (1)-(6). The absorption peak at 406 nm corresponding to Se<sup>2-</sup> ions was increased by adding the LiCl-KCl-Na<sub>2</sub>Se mixture (steps (1)-(3)). The Se concentration in the melt was 0.022 wt% after step (3). After Se was added into the melt by step (4), an absorption band in the range lower

than 406 nm seemed to overlap, which might be due to the formation of Se<sub>2</sub><sup>2-</sup> ions.



In fact, the Se concentration in the melt was increased to 0.027 wt% after 1.5 h and the melt became darker brown as visually observed in Fig. 2.

After the Cu rod immersion (step (6)), the absorption peak gradually decreased and went back to 406 nm, which might be due to the decomposition of Se<sub>2</sub><sup>2-</sup> to give Se<sup>2-</sup> and Cu<sub>2</sub>Se.



In summary, the results of this spectroscopic study are consistent with the results of electrochemical measurement [2]. However, the Se concentration was finally decreased to 0.013 wt% and the absorption peak at 406 nm became low. The reasons for mass loss should be clarified.

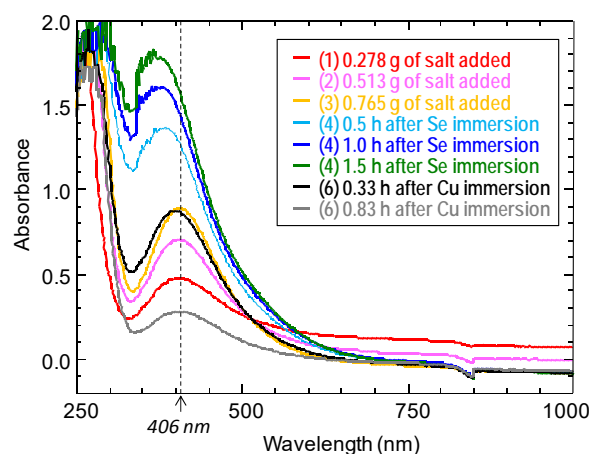


Fig. 1 Absorption spectra of LiCl-KCl-Na<sub>2</sub>Se melt measured during steps (1)-(6).

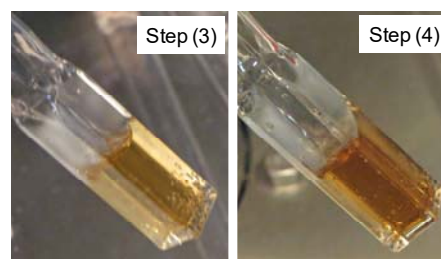


Fig. 2 The quartz cell containing LiCl-KCl-Na<sub>2</sub>Se melt after steps (3) and (4).

#### REFERENCES:

- [1] Y. Sakamura and M. Akagi, Nucl. Technol. **179** (2012) 220-233.
- [2] Y. Sakamura and M. Iizuka, Proc. The 48th Symposium on Molten Salt Chemistry, p. 1-2, Niigata Univ., Japan, Nov. 24-25, 2016, in Japanese.
- [3] D. Warin, Z. Tomczuk and D.R. Vissers, J. Electrochem. Soc., **130** (1983) 64-70.
- [4] T. Nagai, T. Fujii, O. Shirai and H. Yamana, J. Nucl. Sci. Technol., **41** (2004) 690-695.

## PR3-5 Coordination Structure around $\text{La}^{3+}$ Ion in Concentrated Aqueous Solutions of LiCl

N. Ohtori, Y. Ishii<sup>1</sup>, A. Uehara<sup>2</sup>, T. Fujii<sup>3</sup>

Department of Chemistry, Niigata University

<sup>1</sup>Graduate School of Science and Technology, Niigata University

<sup>2</sup>Research Reactor Institute, Kyoto University

<sup>3</sup>Department of Sustainable Energy and Environmental Engineering, Graduate School of Engineering, Osaka University

**INTRODUCTION:** Recently, hydrate melts such as concentrated alkali halide aqueous solutions attract some attention as one of the novel candidates for solvents useful for reprocessing of spent nuclear fuels[1]. We performed molecular dynamics (MD) simulation of LiCl aqueous solutions containing uranyl ion and reported some results such as diffusion coefficients and average local structure around uranyl ion in the previous report[2]. Then, we analyzed coordination structure around uranyl ions in 14 M LiCl aqueous solution in more detail and compared the results with experimental results[3]. In this study, we report the results of MD simulation for concentrated aqueous solutions of LiCl containing  $\text{La}^{3+}$  ion and discuss coordination structure around  $\text{La}^{3+}$  ion.

**CALCULATION:** MD calculation has been performed under *NVE* ensemble. The SPC/E model was used for water molecule. The other parameters were taken from the references cited in [3, 4]. The water molecules were constrained by SHAKE algorithm. The number of particles included in the simulation cell is shown in Table 1. Time step was 1.0 fs.

**RESULTS:** Figures 1 and 2 show the radial distribution function and coordination number of O atom or  $\text{Cl}^-$  ion around  $\text{La}^{3+}$  ion in 14 M aqueous solution of LiCl. Although, regarding distances between  $\text{La}^{3+}$  and O or  $\text{Cl}^-$ , the present MD results are in good agreement with those of first-principles MD[5], regarding the peak heights, it shows poor agreements. Although the experimental results of coordination number follow rather simple

Table 1 Number of particles included the simulation cell for aqueous solutions of LiCl containing  $\text{La}^{3+}$  ion.

[Cl <sup>-</sup> ]/ mol dm <sup>-3</sup>	H <sub>2</sub> O	Number of unit		
		Li <sup>+</sup>	Cl <sup>-</sup>	La <sup>3+</sup>
0	1108	0	3	1
1	1086	20	23	1
3	1040	60	63	1
8	924	160	163	1
14	782	280	283	1

composition ratio, the present MD results show some underestimates in La-Cl and overestimates in La-O.

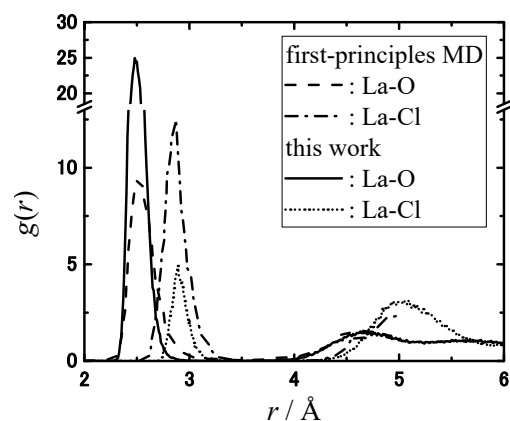


Fig.1 Radial distribution function of O atom or  $\text{Cl}^-$  ion around  $\text{La}^{3+}$  ion in 14 M aqueous solution of LiCl.

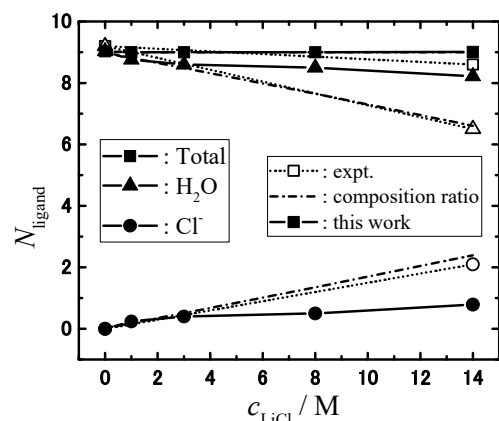


Fig.2 Concentration dependence of coordination number of O atom or  $\text{Cl}^-$  ion around  $\text{La}^{3+}$  ion in aqueous solution of LiCl.

### REFERENCES:

- [1] A. Uehara, O. Shirai, T. Fujii, T. Nagai and H. Yamana, *J. Appl. Electrochem.*, **42**, 455(2012).
- [2] N. Ohtori, Y. Ishii, Y. Nagata, A. Uehara, T. Fujii, H. Yamana, K. Minato and Y. Okamoto, KURRI Progress Report 2012, PR2-1(2013).
- [3] N. Ohtori, Y. Ishii, A. Uehara, T. Fujii, H. Yamana, and Y. Okamoto, KURRI Progress Report 2013, PR1-12(2014).
- [4] S. Díaz-Moreno, S. Ramos, and D.T. Bowron, *J. Phys. Chem. A*, **115**, 6575 (2011).
- [5] L. Petit, R. Vuilleumier, P. Maldivi, and C. Adamo, *J. Phys. Chem. B*, **112**, 10603 (2008).

## PR3-6 Study of Isotope Separation of Strontium and Calcium via Chemical Exchange Reaction

R. Hazama, Y. Sakuma<sup>1</sup>, T. Yoshimoto, T. Fujii<sup>2</sup>, T. Fukutani<sup>3</sup>, Y. Shibahara<sup>3</sup>

Graduate School of Human Environment, Osaka Sangyo University

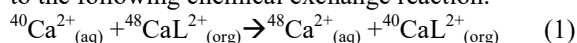
<sup>1</sup>Research Laboratory for Nuclear Reactors, Tokyo Institute of Technology,

<sup>2</sup>Graduate School of Engineering, Osaka University

<sup>3</sup>Research Reactor Institute, Kyoto University

**INTRODUCTION:** Calcium is congener of strontium and easy to handle to check the isotope effects. By utilizing chemical separation method for calcium isotope effect in liquid-liquid extraction (LLE), an appropriate crown-ether can be used not only for separation of metal ions, but also for separation of isotope[1].

**EXPERIMENTS:** Isotopic enrichment occurs according to the following chemical exchange reaction:



where L represents macrocyclic polyether(18-crown-6). A 20 ml aqueous solution (3M CaCl<sub>2</sub>) and 200 ml organic solution (0.07M DC18C6 in chloroform) were stirred by a magnetic stirrer for 30 m/60 m at room temperature and separated. This LLE was iterated six times (1 – 6)[2].

Natural samples of Ca must be purified to remove potassium because <sup>40</sup>K interferes on <sup>40</sup>Ca, thus purification by cation exchange resin (DOWEX 50WX8) was conducted prior to isotope analysis. Samples with ultrapure 0.1M HNO<sub>3</sub> were loaded onto this ion exchange column in order to extract the Ca-fraction. After rinsing the column with ultrapure 8M HNO<sub>3</sub> the Ca-fraction was collected, evaporated to dryness and then dissolved in ultrapure HNO<sub>3</sub> to form Ca(NO<sub>3</sub>)<sub>2</sub>. About 30 μg of Ca in the nitrate form (1 μL) are loaded onto the single Re filament in combination with the so called “sandwich-technique” of Ta<sub>2</sub>O<sub>5</sub>-activator, which stabilizes the signal intensity [3].

All Ca isotope measurements were carried out by the TIMS, KURRI. The TRITON multicollector is operated in positive mode with a 10 kV acceleration voltage and equipped with nine Faraday cups as detection system, but cannot account for the dispersion of the whole Ca isotope mass range from 40 to 48 amu. During the first sequence, the masses of 40, 42, 43 and 44 are measured simultaneously and during the second sequence, the masses 43, 44 and 48 are measured. Table 1 shows a summary of the experimental conditions for Ca isotope analysis using

TIMS.

Property	Setting
Accelerating voltage	10 kV
Source vacuum	1 × 10 <sup>-7</sup> mbar
Analyzer vacuum	6 × 10 <sup>-9</sup> mbar
Faraday cup	9
Baseline(each block)	Delay time: 10 s Integration time: 16 s
Data collection	Blocks/run: 6 Scans/block: 10 Integration time: 4 s Idle time: 3 s
Analyzing temperature	1500 – 1580 °C: 3A Boiling point@1 atm: 1487°C

Table 1. Experimental condition used for Ca isotope analysis by TIMS.

**RESULTS:** The linearity of the plots in Fig. 1 indicates that the isotope effects show the normal mass dependence.

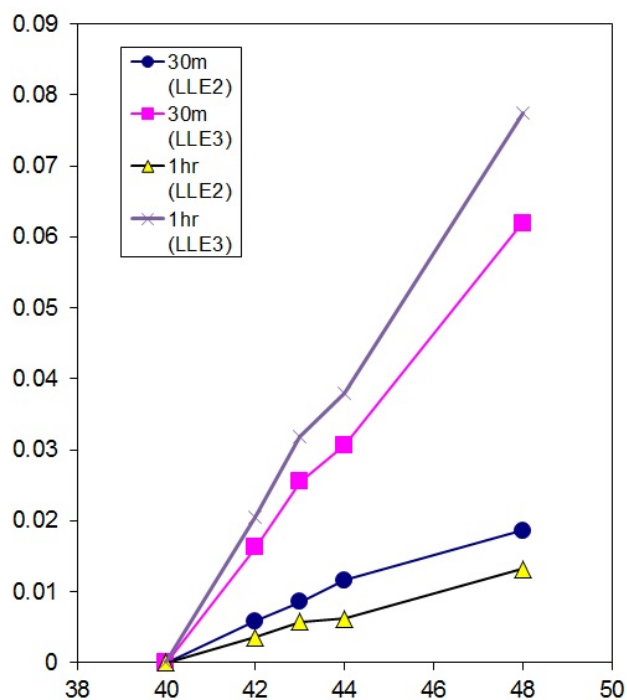


Fig. 1. Mass dependence of observed Ca isotope separation: Preliminary. Circle/Square:30m, Triangle/Cross: 60m for stirring and standing for separation, respectively.

### REFERENCES:

- [1]B.E. Jepson *et al.*, J. Inorg. Nucl. Chem.**38**(1976)1175.
- [2]R. Hazama *et al.*, Proc. 6<sup>th</sup> Recontres du Vietnam, The Gioi Publishers (2007) 383: arXiv: 0710.3840.
- [3]A. Heuser *et al.*, Int.J.Mass Spec. **220**(2002)385.

H. Sekimoto<sup>1</sup>, A. Uehara<sup>2</sup>, T. Fujii<sup>3</sup>

<sup>1</sup>Department of Physical Science and Materials Engineering, Iwate University

<sup>2</sup>Research Reactor Institute, Kyoto University

<sup>3</sup>Department of Sustainable Energy and Environmental Engineering, Osaka University

## INTRODUCTION:

Mutual separation of Nd, Dy and Pr is essentially important for the recycling of the neodymium magnet. Uehara et al. reported on the mutual separation of La and Nd utilizing the disproportionation reaction of Nd(II) to metallic Nd and Nd(III) in LiCl-KCl molten salt [1]. This technique seems quite attractive comparing with the conventional processes such as the ion exchange process and the solvent extraction process in terms of the environmental load. We have investigated the absorption spectra of ions of Nd, Dy and Pr in CaCl<sub>2</sub>-LiCl eutectic molten salt and the electrochemical behaviors them [2,3]. In this study, the mutual separation of Nd and Pr in CaCl<sub>2</sub>-LiCl eutectic molten salt using molten metallic tin cathode and graphite anode was examined.

## EXPERIMENTS:

Electrochemical experiments and the absorption spectrometry were conducted in the argon atmosphere, where the concentration of oxygen and water was controlled below 1 ppm. 4 g of metallic tin, 6.20 g of CaCl<sub>2</sub>, and 3.80 gram of LiCl were weighed and inserted in a quartz optical cell attached with cylindrical quartz tube. The sample heated at 750 °C in an electric furnace to be melt. 0.0370 g of NdCl<sub>3</sub> and 0.0384 g of PrCl<sub>3</sub> were dissolved in the molten salt, and thus, the initial concentration of Nd(III) and Pr(III) in the molten salt was 0.211 mass% and 0.217 mass%, respectively. The temperature was then controlled to be kept at 700 °C. After that, a tungsten rod was immersed in the molten metallic tin phase to make working electrode. A graphite rod and the Ag-AgCl reference electrode also immersed in the molten salt phase as counter electrode and reference electrode respectively. Potentiostatic electrolysis was conducted at -1300 mV vs the Ag-AgCl electrode for 2700 s.

Absorbances of Nd(III) and Pr(III) dissolved in the CaCl<sub>2</sub>-LiCl eutectic molten salt were measured before and after electrolysis. The concentrations of neodymium and praseodymium in the molten salt phase and metallic tin phase were determined by ICP-OES.

## RESULTS:

Figure 1 shows absorption spectra of the molten salt containing Nd(III) and Pr(III). Solid line and dotted line corresponds the spectrum before and after electrolysis, respectively. The peak intensity at 589 nm which is due to the absorption by Nd(III) decreased from 0.62 to 0.34. The peak intensity at 1546 nm which is due

to the absorption by Pr(III) decreased from 0.082 to 0.060. This means that Nd(III) and Pr(III) were electrochemically reduced. The concentration of Nd and Pr in the molten salt after the electrolysis determined by ICP-AES were 0.145 mass% and 0.148 mass% and, respectively. The concentration ratio of Nd and Pr in the molten salt after the electrolysis was 0.98, which was almost same value as that before the electrolysis; 0.97. On the other hand, the concentration of Nd and Pr was 0.0566 mass% and 0.0702 mass%, respectively. The concentration ratio of Nd and Pr in the molten salt after the electrolysis was 0.81. In CaCl<sub>2</sub>-LiCl eutectic molten salt, Nd(III) is reduced to Nd(II) which is then decomposed to metallic neodymium and Nd(III) with disproportionation reaction, while Pr(III) is reduced to Pr [3]. It is considered that Pr(III) was reduced on molten metallic tin cathode to form Sn-Pr alloy. But, Nd(III) is reduced to on the tin cathode Nd(II), which decomposed to metallic neodymium and Nd(II) in molten salt phase. A part of the metallic neodymium react with Sn to form Sn-Nd alloy. Consequently, the concentration ratio of Nd and Pr in metallic tin decreased comparing that in molten salt.

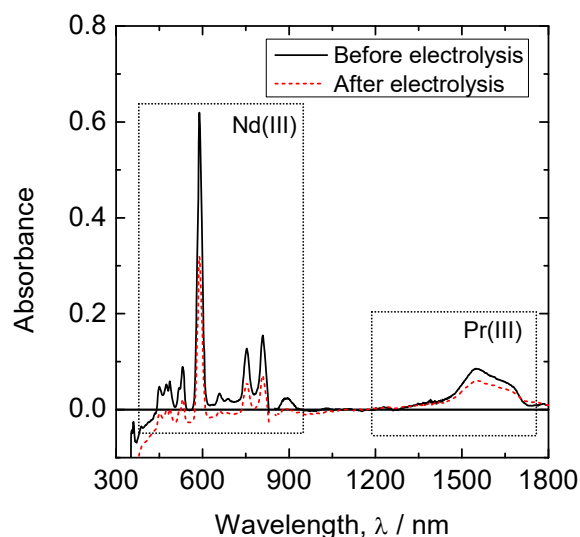


Fig. 1. Absorption spectra of the molten salt containing Nd(III) and Pr(III). Solid line and dotted line corresponds the spectrum before and after electrolysis, respectively.

## REFERENCES:

- [1] A. Uehara, K. Fukasawa, T. Nagai, T. Fujii, and H. Yamana, *J. Nuclear Mater.*, **414**, 336 (2011).
- [2] H. Sekimoto, A. Uehara, T. Fujii, H. Yamana, KURRI Progress report, (2014).
- [3] H. Sekimoto, A. Uehara, T. Fujii, H. Yamana, KURRI Progress report, (2016).

T. Kubota, S. Fukutani, Y. Shibahara, T. Ohta<sup>1</sup>

Research Reactor Institute, Kyoto University

<sup>1</sup>Central Research Institute of Electric Power Industry

**INTRODUCTION:** The migration of radioactive cesium in plants is often investigated with respect to the competition of potassium. Among potassium isotopes,  $^{43}\text{K}$  is useful for tracer experiments. This nuclide can be produced from calcium and is referred to carrier free; its radioactivity can be regulated to enough for experiments. The immediate purification of  $^{43}\text{K}$  is required because of its short half life,  $T_{1/2} = 22.3$  h. In this study the purification methods are investigated by using  $^{134}\text{Cs}$  and  $^{137}\text{Cs}$ , instead of  $^{43}\text{K}$ , for the convenience of experiment and on considering that both elements are alkaline metals and hence exhibit a similar chemical behavior. In addition, these cesium nuclides were used to correct coincidence sum effect on  $\gamma$ -spectrometry. Without attention to this effect, the evaluation of  $^{134}\text{Cs}$  radioactivity would be incorrect. In order to correct the coincidence sum effect,  $^{134}\text{Cs}$  and  $^{137}\text{Cs}$  were produced through a photo nuclear reaction and the isotopic ratios of  $^{134}\text{Cs}$  to  $^{137}\text{Cs}$  measured by Thermal Ionization Mass Spectrometry (TIMS) and  $\gamma$ -spectrometry were compared.

**EXPERIMENTS:** Radioactive cesium nuclides,  $^{134}\text{Cs}$  and  $^{137}\text{Cs}$ , were produced through irradiation of barium chloride with photons generated by the bombardment of platinum with high-energy electrons. The barium target material was encapsulated in a quartz tube under vacuum. The irradiated material dissolved with  $\text{H}_2\text{O}$  was added with ammonium carbonate [1] or ammonium oxalate [2] to precipitate barium and thus to purify cesium in the solution. The cesium solution, containing ammonium chloride and/or oxalate, was evaporated to remove these salts. An aliquot of the purified solution was used to determine an isotopic ratio by TIMS [3] and the obtained value was converted to activity ratio of  $^{134}\text{Cs}/^{137}\text{Cs}$ . A 5 mL of the solution was used to determine radioactivity with a high-purity Ge semiconductor detector where the sample was located 0 cm and 10 cm away from the detector. The radioactivity of  $^{134}\text{Cs}$  and  $^{137}\text{Cs}$  was evaluated from 605-keV and 661-keV gamma ray, respectively.

**RESULTS:** The irradiated barium chloride sample was stored for four months prior to cesium separation. The cesium separation was conducted by precipitating barium carbonate or barium oxalate. Both precipitation methods showed high decontamination factor and high cesium recovery. However, ammonium carbonate was adopted to

remove barium because the deposition of oxalate occurred and this remaining cannot be removed by evaporation. The activity ratio of  $^{134}\text{Cs}/^{137}\text{Cs}$  in purified cesium solution was determined by TIMS and  $\gamma$ -spectrometry. The isotopic ratio of  $^{134}\text{Cs}/^{137}\text{Cs}$  measured by TIMS was 0.126, which was equivalent to 1.824 in activity ratio. The radioactivity ratio of  $^{134}\text{Cs}/^{137}\text{Cs}$  measured by  $\gamma$ -spectrometry was 1.63 and 1.82 at 0 cm and 10 cm from the detector surface, respectively (Fig. 1) and this difference was ascribed to the coincidence sum effect. The value obtained at 10 cm was agreement with the value by TIMS, which means the sum effect can be ignored by keeping a distance of 10 cm from the detector surface.

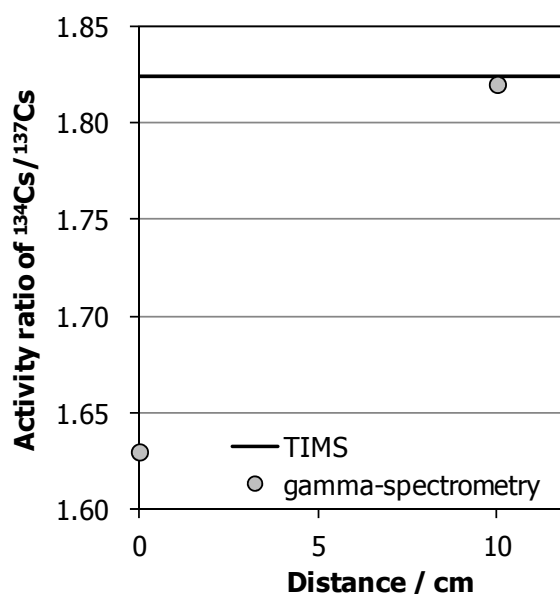


Fig. 1. Activity ratio of  $^{134}\text{Cs}$  and  $^{137}\text{Cs}$  as a function of distance between the sample and the detector surface.

**REFERENCES:**

- [1] Handley *et al.*, Anal. Chem., **31** (1959) 332.
- [2] Sugihara *et al.*, Anal. Chem., **31** (1959) 44.
- [3] Y. Shibahara *et al.*, J. Nucl. Sci. and Tech., **54**, (2016) 158-166.

Y. Ohkubo

*Research Reactor Institute, Kyoto University*

### Objective and Participating Research Subjects

The main objectives of this project research are the investigation of the nuclear structure of unstable neutron-rich nuclei and also the local properties of matters using short-lived nuclei.

This period is the last year of the project. Unfortunately, as in the previous two periods, no experiments in all five-research subjects of the project (28P4) were executed owing to the suspension of the reactor operation. Here, we present two reports showing results which were obtained in previous periods:

- Report 1. Site-to-Site Migration of In Impurity in  $\text{Fe}_3\text{O}_4$
- Report 2. Atmospheric Dependence of Formation Process of Oxygen Vacancy in Zinc Oxide

### Main Points Described in the Reports in the Following Two Pages

The two reports are concerned with the behavior of indium impurities (about 100 ppt) in metal oxides,  $\text{Fe}_3\text{O}_4$  and 100-ppm Al doped ZnO. Impurities (not limited to indium) in these oxides may modify their intrinsic properties to be functional materials. They obtained information on the behavior of indium impurities by measuring hyperfine fields (specifically, electric field gradients) at  $^{111}\text{Cd}$  arising from  $^{111}\text{In}$  via electron capture. The experimental technique used to measure the hyperfine fields are in common:  $\gamma$ - $\gamma$ -rays time-differential perturbed-angular-correlation (TDPAC) technique.

The main point of Report 1 is that indium ions occupying the *A* sites (tetrahedral sites) of  $\text{Fe}_3\text{O}_4$  at room temperature migrate to the *B* sites (octahedral sites) at a high temperature with a certain probability.

The main point of Report 2 is that indium ions forming aggregates with Al in ZnO at room temperature migrate to the defect-free Zn sites at a high temperature in argon gas atmosphere with an activation energy, which is related to the formation of oxygen vacancy.

W. Sato, T. Ida, S. Komatsuda<sup>1</sup>, T. Fujisawa<sup>2</sup>, S. Takenaka<sup>2</sup> and Y. Ohkubo<sup>3</sup>

*Institute of Science and Engineering, Kanazawa University*

<sup>1</sup>*National Institute of Technology, Ichinoseki College*

<sup>2</sup>*Graduate School of Natural Science and Technology, Kanazawa University*

<sup>3</sup>*Research Reactor Institute, Kyoto University*

**INTRODUCTION:** Magnetite (Fe<sub>3</sub>O<sub>4</sub>) is one of the most promising iron compounds applicable to spintronic devices due to its excellent electric conductivity and magnetic property. In addition to the intriguing nature of pure Fe<sub>3</sub>O<sub>4</sub>, it is well known that impurity-doped Fe<sub>3</sub>O<sub>4</sub> exhibits different physical properties, which allows us to control and optimize the properties for wider application of the doped oxide.

In this respect, our interest was directed to thermal stability and behavior of nonmagnetic indium ions (In<sup>3+</sup>) in Fe<sub>3</sub>O<sub>4</sub>. Although the residential site of In ions have still been controversial [1, 2], our recent experiment by means of the time-differential perturbed angular correlation (TDPAC) technique revealed that radioactive <sup>111</sup>In ions exclusively occupy the substitutional *A* sites at room temperature [3]. In addition to the information, in this report, we show an evidence for thermal behavior of impurity In ions, which migrate into the *B* site at around the Curie temperature ( $T_C = 858$  K).

**EXPERIMENTS:** Commercially available <sup>111</sup>In HCl solution was added in droplets onto a disk of polycrystalline Fe<sub>3</sub>O<sub>4</sub>. It then underwent heat treatment in a vacuum quartz tube at 1373 K for 3 h for the diffusion of the radioisotope. TDPAC measurements of the <sup>111</sup>Cd( $\leftarrow$ <sup>111</sup>In) probe were performed for the synthesized samples at various temperatures.

**RESULTS:** The TDPAC spectra of <sup>111</sup>Cd( $\leftarrow$ <sup>111</sup>In) embedded in Fe<sub>3</sub>O<sub>4</sub> are shown in Fig. 1. The spectral pattern obtained above  $T_C$  drastically changes due to magnetic transition from ferrimagnetism to paramagnetism. For the measurement above  $T_C$ , the spectrum in Fig. 1(a) can be analyzed assuming only electric quadrupole interaction between the probe nucleus and the extranuclear charge distribution. The spectral analysis provided the value of the nuclear quadrupole frequency  $\omega_Q = 7.04(4)$  Mrad s<sup>-1</sup> at 900 K. Here, one should note the fact that the oscillatory structure in Fig. 1(a) is on a plateau-like high base line, which is ascribable to majority <sup>111</sup>In ions residing in the *A* site in cubic symmetry. For the spectra obtained below  $T_C$  shown in Figs. 1(b) and 1(c), on the other hand, typical magnetic perturbation was observed. However, we notice a gradually damped structure in Fig. 1(b), and the

spectrum was reproduced with two components having slightly different Larmor frequencies  $\omega_L$ . Because the probe site of the minor second component experiences an electric field gradient above  $T_C$  as stated above, the damped spectrum in Fig. 1(b) was fitted on the presumption that the second component is perturbed by a magnetic interaction combined with an electric quadrupole interaction, whereas the first component at the *A* site is perturbed only by a magnetic interaction. The values of the Larmor frequencies optimized by the fit are  $\omega_{LA} = 74.99(1)$  and  $\omega_{LB} = 70.30(1)$  Mrad s<sup>-1</sup> for the first and second components, respectively. Because their ratio  $\omega_{LA}/\omega_{LB} = 1.067$  is in excellent agreement with that of the hyperfine fields at Fe nuclei occupying the *A* and *B* sites  $H_A/H_B = 1.068$ , revealed by Mössbauer spectroscopy [4], this observation undoubtedly suggests that the second component having appeared at the high temperature is assignable to <sup>111</sup>In at the *B* site. The present observation demonstrates that the site-to-site migration of In takes place at around the magnetic transition; this phenomenon implies that doped Fe<sub>3</sub>O<sub>4</sub> is a promising material that realizes charge transportation triggered by magnetic transition.

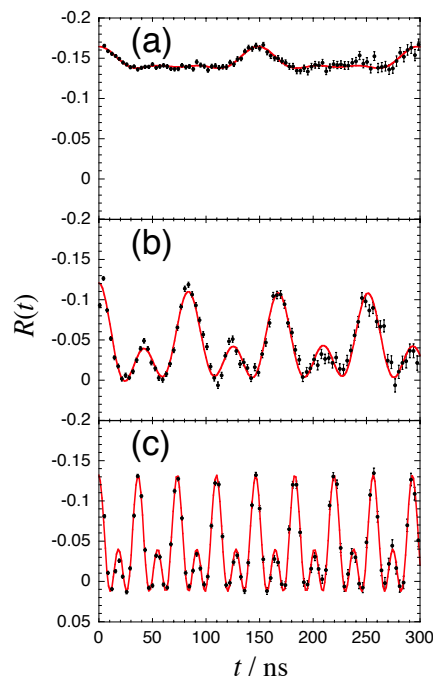


Fig. 1. TDPAC spectra of <sup>111</sup>Cd( $\leftarrow$ <sup>111</sup>In) in Fe<sub>3</sub>O<sub>4</sub> (a) at 900 K, (b) at 773 K, and (c) at R. T.

#### REFERENCES:

- [1] K. Asai *et al.*, J. Phys. Soc. Jpn. **54** (1985) 4325-4330.
- [2] I. T. Matos *et al.*, J. Appl. Phys. **117** (2015) 17D511 (1-4).
- [3] W. Sato *et al.*, J. Appl. Phys. **120** (2016) 145104 (1-7).
- [4] W. Kündig *et al.*, Solid State Comm. **7** (1969) 223-227.

## PR4-2 Atmosphere Dependence of Formation Process of Oxygen Vacancy in Zinc Oxide

S. Komatsuda, W. Sato<sup>1</sup> and Y. Ohkubo<sup>2</sup>

Department of General Education, National Institute of Technology, Ichinoseki College

<sup>1</sup>Institute of Science and Engineering, Kanazawa University

<sup>2</sup>Research Reactor Institute, Kyoto University

**INTRODUCTION:** Defect-induced properties of zinc oxide (ZnO) have been attracting much attention toward their application to functional materials in a wide field of industry. Especially, physical properties brought about by Al ions and/or oxygen vacancies in ZnO are one of the most intriguing topics for the development of future electronic devices. For a practical use of Al-doped ZnO device, therefore, we have investigated the local structures in Al-doped ZnO under various ambient conditions by means of the time-differential perturbed angular correlation (TDPAC) method. In one of our previous TDPAC studies, we observed contrasting atmosphere dependence of the stability of aggregations of <sup>111</sup>In and Al impurities doped in 100 ppm Al-doped ZnO: (i) Al and In impurities associate with each other by their thermal diffusion in air, and (ii) the <sup>111</sup>In probe is detrapped from the Al aggregations in high-temperature vacuum, resulting in substitution at defect-free Zn sites [1,2]. Detailed investigation of the thermal behavior of the impurities has revealed that the dissociation reaction is triggered by the formation of oxygen vacancies. Furthermore, the formation energy of oxygen vacancy in vacuum was evaluated from the temperature variation of the rate constants estimated from the annealing time dependence of the TDPAC spectra [3]. In the present work, based on the further investigation of TDPAC spectra for Al-doped ZnO obtained by isochronal annealings in Ar gas atmosphere, we examine the atmosphere dependence of the formation process of oxygen vacancy.

**EXPERIMENTS:** For the synthesis of 100 ppm Al-doped ZnO, stoichiometric amounts of Al(NO<sub>3</sub>)<sub>3</sub> · 9H<sub>2</sub>O and ZnO powder were mixed in ethanol. The suspension was heated to evaporate the ethanol until dryness. The powders were pressed into disks and sintered in air at 1273 K for 3 h. Commercially available <sup>111</sup>In HCl solution was added in droplets onto the sintered disks. The initial concentration of <sup>111</sup>In ions in the sample was typically ~100 ppt. After the disks were dried up by heat, they again underwent heat treatment in air at 1373 K for 2 h. Following the doping of <sup>111</sup>In, each disk was separately sealed in different quartz tubes in Ar gas atmosphere, and 24-h isochronal annealing was performed one by one at different temperatures (873~1148 K). The TDPAC measurements were carried out for the 171-245 keV cascade  $\gamma$  rays of the <sup>111</sup>Cd( $\leftarrow$ <sup>111</sup>In) probe with the intermediate state of  $I = 5/2$  having a half-life of 85.0 ns.

**RESULTS:** It was found from the TDPAC spectra of the <sup>111</sup>In( $\rightarrow$ <sup>111</sup>Cd) in 100 ppm Al-doped ZnO heat-treated at various temperatures that <sup>111</sup>In probes are detrapped from the Al aggregations during the annealing in Ar gas by degrees. It was revealed that this detrapping process is controlled by the first-order rate law. For the first-order reaction of the dissociation process, we obtained the rate constant  $k$  at different temperatures. Figure 1 shows the temperature variation of  $k$  values. A least-squares fit to the  $k$  values was then carried out with the following Arrhenius equation:

$$k = \nu_0 \exp(-E_a / k_B T)$$

and the activation energy,  $E_a$ , was evaluated to be 2.05 (15) eV. Because the dissociation process of the <sup>111</sup>In probe and Al would be induced by the formation of oxygen vacancies, we suggest that the observed  $E_a$  is closely related to the formation energy of oxygen vacancies in Al-doped ZnO sample[3]. This  $E_a$  value is larger than that obtained in vacuum (0.72(6) eV[3]). This atmosphere dependence of the formation energy of oxygen vacancies is now under consideration.

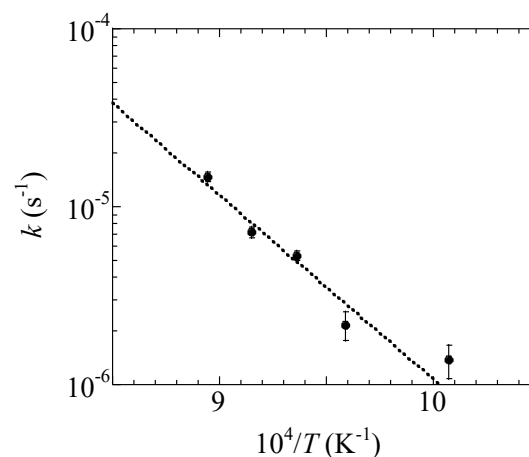


Fig. 1. Temperature dependence of the rate constant,  $k$ . An Arrhenius equation was used for the fit.

### REFERENCES:

- [1] S. Komatsuda *et al.*, *J. Phys. Soc. Jpn.* **80** (2011) 095001 (1-2).
- [2] S. Komatsuda *et al.*, *J. Radioanal. Nucl. Chem.* **303** (2015) 1249-1252.
- [3] S. Komatsuda *et al.*, *J. Appl. Phys.* **116** (2014) 183502 (1-5).
- [4] S. Lany *et al.*, *Phys. Rev. Lett.* **98** (2007) 045501 (1-4).
- [5] F. Oba *et al.*, *Phys. Rev. B* **77** (2008) 245202 (1-6).

## PR5 Project Research on the Advanced Utilization of Multi-Element Mössbauer Spectroscopy for the Study on Condensed Matter Science

M. Seto

Research Reactor Institute, Kyoto University

### OBJECTIVES AND PERFORMED RESEARCH SUBJECTS:

The main objectives of this project research are the investigation of the fundamental properties of new materials and the development of the advanced experimental methods by using multi-element Mössbauer spectroscopy. Combination use of the high-magnetic-field superconducting magnet was also essential to study the magnetism of the materials. As the Mössbauer resonance line is extremely narrow, hyperfine interactions are well resolved and give us the information on the surrounding electronic states and magnetism. Thus, the Mössbauer spectroscopy is applied to widely various areas of researches, such as physical, chemical, biological, and earth sciences. Moreover, element-specific or isotope-specific information is one of the most irreplaceable features of the Mössbauer spectroscopy. Therefore, promotion of the variety of Mössbauer isotope provides more useful and valuable methods for modern precise materials science of complex systems, such as biological substances, multi-layer films, and complicated-structured matter.

In this term of the year, some of the planned researches have not been performed because of the shutdown of the research reactor. The research subjects performed are as follows:

- P5-2 Mössbauer microspectrometer using Si-PIN semi-conductor detector and its application to mineral science (K. Shinoda *et al.*)
- P5-3  $^{57}\text{Fe}$  Mössbauer spectra of  $\text{Sr}_2\text{VFeAsO}_{3-d}$  ( $d=0.232, 0.267, \text{ and } 0.509$ ) (Y. Kamihara *et al.*)
- P5-4 Relationship between Heme Electronic Structure and Oxygen Affinity of Myoglobin (Y. Yamamoto *et al.*)
- P5-8 Development of Mössbauer spectroscopy system on  $^{67}\text{Zn}$  (M. Saito *et al.*)
- P5-9 Mössbauer Study of  $\text{Ba}_{0.6}\text{K}_{0.4}\text{Fe}_2\text{As}_2$  under High Magnetic Fields (S. Kitao *et al.*)

### MAIN RESULTS AND CONTENTS OF THIS REPORT:

The following reports were contributed by research groups in this project research.

K. Shinoda *et al.* (P5-2) have developed Mössbauer microspectrometer using Si-PIN semiconductor detector and applied to studies of crystallographically-oriented single crystals of thin sections of augite from different occurrences. Obtained three sets of quadrupole doublets were well identified with  $\text{Fe}^{2+}$  in M1 and M2 sites, and  $\text{Fe}^{3+}$  in M1 site in pyroxene structure. From the intensity ratio of each doublets, the orientation of the electric field gradient vector was discussed. As a result, good concentration of orientation in  $\text{Fe}^{2+}$  in M2 site was found, although  $\text{Fe}^{2+}$  in M1 site did not show concentration.

Y. Kamihara *et al.* (P5-3) studied  $\text{Sr}_2\text{VFeAsO}_{3-d}$ , which are related compounds of FeAs-based superconductor with blocking layer and some of which show superconductivity and antiferromagnetic ordering of Vanadium. Mössbauer spectroscopy was applied to investigate magnetism of Fe in these compounds. For the samples with  $d = 0.232, 0.267, \text{ and } 0.509$ , the spin density wave phase was observed, while magnetically-ordered Fe was not observed for superconducting  $\text{Sr}_2\text{VFeAsO}_{3-d}$ . The result indicates that Fe has two different magnetic phase, depending on the oxygen deficiency.

Y. Yamamoto *et al.* (P5-4) investigated the Mössbauer spectroscopy to elucidate the relationship between electronic structure of heme Fe atom and oxygen affinity of myoglobin(Mb). Through the studies of chemically-modified heme cofactors, obtained isomer shifts could not be simply interpreted as the electronic nature of the hemes. On the other hand, quadrupole splitting values decreased with decreasing the electron density of the hemes. These facts are useful to elucidate the electronic structure of the oxy form of Mb, to understand the oxygenation and autoxidation processes of Mb.

M. Saito *et al.* (P5-8) attempted to observe the  $^{67}\text{Zn}$  Mössbauer absorption spectrum, which could be useful for experiments requiring extremely high energy resolution. To obtain the  $^{67}\text{Cu}$  Mössbauer source, ZnO crystals were irradiated by KURRI-LINAC through photonuclear reaction. Although measurement of the Mössbauer spectrum was tried, expected absorption was not observed. It is considered to be due to the vibrational noise of the vacuum chamber. Further development of the  $^{67}\text{Zn}$  Mössbauer spectroscopic system is in progress.

S. Kitao *et al.* (P5-9) measured detailed temperature dependences of Mössbauer spectra under high magnetic fields to reveal the magnetic properties of the Fe-based superconductor  $\text{Ba}_{0.6}\text{K}_{0.4}\text{Fe}_2\text{As}_2$ . From the temperature dependence of Mössbauer spectra, small broadening of the line width were observed at the temperature a little above the superconducting transition temperature. The measurements under high magnetic fields revealed the line broadenings are due to quadrupole splittings, which is consistent to the fact that the electronic nematic states has the small asymmetry in the structure.

## PR5-1 Mössbauer Microspectrometer Using Si-PIN Semi-conductor Detector and its Application to Mineral Sciences

A. Marutani<sup>1</sup>, K. Shinoda<sup>1</sup>, Y. Kobayashi<sup>2</sup>

<sup>1</sup>Department of Geosciences,  
Graduate School of Science, Osaka City University  
<sup>2</sup>Research Reactor Institute, Kyoto University

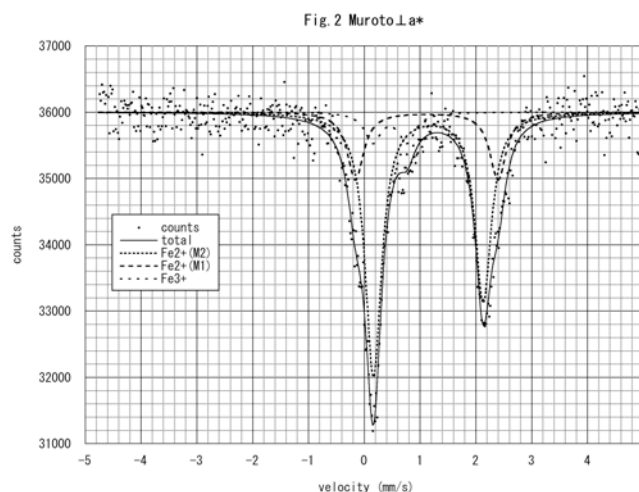
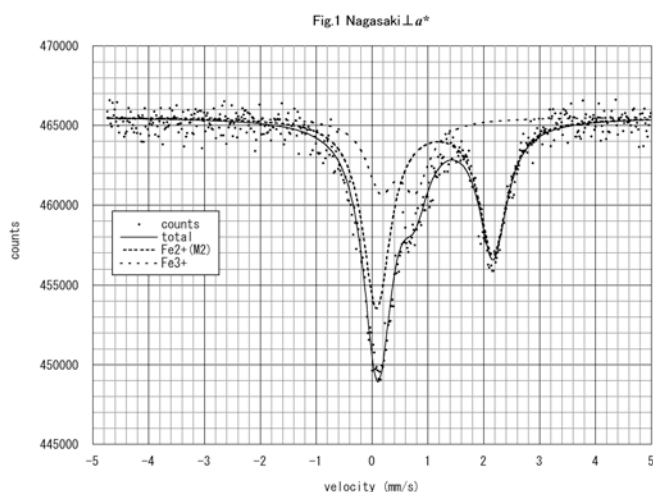
**INTRODUCTION:** Mössbauer microspectrometer using Si-PIN semi-conductor detector was used to measure Mössbauer spectra of single crystals of mineral thin sections. A Pb pin-hole (1mm $\phi$ ) was used to limit measuring region in a thin section. A Si-PIN semi-conductor of which energy resolution is better than a proportional counter is suitable for micro-measurements. Whereas two peaks' intensity of Q-splitting doublets is equal for powder sample, intensity ratio of Q-splitting doublet of single crystal varies between 0.6 and 3 depending on the angle between  $\gamma$ -ray and electric field gradient vector. Augite is a major rock-forming mineral including Fe<sup>2+</sup> and Fe<sup>3+</sup>, and they distribute at M1 and M2 sites in pyroxene structure. To fitting out M1Fe<sup>2+</sup>, M2Fe<sup>2+</sup> and M1Fe<sup>3+</sup> Q-splitting doublets from raw Mössbauer data of single crystal thin section of augite, orientations of electric field gradient vector of M1 and M2 sites for Fe<sup>2+</sup> and Fe<sup>3+</sup> is important. In this study, the orientation of electric field gradient vector of M1Fe<sup>2+</sup> and M2Fe<sup>2+</sup> were estimated by measuring thin sections of augite of which crystal graphic orientation were determined by X-ray precession camera.

**EXPERIMENTS and RESULTS:** Crystal graphically oriented thin sections perpendicular to  $a^*$ -  $b^*$ - and  $c^*$ -axes of augite from two different occurrences (Muroto and Nagasaki) were prepared for Mössbauer microspectrometer. Fig.1 shows Mössbauer spectrum of augite thin section perpendicular to  $a^*$  axis from Na-

gasaki. Two sets of Q-splitting doublets were identified. The wider Q doublet of 2.08mm/s was assigned to M2Fe<sup>2+</sup> and the narrower doublet of 0.60 mm/s was M1Fe<sup>3+</sup>. On the fitting of raw data of Fig.1, the ratio of intensity of the narrower doublet was fixed to 1:1, and that of the wider doublet was not fixed and calculated to 0.716. Fig.2 shows Mössbauer spectrum of augite thin section perpendicular to  $a^*$  axis from Muroto. three sets of Q-splitting doublets were identified. The first is strong doublet of 1.97 mm/s Q-splitting which is due to M2Fe<sup>2+</sup>, the second is middle doublet of 2.55 mm/s due to M1Fe<sup>2+</sup> and weak doublet of 0.61 mm/s due to M1Fe<sup>3+</sup>. On the fitting of raw data of Fig.2, the ratio of intensity of the weak doublet was fixed to 1:1, the strong doublet due to M2Fe<sup>2+</sup> was fixed to 0.716 from Fig.1 and intensity ratio of middle doublet was not fixed and finally calculated to 1.00. From the relation between the intensity ratio of doublet ( $x$ ) and the angle between  $\gamma$ -ray and electric field gradient vector of augite ( $\theta$ ),

$$x = \frac{1 + \cos^2 \theta}{2/3 + \sin^2 \theta}$$

$\theta$  of six thin sections were calculated. From the two sets of  $\theta$ s, orientations of electric field gradient vector of M1Fe<sup>2+</sup> and M2Fe<sup>2+</sup> of augite were plotted on stereographic projections. As the results, M2Fe<sup>2+</sup> shows good concentration of orientation, but M1Fe<sup>2+</sup> was not show concentration. To improve data fitting, the proper doublet parameter of M1Fe<sup>3+</sup> must be used.



Y. Tojo, H. Fujioka, M. Matoba, S. Kitao<sup>1</sup>, M. Seto<sup>1</sup> and Y. Kamihara

Department of Applied Physics and Physico-Informatics,  
Keio University

<sup>1</sup>Research Reactor Institute, Kyoto University

**INTRODUCTION:** Layered oxypnictide Ae<sub>2</sub>T<sub>M</sub>FePnO<sub>3-d</sub> (Ae = Alkaline earth metal, T<sub>M</sub> = Transition metal) (21113) consists of carrier conducting FePn (Pn = P and As) layer and carrier blocking Ae<sub>2</sub>T<sub>M</sub>O<sub>3</sub> layer. Several 21113 compounds show superconducting phase at low temperatures. Hyperfine fields ( $B_{hf}$ ) measurements experienced by nuclei of atoms at crystallographic sites in magnetic and/or antiferromagnetic metals are of interest in view point of hyperfine interactions and important for their use in the determinations of nuclear magnetic dipole moments by a variety of methods including those based on low-temperature nuclear orientation. Guang-Han Cao et al reported that Sr<sub>2</sub>VFeAsO<sub>3-d</sub> is an FeAs-based layered oxypnictide superconductor, which exhibits antiferromagnetic ordering under 150 K originating in local d-electron moments of vanadium, and the superconducting transition temperature  $T_c$  is 24 K.[1,2] In this study, we focus on magnetic phase of Sr<sub>2</sub>VFeAsO<sub>3-d</sub> as a complex magnetic compounds. [1-8]

Element-specific magnetism and electronic phase of Fe sublattice in Sr<sub>2</sub>VFeAsO<sub>3-d</sub> are elucidated using <sup>57</sup>Fe Mössbauer spectroscopy. Studies on hyperfine fields  $B_{hf}$  experienced by nuclei are of interest in view point of hyperfine interactions and important for their use in the determinations of nuclear magnetic dipole moments.

**EXPERIMENTS:** Polycrystalline samples of Sr<sub>2</sub>VFeAsO<sub>3-d</sub> were prepared by the solid-state reactions in a sealed silica tube using dehydrated SrO, FeAs, Vanadium oxides, and V as starting materials. Then, a mixture of the three powders was pressed into pellet and heated in doubly sealed silica tubes at 1050-1300 °C for 40 h. All procedures were carried out in an Ar-filled glove box (MIWA Mfg; O<sub>2</sub>, H<sub>2</sub>O < 1 ppm). The crystal phase of the obtained product was examined by powder X-ray diffraction (XRD; RigakuRINT-2500) using CuK $\alpha$  radiation. Almost all the diffraction peaks are assigned to the Sr<sub>2</sub>VFeAsO<sub>3-d</sub> phase. Electrical resistivity measurements were performed at 2–300 K by a dc four-probe technique using silver paste as electrodes. Magnetization measurements were performed for polycrystalline samples using a Quantum Design magnetic properties measurement system (MPMS). The <sup>57</sup>Fe Mössbauer (MS) experiment on the two series of compounds, Sr<sub>2</sub>VFeAsO<sub>3-d</sub> (x = 0.232, 0.267, and 0.509) was performed with conventional <sup>57</sup>Fe MS equipment using 14.4 keV  $\gamma$ -rays from a <sup>57</sup>Co source in an Rh matrix.

**RESULTS:** <sup>57</sup>Fe MS to the samples of d=0.232, 0.267, and 0.509 of Sr<sub>2</sub>VFeAsO<sub>3-d</sub> were measured and analyzed

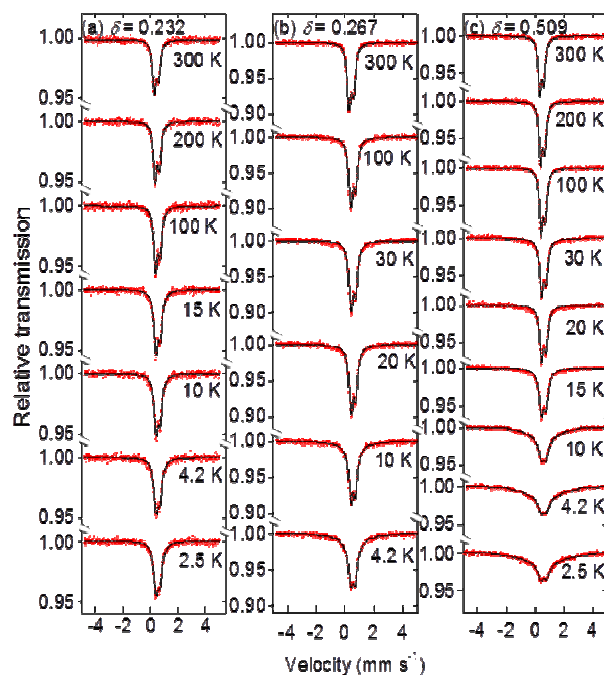


Fig. 1. <sup>57</sup>Fe Mössbauer spectra (MS) of polycrystalline Sr<sub>2</sub>VFeAsO<sub>3-d</sub> (d = 0.232, 0.267 and 0.508) at several temperatures described in the figure. The solid lines for each samples are fitted patterns provided that internal magnetic fields with wide distribution exist around <sup>57</sup>Fe. Such internal magnetic field indicate existence of spin density wave in Sr<sub>2</sub>VFeAsO<sub>3-d</sub> (d = 0.232, 0.267 and 0.508).

for obtaining quantitative value of internal magnetic field. As a result, the existence of spin density wave phase are observed for x = 0.232, 0.267, 0.509, while magnetic ordered Fe are not observed for superconducting Sr<sub>2</sub>VFeAsO<sub>3-d</sub> samples.[9] The result indicates that Fe of Sr<sub>2</sub>VFeAsO<sub>3-d</sub> shows two magnetic phase, which stabilities depend on oxygen deficiency.

#### REFERENCES:

- [1] X. Zhu, et al., Phys. Rev. B 79, 220512 (2009).
- [2] G. H. Cao et al., Phys. Rev. B 82, 104518 (2010).
- [3] Y. Kamihara et al., New J. Phys. 12, 033005 (2010).
- [4] H. Kotegawa et al., J. Phys. Soc. JPN 78, 123707 (2009).
- [5] S. Tatematsu, et al, J. Phys. Soc. JPN 79, 123712 (2010).
- [6] D. Suetin, J. Mater. Sci. 47, 3663 (2010).
- [7] H. Nakamura and M. Machida, Phys. Rev. B 82, 094503 (2010).
- [8] Y. Tojo, J. Appl. Phys. 113, 17E157 (2013).
- [9] Y. Tojo, et al, unpublished.

## PR5-3 Relationship between Heme Electronic Structure and Oxygen Affinity of Myoglobin

K. Hasegawa, M. Saito<sup>1</sup>, M. Seto<sup>1</sup>, Y. Kobayashi<sup>1</sup>, T. Ohta<sup>2</sup>, S. Yanagisawa<sup>2</sup>, T. Ogura<sup>2</sup>, Y. Yamamoto, T. Shibata, S. Neya<sup>3</sup> and A. Suzuki<sup>4</sup>

Department of Chemistry, University of Tsukuba

<sup>1</sup> Research Reactor Institute, Kyoto University

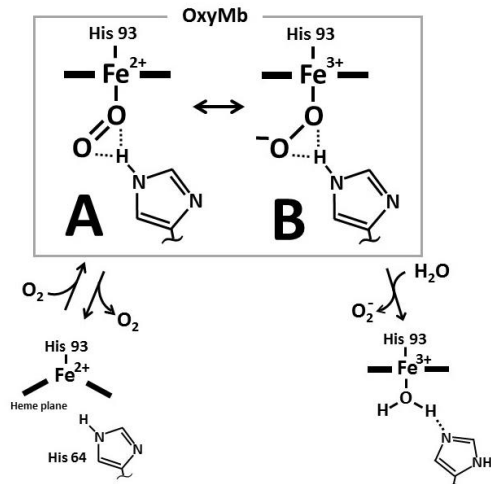
<sup>2</sup> Graduate School of Life Science, University of Hyogo

<sup>3</sup> Graduate School of Pharmaceutical Sciences, Chiba University

<sup>4</sup> Department of Materials Engineering, Nagaoka National College of Technology

**INTRODUCTION:** The function of an oxygen storage hemoprotein, myoglobin (Mb), is regulated through heme electronic structure, in addition to heme environment furnished by nearby amino acid residues. We found that a decrease in the electron density of the heme Fe atom ( $\rho_{\text{Fe}}$ ) leads to lowering oxygen affinity and a decrease in the autoxidation rate of the protein.<sup>1</sup> These findings could be reasonably explained in terms of the effect of a change in the  $\rho_{\text{Fe}}$  on the resonance  $A \leftrightarrow B$  of oxy form of Mb (oxyMb) (scheme 1). In this study, we measured Mössbauer spectra of oxyMbs reconstituted with some chemically-modified heme cofactors (Fig. 1) in order to characterize the relationship between the  $\rho_{\text{Fe}}$  and the resonance  $A \leftrightarrow B$ . The formal charges of heme Fe in the canonical structures A and B are +2 and +3, respectively, and hence the effect of a change in the  $\rho_{\text{Fe}}$  on the resonance  $A \leftrightarrow B$  could be analyzed through the resonance hybrid of the formal charge of heme Fe which is sharply reflected in the Mössbauer spectral parameters, i.e., isomer shift (IS) and quadrupole splitting (QS).

**EXPERIMENTS:** ApoMb was prepared from sperm whale Mb, using the standard procedure, and reconstituted with <sup>57</sup>Fe-labelled heme cofactors. 2 mM Mbs in 50 mM potassium phosphate buffer, pH = 7.4, were cooled rapidly in liquid nitrogen bath. The Mössbauer measurements were performed at 3-6 K.



Scheme 1. Oxygenation and autoxidation of Mb, and the resonance structures A and B of oxyMb.

Heme	IS(mm/s)	QS(mm/s)
Meso	0.260	2.36
3,8-DMD	0.260	2.32
Proto	0.271	2.29
7-PF	0.264	2.28
2,8-DPF	0.270	2.21

Heme	R <sub>2</sub>	R <sub>3</sub>	R <sub>7</sub>	R <sub>8</sub>
Meso	CH <sub>3</sub>	CH <sub>2</sub> CH <sub>3</sub>	CH <sub>3</sub>	CH <sub>2</sub> CH <sub>3</sub>
3,8-DMD	CH <sub>3</sub>	CH <sub>3</sub>	CH <sub>3</sub>	CH <sub>3</sub>
Proto	CH <sub>3</sub>	CH=CH <sub>2</sub>	CH <sub>3</sub>	CH=CH <sub>2</sub>
7-PF	CH <sub>3</sub>	CH <sub>2</sub> CH <sub>3</sub>	CF <sub>3</sub>	CH <sub>2</sub> CH <sub>3</sub>
2,8-DPF	CF <sub>3</sub>	CH <sub>3</sub>	CH <sub>3</sub>	CF <sub>3</sub>

Fig. 1. Chemically-modified heme cofactors used in the study, and the obtained Mössbauer spectral parameters.

**RESULTS:** The Mössbauer spectrum of oxyMb reconstituted with <sup>57</sup>Fe-labelled proto (Fig. 2) was almost identical to that previously reported.<sup>2</sup> The IS values of the heme cofactors ranged from 0.260 to 0.271 mm/s and could not be simply interpreted on the basis of the electronic nature of the hemes. On the other hand, the heme cofactors were arranged as 2,8-DPF < 7-PF  $\approx$  Proto < 3,8-DMD < Meso, in order of increasing QS (Fig. 1), indicating that the QS decreases with decreasing the  $\rho_{\text{Fe}}$ . This result confirmed that a decrease in the  $\rho_{\text{Fe}}$  results in shifting the resonance  $A \leftrightarrow B$  toward structure A. Proto and 7-PF exhibited similar QS values, supporting that the  $\rho_{\text{Fe}}$  values of the two heme cofactors are closely similar to each other. Thus, Mössbauer spectroscopy is a powerful tool to elucidate the electronic structure of oxyMb.

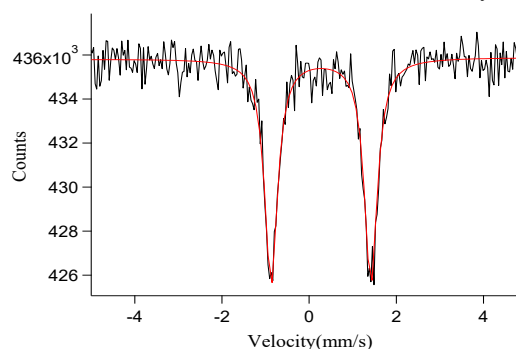


Fig. 2. Mössbauer spectrum of oxyMb (proto) at 3 K.

### REFERENCES:

- [1] T. Shibata, D. Matsumoto, R. Nishimura, H. Tai, A. Matsuoka, S. Nagao, S. Matsuo, S. Hirota, K. Imai, S. Neya, S. Suzuki, and Y. Yamamoto, *Inorg. Chem.*, **51**, (2012) 11955–11960.  
 [2] B. Boso, P. G. Debrunner, G. C. Wagner, and T. Inubushi, *Biochem. Biophys. Acta*, **791**, (1984) 244-251.

## PR5-4 Magnetic Property and Local Structures of Functional Irons in Glass by Mössbauer Spectroscopy

N. Umesaki, K. Okada<sup>1</sup>, Y. Kobayashi<sup>2</sup>  
Graduate School of Engineering, Osaka University  
<sup>1</sup>Research & Utilization division, JASRI  
<sup>2</sup>Research Reactor Institute, Kyoto University

**INTRODUCTION and AIM:** Glass is used in many applications in our every-day lives and has new applications. Coexisting divalent iron ions ( $\text{Fe}^{2+}$ ) and trivalent iron ions ( $\text{Fe}^{3+}$ ) in glass affect the transmission from the near-ultraviolet (NUV) to the near-infrared (NIR) range (hereinafter denoted as “transmission<sub>NUV-NIR</sub>”) and coloring (value, chroma, hue) of glass.<sup>[1]</sup> The transmission<sub>NUV-NIR</sub> and coloring determine the utilization purpose of glass in industry. Commercial glass ineluctably contains very low concentrations of irons (about 0.01-0.1 wt.% iron oxide concentration), which are derived from raw materials or industrial processes. Higher iron concentration are added by manufacturing design. The iron concentrations mainly affect the value of coloring.  $\text{Fe}^{2+}$  and  $\text{Fe}^{3+}$  mainly affect the chroma and hue of coloring.  $\text{Fe}^{2+}$  gives absorption mainly in the NIR range, resulting in bluish coloring.<sup>[1]</sup>  $\text{Fe}^{3+}$  gives strong absorption mainly in the visible to NUV range, resulting in yellowish coloring.<sup>[1]</sup>

Two macro parameters have been used in industry to control transmission<sub>NUV-NIR</sub> and coloring: (1) the total iron ion mass concentration in terms of  $\text{Fe}_2\text{O}_3$  (hereinafter denoted as “iron oxide concentration;  $M_{\text{Fe}_2\text{O}_3}$ ”), and (2) the ratio of the number of  $\text{Fe}^{2+}$  to the number of total irons (hereinafter denoted as “ $\text{Fe}^{2+}/\Sigma_n\text{Fe}$ ”).

Three dimensional (3D) local structures and property of iron ions should also contribute to the transmission<sub>NUV-NIR</sub> and coloring. Although many scientists proposed structures of  $\text{Fe}^{2+}$  and  $\text{Fe}^{3+}$  by traditional measuring methods, they could not explain the property of irons in glass completely.

By enriching with  $^{57}\text{Fe}$ , we made basic soda-lime glass samples that had 0-0.6  $^{57}\text{Fe}^{2+}/\Sigma_n\text{Fe}$  and  $M_{\text{Fe}_2\text{O}_3}$  of 0.1, 0.5, 1.5, and 5.0 wt.%.

We have investigated these samples by nuclear resonant inelastic scattering (NRIS) and XAFS methods at synchrotron radiation, and revealed the 3D local structure around iron atoms in sub-nanometer region (Okada et al, submitted to X-ray Spectrometry). And we found the capability of complex magnetic fields of  $\text{Fe}^{3+}$  in glass at RT. Then we have proposed Mössbauer measurements to reveal the magnetic states and internal magnetic fields from  $\text{Fe}^{3+}$  and  $\text{Fe}^{2+}$  atoms, independently, at various temperatures.

**EXPERIMENTS:** The measurements were performed using conventional Mössbauer spectrometer. The specimens for Mössbauer measurements were tuned to 10 mm-phi pellet from the  $^{57}\text{Fe}$  enriched glass powders. We investigated samples at room temperature (RT), 150 K and 77 K.

**RESULTS and DISCUSSION:** The three glass samples

with 0.5 wt.%  $M_{\text{Fe}_2\text{O}_3}$  were measured at RT. As shown in Fig. 1, there were the differences of continuous components between samples that had different  $\text{Fe}^{2+}/\Sigma_n\text{Fe}$ . These wide structures indicated the local magnetization around iron atoms. The two  $\text{Fe}^{3+}$  components with large internal magnetic field and the two  $\text{Fe}^{2+}$  components with large quadrupole splitting have been determined from their isomer shifts by our fittings shown in Fig. 1. And the results from glass with 0.1-5 wt.%  $M_{\text{Fe}_2\text{O}_3}$ , indicated that the  $\text{Fe}^{3+}$  and  $\text{Fe}^{2+}$  atoms in glass had separate structures. Moreover we measured glass with 0.5 wt.%  $M_{\text{Fe}_2\text{O}_3}$  and with 0  $\text{Fe}^{2+}/\Sigma_n\text{Fe}$  at 150 K and 70 K. The internal magnetic field from  $\text{Fe}^{3+}$  in the sample was about 51 T and had internal distribution. We concluded that about 90 % of the  $\text{Fe}^{3+}$  in glass had local magnetic order like antiferromagnetic materials. On the other hand, we concluded that  $\text{Fe}^{2+}$  atoms had no magnetic order.

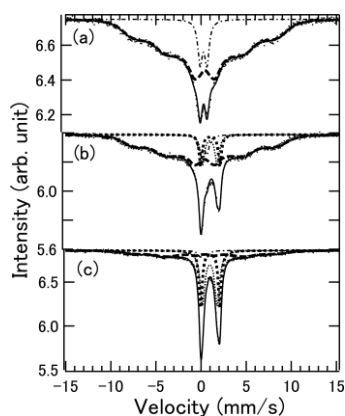


Fig. 1. Mössbauer spectra of glass at RT with 0.5 wt.%  $M_{\text{Fe}_2\text{O}_3}$  and with  $\text{Fe}^{2+}/\Sigma_n\text{Fe}$  of (a) 0, (b) 0.2, and (c) 0.6. The dot lines and dot-and-dash lines were fitting curves from  $\text{Fe}^{3+}$  and  $\text{Fe}^{2+}$ , respectively. The solid line showed the total fit.

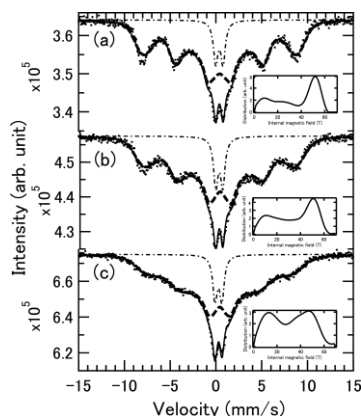


Fig. 2. Mössbauer spectra of sample glass at (a) 70 K, (b) 150 K, and (c) R.T. with 0.5 wt.%  $M_{\text{Fe}_2\text{O}_3}$  and with 0  $\text{Fe}^{2+}/\Sigma_n\text{Fe}$ . Same lines as Fig. 1. The inset panels showed internal magnetic fields of each temperature.

## REFERENCE:

[1] F. N. Steele *et al.*, *Phys. Chem. Glass.* 1965; **6**: 246.

M. Saito, Y. Kobayashi, R. Masuda, M. Kurokuzu, S. Kitao and M. Seto

Research Reactor Institute, Kyoto University

**INTRODUCTION:** Among various Mössbauer spectroscopy systems,  $^{67}\text{Zn}$  Mössbauer spectroscopy system shows relatively very high energy resolution: the energy width of the gamma rays is narrow  $\Delta E \sim 50$  peV comparing with the gamma-ray's energy  $E_0 \sim 93$  keV, and the relative energy uncertainty of the gamma rays  $\Delta E/E_0$  is the order of  $\Delta E/E_0 \sim 10^{-15}$ . [1,2]

Therefore,  $^{67}\text{Zn}$  Mössbauer spectroscopy system has been used to study the various physics experiments which require high energy resolution such as the detection of the gravitational red shift of the photons as well as to study the solid state physics on materials including  $^{67}\text{Zn}$ .

However, in spite of its usefulness, only few group succeeded to develop  $^{67}\text{Zn}$  Mössbauer spectroscopy so far owing to its difficulty: the system requires very accurate control of the relative velocity between the source and the absorber. Recently, by trial experiment, the Mössbauer absorption of  $^{67}\text{Zn}$  has been observed by authors using the radioactive Mössbauer source produced by the electron linear accelerator (KURRI-LINAC).

The purpose of this study is to establish the  $^{67}\text{Zn}$  Mössbauer spectroscopy system by controlling velocity accurately using a piezo driving system.

**EXPERIMENTS:** In this experiment, the source of  $^{67}\text{Zn}$  Mössbauer spectroscopy is  $^{67}\text{Zn}$  in ZnO mono-crystal produced by the  $^{68}\text{Zn}(\gamma, p)^{67}\text{Cu}$  reaction using high energy gamma-rays from the platinum target of the LINAC. The ZnO mono-crystal was irradiated by the high energy gamma-rays for three days and taken out from the target room one-day later after the irradiation. The source was, then, annealed at 700 °C for 9 hours in Ar atmosphere. Gamma rays and X rays were detected by Ge-semiconductor detector. In Fig. 1, we show the obtained energy spectrum.

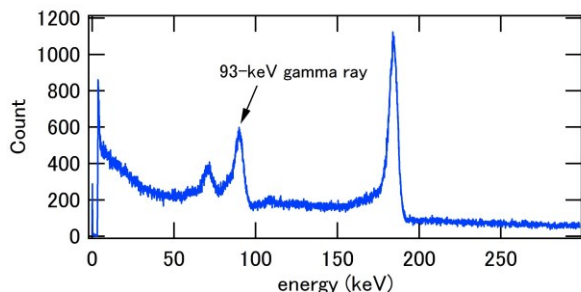


Fig. 1. Energy spectrum of radiations from the source.

The 93-keV gamma-rays from  $^{67}\text{Zn}$  source could be nicely observed and selectively used to obtain the Mössbauer spectrum. The source and the  $^{67}\text{ZnO}$  mono-crystal

absorber were set to the vacuum chamber and cooled down to around 10 K. The chamber was put on the vibration-isolated table for the isolation from the external vibration and a piezo driving stage (P752, PI Japan Co., Ltd.) was used for a velocity control. Against for the stable absorber, a sinusoidal motion with the amplitude of 12  $\mu\text{m/s}$  was induced to the source.

**RESULTS:** The obtained  $^{67}\text{Zn}$  Mössbauer spectrum is shown in Fig. 2. The velocity calibration was performed by the time dependence of the piezo elongation. The error bar shows the standard deviation of the obtained value.

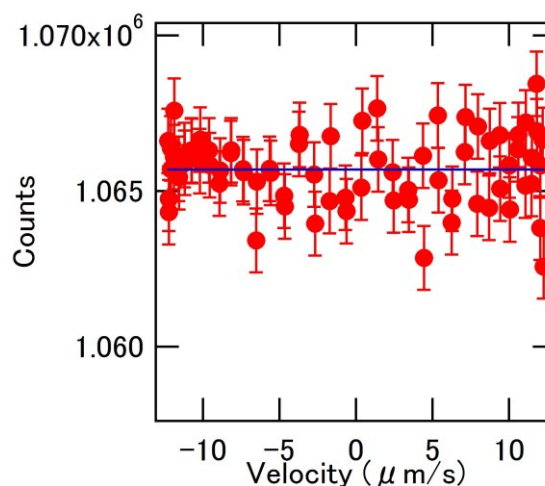


Fig. 2. Obtained  $^{67}\text{Zn}$  Mössbauer spectrum.

From the previous studies, absorption with the absorption depth ratio of 0.7 % is expected at zero position of the velocity.[1] However, from the experiment, the absorption depth ratio is, if any, estimated to be less than 0.1 %. This result suggests that the strong reduction of the depth of the absorption occurs.

After the experiment, we checked the vibrational noise of the vacuum chamber by using the laser-Doppler velocimeter. The result suggests that the vibrational noise of our system is larger than our expectation and too large to obtain the  $^{67}\text{Zn}$  Mössbauer spectrum.

From the experiment, we could obtain fundamentally important knowledge about the current system such as the gamma-rays count-rate and degree of the external noise. Based on the obtained knowledge, further development of the  $^{67}\text{Zn}$  Mössbauer spectrum is in progress.

#### REFERENCES:

- [1] W. Potzel, A. Forster, and G. M. Kalvius, *J. Phys. Colloques* **37** (1976) C6-691.
- [2] N.N. Greenwood, and T. C. Gibb, "Mössbauer spectroscopy" (Chapman and Hall Ltd., London, 1971).

S. Kitao, M. Kurokuzu, Y. Kobayashi and M. Seto

Research Reactor Institute, Kyoto University

**INTRODUCTION:** After the discovery of so-called “1111” series of Fe-oxypnictide superconductors,  $\text{LaFeAsO}_{1-x}\text{F}_x$ [1], several series of Fe-based superconductors have been extensively investigated. Among related Fe-based superconductors, so-called “122” series has been of great interest because the superconductivity emerges with various doping methods. That is, the superconductivity was observed not only with hole doping,  $\text{Ba}_{1-x}\text{K}_x\text{Fe}_2\text{As}_2$ [2] or electron doping,  $\text{Ba}(\text{Fe}_{1-x}\text{Co}_x)_2\text{As}_2$ , but also with isovalent doping,  $\text{BaFe}_2(\text{As}_{1-x}\text{P}_x)_2$ . Recently, the electronic nematic phase was found in the isovalent-doped  $\text{BaFe}_2(\text{As}_{1-x}\text{P}_x)_2$ [3]. This electronic nematic phase is considered to have an important relationship with superconductivity. The electronic nematic phase was also found in  $\text{Ba}(\text{Fe}_{1-x}\text{Co}_x)_2\text{As}_2$ . However, it is not clear in the case of  $\text{Ba}_{1-x}\text{K}_x\text{Fe}_2\text{As}_2$ . Therefore, it is important to investigate the electronic nematic phase in  $\text{Ba}_{1-x}\text{K}_x\text{Fe}_2\text{As}_2$ .

Since  $^{57}\text{Fe}$ -Mössbauer spectroscopy is an essential method to extract the electronic states of Fe, a number of Mössbauer studies on these Fe-based superconductors have been carried out and revealed many important facts, for example, in  $\text{LaFeAsO}_{1-x}\text{F}_x$ [4]. Moreover, Mössbauer spectroscopy under high magnetic fields has advantageous to reveal the nature of magnetism in these compounds[5]. In this study, detailed temperature dependences of Mössbauer spectra under high magnetic fields were measured to investigate the properties of the electronic nematic phase.

**EXPERIMENTS:**  $\text{Ba}_{1-x}\text{K}_x\text{Fe}_2\text{As}_2$  was synthesized by heating of a stoichiometric mixture of ground Ba and FeAs with a little excess of K in a crucible of aluminum oxide sealed in a quartz tube, as in the reported method[2]. The obtained polycrystalline powder was characterized by x-ray diffraction and magnetic susceptibility measurements. The doping level of  $x = 0.4$  is the optimal doping, that is, the superconducting transition temperature ( $T_c$ ) has the maximum value of about 38 K.  $^{57}\text{Fe}$ -Mössbauer spectra were measured using a pellet of powder sample using a  $^{57}\text{Co}$  source in Rh matrix with a nominal activity of 1.85 GBq. The velocity scales are referenced to  $\alpha$ -Fe. Magnetic fields were applied by a superconducting-magnet cryostat with a direction parallel to the  $\gamma$ -rays.

**RESULTS AND DISCUSSION:** Mössbauer spectra of  $\text{Ba}_{0.6}\text{K}_{0.4}\text{Fe}_2\text{As}_2$  showed a singlet pattern down to 4.2 K as in Fig 1(a). This implies the optimally-doped superconductor  $\text{Ba}_{0.6}\text{K}_{0.4}\text{Fe}_2\text{As}_2$  has no magnetic order down to 4.2 K. However, the line width at a little above  $T_c$ , showed a small broadening. This line broadening is considered to be due to the electronic nematic phase at a little

above  $T_c$ . On the other hand, the line width broadening was not clearly observed below  $T_c$ .

When high magnetic fields were applied, the spectra showed 4-line patterns under the magnetic fields as shown in Fig. 1(b). This pattern can be well understood as a paramagnetic feature, where the magnetic moments are entirely aligned to the direction of the applied magnetic fields. However, Mössbauer spectra under the magnetic fields did not show specific broadened feature even at a little above  $T_c$ . Since the spectra did not show broadened magnetically-split spectra, the line broadening due to small internal magnetic fields was excluded. That is, the broadening may not be originated by internal magnetic fields but by quadrupole splittings. This fact implies the nature of the nematic phase is due to asymmetry in the structure. This is consistent with the original finding of the nematic phase due to small structural anisotropy in the magnetic torque measurements[3].

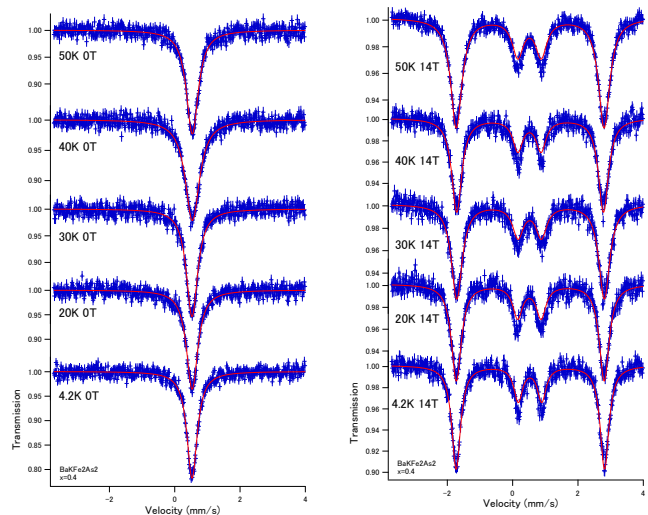


Fig. 1 Typical Mössbauer spectra of  $\text{Ba}_{0.6}\text{K}_{0.4}\text{Fe}_2\text{As}_2$  (a) without magnetic fields and (b) under magnetic fields of 14T.

#### REFERENCES:

- [1] Y. Kamihara, T. Watanabe, M. Hirano and H. Hosono, *J. Am. Chem. Soc.* **130** (2008) 3296.
- [2] M. Rotter, M. Tegel and D. Johrendt, *Phys. Rev. Lett.* **101** (2008) 107006.
- [3] S. Kasahara, H. J. Ishi, K. Hashimoto, S. Tonegawa, Y. Mizukami, T. Shibauchi, K. Sugimoto, T. Fukuda, T. Terashima, A. H. Nevidomskyy and Y. Matsuda, *Nature* **486** (2012) 382.
- [4] S. Kitao, Y. Kobayashi, S. Higashitaniguchi, M. Saito, Y. Kamihara, M. Hirano, T. Mitsui, H. Hosono and M. Seto, *J. Phys. Soc. Jpn.* **77** (2008) 103706.
- [5] S. Kitao, Y. Kobayashi, S. Higashitaniguchi, M. Kurokuzu, M. Saito, T. Mitsui, Y. Kamihara, M. Hirano, H. Hosono and M. Seto, *J. Phys.: Conf. Ser.* **217** (2010) 012120.

M. Suzuki

*Research Reactor Institute, Kyoto University*

### Background and Objective

Using Kyoto University Research Reactor (KUR), patients with malignant tumors greater than 500 have been treated with boron neutron capture therapy (BNCT). Malignant brain tumors and head and neck cancers have been main malignancies treated with BNCT. Our laboratory (Division of Particle Radiation Oncology) has investigated the possibilities for new applications for BNCT. According to promising results in pre-clinical study, we have already treated some patients with liver cancers with BNCT and carried out clinical study on phase I study on BNCT for malignant pleural mesothelioma (MPM).

Promising clinical results of BNCT using the research reactor encouraged us to go to further stage of BCNT using an accelerator-based (AB) BNCT system. Co-operation of Kyoto University Research Reactor Institute and Sumitomo Heavy Industry have developed AB BNCT system with compact cyclotron as an accelerator. In 2012 and 2014, clinical studies on BNCT for recurrent malignant brain tumors and head and neck tumors to get an approval as a medical device from the Pharmaceuticals and Medical Devices Agency (PMDA), a Japanese regulatory agency. In a transition period from reactor-based (RB) BNCT into AB-based BNCT, many research issues should be dissolved from impending and long-term viewpoints.

Main objectives of our project is to dissolve many impending clinical issues to perform BNCT safely in AB-BNCT system and to investigate many research projects for many patients with cancer to be treated with AB-BNCT system.

### Research Subjects

To advance RB-BNCT into AB-BNCT, a lot of researchers in various research fields such as clinical radiation oncology, medical physics, pharmacology, boron chemistry, and accelerator engineering are needed to be involved in our research projects. In this viewpoint, this research project consists of three research subjects (RS) as follows,

RS1. Clinical studies on BNCT

RS2. Pre-clinical studies on physiological and pharmacological aspects of BNCT

RS3. Medical physics studies on BNCT.

### Main Results

Six reports could be submitted although KUR has been unavailable since May in 2014.

#### RS1. Clinical studies on BNCT

No BNCT was carried out since KUR has been unavailable in 2016.

#### RS2. Pre-clinical studies on physiological and pharmacological aspects of BNCT

Yanagie et al. reported two pre-clinical studies. One was a preclinical study for evaluating <sup>10</sup>Boronophenylalanine (BPA) – entrapped water-in-oil in water (WOW) emulsion. Another one was a study for checking.

Fujimoto et al. investigated biodistribution of BPA in metastatic bone of human cancer-bearing animal model.

#### RS3. Medical physics studies on BNCT

Taketa et al. developed a patient-position-error measuring system and tested the system.

Tanaka K et al. investigated suitable configuration of the converter to combine with the imaging plate.

Sakurai et al. reported the development of the remote-changeable Bonner-sphere spectrometer.

### Translational research on BNCT looking toward accelerator-based BNCT era.

For three years when KUR has not worked, clinical trials using AB-BNCT system has made steady progress. Therefore, more strategic translational research leading to clinical application in AB-BNCT may be desired. These researches should be carried out with attention to regulatory science. On the other hand, more innovative or fundamental translational researches are needed looking toward the future 10 or 20 years later.

## PR6-1 Preliminary formulation of <sup>10</sup>Borono-phenylalanine entrapped WOW emulsion for Neutron Capture Therapy to Hepatocellular Carcinoma

Hironobu Yanagie<sup>1,2,3</sup>, Mitsuteru Fujihara<sup>4</sup>, Ryuji Mizumachi<sup>5</sup>, Yuji Murata<sup>5</sup>, Yuriko Sakurai<sup>1,3</sup>, Kikue Mouri<sup>1,3</sup>, Atsuko Shinohara<sup>6,7</sup>, Takehisa Matsukawa<sup>7</sup>, Ayano Kubota<sup>7</sup>, Yasuyuki Morishita<sup>8</sup>, Novriana Dewi<sup>2</sup>, Masashi Yanagawa<sup>9</sup>, Sho Yui<sup>1,3</sup>, Kazuhito Yokoyama<sup>7</sup>, Yasumasa Nonaka<sup>1</sup>, Hirotaka Sugiyama<sup>1</sup>, Yoshitaka Furuya<sup>1</sup>, Yoshinori Sakurai<sup>10</sup>, Hiroki Tanaka<sup>10</sup>, Minoru Suzuki<sup>10</sup>, Shinichiro Masunaga<sup>10</sup>, Koji Ono<sup>10</sup>, Minoru Ono<sup>3,11</sup>, Jun Nakajima<sup>3,12</sup>, Masazumi Eriguchi<sup>13</sup>, and Hiroyuki Takahashi<sup>2,3</sup>

<sup>1</sup>Dept of Innovative Cancer Therapeutics: Alpha particle & Immunotherapeutics, Meiji Pharmaceutical University, <sup>2</sup>Dept of Nuclear Engineering & Management, Graduate School of Engineering, The University of Tokyo, <sup>3</sup>Cooperative Unit of Medicine & Engineering, The University of Tokyo Hospital, <sup>4</sup>SPG Techno Ltd. Co., <sup>5</sup>LSI Medience Ltd Co, <sup>6</sup>The Graduate School of Seisen University, <sup>7</sup>Jyuntendo University, <sup>8</sup>Dept of Human & Molecular Pathology, Graduate School of Medicine, The University of Tokyo, <sup>9</sup>Veterinary Medical Center, Obihiro University of Agriculture & Veterinary Medicine, <sup>10</sup>Research Reactor Institute, Kyoto University, <sup>11</sup>Dept of Cardiac Surgery, The University of Tokyo Hospital, <sup>12</sup>Dept of Thoracic Surgery, The University of Tokyo Hospital, <sup>13</sup>Dept of Surgery, Shin-Yamanote Hospital

**INTRODUCTION:** Water-in-oil-in-water (WOW) emulsion has been used as the carrier of anti-cancer agents by modifying of IPSO on intra-arterial injections in clinical. Higashi et al prepared a long term inseparable WOW for use in arterial injection therapy to treat patients with hepatocellular carcinoma (HCC) by the double emulsification technique [1]. We have previously performed the preclinical BNCT study for VX-2 rabbit tumour model using <sup>10</sup>BSH entrapped WOW [2, 3], and we also proceeded clinical BNCT study for HCC using this system [4].

In this study, we prepared <sup>10</sup>BPA-entrapped WOW emulsion and evaluated the boron encapsulating activity by measuring the <sup>10</sup>B concentrations of WOW using ICP-AES.

**EXPERIMENTS:** We prepared the <sup>10</sup>BPA-entrapped WOW emulsion evaluate the properties by determining boron concentrations of the WOW emulsion was using ICP-AES at Juntendo University.

**RESULTS:** <sup>10</sup>BPA-entrapped WOW emulsion was prepared by mixing 37.5mg of <sup>10</sup>BPA, 83.3 mg of Fructose in 8mL of WOW emulsion. <sup>10</sup>B concentration of precipitate of WOW emulsion, supernatant, and total homogeneous mixing emulsion, were measured to be 255.5 µg/mL, 93.8 µg/mL, and 222.4±5.2 µg/mL, respectively.

In the case of <sup>10</sup>BSH WOW emulsion, the original <sup>10</sup>B concentration was found to be 7000~13000 ppm, while in the case of <sup>10</sup>BPA, <sup>10</sup>B concentration was 250 ppm. The <sup>10</sup>B concentration is very low, but <sup>10</sup>BPA is incorporated into the tumor cells by LAT-1 transporter. Therefore, it is expected that we could evaluate whether the original concentration is effective or not, in the VX-2 hepatic tumor model.



Figure 1. Formulation of <sup>10</sup>BPA WOW emulsion. Left: Precipitate, Center: Supernatant, Right: Mix

The calculated osmotic pressure of each WOW emulsion were as below:

Epirubicin WOW : 632 mOsm/L

<sup>10</sup>BSH WOW (BSH 175mg+ D.W. 2.0mL): 909 mOsm/L

<sup>10</sup>BPA WOW: 641 mOsm/L

The osmolality of <sup>10</sup>BPA WOW was the same as epirubicin entrapped WOW emulsion, so it will be easily injected by catheter on the intra-hepatic administration.

We hope to perform toxicity examinations of WOW emulsion to develop the more suitable WOW emulsion for intra-arterial born delivery system.

### REFERENCES:

- [1] S Higashi S *et al.*, Cancer, **75**(1995):1245–1254.
- [2] S Mikado *et al.*, Nucl. Instr. and Meth. A, **605** (2009): 171-174.
- [3] H Yanagie *et al.*, Appl Radiat Isot., **69**(2011): 1854-7.
- [4] H Yanagie *et al.*, Appl Radiat Isot., **88**(2014):32-7.

## PR6-2 Pre-BNCT Biodistribution of *p*-borono-L-phenylalanine in Metastatic Bone of Human Breast Cancer-bearing Animal Model

T. Fujimoto<sup>1</sup>, T. Andoh<sup>2</sup>, Y. Sakurai<sup>3</sup>, M. Suzuki<sup>3</sup> and H. Ichikawa<sup>2</sup>

<sup>1</sup>Hyogo Cancer Center,

Department of Orthopaedic Surgery

<sup>2</sup>Faculty of Pharmaceutical Sciences and Cooperative Research Center of Life Sciences, Kobe Gakuin University

<sup>3</sup>Research Reactor Institute, Kyoto University

**INTRODUCTION:** Breast cancer, the most morbid malignancy in women, is frequently encountered in Japan. Although most breast cancer is diagnosed at an early stage, 20-30% of cases turn metastatic [1]. Furthermore, about 70% of such cases metastasize to the bone [2]. When systematic pharmacotherapy is not effective in such cases, the disease is difficult to control. Especially in the case of bone metastasis of lower extremities, there is constant danger of pathological fracture that leads to a lowering of the quality of life. Therefore, mainly surgery with the use of intramedullary nails is carried out to prevent pathological fracture. Nonetheless, this entails not only patient physiological distress, but also the enormous treatment costs of surgery, rehabilitation and postoperative radiotherapy. Here, then, is where BNCT proffers the only option, presently, for resolving these problems. BNCT destroys, by one brief irradiation, individual tumor cells without affecting surrounding normal tissue; therefore, for the management of bone metastasis with BNCT, we evaluated the distribution of <sup>10</sup>B in the bone of a newly established human breast cancer-bearing animal model.

**EXPERIMENTS:** All animal experiments were carried out according to the regulations of the Animal Care and Use Committee.

(1) Tumor cell line: Cells of human breast cancer cell line MDA-MB-231-luc were cultured in Leibovitz's L-15 medium with fetal bovine serum in a 5% CO<sub>2</sub> humidified incubator at 37°C.

(2) Producing bone metastasis in the human breast cancer-bearing animal model: Cells of MDA-MB-231-luc suspended in Matrigel® were transplanted into the tibia of the left hind leg of the nude mice. Eight weeks thereafter, micro-CT scans disclosed the formation of a tumor in the left tibia. Histological examinations were then carried out by HE staining.

(3) Biodistribution of <sup>10</sup>B in the bone-metastasis animal model: *p*-borono-L-phenylalanine (BPA)-Fr (24 mg <sup>10</sup>B/kg) was intravenously injected into the tibia of the human breast cancer-bearing animal model and, at pre-determined intervals, blood and normal bone samples were collected immediately after the mice were killed. The concentration of boron in the samples was then measured by ICP-AES.

**RESULTS:** Bone metastasis was successfully produced in the human breast cancer-bearing animal model. The formation of a solid tumor mass in the left tibia was confirmed by macroscopic observation, micro-CT scans and microscopic analysis [Fig. 1]. Biodistribution of <sup>10</sup>B: 1.5 hours after the intravenous injection of BPA-Fr into the bone-metastasis animal model, tumor-specific and high-level <sup>10</sup>B accumulation at a concentration of 22.7 μg <sup>10</sup>B/g of wet tumor tissue was identified in the bone tumor compared with normal bone [Fig. 2], with a tumor-to-normal bone ratio of 2.3. These results prognosticated that boron accumulates specifically in the bone tumor and that BNCT destroys tumor cells only at the site of the bone metastasis, preventing bone fracture.

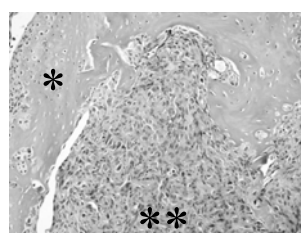


[Fig.1] HE staining. Tumorigenesis within the tibial marrow cavity in the human breast cancer-bearing bone metastasis animal model. \*: cortex, \*\*: tumor.

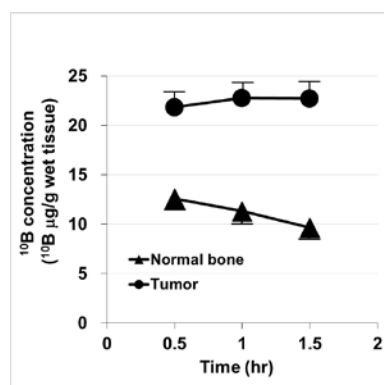


[Fig.2] Biodistribution of <sup>10</sup>B in the tumor and the normal bone of the human breast cancer-bearing animal model. ●: Tumor, ▲: Normal bone.

### REFERENCES:

- [1] Metastatic behavior of breast cancer subtypes. H. Kennecke *et al.* J Oncol, **28**(2010) 3271-7.
- [2] Clinical management of women with metastatic breast cancer: a descriptive study according to age group. K. Manders *et al.* BMC Cancer, **6**(2006).

### PR6-3 Nanoparticle-assisted Boron Neutron Capture Therapeutics: Design of Novel Boron-containing Nanoparticle for ROS Scavenging Ability Improving Therapeutic Efficiency with Low Adverse Effect

Zhenyu Gao<sup>a,b</sup>, Yukichi Horiguchi<sup>a</sup>, Kei Nakai<sup>b</sup>, Akira Matsumura<sup>b</sup>, Minoru Suzuki<sup>c</sup>, Koji Ono<sup>c</sup>, Yukio Nagasaki<sup>a, b, d\*</sup>

<sup>a</sup>Graduate School of Pure and Applied Sciences, University of Tsukuba,

<sup>b</sup>Graduate School of Comprehensive Human Sciences, University of Tsukuba

<sup>c</sup>Research Reactor Institute, Kyoto University,

<sup>d</sup>WPI-MANA, NIMS

**INTRODUCTION:** Boron neutron capture therapy (BNCT) has attracted much attention during recent decades. The success of BNCT is dependent on the boron delivery system to achieve high specific tumor accumulation, keeping low adverse effect. However, the low molecular weight boron compounds currently used in clinical trial of BNCT are excluded rapidly from the blood circulation, which causes non-specific dispersing in whole body. It is confirmed that high-dispersion stable nanoparticle tends to accumulate in tumor environment due to the leaky neovascularization and immature lymphatic systems, which is called enhanced permeability and retention (EPR) effect<sup>1</sup>. Furthermore, during the treatment process, large amount generated reactive oxygen species (ROS) will cause adverse effect such as inflammation. The objective of this study is to design a novel boron nano-delivery-system that enhance the therapeutic efficiency as well as suppress the adverse effect

**EXPERIMENTS:** The novel boron-containing nanoparticles (BNP) in this study was prepared by mixing a newly synthesized boron-cluster-containing anionic block copolymer (PEG-*b*-PMBSH) and a redox cationic block copolymer (PEG-*b*-PMNT) via the ion complex in phosphate buffered saline (PBS) solution. The BNCT effect was evaluated by using tumor bearing BALB/c mice given BNP at dose of 15 and 5 mg <sup>10</sup>B/kg body weight 72

h before irradiation. Mice given boronophenylalanine (BPA)-fructose complex at dose of 40 mg <sup>10</sup>B/kg body weight and PBS 2.5 h before irradiation were used as positive and negative control. Tumor volume growing was monitored. White blood cell levels were confirmed 3 d after irradiation.

**RESULTS:** The size of the BNP was evaluated by dynamic light scattering (DLS), showing average size of 35 nm and neutral surface. In the *in vivo* BNCT effect evaluation study, the tumor volume in PBS treated group grew up to 1.3 cm<sup>3</sup> 13 d after irradiation. In contrast, the growth of tumors was effectively suppressed in the BNP treated groups (average size was about 0.4 cm<sup>3</sup>, while the doses of <sup>10</sup>B were 15 and 5 mg/kg). The suppression of tumor growth was also observed in the mice treated by BPA with dose of <sup>10</sup>B at 40 mg/kg, (average size was 0.7 cm<sup>3</sup>). By much lower dose, 5 mg <sup>10</sup>B/kg (5 ppm boron in tumor tissue), BNP showed better therapeutic effect compared with BPA. Furthermore, we observed high white blood cell (WBC) level in BPA treated group, indicating the inflammation was occurred. However the WBC level in BNP treated group (15 mg/kg) showed almost similar as the non-tumor-bearing healthy mice, probably because of the ROS scavenging ability of BNP. These results strongly indicates that this novel boron-containing nanoparticle is a suitable potential candidate for high performance of BNCT improving the therapeutic efficiency with low adverse effect.

#### REFERENCES:

[1] Y. Matsumura, H. Maeda, Cancer Research 46: 6387–92 (1986)

## PR6-4 Toxicity Evaluation of <sup>10</sup>BSH entrapped WOW emulsion on intra-arterial delivery in Rabbits for Neutron Capture Therapy to Hepatocellular Carcinoma

Hironobu Yanagie<sup>1,2,3</sup>, Tsuyoshi Higuchi<sup>4</sup>, Mitsuteru Fujihara<sup>5</sup>, Ryoji Mizumachi<sup>4</sup>, Yuji Murata<sup>4</sup>, Yuriko Sakurai<sup>1,3</sup>, Kikue Mouri<sup>1,3</sup>, Yasuyuki Morishita<sup>6</sup>, Novriana Dewi<sup>1</sup>, Masashi Yanagawa<sup>1,7</sup>, Yasumasa Nonaka<sup>1</sup>, Hirotaka Sugiyama<sup>1</sup>, Yoshitaka Furuya<sup>1</sup>, Yoshinori Sakurai<sup>8</sup>, Hiroki Tanaka<sup>8</sup>, Minoru Suzuki<sup>8</sup>, Shinichiro Masunaga<sup>8</sup>, Koji Ono<sup>8</sup>, Minoru Ono<sup>3,9</sup>, Jun Nakajima<sup>3,10</sup>, Masazumi Eriguchi<sup>11</sup>, and Hiroyuki Takahashi<sup>2,3</sup>

<sup>1</sup>Dept of Innovative Cancer Therapeutics: Alpha particle & Immunotherapeutics, Meiji Pharmaceutical University,

<sup>2</sup>Dept of Nuclear Engineering & Management, Graduate School of Engineering, The University of Tokyo,

<sup>3</sup>Cooperative Unit of Medicine & Engineering, The University of Tokyo Hospital, <sup>4</sup>LSI Medience Ltd Co, <sup>5</sup>SPG Techno Ltd. Co., <sup>6</sup>Dept of Human & Molecular Pathology, Graduate School of Medicine, The University of Tokyo,

<sup>7</sup>Veterinary Medical Center, Obihiro University of Agriculture & Veterinary Medicine, <sup>8</sup>Research Reactor Institute, Kyoto University, <sup>9</sup>Dept of Cardiac Surgery, The University of Tokyo Hospital, <sup>10</sup>Dept of Thoracic Surgery, The University of Tokyo Hospital, <sup>11</sup>Dept of Surgery, Shin-Yamanote Hospital

**INTRODUCTION:** Water-in-oil-in-water (WOW) emulsion has been used as the carrier of anti-cancer agents by modifying of IPSO on intra-arterial injections in clinical. Higashi et al prepared a long term inseparable WOW by the double emulsification technique to be used in arterial injection therapy to treat patients with hepatocellular carcinoma (HCC) [1]. We previously performed preclinical BNCT study for VX-2 rabbit tumour model using <sup>10</sup>BSH-entrapped WOW [2, 3, 4], and we also proceeded clinical BNCT study for HCC using this system [5].

In this study, we prepared <sup>10</sup>BSH-entrapped WOW, and evaluated the toxicity by checking survival conditions and biochemical data after intra-hepatic injection of <sup>10</sup>BSH entrapped WOW emulsion in healthy rabbits.

**EXPERIMENTS:** <sup>10</sup>BSH-entrapped WOW was administrated with intra-arterial injections via proper hepatic artery on healthy rabbits. As a part of the safety evaluation of <sup>10</sup>BSH-entrapped WOW emulsion, the test article was dosed once by hepatic arterial administration to 3 male rabbits at 0.075 and 0.15 mL/kg to investigate its toxicity. The control group was given lactose entrapped WOW emulsion at 0.15 mL/kg.

The investigated items included clinical observation, measurement of body weights and food consumption, blood chemistry, necropsy, and histopathology.

**RESULTS:** *Body weight;* no statistically significant difference was noted in the 0.075 mL/kg group on Day 3 or 7 compared with the control group. However, decreased

body weights were noted in all animals in the control and test article (0.075 and 0.15 mL/kg) groups on Day 3.

*Blood chemistry;* increases in the  $\alpha_1$  globulin,  $\alpha_2$  globulin,  $\beta$  globulin, and total cholesterol, as well as decreases in the albumin (g/dL and %) and A/G ratio were noted in 1 male (No. 8) in the 0.15 mL/kg group on Day 7. These were not considered to be attributed to BSH.

*Surviving animals;* there were no test article-related changes in any of the BSH administration groups. Adhesion was noted between the lobules of the liver in 1 male each of the 0.075 and 0.15 mL/kg groups and between the gallbladder and omental, duodenum, or liver in 2 males of the 0.075 mL/kg group and in 1 male of the 0.15 mL/kg group. All of the changes were treatment-related; however, as they were also noted in the control group or absent in the 0.15 mL/kg group, they were not considered to be attributed to BSH. There were no intergroup differences in their occurrence, so they were not considered to be attributed to BSH.

The minimum dose of WOW emulsion-containing BSH is 3 mL in clinical practice. Based on the assumption that it was given to an individual weighing 50 kg, the minimum dose was calculated to be 0.06 mL/kg (3 mL/50 kg = 0.06 mL/kg). Accordingly, the lowest dose for hepatic artery injection to rabbits was set at 0.075 mL/kg, which is higher than the minimum dose (0.06 mL/kg), and the highest dose at 0.15 mL/kg, which is twice the lowest dose (0.075 mL/kg) in this study.

We hope to refer these results of toxicity examinations to the clinical studies of BNCT to hepatocellular carcinoma with intra-arterial boron delivery using WOW emulsion.

### REFERENCES:

- [1] S Higashi S *et al.*, Cancer, **75**(1995):1245–1254.
- [2] S Mikado *et al.*, Nucl. Instr. and Meth. A, **605** (2009): 171-174.
- [3] H Yanagie *et al.*, Appl Radiat Isot., **69**(2011): 1854-7.
- [4] H Yanagie *et al.*, Br J Radiol. (2017) [Epub ahead of print] doi:10.1259/bjr.20170004.
- [5] H Yanagie *et al.*, Appl Radiat Isot., **88**(2014):32-7.

## PR6-5 Exfoliation of Hexagonal Boron Nitride Nanosheet with Chlorin e6 and Application of the Composite to Cancer Photodynamic Therapy

Maruyama Kyouhei, Komatsu Naoki

*Graduate School of Human and Environmental Studies, Kyoto University*

Recently, we directly fabricated the graphene-based composite from graphite in the presence of chlorin e6 (Ce6) by sonication in aqueous phase.<sup>1</sup> The composite (G/Ce6) was found to deliver the Ce6 into cancer cells and work as a photosensitizer for cancer photodynamic therapy (PDT). In this paper, we used h-BN in place of graphite and realized much higher Ce6 concentration in the composite of h-BN/Ce6 than that of G/Ce6.

Aqueous dispersion of h-BN/Ce6 was prepared by use of commercially available h-BN and Ce6 under the same conditions as those in the preparation of G/Ce6. The formation of h-BN/Ce6 was confirmed by the red shift of Q band in the absorption spectra and quenching of the fluorescence. In comparison of these dispersions shown in Table 1, the contents of Ce6 and the carrier were 10 and 20 times larger in h-BN/Ce6 than G/Ce6, respectively. Since the size of h-BN is much smaller than that of graphite, it is concluded that h-BN was exfoliated much more easily than graphite in the presence of Ce6 in water. This is supported by the phenomenon that the loading capacity of Ce6 on h-BN is half of that on graphene shown in Table 1.

The cytotoxicity of h-BN/Ce6 to HeLa cells was confirmed under irradiation of 660 nm LED light as shown in Fig. 1. While Ce6 without carrier exhibited no cytotoxicity, viability of the cells significantly decreased to less than 20% at the Ce6 concentration of 0.4 mg/mL. This PDT effect by use of h-BN/Ce6 is quite similar to that of G/Ce6, indicating no difference between h-BN and graphene as a drug carrier.

Table 1. Comparison of h-BN/Ce6 with G/Ce6.

	Ce6 ( $\mu\text{g/mL}$ )	Carrier ( $\mu\text{g/mL}$ )	Loading (%)
h-BN/Ce6	392	438	80
G/Ce6	36	22	160

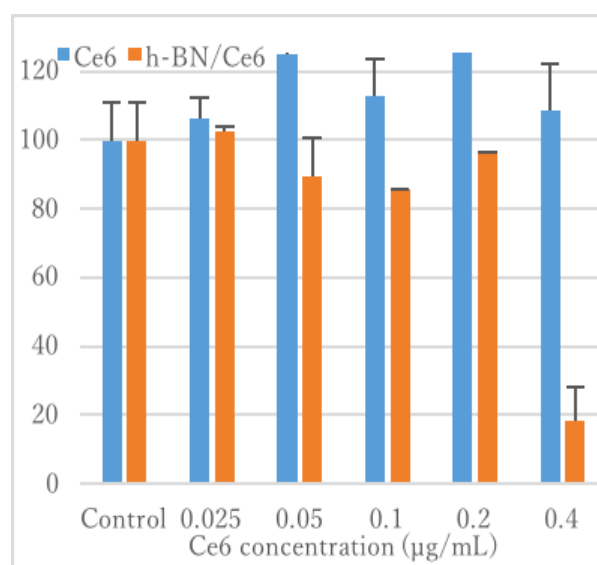


Figure 1. Viability of HeLa cells in presence of h-BN/Ce6 and Ce6 under light irradiation.

### REFERENCE:

- [1] G. Liu, H. Qin, T. Amano, T. Murakami, N. Komatsu, *ACS Appl. Mater. Interfaces*. **2015**, *7*, 23402.

Y. Sakurai, H. Ueda<sup>1</sup>, R. Uchida<sup>1</sup>, T. Takata, H. Tanaka, K. Okazaki<sup>1</sup>, T. Kawamura<sup>1</sup>, K. Akita<sup>1,2</sup> and M. Suzuki<sup>1</sup>

*Research Reactor Institute, Kyoto University*

<sup>1</sup>*Graduate School of Engineering, Kyoto University*

<sup>2</sup>*Osaka Medical School*

**INTRODUCTION:** Research and development into several types of accelerator-based irradiation systems for boron neutron capture therapy (BNCT) is underway [1,2]. In the near future, BNCT using these newly developed irradiation systems may be carried out at multiple facilities across the world. Considering this situation, it is important that the estimations for dose quantity and quality are performed consistently among several irradiation fields, and that the equivalency of BNCT is guaranteed, within and across BNCT systems. Then, we are establishing the quality assurance and quality control (QA/QC) system for BNCT irradiation field. As part of the QA/QC system, we are developing estimation method for neutron energy spectrum using Bonner sphere [3].

**METHODS:** Liquid such as pure water and/or boric acid solution is used as the moderator. A multi-layer concentric-sphere case with several sphere shells is prepared. The moderator and its diameter are changeable without entering the irradiation room, by the remote supply and drainage of liquid moderator in the several layers. For the detector, activation foils are remotely changed, or online measurement is performed using SOF (scintillator with optical fiber) detector containing boron [4], etc.. The development of this remote-changeable Bonner-sphere spectrometer is reported. The combination of the moderators for boron-10 (B-10) concentration and diameter was optimized by our originally-developed method, “High Independence Selection (HIS)” [5]. The optimized combination was decided among 101 combinations; the combinations of ten B-10 concentrations and ten diameters, additionally the case of manganin foil only without the moderator.

**RESULTS:** Figure 1 shows the response functions for the selected combinations. The optimized combination was selected by HIS as follows: manganin foil only, 0.7-wt% boron acid solution of 13 cm in diameter, 0.7-wt% boron acid solution of 18 cm in diameter, 0-wt% boron acid solution (namely pure water) of 18 cm in diameter, and 0.028-wt% boron acid solution of 20 cm in diameter. Then, the optimized structure of the spec-

trometer was decided as follows: three sphere shells such as 13, 18 and 20 cm in diameter, and three liquid moderators such as pure water, 0.028-wt% boron acid solution and 0.7-wt% boron acid solution, as shown in Fig.2.

**CONCLUSION:** We have a plan to make the remote-changeable Bonner-sphere spectrometer, based on the optimization result. Additionally, we have a plan to perform the spectrometry experiments at Kyoto University Reactor (KUR), etc., in order to confirm the efficacy of this spectrometer.

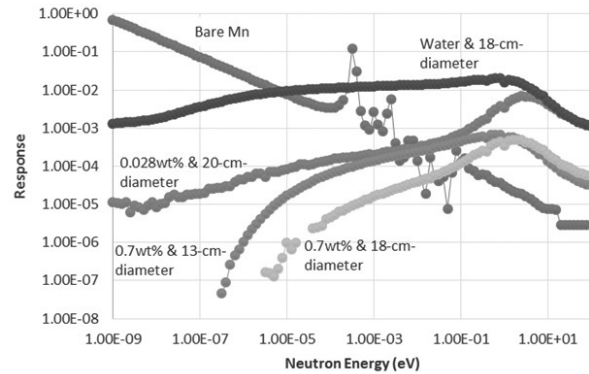


Fig. 1. Response functions for the selected combinations.

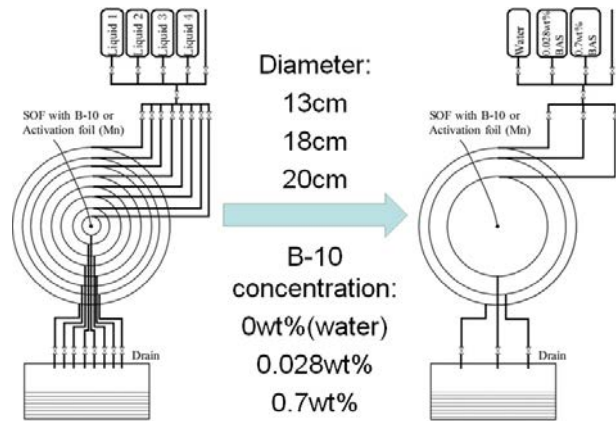


Fig. 2. Optimization for the structure of the remote-changeable Bonner-sphere spectrometer.

### REFERENCES:

- [1] H. Tanaka *et al.*, Nucl. Instr. Meth. B **267** (2009) 1970-1977.
- [2] H. Kumada *et al.*, Appl. Radiat. Isot. **88** (2014) 211-215.
- [3] H. Ueda *et al.*, Appl. Radiat. Isot. **104** (2015) 25-28.
- [4] M. Ishikawa *et al.*, Radiat. Oncol. **11** (2016) 105(1-10).
- [5] H. Ueda, Doctoral Thesis (2016).

## PR6-7 Calculational Survey of Converter Configuration for Quality Assurance of Beam Component Distribution at KUR Using Imaging Plate

K. Tanaka, Y. Sakurai<sup>1</sup>, T. Kajimoto, H. Tanaka<sup>1</sup>, T. Takata<sup>1</sup>, M. Suzuki<sup>1</sup> and S. Endo

Graduate School of Engineering, Hiroshima University  
<sup>1</sup>Research Reactor Institute, Kyoto University

**INTRODUCTION:** It is important to check the spatial distributions of neutrons and gamma rays in the quality assurance and quality control of boron neutron capture therapy (BNCT). This study investigates the usage of the imaging plate (IP) for this purpose. The suitable configuration of the converter to combine with the IP is investigated with calculational survey<sup>1</sup>.

**METHODS:** In order to separate the beam components, the converters to enhance the beam components is supposed to be used as follows: thermal and epithermal neutrons will be enhanced by the secondary particles from (n,α) reactions of the nuclides such as <sup>6</sup>Li, which reacts with low-energy neutrons; fast neutrons enhanced by the recoiled protons from the hydrogen-rich material. For gamma rays, carbon is used so that gamma rays are not depressed or neutrons are not enhanced.

The converter configuration in order for the attempted beam component to dominate the IP signal intensity is investigated using PHITS 2.76. The geometry is shown in Fig. 1. The assumed irradiation fields are the standard thermal neutron irradiation mode, mixed neutron irradiation mode, and epithermal neutron irradiation mode in KUR-HWNIF, with a power of 5 MW. The IP assumed is “BAS-TR” from Fuji Film Corporation, Japan. The energy deposition at the IP-sensitive region is computed as a representative of the IP signal.

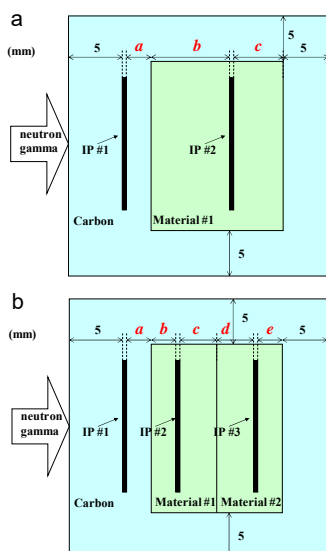


Fig. 1 Calculation geometry.

**RESULTS and DISCUSSION:** As an example of the results, the energy deposition contribution in IP #2 in 10-wt% <sup>6</sup>Li-P.E. for its thickness “b” varied, with a = c = d = e = 1 mm in Fig. 1 (b), is shown in Fig. 2 for standard epithermal neutron irradiation mode. The epithermal neutron component is attempted in the IP #2. As “b” increased, the contribution of thermal neutrons decreased, which resulted in 1.5% for the thickness at 4 mm. In addition, the contribution of epithermal neutrons slightly increased from 94.4% to 96.7%. As a potential option, b = 4 mm was chosen.

As summary, the converter configuration selected and contribution of attempted beam component to energy deposition in IP is shown in Table 1.

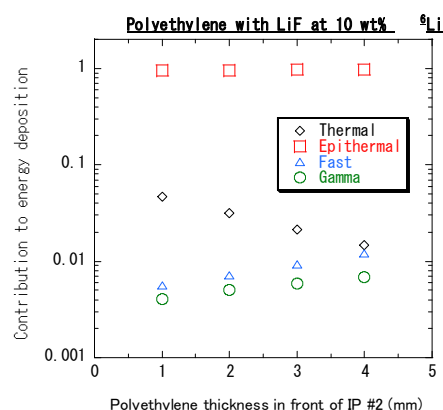


Fig. 2 Energy deposition contribution in IP #2.

Table 1. Converter configuration selected. The attempted beam component is shown in parenthesis.

Mode	Geometry	IP#	Converter material	Contribution (%)
Thermal	Fig. 1 (a) with (a, b, c) = (1, 1, 1 mm)	1	Carbon	51.8 (γ)
		2	10-wt% <sup>6</sup> Li-P.E.	99.3 (th)
Mixed	Fig. 1 (b) with (a, b, c + d, e) = (1, 1, 5, 1 mm)	1	Carbon	54.9 (γ)
		2	10-wt% <sup>6</sup> Li-P.E.	93.2 (th)
		3	10-wt% <sup>6</sup> Li-P.E.	48.0 (epi)
Epithermal	Fig. 1 (b) with (a, b, c, d, e) = (1, 4, 1, 1, 1 mm)	1	Carbon	69.4 (γ)
		2	10-wt% <sup>6</sup> Li-P.E.	96.7 (epi)
		3	without LiF	30.9 (fast)

### REFERENCE:

[1] K. Tanaka *et al.*, Appl. Rad. Isot. **115** (2016) 212-220.

# PR6-8 Initial Test Operation of Patient-Position-Error Measuring System for BNCT Irradiation

T. Takata, Y. Sakurai, H. Tanaka and M. Suzuki

Research Reactor Institute, Kyoto University

**INTRODUCTION:** In boron neutron capture therapy (BNCT) irradiations carried out at Kyoto University Research Reactor, sitting position has been applied in many cases, considering a flexibility of patient positioning and structural restriction of an irradiation facility. In those cases, the patient position is sometimes unstable, resulting in a displacement from an initial set-up position determined by a treatment planning process. The displacement and motion during an irradiation period cause uncertainty in estimation of delivered dose.

Aiming to improve the dose estimation accuracy, we have been preparing a patient-position-error measuring system using a motion sensor [1]. The results of initial test operation of the position measurement are described.

**MATERIALS AND METHODS:** A MEMS motion sensor module (IMU-Z 2, ZMP Inc., Tokyo) consisting of tri-axial accelerometer, gyroscope and magnetometer was used to track a position and a rotation angle. The sensor module (36×52×11 mm) and a battery box (36×62×15 mm) were fixed to each other, and mounted on the top of the head of a subject as shown in Fig. 1. The data was acquired every 20 ms and registered in the PC by the wireless data transmission function built in the module. The data registered was analyzed to estimate the position and the rotation angle.

At first, the original measured data was smoothed by applying a low-pass filter to remove the high-frequency fluctuation component. Then, each vector data was transformed from the sensor coordinate system to the room coordinate system. After that, the phase of motion, that is, at rest or in motion was determined based on the change rate in magnitude of the acceleration vector. The position displacement was calculated by integrating the accelerometer data twice with respect to time. Also, the rotation angle was calculated by integrating gyroscope data with respect to time in motion phase and by comparing the direction of gravitational acceleration and geomagnetic field to the initial direction in resting phase.

**RESULTS:** Figure 2 shows an estimation result for the rotation angle around each axis in the case of the head shaking motion from side to side, followed by the nodding motion. The periods of these motions were around 5 seconds. The room coordinate system were defined as the initial sensor coordinate system as illustrated in Fig. 1. The shaking is corresponding to the rotation around Z axis and the nodding to the rotation around Y axis. It was found that the rotation angle could be tracked correctly by this system for the shaking motion during the elapsed time of 5 to 20 seconds and for the nodding motion during the time of 20 to 30 seconds.

Figure 3 shows an estimation result for the position dis-

placement along each axis during the rotation motion described above. The result showed no displacement during the first 20 seconds and then showed large divergence after the beginning of nodding motion while the actual displacement was in a range of several centimeters. It was found that the system could not work correctly in the displacement estimation in this case.

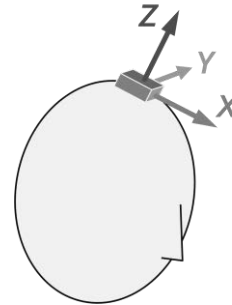


Fig. 1. Mounting of the sensor system and the coordinate system definition.

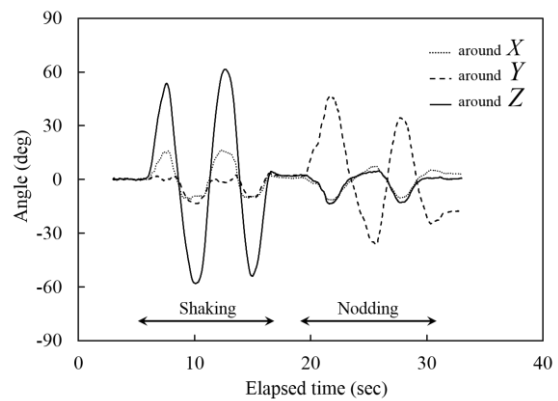


Fig. 2. Estimated rotation angle during head shaking and nodding motion.

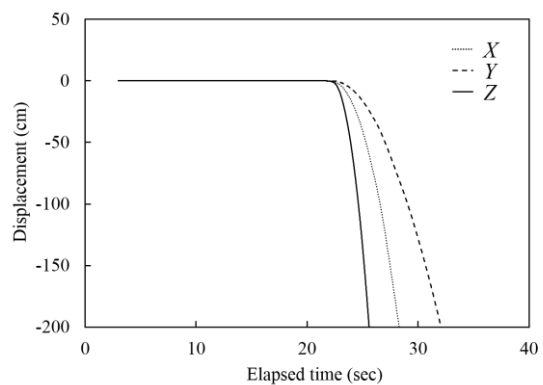


Fig. 3. Estimated position displacement during head shaking and nodding motion.

## REFERENCE:

- [1] T. Takata *et al.*, KURRI Progress Report 2015 (2016) 49.

## PR7 Analyzing Tumor Microenvironment and Exploiting its Characteristics in Search of Optimizing Cancer Therapy Including Neutron Capture Therapy

S. Masunaga

Research Reactor Institute, Kyoto University

**BACKGROUNDS AND PURPOSES:** Human solid tumors contain moderately large fractions of quiescent (Q) tumor cells that are out of the cell cycle and stop cell division, but are viable compared with established experimental animal tumor cell lines. The presence of Q cells is probably due, in part, to hypoxia and the depletion of nutrition in the tumor core, which is another consequence of poor vascular supply. As a result, Q cells are viable and clonogenic, but stop cell division. In general, radiation and many DNA-damaging chemotherapeutic agents kill proliferating (P) tumor cells more efficiently than Q tumor cells, resulting in many clonogenic Q cells remaining following radiotherapy or chemotherapy. Therefore, it is harder to control Q tumor cells than to control P tumor cells, and many post-radiotherapy recurrent tumors result partly from the regrowth of Q tumor cells that could not be killed by radiotherapy. Similarly, sufficient doses of drugs cannot be distributed into Q tumor cells mainly due to heterogeneous and poor vascularity within solid tumors. Thus, one of the major causes of post-chemotherapy recurrent tumors is an insufficient dose distribution into the Q cell fractions.

With regard to boron neutron capture therapy (BNCT), with  $^{10}\text{B}$ -compounds, boronophenylalanine- $^{10}\text{B}$  (BPA) increased the sensitivity of the total cells to a greater extent than mercaptoundecahydrododecaborate- $^{10}\text{B}$  (BSH). However, the sensitivity of Q cells treated with BPA was lower than that in BSH-treated Q cells. The difference in the sensitivity between the total and Q cells was greater with  $^{10}\text{B}$ -compounds, especially with BPA. These findings concerning the difference in sensitivity, including other recovery and reoxygenation following neutron irradiation after  $^{10}\text{B}$ -compound administration were mainly based on the fact that it is difficult to deliver a therapeutic amount of  $^{10}\text{B}$  from  $^{10}\text{B}$ -carriers throughout the target tumors, especially into intratumor hypoxic cells with low uptake capacities.

Hypoxia is suggested to enhance metastasis by increasing genetic instability. Acute, but not chronic, hypoxia was reported to increase the number of macroscopic metastases in mouse lungs. We recently reported the significance of the injection of an acute hypoxia-releasing agent, nicotinamide, into tumor-bearing mice as a combined treatment with  $\gamma$ -ray irradiation in terms of repressing lung metastasis. As the delivered total dose increased with irradiation, the number of macroscopic lung metastases decreased reflecting the decrease in the number of clonogenically viable tumor cells in the primary tumor. The metastasis-repressing effect achieved through a reduction in the number of clonogenic tumor cells by irradiation is much greater than that achieved by releasing tumor cells from acute hypoxia. On the other hand, more  $^{10}\text{B}$  from BPA than from BSH could be distributed into the acute hypoxia-rich total tumor cell population, resulting in a greater decrease in the number of highly clonogenic P tumor cells with BPA-BNCT than with BSH-BNCT and with neutron beam irradiation only.

BPA-BNCT rather than BSH-BNCT has some potential to decrease the number of lung metastases, and an acute hypoxia-releasing treatment such as the administration of nicotinamide or bevacizumab may be promising for reducing numbers of lung metastases. Consequently, BPA-BNCT in combination with nicotinamide and/or bevacizumab treatment may show a little more potential to reduce the number of metastases. Now, it has been elucidated that control of the chronic hypoxia-rich Q cell population in the primary solid tumor has the potential to impact the control of local tumors as a whole, and that control of the acute hypoxia-rich total tumor cell population in the primary solid tumor has the potential to impact the control of lung metastases.

The aim of this research project is focused on clarifying and analyzing the characteristics of intratumor microenvironment including hypoxia within malignant solid tumors and optimizing cancer therapeutic modalities, especially radiotherapy including BNCT in the use of newly-developed  $^{10}\text{B}$ -carriers based on the revealed findings on intratumor microenvironmental characteristics.

### RESEARCH SUBJECTS:

The collaborators and allotted research subjects (ARS) were organized as follows;

**ARS-1 (28P7-1):** Optimization of Radiation Therapy Including BNCT in terms of the Effect on a Specific Cell Fraction within a Solid Tumor and the Suppressing Effect of Distant Metastasis. (S. Masunaga, *et al.*)

**ARS-2 (28P7-2):** Development of Hypoxic Microenvironment-Oriented  $^{10}\text{B}$ -Carriers. (H. Nagasawa, *et al.*)

**ARS-3 (28P7-3):** Clarification of Mechanism of Radio-Resistance in Cancer Using Optical Imaging at Tissue Level. (H. Harada, *et al.*)

**ARS-4 (28P7-4)\*:** Analysis of Radiation-Induced Cell-Killing Effect in Neutron Capture Reaction. (R. Hirayama, *et al.*)

**ARS-5 (28P7-5)\*:** Transdermal Drug Delivery System using Hyaluronan-Conjugated Liposomes as  $^{10}\text{B}$ -Carrier in Boron Neutron Capture Therapy for Melanoma (S. Kasaoka, *et al.*)

**ARS-6 (28P7-6)\*:** Evaluation of Inclusion Complex of Carborane Modified Kojic Acid and Cyclodextrin as  $^{10}\text{B}$ -Carrier in Boron Neutron Capture Therapy. (T. Nagasaki, *et al.*)

**ARS-7 (28P7-7)\*:** Molecular Design and Synthesis and Functional Evaluation of Anticancer and Molecular Targeting Agents. (Y. Uto, *et al.*)

**ARS-8 (28P7-8)\*:** Analyzing Biological Effect of BNCT from the Viewpoint of the Changes in Oxygenation Level. (H. Yasui, *et al.*)

**ARS-9 (28P7-9):** Analyses on the Responsiveness of Malignant Tumors to BNCT. (M. Masutani, *et al.*)

**ARS-10 (28P7-10)\*:** Assay for Tumor Cell Survival and Tumor Growth Delay through Neutron Capture Reaction according to the Changes in Intracellular Concentrations within Solid Tumors of Newly-Developed  $^{10}\text{B}$ -Carriers. (K. Nakai, *et al.*)

**ARS-11 (28P7-11)\*:** Antitumor and Metastasis-Repressing Effect of BNCT on Human Breast and Pancreatic Cancer Cell Lines. (Y. Matsumoto, *et al.*)

(\*Due to the absence of operating our reactor in 2016, no data were obtained, resulting in no reporting here.)

## PR7-1 Effect of Oxygen Pressure during Incubation with a $^{10}\text{B}$ -carrier on $^{10}\text{B}$ Uptake Capacity of Cultured *p53* Wild-type and Mutated Tumor Cells, Referring to Dependency on *p53* Status of Tumor Cells and Types of $^{10}\text{B}$ -Carriers

S. Masunaga, H. Tatebe<sup>1</sup>, Y. Nishimura<sup>1</sup>, K. Tano, Y. Sanada, Y. Sakurai, H. Tanaka, M. Suzuki, N. Kondo, T. Watanabe, Y. Tamari, T. Takata, A. Maruhashi and K. Ono

Research Reactor Institute, Kyoto University  
<sup>1</sup>Department of Radiation Oncology, Kinki University  
School of Medicine

**INTRODUCTION:** We attempted to evaluate the uptake capacity of  $^{10}\text{B}$  from a  $^{10}\text{B}$ -carrier under aerobic and hypoxic conditions in cultured head and neck tumor cell lines using the two common  $^{10}\text{B}$ -carriers, *L-para-boronophenylalanine- $^{10}\text{B}$*  (*BPA*,  $\text{C}_9\text{H}_{12}^{10}\text{BNO}_4$ ) or *sodium mercaptoundecahydrododecaborate- $^{10}\text{B}$*  (*sodium borocaptate- $^{10}\text{B}$* , *BSH*,  $\text{Na}_2^{10}\text{B}_{12}\text{H}_{11}\text{SH}$ ) as a  $^{10}\text{B}$ -carrier. Further, the effect of the *p53* status of intratumor cells on the uptake capacity using two different tumor cell lines identical in genetic background except for *p53* status was also evaluated.

**MATERIALS AND METHODS:** Cultured human head and neck squamous cell carcinoma cell line transfected with mutant *TP53* (*SAS/mp53*), or with a *neo* vector as a control (*SAS/neo*) was incubated with *BPA* or *BSH* as a  $^{10}\text{B}$ -carrier at the  $^{10}\text{B}$  concentration of 60 ppm for 24 hours under aerobic (20.7 % of oxygen) or hypoxic (0.28 % of oxygen) conditions. Immediately after incubation, cultured tumor cells received reactor thermal neutron beams, and a cell survival assay was performed.  $^{10}\text{B}$  concentration of cultured *SAS/neo* or *SAS/mp53* cells incubated under aerobic or hypoxic conditions was determined with a thermal neutron guide tube.

**RESULTS:** Hypoxic incubation significantly decreased  $^{10}\text{B}$  concentration of cultured cells with a clearer tendency observed following *BPA* than *BSH* treatment in both *SAS/neo* and *SAS/mp53* cells. In both tumor cells, the aerobic incubation with *BPA* produced significantly higher  $^{10}\text{B}$  concentrations than with *BSH*. However, after the hypoxic incubation with *BPA*, the  $^{10}\text{B}$  concentrations were significantly lower than those with *BSH*. The  $^{10}\text{B}$  concentrations after aerobic incubation with *BPA* or *BSH* in *SAS/neo* were higher than in *SAS/mp53* tumor cells although not significantly. However, the  $^{10}\text{B}$  concentrations after hypoxic incubation with *BPA* in *SAS/neo* tumor cells were lower than those in *SAS/mp53* tumor cells again without significant differences. Those after hypoxic incubation with *BSH* in both *SAS/neo* and *SAS/mp53* cells were almost the same each other. Following neutron beam irradiation, *SAS/mp53* cells showed significantly higher relative biological effectiveness values than *SAS/neo* cells because of the significantly lower

radio-sensitivity of *SAS/mp53* to  $\gamma$ -rays than *SAS/neo* cells.

**DISCUSSION:** Solid tumors are composed of proliferating (P) and quiescent (Q) tumor cell populations, and human tumors are thought to contain a high proportion of Q cell population [1]. The presence of Q cell population is partly due to hypoxia and the depletion of nutrition in the tumor core, which may be another consequence resulting from poor vascular supply [1]. As Q cell populations have been shown to have a much larger hypoxic fraction (HF) than total (= P + Q) cell populations [1], and Q tumor cell populations also showed a significantly lower sensitivity to the boron neutron capture reaction than the total cell populations [1], it follows that hypoxic tumor cells probably exhibit less uptake capacity of  $^{10}\text{B}$  from a  $^{10}\text{B}$ -carrier than aerobic cells [1].

It has been thought that the intracellular distribution of  $^{10}\text{B}$  from *BSH* was mostly dependent on the diffusion of the drug, and that  $^{10}\text{B}$  from *BPA* is more dependent on the ability of the cells to take up  $^{10}\text{B}$ . On the other hand, Q cell populations were shown to have a much larger hypoxic fraction than total cell populations [1], and have a lower uptake capacity than the total cell population [1]. Thus, it follows that hypoxic cells are thought to exhibit less uptake than aerobic cells, and that the distribution of  $^{10}\text{B}$  from  $^{10}\text{B}$ -carriers into hypoxic cells is more dependent on the diffusion of the drugs than on the cellular uptake of the cells. *SAS/neo* cells have a functional *p53* protein and *SAS/mp53* cells express a dominant negative *p53* protein. Thus, it was thought to be reasonable that *SAS/neo* showed a significantly clearer decrease in the  $^{10}\text{B}$  uptake capacity as a response to hypoxic stress than *SAS/mp53* cells. Further, hypoxic cells are thought to show less  $^{10}\text{B}$  uptake capacity than aerobic cell in general. Therefore, it was also reasonable that the  $^{10}\text{B}$  uptake capacity from *BPA* was significantly decreased through hypoxic stress compared with that from *BSH* because of the more dependency on the ability of cells to take up  $^{10}\text{B}$  from a  $^{10}\text{B}$ -carrier in the use of *BPA* than *BSH*, resulting in lower  $^{10}\text{B}$  concentrations after hypoxic incubation with *BPA* than *BSH* in both *SAS/neo* and *SAS/mp53* cells.

**CONCLUSION:** Oxygen pressure during incubation with a  $^{10}\text{B}$ -carrier had a critical impact on the  $^{10}\text{B}$  uptake of cultured tumor cells with a more clearly tendency with the use of *BPA* than *BSH* and in *SAS/neo* than in *SAS/mp53* tumor cells [2].

### REFERENCES:

- [1] S. Masunaga, *et al.*, *J Radiat Res* **43** (2002) 11-25.
- [2] S. Masunaga, *et al.*, *Int J Radiat Biol Phys* **92**(4) (2016) 187-94. doi: 10.3109/09553002.2016.1137104. Epub 2016 Feb 18.

## PR7-2 Design and Synthesis of Pepducin-BSH Conjugates with Polyamine Linker

A. Isono, T. Hirayama, K. Okuda<sup>1</sup>, S. Masunaga<sup>2</sup> and H. Nagasawa<sup>1</sup>

Laboratory of Medicinal & Pharmaceutical Chemistry, Gifu Pharmaceutical University

<sup>1</sup>Laboratory of Organic Chemistry, Kobe Pharmaceutical University

<sup>2</sup>Research Reactor Institute, Kyoto University

**INTRODUCTION:** Although sodium borocaptate (BSH) has been used clinically as a boron carrier for BNCT, it is impermeable to plasma membrane due to its high hydrophilicity and anionic charges. To improve intracellular uptake of boron-cluster such as BSH to tumor cells, pepducin chemistry was exploited as membrane-permeable carrier. Pepducins are artificial lipopeptides derived from an inner loop domain of G protein-coupled receptors (GPCRs) which enabled anionic molecule such as fluorescein to penetrate membrane directly via flip-flop movement.<sup>1</sup> We focused on the ability of transmembrane translocation of pepducin and new pepducin-BSH hybrid compounds were designed as boron carriers for BNCT (Fig. 1).

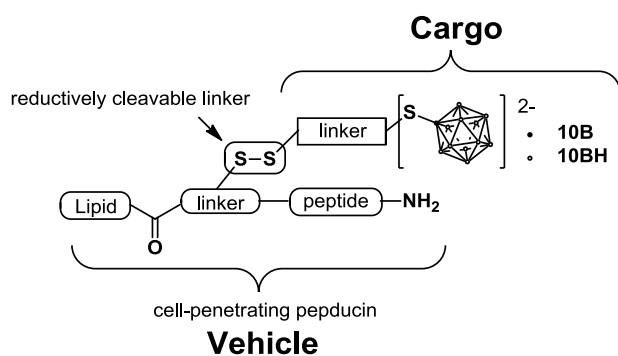


Fig. 1 Design of pepducin-BSH conjugates

Pepducin (Pep) as a vehicle was connected to boron cluster (BSH) as a cargo through an appropriate linker. When this molecule is internalized into the cytosol, intracellular glutathione can cleave the disulfide bond (SS) to release the boron cluster cargo into the cytosol. Once BSH is released into cytosol, 10B atoms may be accumulated in the cells due to hydrophilicity of the anionic property. We newly evaluated linker structure in cargo moiety. BSH is membrane impermeable due to its two anionic charges. Polyamine was inserted between BSH moiety and reductively cleavable S-S linker to make the cargo unit neutral or positively charged under physiolog-

ical condition to increase membrane affinity. Structures of new pepducin-BSH conjugates **1** and **2** with piperazine and linear polyamine linkers respectively were shown in Fig. 2.

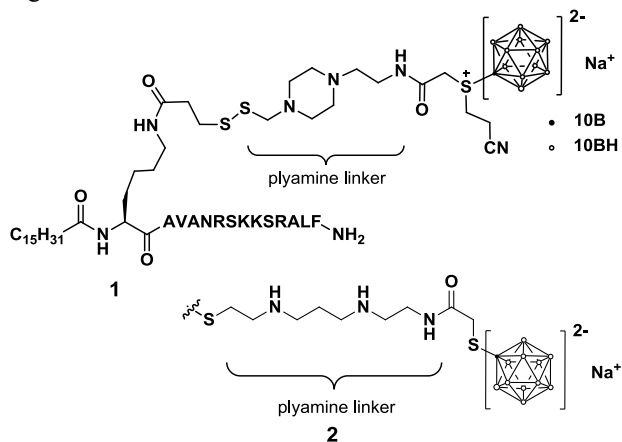


Fig. 2 Structure of new pepducin-BSH conjugates **1** and **2**

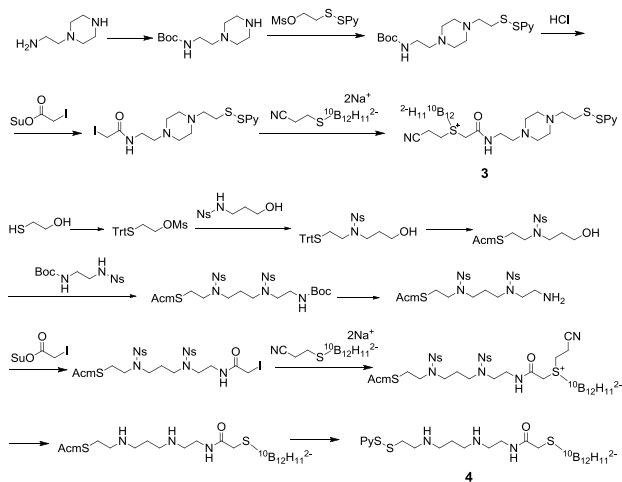


Fig. 3 Synthesis of polyamine linker **3** and **4**

Polyamine linkers **3** and **4** were synthesized in good yields (Fig. 3). Then they were combined with pepducin unit to afford compound **1** and **2** in moderate yields respectively. Now their intracellular uptake into T98G cells is examined by ICP-AES.

### REFERENCE:

[1] M. Tsuji *et al.*, *Org. Biomol. Chem.*, **11**(2013), 3030-3037.

## PR7-3 UCHL1-HIF-1 Axis-mediated Antioxidant Property of Cancer Cells as a Therapeutic Target for Radiosensitization

H. Harada<sup>1,2,3</sup>, R. Nakashima<sup>1,4</sup>, Y. Goto<sup>1,4</sup>, A. Morinibu<sup>1</sup>, M. Kobayashi<sup>1</sup> and S. Masunaga<sup>5</sup>.

<sup>1</sup>Laboratory of Cancer Cell Biology, Department of Genome Dynamics, Radiation Biology Center, Kyoto University.

<sup>2</sup>PRESTO, JST.

<sup>3</sup>Hakubi Center, Kyoto University.

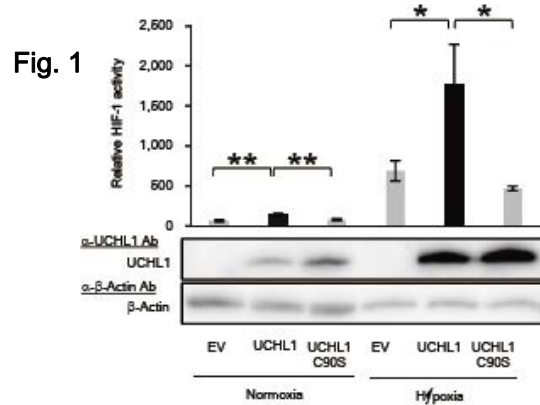
<sup>4</sup>Department of Radiation Oncology and Image-applied Therapy, Graduate School of Medicine, Kyoto University.

<sup>5</sup>Research Reactor Institute, Kyoto University.

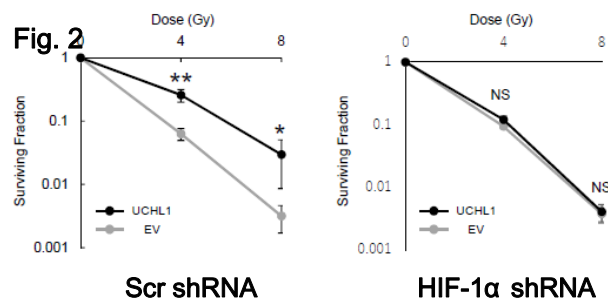
**INTRODUCTION:** Hypoxia-inducible factor 1 (HIF-1) has been recognized as an important mediator of the reprogramming of carbohydrate metabolic pathways from oxidative phosphorylation to accelerated glycolysis. Although this reprogramming has been associated with antioxidant and radioresistant properties of cancer cells, a gene network triggering the HIF-1-mediated reprogramming and a molecular mechanism linking the reprogramming with radioresistance remain to be determined. Here, we show that Ubiquitin C-terminal hydrolase-L1 (UCHL1), which we previously identified as a novel activator of HIF-1, increased the radioresistance of cancer cells by producing an antioxidant, reduced glutathione (GSH), through HIF-1-mediated metabolic reprogramming [1,2].

**EXPERIMENTS:** EMT6 was purchased from the American Type Culture Collection (Manassas, VA, USA). Cells were maintained at 37°C in Dulbecco's modified Eagle's medium (DMEM). Media were supplemented with 10% FBS, 100 U/ml penicillin, and 100 µg/mL streptomycin. Cells were incubated in a well-humidified incubator with 5% CO<sub>2</sub> and 95% air for the normoxic conditions or in a RUSKINN INVIVO2 500 (Ruskinn) for the hypoxic conditions at <0.1% O<sub>2</sub>. Molecular mechanism behind the UCHL1-mediated upregulation of HIF-1 activity was analyzed *in vitro* by performing Western blotting, luciferase assay. LC/MS-based metabolome analysis to quantify the levels of <sup>13</sup>C<sub>6</sub>-labeled lactate, citrate, and isocitrate was performed as described previously[3,4]. Intracellular NADPH levels were quantified using the NADP<sup>+</sup>/NADPH Quantification Kit (BioVision Inc.) and NADP/NADPH-Glo Assay Kit (Promega) according to the manufacturers' instructions. Intracellular GSH levels were quantified using the ApoGSH Glutathione Colorimetric Detection Kit (BioVision Inc.) and GSH/GSSG-Glo Assay Kit (Promega) according to the manufacturers' instructions. Clonogenic cell survival assays were performed to evaluate effect of UCHL1-overexpression, HIF-1α knockdown, or glucose-6-phosphate dehydrogenase X-linked (G6pdx)-knockdown.

**RESULTS:** A luciferase assay to monitor HIF-1 activity demonstrated that the overexpression of UCHL1, but not its deubiquitination activity-deficient mutant (UCHL1 C90S), upregulated HIF-1 activity by stabilizing the regulatory subunit of HIF-1 (HIF-1α) in a murine breast cancer cell line, EMT6 (Fig. 1).



UCHL1 overexpression induced the reprogramming of carbohydrate metabolism from oxidative phosphorylation to glycolysis and increased NADPH levels in a pentose phosphate pathway-dependent manner (data not shown). The UCHL1-mediated reprogramming elevated intracellular levels of GSH, and consequently induced a radioresistant phenotype in a HIF-1-dependent manner (Fig. 2).



**DISCUSSION:** These results collectively suggest that cancer cells acquire antioxidant and radioresistant phenotypes through UCHL1-HIF-1-mediated metabolic reprogramming and provide a rational basis for targeting this gene network for radiosensitization.

### REFERENCES:

- [1] R. Nakashima *et al.* Scientific Reports. in press.
- [2] H. Harada. J Radiat Res. 57:99-105. 2016.
- [3] L. Zeng *et al.*, Oncogene, 34:4758-4766. (2015)
- [4] Y. Goto *et al.* Nature Communications. 6:6153. (2015).

S. Imamichi<sup>1,2</sup>, H. Fujimori<sup>2</sup>, S. Masunaga<sup>3</sup> and M. Masutani<sup>1,2,4</sup>

<sup>1</sup>Division of Boron Neutron Capture Therapy, EPOC, National Cancer Center, <sup>2</sup>Division of Genetics, Research Institute, National Cancer Center

<sup>3</sup>Research Reactor Institute, Kyoto University,

<sup>4</sup>Department of Frontier Life Sciences, Nagasaki University Graduate School of Biomedical Sciences

**INTRODUCTION:** Tumors are consisted of heterogeneous populations including hypoxic cells, cancer stem cells and differentiating cells. Boron neutron capture therapy (BNCT) is a tumor selective therapy that is based on the principle of preferential uptake of 10-boron labeled compound such as boronophenylalanine (BPA) into cancer cells and thermal-neutron irradiation. The nuclear reaction between 10-boron and thermal-neutron generates high LET radiation which causes alpha particle and lithium nuclei in the cells. Boron neutron capture reaction (BNCR) efficiently introduces DNA double strand breaks [1], however, tumor cell killing is affected by various factors [2] including the uptake of boron compounds, thermal neutron fluence. It is therefore important to analyze the responses of various cell lines to BNCR in diverse conditions. We previously observed extensive DNA damage responses including that for DNA strand breaks after BNCR by the observation of remaining  $\gamma$ -H2AX and poly(ADP-ribose) in rat lymphosarcoma model of BNCT [3] and started comprehensive analysis of mRNA expression and proteome of human squamous carcinoma SAS cells after BNCR [4]. In this study, we have investigated and evaluated the cell survival after BNCR or neutron beam irradiation in comparison with the survival of gamma-ray irradiation. Clarifying the radiation sensitivity of cells is important to optimize BNCT achieving high precision as a radiation therapy.

**EXPERIMENTS:** The neutron-beam irradiation with KUR nuclear reactor was not carried out during FY2016. We therefore analyzed the previously irradiated cell samples and cell survival data prepared before. For obtaining cell survival curves, we used the human oral squamous cancer SAS cells and HSG cells, which have been referred as a radiation standard to evaluate relative biological effectiveness. SAS cells and HSG cells were suspended in the polypropylene vials and incubated for 2 hrs with or without 25 ppm of <sup>10</sup>B-BPA [5]. In the previous experiments, neutron-beam irradiations were operated at 1 MW in the KUR facility. Cells were diluted and inoculated into 6 well plates. Thermal neutron fluence and gamma-ray dose were measured with the thermal-luminescence dosimeter. These physical radiation doses were measured by the kind help of Drs. Yoshinori Sakurai and Hiroki Tanaka of KUR. <sup>10</sup>B concentration was measured by prompt-gamma ray analysis (PGA) as described else-

where. For gamma-ray irradiation, cells were prepared as described above without adding <sup>10</sup>B-BPA to the culture medium. Gamma-ray irradiations were operated at National Cancer Center Research Institute (Tokyo) with the <sup>137</sup>Cs source and dose rate was approximately 100 cGy/min.

**RESULTS:** SAS cells and HSG cells after BNCR showed a high radiosensitivity. The surviving curve of HSG cells after BNCR showed a slight two-dimensionality (Fig. 1). This may be due to the experimental condition. The relative biological effectiveness (RBE) of BNCR for HSG and SAS cells was around 2-3 as expected from the literatures.

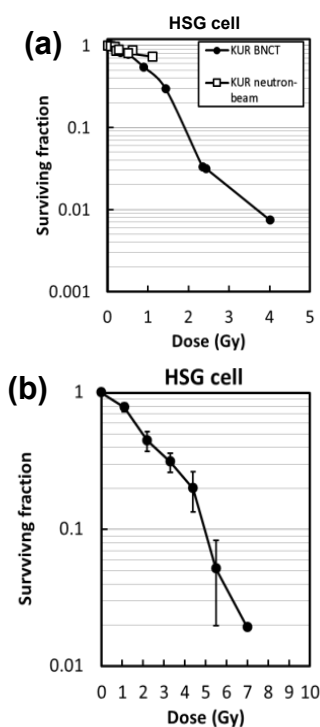


Figure 1: Cell survival after neutron-beam irradiation with/without BPA (a) and after  $\gamma$ -irradiation for HSG cells (b).

#### REFERENCES:

- [1] S.G. Hussein *et al.*, Proc. Montreal Int. Conf. Eds Harvey, Cusson, Geiger, Pearson (U. Mont Press) (1969) 91.
- [2] K. Okano *et al.*, Nucl. Instr. and Meth, 186 (1981) 115-120.
- [3] M. Masutani *et al.*, Appl. Rad. Iso., 104 (2014) 104-108.
- [4] A. Sato *et al.*, Appl. Rad. Iso., 106 (2015) 213-219
- [5] R. B. Firestone, in *Table of Isotopes*, 8<sup>th</sup> ed., edited by V. S. Shirley (Wiley, New York, 1996), Vol.29

K. Takamiya

*Research Reactor Institute, Kyoto University*

**OBJECTIVE:** The chemical and physical characteristics of radioactive materials released from Fukushima Daiichi Nuclear Power Plant to the atmosphere has been investigated by various methods to elucidate the environmental dynamics of the radioactive materials. A radioactive aerosol is one of the most important released materials, and the production mechanism and measurement technique has been studied in this project. The generation method for solution radioactive aerosols had been developed in the previous studies in this project, and the new subject in which the generated solution aerosol had been applied was added in this year period in order to understand the environmental dynamics of the radioactive aerosols.

**RESEARCH SUBJECTS:** The project research is composed by five individual subjects in this year period. Two are developments of production method of radioactive aerosols for simulation experiments, one is development of measurement method of radioactive aerosols, and one is elucidation of the production mechanism of aerosol under the specific situation. And one subject about interaction of radioactive cesium in the environment was added in this year period. The respective subjects of the research groups of this project are described as follows;

P8-1: Development of production method of radioactive aerosols by attaching radioisotopes to aerosol particles

P8-2: Development of measurement method of radioactive aerosols under severity conditions

P8-3: Development of production method of radioactive aerosols by heating radioisotopes

P8-4: Study for production mechanism of radioactive aerosols in the presence of sea water

P8-5: Interaction of radioactive cesium and suspended particles in river water

In this year period, experiments of subjects P8-3 and P8-4 were not carried out because of no operation of KUR.

**RESULTS:** In the subject P8-1, the solution concentration dependence of production behavior for radioactive solution aerosols has been investigated. Primary aerosols were generated from sodium chloride solution of various concentration (0.005, 0.01 and 0.02 M). The production ratio of radioactive aerosols was estimated as attachment ratio of fission products to aerosol particles in a chamber in which  $^{252}\text{Cf}$  spontaneous fission source was placed. The attachment ratio of  $^{104}\text{Tc}$  can be obtained only with enough statistics as a function of total surface area of aerosol particles in this experiment. It was found that there are differences among aerosols of three different concentrations in the relationship. The result might suggest the solute con-

centration of solution aerosols affects the production process of radioactive aerosols. The relationships were fitted by an equilibrium function on the basis of an assumption of the adsorption-desorption equilibrium between fission products and surface of aerosol particles. The order of magnitude of the estimated equilibrium constants is  $0.02 \text{ M} > 0.01 \text{ M} > 0.005 \text{ M}$ . This trend might be caused by density of the anions in the solution aerosol particles.

For the development of measurement method of radioactive aerosols under severity conditions (P8-2), time variation of particle size of the radiation-induced aerosols was tried to be measured in an electron linac facility by using a scanning mobility particle sizer (SMPS) or a wire screen method. According to the SMPS measurement, no aerosol particles were observed in the chamber immediately after the filtration of the irradiated air; however, rapid formation of the aerosol occurred in the chamber. It was found that the particle size increased to approximately 100 nm (geometric mean) with a decrease in the number concentration, and time to maximum size from the end of air sampling was 9 h. The size and concentration are expressed as functions of the rates of formation, coagulation, evaporation, dilution and disappearance due to collision to the inside wall of the chamber.

For the research about interaction of radioactive cesium in the environment (P8-5), the effect of cesium adsorption to suspended particles on the desorption behavior was investigated. The suspended particles were sampled from Abukuma river in Date, Fukushima. For the adsorption of cesium, 100 mg of the particle sample was exposed by the cesium solution aerosol generated by an atomizer containing 0.4 wt% of CsCl, for 2.5 hours or 90 seconds. The amount of loaded cesium on the particles was determined by ICP-MS using a part of particle samples. And the particle samples exposed by the aerosol were mixed with various desorption agents as the cesium desorption treatment. The supernatant was filtered by a 0.45  $\mu\text{m}$  pore size membrane filter, and the cesium concentration in it was measured by ICP-MS to estimate the desorption ratio. The results of desorption experiment indicated that all desorption agents (470 mM NaCl, seawater, 1 M KCl) except ultrapure water desorbed cesium more than 90 % from the high cesium loading sample. In contrast, only 30 % cesium was desorbed from the low cesium loading sample by seawater. As a result, the cesium desorption percentage by seawater was 30 %, where the cesium loading on the suspended particles was about  $1 \mu\text{g/g}$  which was close to the loading amount of 90 seconds aerosol atomized sample ( $= 6.9 \mu\text{g/g}$ ). The observed agreement of the desorption percentages from different way of cesium loading indicates that the desorption behavior is simply governed by the cesium loading amount on the particles rather than the way of loading.

In the near future, experiments with a neutron irradiation using KUR will be performed, and further progress is expected in this project.

K. Takamiya, Y. Nishizawa, S. Sekimoto, Y. Oki and T. Ohtsuki

*Research Reactor Institute, Kyoto University*

**INTRODUCTION:** Large amount of radioactive materials released into the atmosphere from Fukushima Daiichi Nuclear Power Plant have been transported by aerosols. It was suggested that the potential transport medium for radioactive cesium were sulfate aerosols [1, 2]. On the other hand, the initial production process of radioactive aerosols in the reactor building is not clear because there is not direct measurement data. Attachment behavior of fission products to solution aerosol particles have been studied in our previous works [3, 4] to elucidate the production mechanism of radioactive solution aerosol in the initial production process. It was found that there seems to be an adsorption equilibrium process in the radioactive aerosol production and the equilibrium constants depends on a kind of solution. In the present work, the solution concentration dependence of production behavior for radioactive solution aerosols has been investigated.

**EXPERIMENTS:** The production method of radioactive aerosols using a spontaneous fission source of  $^{252}\text{Cf}$  was explained in the previous reports [3, 4]. Primary aerosols were generated from sodium chloride solution of various concentration (0.005, 0.01 and 0.02 M). In order to examine the relationship between surface area of aerosol particles and the production ratio of radioactive aerosol, the primary solution aerosol was classified by size using a differential mobility analyzer in the region of diameter smaller than about 100  $\mu\text{m}$ . In the larger diameter region, the surface of the aerosols was controlled by changing the aerosol number concentrations. The radioactive aerosol produced by attaching fission products to aerosol particles were collected by a polycarbonate filter. On the other hand, all fission products emitted from the  $^{252}\text{Cf}$  source were collected by a grease-applied cellulose filter placed directly on the source. Gamma-ray spectrometry using a Ge-detector was performed for the filters to estimate the production ratio of radioactive aerosols which were produced by attaching fission products to aerosol particles.

**RESULTS:** The production ratio of radioactive aerosols was estimated as attachment ratio of fission products to aerosol particles from the ratio of photopeak areas for each fission product. The attachment ratio of  $^{104}\text{Tc}$  can be obtained only with enough statistics and shown in Fig. 1 as a

function of total surface area of aerosol particles. The symbols of circle, square and triangle show the attachment ratio for sodium chloride solution of 0.005, 0.01 and 0.02 M solution concentrations, respectively. The difference are found among aerosols of three different concentrations, and this result means the solute concentration of solution aerosols affects the production process of radioactive aerosols. The relationships were fitted by an equilibrium function on the basis of an assumption of the adsorption-desorption equilibrium between fission products and surface of aerosol particles. The results of the fitting are shown by lines in Fig. 1. The order of magnitude of the estimated equilibrium constants is  $0.02\text{ M} > 0.01\text{ M} > 0.005\text{ M}$ . This trend might be caused by density of the anions in the solution aerosol particles.

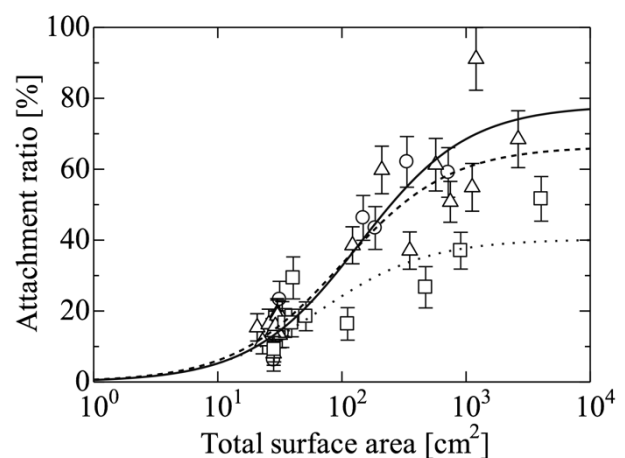


Fig. 1. Relationship between the attachment ratio of  $^{104}\text{Tc}$  to NaCl solution aerosol and the total surface area of the aerosol particles. Circles, triangles and squares show the attachment ratio to NaCl solution aerosols of 0.005, 0.01 and 0.02 M concentrations, respectively.

#### REFERENCES:

- [1] N. Kaneyasu et al., *Environ Sci Technol* **46** (2012) 5720–5726.
- [2] Y. Miyamoto et al., *J. Environ. Radioact.* **132** (2014) 1–7.
- [3] K. Takamiya, et al., *J. Radiat. Prot. Res.* **41** (2016) 350–353.
- [4] K. Takamiya, et al., *J. Radioanal. Nucl. Chem.* **307** (2016) 2227–2230.

## PR8-2 Growth of Aerosol Particles in Irradiated Air of an Accelerator Room

Y. Oki, K. Takamiya, N. Osada<sup>1</sup>, S. Sekimoto and T. Ohtsuki

*Research Reactor Institute, Kyoto University*  
<sup>1</sup>*Advanced Science Research Center, Okayama University*

**INTRODUCTION:** Radioactive aerosols were released to the environment in both accidents of the Fukushima Daiichi Nuclear Power Plant (FDNPP) and Japan Proton Accelerator Research Complex (J-PARC). The release occurred due to melting of the highly radioactive nuclear fuel or the metallic target. Radionuclides evaporated from the molten fuel or metals are incorporated into ambient aerosol particles to form the radioactive aerosols of various radionuclides. The radiation-induced aerosol is a principal ambient aerosol in intense radiation fields; however, most of its nature concerning formation and growth in radiation fields remain unexplained.

In this work, time variation of particle size of the radiation-induced aerosols was studied using a scanning mobility particle sizer (SMPS) from the time of their birth in an electron linac facility. In addition, a wire screen method was also applied for the size measurement [1].

**EXPERIMENTS:** An air irradiation experiment was carried out in the 46-MeV electron linear accelerator of the Research Reactor Institute (KURRI). A tantalum target was installed at the end of the beam line, and was bombarded with a 30-MeV electron beam to produce bremsstrahlung and neutrons. The bremsstrahlung ionizes air and produces radiation-induced aerosol. The beam current was ca. 100  $\mu\text{m}$ . During the irradiation, the air ventilation in the target room was stopped not to disturb air. Air was collected from the target room to a 200-L vacuum aerosol chamber through a sampling tube penetrating a 3-m thick shielding wall. The target room air was introduced to the vacuum chamber after filtration with a HEPA filter. A 1.5-L ionization chamber was used for monitoring concentration of radioactive gases.

The particle size distribution and number concentration of the aerosols were measured continuously with SMPS. The irradiated air was sampled from the chamber to the SMPS at the flow rate of 0.3 L/min. A filtered aerosol-free air was supplied to the chamber at the same flow rate to keep pressure in the chamber.

A screen device consisting of a stack of 20 pieces of 500-mesh stainless steel wire screens was also employed

for size measurement of the aerosol. The particle size distribution was calculated from penetration ratios for the screens obtained with condensation particle counter (CPC).

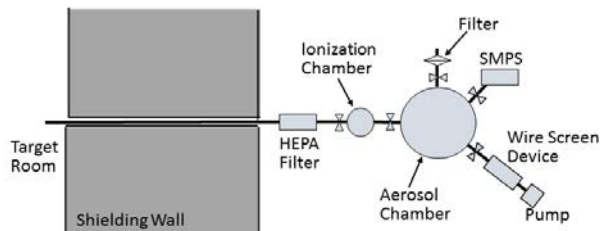


Fig. 1 Experimental Setup for Sampling of the irradiated air from the target room

**RESULTS:** According to the SMPS measurement, no aerosol particles were observed in the chamber immediately after the filtration of the irradiated air; however, rapid formation of the aerosol occurred in the chamber.

Preliminary results showed that the particle size increased to approximately 100 nm (geometric mean) with a decrease in the number concentration. It took 9 h to reach the maximum size from the end of air sampling. The size and concentration are expressed as functions of the rates of formation, coagulation, evaporation, dilution and disappearance due to collision to the inside wall of the chamber.

Oxygen-15 (half life: 2 min), <sup>13</sup>N (9.965 min) and <sup>41</sup>Ar are principal radionuclides formed in the target room air. Nitrogen-13 was a dominant gaseous nuclide in the chamber. The radioactivity in the chamber is considered to influence the formation rate. The formation rate decreased as <sup>13</sup>N decayed.

The screen device was not applied to radioactivity-based particle size measurement because conversion of radioactive <sup>13</sup>N gas to aerosols was not observed in the chamber. In the number-based particle size measurement, the number concentration of the aerosols was measured by varying the sampling flow rate to the device, not by changing number of the screens, in order to minimize the sampling volume from the chamber.

### REFERENCE:

[1] Y. Oki, et al., J. Radiat. Prot. Res., 41 (2016) 216-221.

## PR8-3 Interaction of Radioactive Cesium and Suspended Particles in River Water

A. Kirishima, M. Onodera, K. Takamiya<sup>1</sup>, T. Ohtsuki<sup>1</sup>, Y. Oki<sup>1</sup>, S. Sekimoto<sup>1</sup> and N. Sato

*Institute of Multidisciplinary Research for Advanced Materials, Tohoku University*

<sup>1</sup>*Kyoto University Research Reactor Institute*

**INTRODUCTION:** Radioactive Cs deposited in river due to the nuclear accident of Fukushima in 2011 is thought to be adsorbed in suspended particles (SP) and migrate along the river flow. Because SP are mainly composed by clay minerals, they can retain Cs on the surface and inter-layers of clay minerals by cation-exchange reaction. When retained radioactive Cs arrives at brackish water area, they could be desorbed from SP in response to solution condition change. The understanding of this Cs speciation change mechanism is very important for the prediction of Cs migration from mountain area to coast area. Therefore, this study carried out cesium adsorption and desorption experiment for SP by batch method. To investigate the effect of the Cs adsorption method to the particle on the desorption behavior, cesium desorption experiment from the suspended particles that adsorbed cesium by atomizing cesium aerosol was carried out in this study.

**EXPERIMENTS:** SP was sampled from Date place located in about 60 km northwest of the 1F NPS (Yanagawa-Ohashi, Yanagawa-cho, Date-shi, Fukushima prefecture, Japan) of Abukuma river and named as Date Sample. The river water containing suspended particles were collected about 20 L by a Teflon container. The suspended particles were then collected on a filter having 0.45  $\mu\text{m}$  pore, and these particles were freeze dried. Finally, black brown color powdered suspended particles were obtained. Solution aerosols were generated using a combined system of an atomizer 3076 (TSI, Shoreview, MN) containing 0.4 wt % of CsCl, a electric furnace, and a diffusion dryer. Nitrogen gas was supplied at pressure of 2.5  $\text{kg}/\text{cm}^2$  to the atomizer to discharge CsCl solution aerosols [1]. The aerosols were passed through the furnace, which was kept constant at 80  $^\circ\text{C}$  and the diffusion dryer with an infill of silica gel sequentially. For the adsorption of cesium, 100 mg of the Date sample was exposed by the cesium aerosol for 2.5 hours or 90 seconds with mixing the particles every 30 minutes and 10 second, respectively by a spatula. To determine the loaded cesium amount on the suspended particles, about 4 mg of the aerosol exposed Date samples were dissolved in the mixed solution of 3 ml of conc.  $\text{HNO}_3$  and 300  $\mu\text{l}$  of 46 wt % Hydrofluoric acid in a PTFE beaker (Heatable beaker, Sanplatec Co.) with heating at 160  $^\circ\text{C}$ . After the complete dissolution of the particles, the solution was dried up, then about 5 ml of 1 M  $\text{HNO}_3$  solution was

added to dissolve remained salts. The cesium concentration in this solution was then measured by an induced coupled plasma – mass spectrometry spectrometer (ICP-MS, ELEMENT II, Thermo Fisher Scientific Co.) using tellurium ion as the internal standard. These dissolution and measurement procedure were repeated 4 times for one sample of the suspended particles to get an average value of the cesium concentration. The loaded cesium concentration of the Date sample from the cesium aerosol was thus calculated from the measured cesium concentration by ICP-MS. Subsequently, the Date samples exposed by the aerosol were mixed with desorption agents in a solid-to-liquid ratio of 0.17 g/l for 6 days at 25  $^\circ\text{C}$  as the cesium desorption treatment. The supernatant was then, filtered by the 0.45  $\mu\text{m}$  pore size membrane filter, and the cesium concentration in it was measured by ICP-MS. Finally the desorption percentages were calculated by following equation:

$$\text{Desorption [\%]} = (C/C_0) \times (S/L) \times 100, \quad (1)$$

where  $C_0$  is initial cesium concentration (g/g) in the Date sample exposed by the aerosol, and  $C$  is cesium concentration (g/l) in the supernatant solution after the desorption treatment,  $(S/L)$  is solid-to-liquid ratio (g/l) at the desorption treatment.

**RESULTS:** The loaded cesium amount on the Date samples atomized by the CsCl aerosol were determined to be 113  $\mu\text{g}/\text{g}$  for 2.5 hours of the atomization sample and 6.9  $\mu\text{g}/\text{g}$  for 90 seconds atomization by ICP-MS. The results of desorption experiment indicated that all desorption agents (470 mM NaCl, seawater, 1 M KCl) except ultrapure water desorbed cesium more than 90 % from the high cesium loading sample (2.5 hours atomization). In contrast, only 30 % cesium was desorbed from the low cesium loading sample (90 seconds atomization) by seawater. In the desorption experiment using cesium adsorbed particles from the solution, the cesium desorption percentage by seawater was 30 %, where the cesium loading on the suspended particles was about 1  $\mu\text{g}/\text{g}$  which was close to the loading amount of 90 seconds aerosol atomized sample (= 6.9  $\mu\text{g}/\text{g}$ ). The observed agreement of the desorption percentages from different way of cesium loading indicates that the desorption behavior is simply governed by the cesium loading amount on the particles rather than the way of loading.

### REFERENCE:

[1] K. Takamiya, T. Tanaka, S. Nitta, S. Itosu, S. Sekimoto, Y. Oki, T. Ohtsuki, Attachment Behavior of Fission Products to Solution Aerosol. *J Radiat Prot Res*, (2016) 41, 350–353.

## PR11 Project Research on a Study on Biological Character and Use of the Particle Induced by the Boron Neutron Capture Reaction

Y. Kinashi

*Research Reactor Institute, Kyoto University*

### Objectives and Participating Research Subjects

In this project, we are intending to develop the new application using the characteristics of the particles from the neutron capture reaction. Our project researchers were not able to carry out own experiments because KUR has been stopping during this year.

PRS-2 was not able to carry out its experiments because KUR has been stopping during this year.

PRS-3 was not able to carry out its experiments because KUR has been stopping during this year.

PRS-4 was not able to carry out its experiments because KUR has been stopping during this year.

PRS-1 Analysis of mutation in the mammalian cells induced by BNCR (boron neutron capture reaction)  
( Y. Kinashi *et al.* )

PRS-2 Analysis of double strand breaks in the mammalian cells induced by BNCR  
( S.Takahashi *et al.* )

PRS-3 Development of the PARP repressor reinforced in its function by BNCR  
( Y.Uto *et al.* )

PRS-4 Development of the model animal showing the blood vessel damage by BNCR  
( R. Wate *et al.* )

### Main Results and Contents

PRS-1 could not carry out the experiment of the mutation in the mammalian cells induced by BNCR because KUR (Kyoto University Research Reactor) has been stopping during this year.

Using the gamma-ray irradiation facility, biological effects of the combination of the gamma-ray irradiation and Temozolomide(TMZ) that is DNA alkylating agent on the T98G human glioblastoma cells were investigated. The result suggested that TMZ treatment has the sensitization effect of radiation in CHO cells with low MGMT(methylguanine methyltransferase) gene expression that is the DNA repair enzyme, whereas that T98G cells with MGMT gene expression were resistance to TMZ. The enhancement effect of the combination of radiation and TMZ treatment was not found in T98G cells.

Y. Kinashi, T. Ikawa and S. Takahashi

Research Reactor Institute, Kyoto University

**INTRODUCTION:** Most BNCT (boron neutron capture therapy) patients have already received chemotherapy. Especially many brain tumor patients are taking temozolomide(TMZ) treatment. TMZ is a DNA-alkylating agents and particularly effective cancer drug for glioblastoma. The purpose of this study is to investigate the biological effects of the combination of TMZ and ionizing radiation by the study of the cell lethal effects.

**MATERIALS & METHODS:** T98G human glioblastoma tumor cells and CHO (Chinese hamster ovary) cells are purchased from Riken BRC Cell Bank. T98G cells are resistance to TMZ because they have MGMT(methylguanine methyltransferase) gene expression that is the DNA repair enzyme. TMZ solution prepared by the medium, and removal washing with phosphate buffered saline after 23 hours incubation. In the experiment exposed with TMZ, T98G cells showed TMZ resistance about 4 times higher than CHO cells. The concentration of TMZ with  $\gamma$ -ray radiation was 100  $\mu\text{m}$  in CHO cells and 400  $\mu\text{m}$  in T98G cells, respectively. The gamma-rays irradiation for cells was carried out using Co-60 gamma-ray facility of KURRI. After gamma-ray irradiation, cells were seeded on a Petri dish and incubated for 14 days. The survival curve creates a Plating Efficiency of each treatment and control groups compared survival rate.

**RESULTS and DISCUSSION:** Figure 1 shows the survival data observed differences in sensitivity of the between two cells. D0 values are T98G 5.03 Gy, CHO: 5.21 Gy after gamma-ray irradiation. In the combination study of gamma-rays and TMZ, D0 value of T98G was 5.40 Gy. D0 value of CHO was 3.38 Gy. In CHO cells, D0 value was decreased 1.83 Gy. There was no apparent change in the D0 value of T98G cells by gamma-ray irradiation with TMZ treatment. D10 value also decreased 1.81 Gy after the gamma-ray and TMZ in CHO cells. These results show that TMZ treatment has the sensitization effect of radiation in

CHO cells.

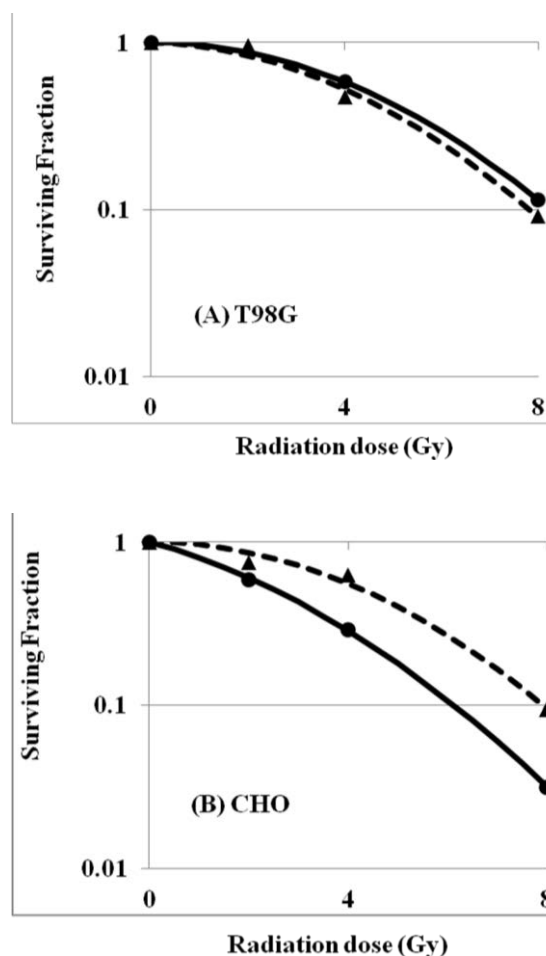


Fig. 1 Survival curves of gamma-ray irradiation with TMZ(—●—)compared without TMZ (- -▲- -) (A)T98G cell study, (B) CHO cell study

The CHO cells that alkylation repair activity is low and cells have high susceptibility to TMZ. TMZ concluded that further enhance the cell-killing effect of radiation. It is generally known that patients with glioblastoma with MGMT gene silencing have the benefit from TMZ and survival benefit for the chemoradiotherapy<sup>[1]</sup>. Further studies will be needed to analyze whether synergy effect of the combination of BNCT and TMZ in various brain tumors showing low TMZ expression to aim the clinical effect improvement of BNCT.

[1] M.E.Hegi *et al.*, N. Engl. J. Med., 352(2005)997-1003.

## PR12 Improvement of Characterization Techniques in High-Energy-Particle Irradiation Research

A. Kinomura

*Research Reactor Institute, Kyoto University*

**OBJECTIVES:** Irradiation facilities of high-energy particles for neutrons (Material Controlled irradiation Facility), ions (e.g., Heavy ion irradiation facility) and electrons (Low temperature irradiation facility, KUR-LINAC) have been extensively developed at the Research Reactor Institute. The developed facilities have been in operation and opened for joint research projects. One of the objectives of this project is to improve or optimize irradiation facilities for more accurate irradiation experiments.

As characterization techniques for irradiated materials, a slow positron-beam system and a focused ion beam system have been developed and introduced, respectively, in addition to previous characterization facilities such as an electron microscope, an electron-spin-resonance spectrometer, a bulk positron annihilation spectrometer and a thermal desorption spectrometer. Another objective is to introduce new techniques or reconsider analytical methods of previously used characterization techniques.

Based on these two objectives, we expect promotion of previous research and attraction of new users for the joint research program. The allotted research subject (ARS) and individual co-researchers are listed below.

ARS-1:

Study on efficient use of positron moderation materials (A. Kinomura *et al.*)

ARS-2:

Effects of electron-irradiation on Cu solubility and diffusivity in Fe studied by three dimensional atom probe (K. Nagumo *et al.*)

ARS-3:

Irradiation defects of F82H irradiated at SINQ using positron annihilation spectroscopy (K. Sato *et al.*)

ARS-4:

Study on irradiation effect and electrical and optical properties of compound semiconductors (K. Kuriyama *et al.*)

ARS-5:

Validation of D3×t0.5 TEM disk size miniature test specimens for post-irradiation thermal diffusivity measurement (M. Akiyoshi and A. Kinomura)

ARS-6:

Positron annihilation study on Fe-Cr binary alloy after electron irradiation (T. Onitsuka *et al.*)

ARS-7:

Positron annihilation study on free-spaces in DLC and heteroelement-containing DLC films (K. Kanda *et al.*)

ARS-8

Thermal stability of diamond-like carbon films (S. Nakao *et al.*)

**RESULTS:** In ARS-1, the performance of the bright-

ness enhancement system of the slow positron-beam system of Kyoto University research Reactor (KUR) was evaluated by using an electron beam instead of a positron beam with emphasis on focused beam sizes as function of extraction coil current.

In ARS-2, a sample holder for temperature-controlled electron irradiation by KURRI-LINAC has been developed to investigate radiation-enhanced diffusion processes of impurity atoms in Fe. The experiments indicated that the dissipation of beam heat is important to control irradiation temperatures.

In ARS-3, reduced activation ferritic martensitic (RAFM) steels irradiated by a spallation neutron source and an electron beam were compared to investigate the He effects on irradiation-induced defects. Positron annihilation coincidence Doppler broadening (CDB) measurements were performed to characterize the samples.

In ARS-4, GaN samples after gamma-ray irradiation to a total absorption dose of 160 kGy were characterized by Rutherford backscattering spectrometry using a 1.5 MeV proton beam to investigate the effect of gamma-rays during transmutation doping by neutron irradiation.

In ARS-5, TEM disk size miniature test specimens to investigate the influence of irradiation on thermal diffusivity was examined by 8 MeV electron beam irradiation using KURRI-LINAC. It is concluded that the use of miniature specimens is validated.

In ARS-6, simple binary Fe-40Cr alloy samples after 9 MeV electron irradiation by KURRI-LINAC were characterized by positron annihilation lifetime spectroscopy and positron annihilation coincidence Doppler broadening (CDB) measurement.

In ARS-7, positron annihilation lifetime measurements for DLC films by a slow positron beam were planned but no experiment was performed as KUR was not in operation.

In ARS-8, the relationship between thermal stability and the bonded hydrogen in several types of DLC films by thermal desorption spectroscopy (TDS). The results indicated that the structural changes may be driven by the creation and annihilation of defects caused by hydrogen desorption.

**CONCLUSION:** Developments and improvements on the slow positron-beam system and electron irradiation have been performed. Combinations of new materials and different irradiation/characterization techniques have been examined. These studies were performed in the line of the two objectives in this project. Further studies are expected in the following year.

A. Kinomura, N. Oshima<sup>1</sup> and A. Yabuuchi

Research Reactor Institute, Kyoto University  
<sup>1</sup>National Institute of Advanced Industrial Science and Technology (AIST)

**INTRODUCTION:** Positron annihilation spectroscopy is widely known as a method to probe vacancies, vacant spaces and free volume of atomic scales. It is considerably important to obtain intense and mono-energetic slow positron beams to perform positron annihilation spectroscopy of thin films or surface layers. Positron sources based on pair creation can generate more intense slow positron beam than radioisotope-based positron sources. Therefore, positron sources using pair-creation by gamma-rays from a nuclear reactor have been developed to obtain an intense slow positron beam at Kyoto University Research Reactor Institute. Sizes of reactor-based positron sources are generally wider than accelerator-based sources. In the case of the slow positron beam system at Kyoto University research Reactor (KUR), the size of the positron source is approximately 30 mm in diameter. As sample sizes of actual samples are often less than 10 mm, it is necessary to reduce beam sizes efficiently with keeping beam intensity as high as possible. For positron beams differently with electron beam, brightness enhancement methods are used for this purpose, where strong focusing and efficient positron re-moderation are essential. In this study, we concentrate on the brightness enhancement system in the KUR slow positron beam system.

**EXPERIMENTS:** Electron beams have been used as an alternative methods. Two types of electron sources were prepared for this study. They are a photoelectric source using ultraviolet light illumination and a thermal electron source using a filament. The photoelectron source is used for weak beam measurements comparable with positron sources. The thermal electron source is used for transport efficiency measurements with relatively intensive beams that can be detected by an ammeter. For both methods, phosphor screens with microchannel plates were used to monitor beam shapes.

Focusing performance of the brightness enhancement system was evaluated with the electron beams. Figure 1 shows the schematic view of the brightness enhancement system of the KUR slow positron beam system [1]. Positrons (electrons) are transported by guiding magnetic fields by solenoid and Helmholtz coils along the beamline. However, the beam has to be extracted from the guiding magnetic fields for focusing using magnetic lens as the guiding magnetic fields interfere with the focusing magnetic field. The termination of guiding magnetic fields is achieved by gradually reducing and/or inverting magnetic fields. In Fig. 1, large Helmholtz coils were used for transport magnetic fields and smaller Helmholtz coils (labelled as MA and MB) were used to adjust the termination fields.

**RESULTS:** To examine and optimize the beam extraction method from the guiding magnetic field to the focusing magnetic field, beam diameters were measured as a function of extraction coil (MA in Fig. 1) current in Fig. 2. The second extraction coil (MB) was not used in this case. The electron energy at the source was 10 eV and the acceleration energy at the acceleration gap ('accel. gap' in Fig. 1) was 5 keV. Beam trajectory calculations indicated that the beam divergence at the lens entrance increase with increasing lens current (not shown). The simulation also indicated that the focusing properties of the lens is non-linear and focusing is stronger with increasing radial distance from the beam axis. On the other hand, the influence of spherical aberration gets more significant with increasing radial distance. The variation of the beam diameter in Fig. 2 can be interpreted as a result of combination of the two effects. Thus, optimum extraction coil current must be carefully determined.

In summary, we have evaluated performance of the brightness enhancement system of the KUR slow positron beam system by using an electron beam instead of a positron beam. In particular, the beam extraction from the guiding magnetic field was examined as function of the extraction coil current.

**ACKNOWLEDGEMENT:** We would like to acknowledge the important contribution of Yoshihiro Kuzuya on this study.

**REFERENCE:**

[1] Y. Kuzuya *et al.* J. Phys. Conf. Series 791 (2017) 012012.

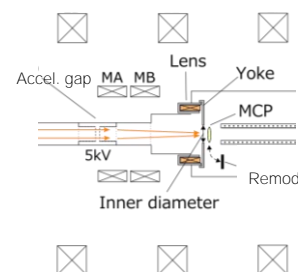


Fig. 1. Schematic view of the Helmholtz coils around the brightness enhancement system.

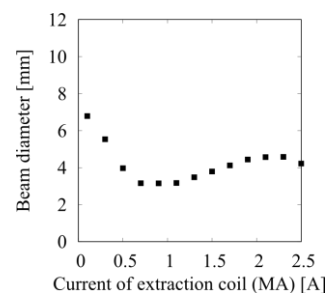


Fig. 2. Beam diameter as a function extraction-coil current at the re-moderator position.

## PR12-2 Effects of Electron-irradiation on Cu Solubility and Diffusivity in Fe Studied by Three Dimensional Atom Probe

K. Nagumo, Y. Nagai, K. Inoue, T. Toyama, Y. Shimizu, B. Han, M. Shimodaira, A. Kimomura<sup>1</sup>, T. Yoshiie<sup>1</sup>, Q. Xu<sup>1</sup>, A. Yabuuchi<sup>1</sup>

*Institute for Materials Research, Tohoku University*  
*<sup>1</sup>Research Reactor Institute, Kyoto University*

**INTRODUCTION:** Reactor pressure vessel (RPV) is one of the most important parts in nuclear power plant since RPV holds nuclear fuels, control rods and primary cooling water. Therefore, irradiation-induced embrittlement of RPV steels is vital issue for the safe operation of nuclear power plants. Substantial studies have revealed that nano-sized Cu precipitates are formed by neutron-irradiation and cause the embrittlement. In order to understand the kinetics of Cu precipitation, the diffusion coefficient and the solubility limit of Cu in Fe are the important basic quantities [1, 2].

It is predicted that diffusivity and solubility may be strongly affected by irradiation [3]; for example, diffusivity is greatly enhanced by irradiation because vacancies and interstitials, which are necessary for diffusion of solute atoms, are remarkably induced during irradiation. Such enhancement of diffusion has been modeled and simulated, however, experimental studies are very limited at present. In this study, we introduce Frenkel pair which can evaluate basic irradiation effect using KUR LINAC, and try to investigate the electron-irradiation effects on Cu diffusivity in Fe. In addition, the electron-irradiation effects on the solubility limit is investigated.

**EXPERIMENTS:** Pure Fe (99.999%) was used as a base material for the sample. It was cut into a plate shape of about 5 mm × 5 mm × 1 mm and the surface of the sample was mechanically polished with abrasive papers of #2000. After removal of the machined layer by chemical polishing, the sample was evacuated to 10<sup>-5</sup> Pa or less. Further, Ar gas sputtering was performed in the vacuum chamber to clean the sample surface. Pure Cu (99.999%) was used as the deposition source after chemical polishing with 5% nitric acid to remove the oxide layer on the surface. In the vacuum chamber, electron-beam heating was employed for dissolution of Cu. The deposition thickness of Cu on Fe was ~3 μm, which was sufficient for the diffusion distance (several 100 nm) expected in this experiment.

Electron-irradiation was performed with electron beam with energy of 5 MeV at LINAC. The irradiation temperature and the irradiation time were about 700 K and 30000 seconds, respectively.

After electron-irradiation, needle-like samples containing a copper-iron interface for three-dimensional atom probe (3D-AP) were fabricated with focused-ion beam apparatus. In 3D-AP measurement, a laser pulse mode was employed to reduce the frequency of sample fracture, at temperature of 55 K, a laser energy of 100 pJ, and a repetition frequency of 200 kHz.

**RESULTS:** Figure 1 shows atom maps of Cu, Fe and O in the electron-irradiated Cu-Fe diffusion pair. The interface of Cu-Fe was successfully detected. Cu atoms were hardly observed in Fe matrix region, and its concentration was less than 0.04 in atomic percent. 3D-AP measurements were performed by using several needle-like samples, and the similar results to fig. 1 were obtained. It is noted that O, a typical impurity of this system, was not segregated at the Cu-Fe interface nor penetrated into Fe matrix, showing no impact of such impurities on Cu mobility.

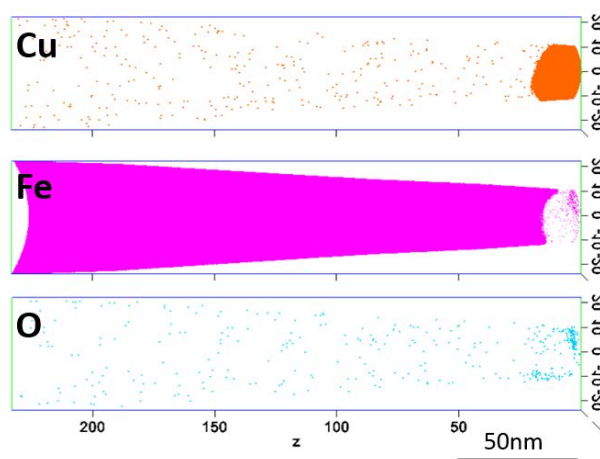


**Fig. 1: Atom map obtained by 3D-AP analysis for Cu and Fe in Cu-Fe diffusion pair electron irradiated at LINAC in KUR at 700 K for 30000 seconds.**

The obtained 3D-AP results show that the solubility limit of Cu in Fe hardly changes even under electron-irradiation. On the other words, it was found that forced solid solution due to excessive atomic vacancies did not occur.

In order to clarify the irradiation effect against diffusion, we plan to evaluate the diffusion coefficient of Cu via the kinetics of Cu precipitation by conducting similar irradiation experiments on Fe-Cu dilute alloy, such as water-quenched Fe-1.0wt. %Cu alloy.

### REFERENCES:

- [1] T. Toyama *et al.*, *Scrip. Mater.*, **83** (2014) 5-8.
- [2] M. Shimodaira *et al.*, *Mater. Trans.*, **9** (2015) 1513-1516.
- [3] R. Sizmann, *J. Nucl. Mater.*, **69&70** (1968) 386-412.

K. Sato, K. Ikemura<sup>1</sup>, V. Krsjak<sup>2</sup>, C. Vieh<sup>2</sup>, R. Brun<sup>2</sup>, Q. Xu<sup>1</sup>, T. Yoshiie<sup>1</sup> and Y. Dai<sup>2</sup>

*Graduate School of Science and Engineering, Kagoshima University*

<sup>1</sup> *Research Reactor Institute, Kyoto University*

<sup>2</sup> *Spallation Neutron Source Division, Paul Scherrer Institut*

**INTRODUCTION:** The reduced activation ferritic/martensitic (RAFM) steels are candidates for the first wall and blanket of fusion reactors [1]. Because of its good irradiation resistance, the study of irradiation effects of the RAFM steels is also important for the structural materials of spallation neutron source including accelerator driven system [2]. One of features of spallation neutron source is high production rate of gas atoms [3], which leads to the formation of a large amount of He bubbles. He bubbles have great influence on mechanical properties of structural materials [4,5], and clarifying the growth mechanism of He bubbles is significant for the development of nuclear materials. In the present study, the defect structures in F82H irradiated with protons and neutrons by SINQ (the Swiss Spallation Neutron Source) were studied using positron annihilation spectroscopy, and the growth process of He filled vacancy clusters by the isochronal annealing test was discussed.

**EXPERIMENTS:** The F82H was irradiated in the second STIP (STIP-II, the SINQ target irradiation program). The irradiation dose, average irradiation temperature, and calculated production of H and He were 7.2 dpa, 385 K, 531.5 appm and 2105 appm, respectively. For comparison, 8 MeV electron irradiation was also performed for 5.5 h (short term,  $7.23 \times 10^{21} \text{ e}^-/\text{m}^2$ ,  $1.3 \times 10^{-4}$  dpa) and for 70 h (long term,  $9.29 \times 10^{22} \text{ e}^-/\text{m}^2$ ,  $1.7 \times 10^{-3}$  dpa). A three-detector system using a fast digital oscilloscope [6] was adopted for the positron annihilation lifetime (PAL) measurements, thereby reducing the background counts and making it possible to measure highly radioactive samples. The time resolution of the system was 150 ps (full width at half maximum). Each spectrum was accumulated to a total of  $1.4 \times 10^6$  counts. The spectra were analyzed using the PALSfit program [7]. Positron annihilation coincidence Doppler broadening (CDB) measurements were also performed. In order to obtain CDB spectra, two Ge-detectors were placed at  $180^\circ$  with respect to one another with a spacing of about 400 mm therebetween. The overall energy resolution of the two Ge-detectors was 1.4 keV at FWHM for 511 keV

$\gamma$ -rays. CDB spectra were accumulated to a total of more than  $1.0 \times 10^7$  counts. Sabelova et al. reported that He effect range of CDB spectra is  $5\text{--}12 \times 10^{-3} mc$  [8]. Therefore, the parameters  $S$  and  $W$  are defined as the ratio of the low-momentum ( $|P_L| < 2.5 \times 10^{-3} mc$ ) and high-momentum ( $7 \times 10^{-3} mc < |P_L| < 12 \times 10^{-3} mc$ ) areas in the Doppler-broadening spectrum to the total area, respectively. Here,  $m$  is the electron rest mass and  $c$  is the velocity of light.

**RESULTS:** Variation in  $S$ -parameter is almost the same as that in mean positron lifetime. This correspondence between  $S$ -parameter and mean lifetime was also obtained in the previous study [9]. The long lifetime decreases as the annealing temperature is increased up to 573 K, and the spectrum does not decompose into two components after annealing at 673 K. The lifetime decrease is due to the absorption of He atoms weakly trapped in the matrix. The increase of the mean lifetime above 873 K results from the growth of He bubbles by absorption of vacancies and the release of H atoms. The vacancy (V)-He<sub>n</sub> complexes dissociate at 773 K and the release of H atoms from proton and spallation neutron-irradiated F82H peaks between 573 and 673 K. We cannot see the conspicuous peak caused by the He atoms in the momentum range of  $5\text{--}12 \times 10^{-3} mc$  in CDB ratio curves. In order to get the He effect on the CDB spectra,  $S$ - $W$  plots were drawn. Maximum error of  $S$  and  $W$  parameters is  $2.5 \times 10^{-4}$  and  $1.2 \times 10^{-4}$ , respectively. In the electron irradiation, only defects are introduced and gas atoms are not formed. Positron trapping rate into He bubbles is smaller than that into empty voids. So, if CDB spectra are influenced by the He atoms of He filled vacancy clusters, the change in  $S$ - and  $W$ -parameter should be different from that of electron-irradiated samples. The slope is slightly different between solid and broken line, and this difference means the effect of He atoms.

### REFERENCES:

- [1] M. Tamura *et al.*, J. Nucl. Mater. 141 (1986) 1067.
- [2] Y. Dai and G.S. Bauer, J. Nucl. Mater. 296 (2001) 43.
- [3] Y. Dai *et al.*, J. Nucl. Mater. 343 (2005) 33.
- [4] Z. Tong and Y. Dai, J. Nucl. Mater. 385 (2009) 258.
- [5] Z. Tong and Y. Dai, J. Nucl. Mater. 398 (2010) 43.
- [6] H. Saito *et al.*, Nucl. Instr. Meth. Phys. Res. A 487 (2002) 612.
- [7] J.V. Olsen *et al.*, Phys. Status Solidi C 4 (2007) 4004.
- [8] V. Sabelova *et al.*, J. Nucl. Mater. 450 (2014) 54.
- [9] V. Krsjak *et al.*, J. Nucl. Mater. 456 (2015) 382.

K. Kuriyama, N. Nishikata, Y. Torita, K. Kushida<sup>1</sup>, A. Yabuuchi<sup>2</sup>, Q. Xu<sup>2</sup> and A. Kinomura<sup>2</sup>

*College of Engineering and Research Center of Ion Beam Technology, Hosei University*

<sup>1</sup>*Osaka Kyoiku University*

<sup>2</sup>*Research Reactor Institute, Kyoto University*

**INTRODUCTION:** Examining the defects caused by various radiations to GaN under the space environment is important. In our previous study [1, 2], we reported that the energy levels relating to nitrogen vacancy ( $V_N$ ) and gallium vacancy ( $V_{Ga}$ ) were induced by neutron and proton irradiated GaN. The neutron irradiation has been used as the neutron transmutation doping into semiconductors such as GaAs [3], GaP [4], and GaN [5]. Atoms in semiconductors mainly transmute by a  $(n, \gamma)$  reaction. Therefore, to survey the radiation effect of gamma ray alone is meaningful. In the present study, we report the lattice displacement in GaN bulk single crystals by gamma-ray irradiation.

**EXPERIMENTS:** GaN bulk single crystals with a thickness of  $450 \pm 50 \mu\text{m}$  were purchased from Furukawa Co. Ltd. The crystals were irradiated at room temperature with gamma-rays of 1.17 and 1.33 MeV from a cobalt-60 source of Kyoto University Research Reactor Institute. Samples were irradiated with an absorption dose rate of 1.771 KGy/h. Total gamma-ray dose was 160 kGy. The resistivity varied from  $30 \Omega\text{cm}$  for an un-irradiated sample to  $10^4 \Omega\text{cm}$  for gamma-ray irradiated one. Rutherford backscattering spectroscopy analysis (RBS) was carried out using 1.5-MeV  $\text{H}^+$  ions from the van de Graaff accelerator of Hosei University.

**RESULTS:** Fig. 1 shows typical random and aligned RBS spectra of as-irradiated and un-irradiated GaN bulk single crystal. The aligned spectra were obtained from scattering along the  $\langle 0001 \rangle$  channeling directions. The minimum yield  $\chi_{\text{min}}$  (the ratio between aligned and random) of Ga and N was evaluated using a width of about 20 channels (120 nm) behind the surface peak. The values of  $\chi_{\text{min}}$  for Ga were 1.5 % for un-irradiated and 2.3 % for gamma-ray irradiated samples. On the other hand, the values of  $\chi_{\text{min}}$  for N were 7.7 % for un-irradiated and 9.5 % for gamma-ray irradiated samples. The number of displaced Ga and N atoms estimated using  $\chi_{\text{min}}$  values were  $3.5 \times 10^{20} \text{cm}^{-3}$  and  $8.7 \times 10^{20} \text{cm}^{-3}$ , respectively. Although the disorder is recognized in Ga and N lattices, the displacement concentration of N atoms is about two times larger than that of Ga atoms. This suggests that N interstitial ( $\text{N}_i$ ) exists in gamma-ray irradiated GaN bulk

single crystal. This result is similar to that of the neutron irradiated GaN [6]. Since  $\text{N}_i$  atoms form the deep acceptor level at 960 meV below the bottom of the conduction band [6], the origin of the high resistivity after the gamma-ray irradiation is attributed to the carrier compensation effect due to the deep level of  $\text{N}_i$ .

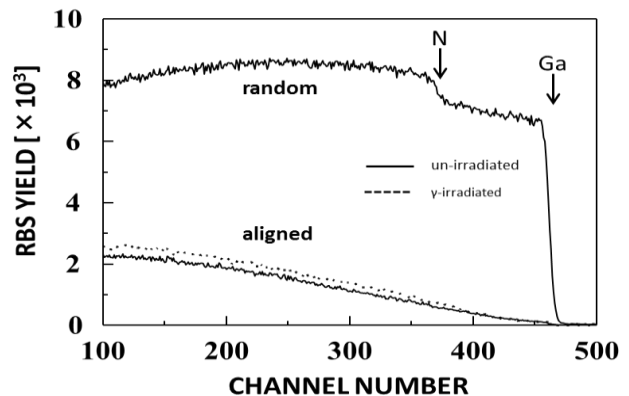


Fig. 1 Random and aligned RBS spectra of un-irradiated and gamma-ray irradiated GaN.

This study has been accepted as Proceedings (Journal of Physics, IOP (UK) ) of International Conference on the Physics of Semiconductors 2016, Beijing.

#### REFERENCES:

- [1] K. Kuriyama, M. Ooi, A. Onoue, K. Kushida, and Q. Xu, *Appl. Phys. Lett.* 88, 132109 (2006).
- [2] T. Nakamura, N. Nishikata, K. Kamioka, K. Kuriyama, and K. Kushida, *Nucl. Instrum. Method Phys. Res. B* 371, 251 (2016).
- [3] M. Satoh, K. Kuriyama, and T. Kawakubo, *J. Appl. Phys.* 67, 3542 (1990).
- [4] K. Kuriyama, Y. Miyamoto, T. Koyama, O. Ogawa, and M. Okada, *J. Appl. Phys.* 86, 2352 (1999).
- [5] K. Kuriyama, T. Tokumasu, J. Takahashi, H. Kondo, and M. Okada, *Appl. Phys. Lett.* 80, 3328 (2002).
- [6] T. Nakamura, K. Kamioka, K. Kuriyama, K. Kushida, Q. Xu, and M. Hasegawa, *Solid State Commun.* 205, 1 (2015).

## Validation of D3 × t0.5 TEM Disk Size Miniature Test Specimens for Post-irradiation Thermal Diffusivity Measurement

M. Akiyoshi and A. Kinomura<sup>1</sup>

Radiation Research Center, Osaka Prefecture University

<sup>1</sup>Research Reactor Institute, Kyoto University

### INTRODUCTION:

Radioactivity levels for conventional thermal diffusivity test specimens are often prohibitively high for handling and measurement outside the hot cell facilities with candidate metallic materials, such as tungsten and reduced activation steels, of near-term technological interest for fusion energy. In addition to this radiological constraint, the steep temperature gradients with specimens due to the high volumetric heating and the extreme cost per volume associated with high flux neutron irradiation in fission reactors strongly incentivize the use of miniaturized test specimens in materials irradiation studies. Therefore, in the ongoing Japan-US PHENIX project, thermal diffusivity measurement is planned to be performed using miniature disc specimens with a diameter (D) of 3mm and a thickness (t) of 0.5mm, which is generally used as specimen disk for TEM. These small specimen dimensions allow a reduction of radioactivity by a factor of 44 as compared with a D10 × t2 standard specimen. This study validates this D3 × t0.5 miniature specimen type for post-neutron irradiation measurement of thermal diffusivity.

In addition, electron-beam irradiation using KURRI-LINAC is now most effective method to study irradiation effects in thermal diffusivity. It requires about one week to achieve 0.01dpa with accelerate energy of 30MeV and highest current (200  $\mu$  A), where the target volume is limited to D10 and thickness was about 2-3 cm. Furthermore, when we use low-energy beam (8MeV) to avoid the activation, it required longer days and thinner target (<1cm). Therefore, the small specimen mentioned above is also important for the electron-beam irradiation.

### EXPERIMENTS and RESULTS:

The thermal diffusivity measurements of D3 × t0.5 tungsten specimens were performed using a Netzsch LFA-457 from room temperature to 500°C. A specimen holder was designed to fit into a Netzsch standard holder (Fig. 1). Since the back-side of a D3 specimen radiates only a small amount of infrared to measure the temperature change after a laser flash, the extrapolation from the temperature dependency above 150°C is required to obtain a reliable thermal diffusivity at room temperature. Furthermore, there was still a systematic difference of 20% from a standard size specimen. In the LFA-457 system, the pulse width of laser flash,  $T_f = 0.33$ ms, is not fast enough compared with the diffusion time of heat in 0.5mm thickness. It is required that  $T_f$  is smaller than 1/10 of  $T_{1/2}$ , then the thickness of the specimen is re-

quired to be larger than 1.3mm for unirradiated tungsten.

Consequently, measurement of the miniature specimens was performed using new Netzsch LFA-467 where the minimum of  $T_f$  is only 20 $\mu$ s. Also the LFA-467 uses optics to condense the radiated infrared from a minimum of D3.2mm, therefore exact measurement was achieved for the miniature specimens at room temperature. However, it was turned out that the effect of surface carbon coating is not ignorable to avoid transmission of laser flash and enhance the radiation efficiency of infrared from the back-side. These coating layer is enough thin and the thermal diffusivity is enough high when using D10 × t2 standard specimen. On the other hand, the coating layer on the miniature specimen of which thickness is 0.5mm is not ignorable any more. Netzsch Japan developed Graphene-Nanoplatelets spray[1] that resolves this problem. They showed almost same thermal diffusivity between D3 × t0.5 miniature specimens and D10 × t2 standard specimens, even using  $\beta$ -SiC that shows thermal diffusivity of > 100mm<sup>2</sup>/s.

### CONCLUSION:

It is concluded that the miniature specimen for measurement of thermal diffusivity is validated and this result will be widely used in future materials irradiation studies.

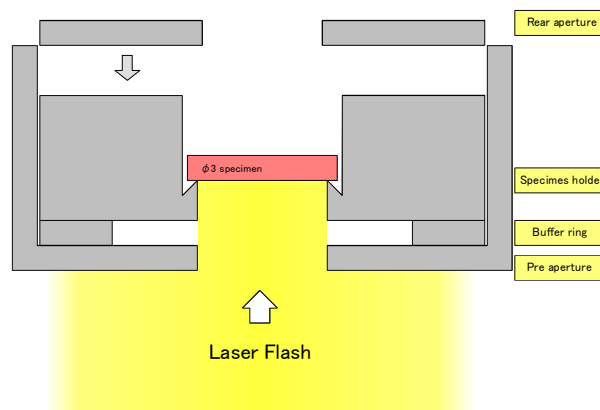


Fig. 1 A schematic image of the specimen holder for D3 small specimens.

### REFERENCE:

[1] Y. Ishibashi *et al.*, The 37th Japan Symposium on Thermophysical Properties, Nov.28-30, 2016, Okayama.

## PR12-6 Positron Annihilation Study on Fe-Cr binary alloy after Electron Irradiation

T. Onitsuka, K. Sato<sup>1</sup> and Q. Xu<sup>2</sup>, J. Kinomura<sup>2</sup> and K. Fukumoto

Research Institute of Nuclear Engineering, Fukui University

<sup>1</sup>Graduate School of Science and Engineering, Kagoshima University

<sup>2</sup>Research Reactor Institute, Kyoto University

**INTRODUCTION:** High-chromium (9-12%Cr) Ferritic/martensitic steels are attractive candidate material for various nuclear energy systems because of their excellent thermal properties, higher swelling resistance and lower activation compared with conventional austenitic stainless steels. The high-chromium steel as also been considered for both in-core and out-of-core applications of fast breeder reactors, and for the first wall and blanket structures of fusion systems, where irradiation induced degradation is expected to be the critical issues for reactor operation [1]. In this present study, the authors focused on a precipitation response for formation of  $\alpha'$ -phase in Fe-Cr binary model alloy subjected to electron irradiation, in order to examine fundamental aspects of radiation effects on  $\alpha'$ -phase precipitate development in iron-chromium alloys. The positron annihilation measurement technique was used to study the behaviour of micro-structural evolution due to irradiation-induced defects and the formation of  $\alpha'$ -phase simultaneously. Because the phase decomposition into Fe-rich ( $\alpha$ ) and Cr-rich ( $\alpha'$ ) phases will co-occur in Fe-Cr alloy, the formation of  $\alpha'$ -phase precipitates can be detected by positron annihilation coincidence Doppler broadening (CDB) technique owing to a lesser positron affinity for Cr than Fe.

**EXPERIMENTS:** Simple binary Fe-40Cr alloy was made by arc melting under argon atmosphere in a water-cooled copper hearth. All the ingots were melted and inverted three times in order to promote chemical homogeneities. The obtained ingot was conducted by solution heat treatment at 1077 °C for 2 h followed by water quenching, and then, machined to the dimensions of 10 mm × 10 mm × 0.5 mm. 9 MeV electrons irradiated at 100 °C in KURRI-LINAC. The irradiation dose and displacement damage range were  $3.0 \times 10^{17}$ - $2.0 \times 10^{18}$  e/cm<sup>2</sup> and 0.04-0.3 mdpa. After the irradiation, all specimens were mechanically polished and then electrolytically polished with methanol : sulfuric acid = 75 : 25 (Vol. %) at 20-30V to remove surface damage from previous steps. Then, positron annihilation lifetime measurement and CDB measurement were performed.

**RESULTS:** Fig. 1. shows the positron annihilation lifetime measurement results of electron irradiated Fe-40Cr alloy. The longer lifetime components ( $\tau_2$ ) around 150 psec corresponds to vacancy type defects. They are slightly smaller than the corresponding lifetimes at single vacancy in pure Fe. Fig. 2 shows the S-W plots obtained from positron CDB measurements for the Fe-40Cr alloy

before (WQ) and after (0.04-0.3 mdpa) the irradiation. In general, positron trapping in vacancies results in an increase (decrease) in the S- (W-) parameter, since the annihilation with the low-momentum valence electrons increased at the vacancies. A high concentration of defects, or an increase in the mean size of defects leads to a larger contribution of annihilations from low momentum electrons because positrons are trapped at defects. This is reflected in CDB measurements by an increase in the S-parameter and a decrease in the W-parameter as irradiation dose is increased. However a rapid and significant decrease of the S-parameter comparable with a rapid and significant increase of the W-parameter respectively observed between 0.1 mdpa and 0.2 mdpa. This behaviour of the S- and the W- parameters suggests that an abrupt change in the very earliest stage of microstructural evolution was detected by positron CDB measurement technique.

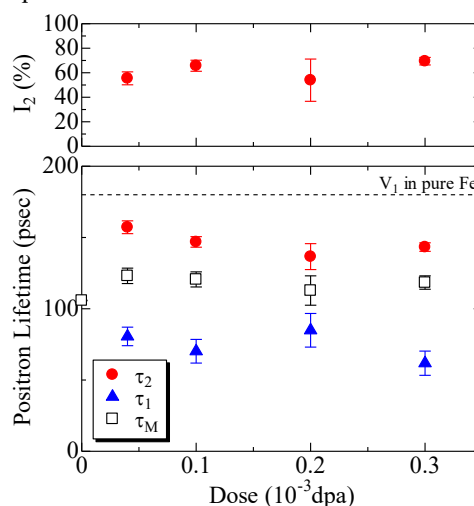


Fig. 1. Changes of the positron lifetime results with dose of electron irradiation of Fe-40Cr alloy

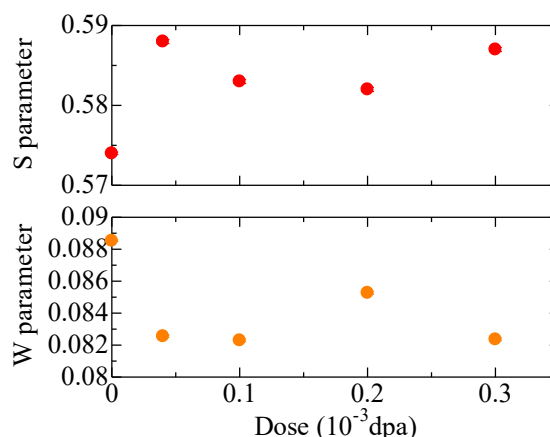


Fig. 2. Changes of the S and the W parameters with dose of electron irradiation of Fe-40Cr alloy

### REFERENCE:

- [1] K. Okano *et al.*, Nucl. Instr. and Meth., **186** (1981) 115-120.

S. Nakao, X. Qu<sup>1</sup>, A. Yabuuchi<sup>1</sup> and A. Kinomura<sup>1</sup>

Structure Materials Research Institute, National Institute of Advanced Industrial Science and Technology  
<sup>1</sup>Research Reactor Institute, Kyoto University

**INTRODUCTION:** Diamond-like carbon (DLC) films have attracted much attention because of their excellent mechanical properties, such as high hardness, high wear resistance and low friction coefficients. However, the thermal stability is relatively low. It is reported that the properties of some films start to be degraded over 200 °C [1]. Therefore, it is important to improve the thermal stability of the films for industrial applications. It is considered that the changes of the microstructure at high temperature should be responsible for the degradation of the properties. The structural changes are related to H desorption and behavior of defects at high temperature. Many studies have been carried out on the thermal stability of DLC films for the purpose of practical use. However, the principal phenomena, such as defect behavior, are not always clear. In addition, many types of DLC or carbon films are presented depending on preparation conditions and methods. Recently, DLC or carbon films are categorized from type I to VI, which includes graphite-like carbon (GLC) and polymer-like carbon (PLC). Therefore, to make clear thermal stability of DLC or carbon films, the examination of every type of DLC films (type I to VI) are necessary. The aim of this study is to clarify the relationship between thermal stability and the behavior of defects and bonded hydrogen in several types of DLC films by positron annihilation and thermal desorption (TDS) method.

**EXPERIMENTS:** In the first attempt, two types of DLC films (type I and IV) are examined by TDS measurements. DLC films of type I, tetrahedral amorphous carbon (ta-C), are prepared by arc ion plating (AIP) method at Nippon ITF Inc. On the other hand, DLC films of type IV, hydrogenated amorphous carbon (a-C:H), are prepared by bipolar-type plasma based ion implantation (PBII) at AIST-Chubu. The details on PBII system are reported elsewhere [2]. Both films are about 0.5 $\mu$ m in thickness. Si wafer is used as substrate. The TDS spectra of Si substrate are also measured for comparison. The samples are thermally annealed from room temperature to approximately 600 °C. H, H<sub>2</sub>, D and DH are detected.

**RESULTS:** Figure 1 shows the results of H (upper) and H<sub>2</sub> (lower) desorption spectra at elevated temperature. For the sample of AIP (sample A), no significant increase of H and H<sub>2</sub> intensity is observed in the range of 600 °C. The sample A is similar in spectrum of Si substrate (Ref). This shows that the sample A includes quite less hydrogen. On the other hand, a clear peak around 400 °C ap-

pears in each H and H<sub>2</sub> desorption spectra for the sample of PBII (sample B). This result clearly shows that hydrogen is released from DLC films over 400 °C for the sample B. It is suggested that thermal stability of sample B is less than that of sample A. In fact, Raman analysis reveals that the structural changes are occurred for the sample B but not for the sample A in the case of 500 °C annealing in vacuum. There is possibility that the structural changes of sample B may be driven by the creation and annihilation of vacancy and defects caused by hydrogen desorption. Positron annihilation measurements will be planned next time.

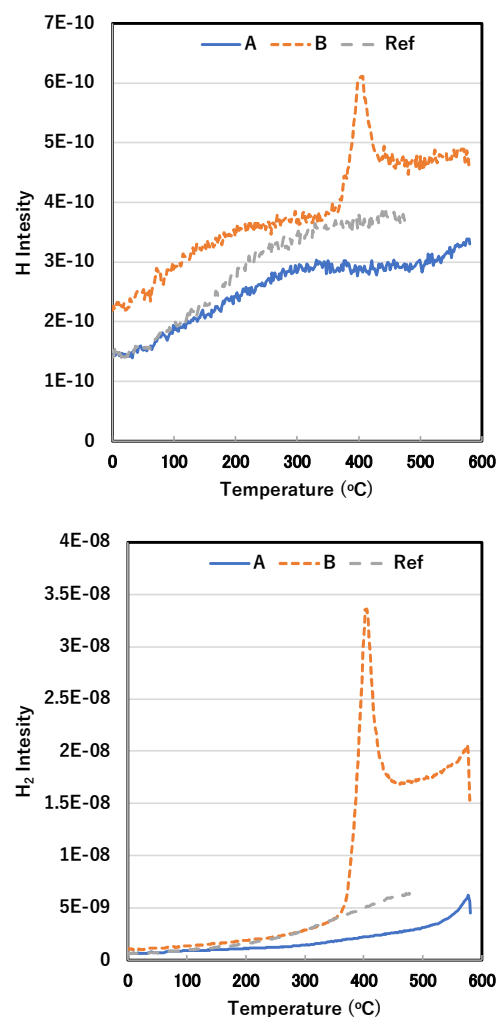


Fig.1 TDS spectra of H and H<sub>2</sub> of DLC films (samples A and B) deposited on Si substrates as a function of annealing temperature. The spectrum of Si substrate is indicated as Ref for comparison.

#### REFERENCES:

- [1] J. Robertson, *Mater. Sci. Eng.*, **R7** (2002) 129-281.
- [2] S. Miyagawa *et al.*, *Surf. Coat. Technol.*, **156** (2002) 322-327.

Y. Saito

*Research Reactor Institute, Kyoto University*

### 1. Objectives and Allotted Research Subjects

Neutron imaging provides valuable information which cannot be obtained from an optical or X-ray imaging. The purpose of this project is to develop the imaging method itself and also the experimental environment for expanding the application area of the neutron imaging. The allotted research subjects are as follows:

- ARS-1 Measurements of Multiphase Dynamics by Neutron Radiography (Y. Saito *et al.*)
- ARS-2 Visualization and Measurement of Flow Behavior in Industrial Equipment (N. Takenaka *et al.*)
- ARS-3 Visualization and Measurement of Adsorption/Desorption Process of Ethanol in Activated Carbon Adsorber for Adsorption Heat Pump (N. Asano *et al.*)
- ARS-4 Neutron Radiography on Tubular Flow Reactor for Supercritical Hydrothermal Synthesis of Nanoparticles (T. Tsukada *et al.*)
- ARS-5 Characteristics of the Void Fraction under Transient Condition (H. Umekawa *et al.*)
- ARS-6 Estimation of the Frosting and Defrosting Phenomena by Using Neutron Radiography (R. Matsumoto *et al.*)
- ARS-7 Neutron imaging and optics development using simulation of VCAD Systems (Y. Yamagata *et al.*)
- ARS-8 Water and Salt Distribution in a Rice Hull Medium under Sodium Chloride Solution Culture (U. Matsushima *et al.*)
- ARS-9 Measurement of Water Content in Hardened Cement Paste by Neutron Imaging (T. Numao *et al.*)
- ARS-10 In-situ Neutron Radiography Investigation on the Hydraulic Behavior of High Strength Cement Paste under High Temperature (M. Kanematsu *et al.*)
- ARS-11 Evaluation of coolant distribution in a flat heat-pipe type heat spreader (K. Mizuta *et al.*)
- ARS-12 Visualization of Organic Materials for Development of Industrial Applications (A. Uritani *et al.*)
- ARS-13 Visualization of Coolant Flow in a Micro-Structured Wick (Y. Tsuji *et al.*)

### 2. Main results and the contents of this report

Due to the termination of KUR, no neutron imaging has been performed for fiscal 2016. However, some results have been obtained by analyzing existing experi-

mental results or by performing X-ray imaging as follows:

ARS-2 applied X-ray imaging to two-phase flow across horizontal tube bundles of in-line and staggered. X-ray radiography was employed for the measurement of void fraction distributions. The transmitted X-ray was converted to visible rays using an image intensifier, and the 10-bit gray-scale radiographs were taken using a high-speed camera (MotionPro Y-4 Lite, IDT Inc.) with an array of  $1024 \times 1024$  pixels and with a pixel size of  $170 \mu\text{m}$ . The frame rate was set at 30 fps and 450 radiographs which correspond to 15 s were taken in each condition. The X-ray was generated at 80 kV and 5 mA. From X-ray visualization, two-dimensional void fraction profiles were obtained varying gas- and liquid-superficial velocities. Heat transfer characteristics in two-phase flow across horizontal tubes are clarified also from heat transfer experiments. For bubbly flow condition, heat transfer coefficient between  $\pm 90$  to  $\pm 180^\circ$  was higher than that in single-phase flow. Void fraction around upstream of the tube was higher than that in the others. Liquid flow agitation by bubbles motion improved the heat transfer around the tube. Under intermittent flow condition, heat transfer coefficient flatten over the tube in comparison to that in single-phase flow. Since the void fraction around the tube was almost uniformly distributed, enhancement of the heat transfer could be obtained by bubbles motion over the entire perimeter of the tube under the condition.

ARS-6 applied X-ray radiography to frosting behavior in cooling heat exchange system. Frost layer was clearly visualized by the X-ray imaging system in the B-4 port of KUR. The X-ray generator was operated at 80kV and 5mA similar to ARS-2. To estimate the frost profile quantitatively, the mass attenuation coefficient of the water and the ice were measured. Experimental results indicate that the mass attenuation coefficient of the ice shows higher value than that of the water. Finally Abel inversion was applied to the X-ray image to reconstruct the frost density profiles under the circularly symmetric frost formation around the cylindrical surface. In addition, 3-dimensional measurement of the frost deposition was tried by using the newly developed X-ray CT system. On the present step of this research, the 3-D frost density distribution is not success due to the less attenuation by the frost layer on the X-ray CT. In the next stage, the X-ray imaging conditions are modified.

## PR13-1 Void Fraction and Heat Transfer Characteristics in Two-Phase Flow across a Horizontal Tube Bundle

H. Murakawa, M. Baba, T. Miyazaki, K. Sugimoto,  
H. Asano, N. Takenaka, D. Ito<sup>1</sup> and Y. Saito<sup>1</sup>

*Department of Mechanical Engineering, Kobe University*  
*<sup>1</sup>Research Reactor Institute, Kyoto University*

**INTRODUCTION:** Heat exchangers such like shell and tube type are commonly used in process industry, chemical industry, and geothermal power plant. To clarify the two-phase flow structures, many experimental studies have been carried out in a rectangular channel with the tube bundle [1-3]. However, many of these investigation evaluate local void fraction at several measurement positions in the tube bundles, and the measurement of the two-dimensional void fraction distributions in the bundles has not been sufficiently carried out.

In this study, two-dimensional void fractions around a tube were obtained by using X-ray radiography. Local heat transfer coefficients were measured by using an electrode made of platinum wire placed on a tube, and the interaction between the void fraction and heat transfer coefficient distributions were investigated.

**EXPERIMENTS:** The test section was a vertical duct with a cross-section of  $90 \times 90 \text{ mm}^2$ . Air was injected into the test section through two porous tubes located at the bottom of the test section. Tube arraignment was an in-line tube bundle with 8 rows of three full tubes and two half tubes. The tubes were 90 mm long and the outer diameter,  $d$ , was 15 mm. The tubes pitch,  $p$ , was 22.5 mm and the pitch-to-diameter ratio,  $p/d$ , was 1.5. The experiments were performed at 20–25 °C under atmospheric pressure condition.

X-ray radiography was employed for the measurement of void fraction distributions. The transmitted X-ray was converted to visible rays using an image intensifier, and the 10-bit gray-scale radiographs were taken using a high-speed camera (MotionPro Y-4 Lite, IDT Inc.) with an array of  $1024 \times 1024$  pixels and with a pixel size of  $170 \mu\text{m}$ . The flame rate was set at 30 fps and 450 radiographs which correspond to 15 sec were taken in each condition. The X-ray was generated at 80 kV and 5 mA.

**RESULTS:** Results of two-dimensional void fraction distributions are shown in Fig. 1. The superficial liquid velocity,  $J_L$ , is 0.2 m/s, and the superficial gas velocity,  $J_G$ , is 0.12 and 0.77 m/s. The flow regimes are bubbly and intermittent flows, respectively. The measurement area is around center tube at the 4th row from the inlet of the bundles. Figure 2 shows the heat transfer coefficients around the tube.  $0^\circ$  indicates at the bottom of the tube, and the counterclockwise rotation is defined as positive degree.

Heat transfer coefficient under liquid single-phase flow increases from  $0^\circ$  and takes the maximum values near  $\pm 90^\circ$ , thereafter takes the minimum values around  $\pm 135^\circ$ .

For bubbly flow condition, heat transfer coefficient between  $\pm 90^\circ$  to  $\pm 180^\circ$  was higher than that in single-phase flow. Void fraction around upstream of the tube was higher than that in the others. Liquid flow agitation by bubbles motion improved the heat transfer around the tube. Under intermittent flow condition, heat transfer coefficient flatten over the tube in comparison to that in single-phase flow. Since the void fraction around the tube was almost uniformly distributed, enhancement of the heat transfer could be obtained by bubbles motion over the entire perimeter of the tube under the condition.

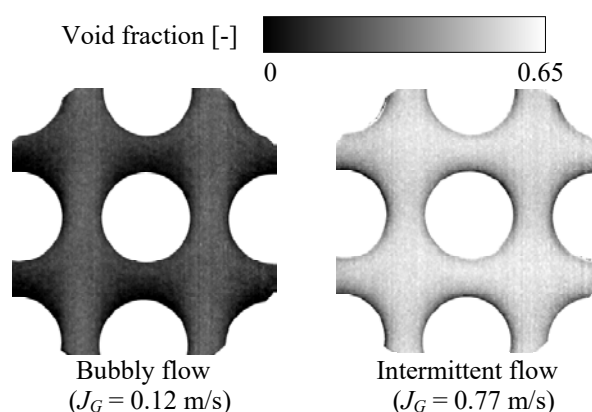


Fig. 1. Time-average two-dimensional void-fraction distributions in in-line tube bundle.

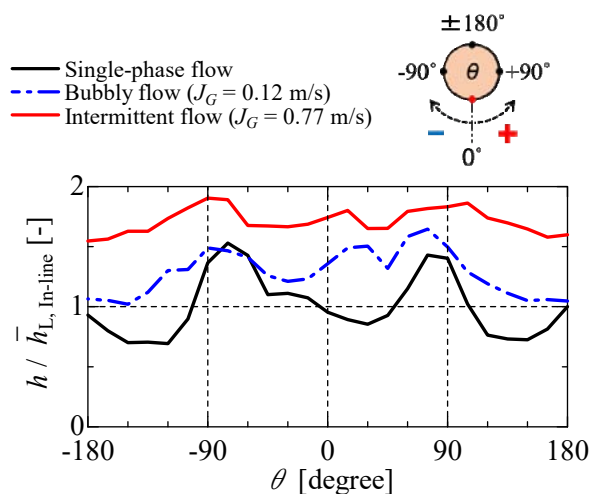


Fig. 2 Heat transfer coefficient around a tube in each flow.

### REFERENCES:

- [1] R. Dowlati *et al.*, *AIChE Journal*, **36** (1990) 765-772.
- [2] D.A. McNeil *et al.*, *Int. J. Multiphase Flow*, **45** (2012) 53-69.
- [3] G.R. Noghrehkarm *et al.*, *Int. J. Multiphase Flow*, **25** (1999) 857-874.

R. Matsumoto, K. Kagebayashi<sup>1</sup>, T. Uechi<sup>1</sup>, Y. Nagasawa<sup>1</sup>, D. Ito<sup>2</sup> and Y. Saito<sup>2</sup>

Faculty of Engineering Science, Kansai University  
<sup>1</sup>Graduate School of Science and Engineering, Kansai University  
<sup>2</sup>Research Reactor Institute, Kyoto University

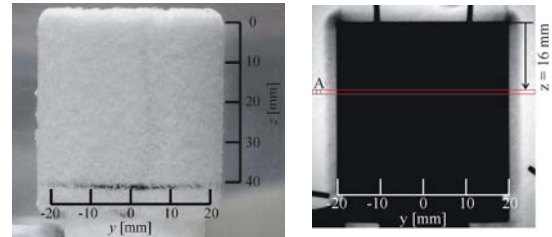
**INTRODUCTION:** Heat exchangers which are operated at below 0 °C are subjected to the frost deposition and its growth. Frost is the porous material of the crystal ice and air. The low thermal conductivity of the frost causes the low heat transfer performance. The frost density profile of the frost layer is the important property for the frost formation estimation. The frost density profiles were measured by the X-ray radiography on the cylindrical cooling surface. The three dimensional distribution of the frost deposition on the plate-fin tube heat exchanger was tried to estimate by the X-ray computed tomography at KUR B-4 radiation port.

**MEASUREMENT OF FROST DENSITY PROFILE BY X-RAY RADIOGRAPHY:** The photograph of the frost formation at 180 min of the frosting time on the cylindrical cooling surface at -14.0 deg.C. is shown in Fig.1(a). The frost layer was clearly shown by the X-ray beam attenuation in the radiography image, Fig.1(b). The X-ray generator was operated at 80kV and 5mA.

To estimate the frost density profile quantitatively, the mass attenuation coefficients of the water and the ice were measured by the calibration test. The gradient of Fig.2 corresponds to the mass attenuation coefficient. Experimental results of the water was close agreement with the reference value. The mass attenuation coefficient of the ice shows higher value than that of the water. The mass attenuation coefficient for the frost density estimation was used that of the ice.

Abel inversion was applied to the X-ray image to reconstruct the frost density profiles under the circularly symmetric frost formation condition around the cylindrical surface [1]. The frost density profile is shown in Fig. 3 at the 16 mm from the reading edge of the cylindrical cooling surface. The experimental result is almost the same density profiles with the previous researches [1], [2]. High frost density is appeared near the cooling surface. Frost density increased with the frosting time. At 180 min after frosting, the density profile shows a relative maximum at a distance about 3 mm from the cooling surface.

**3-D FROST DENSITY PROFILE ON THE HEAT EXCHANGER ESTIMATED BY X-RAY COMPUTED TOMOGRAPHY:** The three dimensional distribution of the frost deposition on the plate-fin tube heat exchanger was tried to estimate by the X-ray CT. Fig.4 shows a schematic of the experimental setup with rotating stage. On the present step of this research, the 3-D frost density distribution is not success due to the less attenuation by the frost layer on the X-ray CT. In the next stage, the X-ray imaging conditions are modified.



(a) Digital camera image (b) X-ray radiography image  
 Fig.1 Frost layer on the cylindrical cooling surface at 180 min of frosting time.

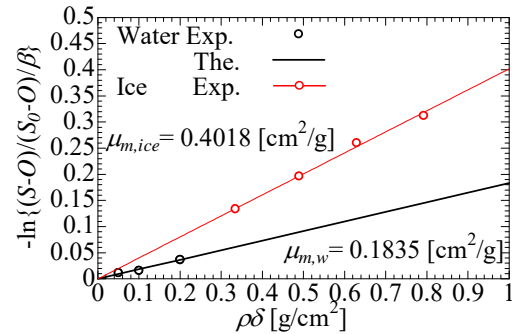


Fig.2 Mass attenuation coefficient of water and ice.

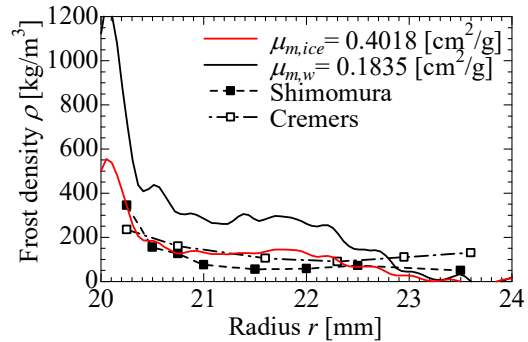


Fig. 3 Distributions of frost density profiles.

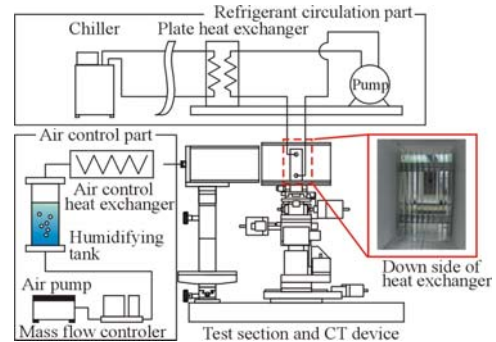


Fig. 4 Experimental setup for estimation the 3-D frost density distributions.

**REFERENCES:**

[1] C. J. Cremers, et al., Advances in Cryogenic Eng., **23** (1978), 371-375.  
 [2] N. Shimomura, et al., Trans. of the JSRAE, **19**(3) (2002), 245-254.

## **I-2. COLLABORATION RESEARCHES**

- 1. Slow Neutron Physics and Neutron Scattering**
- 2. Nuclear Physics and Nuclear Data**
- 4. Material Science and Radiation Effects**
- 5. Geochemistry and Environmental Science**
- 6. Life Science and Medical Science**
- 7. Neutron Capture Therapy**
- 8. Neutron Radiography and Radiation Application**
- 9. TRU and Nuclear Chemistry**
- 10. Health Physics and Waste Management**
- 12. Others**

K. Mori, H. Yoshino, R. Okumura, S. Sato<sup>1</sup>, H. Hiraka<sup>2</sup>,  
K. Iwase<sup>3</sup>, T. Shiono<sup>4</sup> and K. Matsuda<sup>4</sup>

*Research Reactor Institute, Kyoto University (KURRI)*

<sup>1</sup>*High Energy Accelerator Research Organization (KEK)*

<sup>2</sup>*Neutron Science Center, Korea Atomic Energy Research Institute*

<sup>3</sup>*Department of Materials and Engineering, Ibaraki University*

<sup>4</sup>*Graduate School of Engineering, Kyoto University*

**INTRODUCTION:** Neutron diffraction is a powerful tool to determine precisely the positions of light elements (e.g., hydrogen and lithium) in solids. This is the main reason why neutron powder diffractometers are critical for structural investigations of energy storage materials, for example, rechargeable lithium-ion batteries and hydrogen absorbing alloys. The B-3 beam port of Kyoto University Research Reactor (KUR) had long been used as a four-circle single-crystal neutron diffractometer (4CND). For the last decade, however, the 4CND was so old that its research activity on neutron science was quite low. Recently, the compact multipurpose neutron diffractometer (CMND) has been installed instead of the 4CND. Here, we report the current status of the B-3 beam port of KUR.

**SPECIFICATIONS:** The CMND has a wide space around the sample, therefore we can easily install any other system. The neutron wavelength,  $\lambda$ , which is monochromatized by the (220) plane of a Cu single crystal (i.e., Cu monochromator), is 1 Å. The old Cu monochromator stage of the 4CND was removed, and then the new one with two goniometers (RA07A-W and SA05B-RM, Kohzu Precision Co., Ltd.) was placed on the B-3 beam port (see, Fig. 1). In addition, the CMND is equipped with a new beam shutter manufactured by the KURRI factory. To cover the detector area of  $6^\circ \leq 2\theta \leq 150^\circ$ , twenty-five <sup>3</sup>He tube detectors (1/2 inch in diameter) are used, where  $2\theta$  is the scattering angle. The distance from the Cu monochromator to the sample is approximately 2 m, and the distance from the sample to the detector is 1.2 m. A detector bank including the twenty-five <sup>3</sup>He tube detectors is placed on an arm of the HUBER-440 goniometer.

**CURRENT STATUS OF B-3:** Paraffin blocks had frequently been used as radiation shielding properties on the 4CND, however the main concern in working was flammability. Accordingly, all paraffin blocks were replaced by nonflammable radiation shielding properties: B<sub>4</sub>C grit mixed with resin and heavy concrete blocks (see, Fig. 2). The CMND is shown in Fig. 3 (under construction). The goniometers (HUBER-430 and -440) and the beam shutter have already been installed. The detector bank will be installed soon.

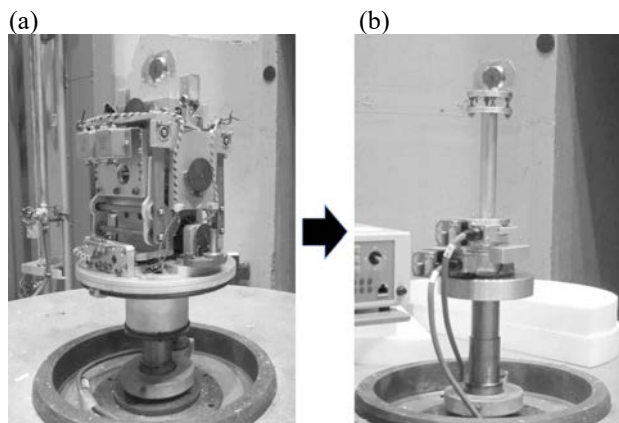


Fig. 1. The Cu monochromator stage: (a) old stage on the 4CND, and (b) new one on the compact multipurpose neutron diffractometer (CMND).

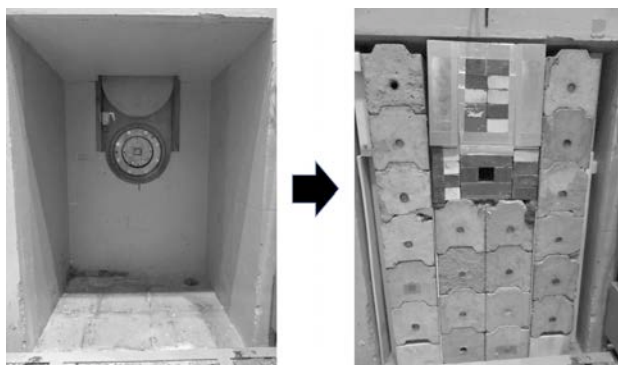


Fig. 2. Radiation shielding properties: B<sub>4</sub>C grit mixed with resin and heavy concrete blocks.

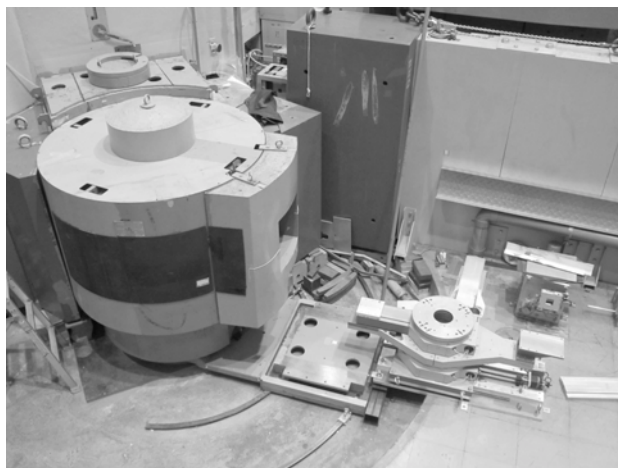


Fig. 3. The compact multipurpose neutron diffractometer, installed at the B-3 beam port (under construction).

## CO1-2 Development of an Ellipsoidal Supermirror with Metallic Substrate

M. Hino, S. Takeda<sup>1</sup>, T. Hosobata<sup>1</sup>, Y. Yamagata<sup>1</sup>, T. Oda, H. Endo<sup>2</sup>, N.L. Yamada<sup>2</sup>, J. Guo<sup>1</sup>, S. Morita<sup>3</sup>, M. Furusaka<sup>4</sup> and Y. Kawabata

Research Reactor Institute, Kyoto Univ., Japan

<sup>1</sup> RAP, RIKEN, Japan

<sup>2</sup> IMSS, KEK, Japan

<sup>3</sup> Tokyo Denki Univ. Japan

<sup>4</sup> Grad. Sch. of Eng., Hokkaido Univ., Japan

**INTRODUCTION:** Progress of neutron optical devices is very significant, however, it is still very difficult for neutron aspherical focusing mirror, especially, two dimensional (2D) aspherical focusing supermirror. We proposed new fabrication method for aspherical focusing supermirror with metal substrate [1, 2]. The metallic substrate is robust and ductile, to which able to fabricate steeply curved surface with high form accuracy. It is also applicable to use under high radiation irradiation and high-temperature field, even at a place close to the neutron target and moderator. Furthermore, it is possible to fabricate a large focusing mirror by combining multiple segmented mirrors with mechanical fastening entailing the usage of screw holes and fixture tabs. The big problem was required surface roughness for neutron mirror. The roughness should be smaller than 0.5 nm even for  $m=3$  supermirror coating. Here  $m$  is the maximum critical angle of the mirror in units of critical angle of natural nickel. By using electroless nickel-phosphorus (Ni-P) plating, we almost overcame the problem in case of one-dimensional aspherical focusing supermirror [3]. In this study, we show a performance test of ellipsoidal supermirror with metallic substrates.

**EXPERIMENTS:** We fabricated an ellipsoidal metallic substrates with the Ni-P plating, based on the technology using ultrahigh precision cutting with correction processing, followed by mechanical precision polishing. The manufacturing, polishing and cleaning of the metallic substrate were conducted at RIKEN. The supermirror coating was conducted with KUR-IBS [4]. The neutron experiments were conducted at the BL06 (VIN ROSE) beam port at J-PARC/MLF [5,6].

**RESULTS:** There is two neutron guide tubes at the BL06 and a cadmium pinhole in which aperture size of 1 mm was located at exit of one of the guide tubes. A U-shape slit and an ellipsoidal supermirror of 300 mm length shown in photograph of Fig.1 were placed between the pinhole slit and a 2D neutron detector. The distance between the pinhole slit and the detector is 2.5 m since the semi-major axis of the mirror is 1.25 m. Without the mirror, as shown in Fig 1(a), the intensity image was U-shape and the peak intensity was about 500 counts. With the mirror, as shown in Fig 1(b), the intensity image was circular spot and the spot size was almost equivalent to that of the pinhole. The peak intensity was about 7000 counts and the intensity gain was about 14 in this setup.

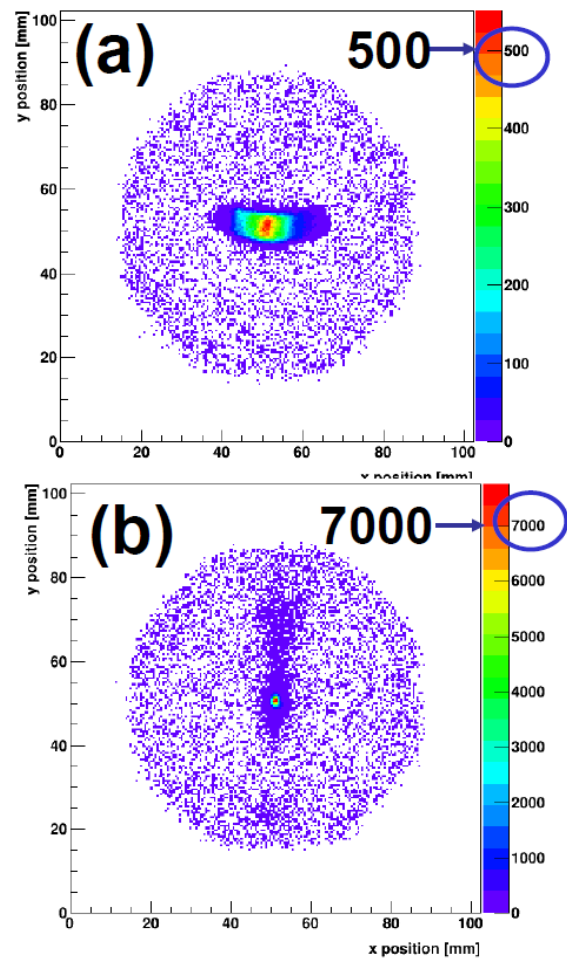


Fig. 1. Photograph of the ellipsoid neutron supermirror at the BL06 at the J-PARC/MLF. Neutron intensity image at detector position (a) without and (b) with the ellipsoid neutron supermirror.

### REFERENCES:

- [1] J. Guo, *et al.*, Optics Express **22**(2014) 063108.
- [2] J. Guo, *et al.*, Review of Scientific Instruments **86**(2015) 063108.
- [3] S. Takeda, *et al.*, Optics Express **24**(2016) 12478.
- [4] M. Hino, *et al.*, Nucl. Instr. and Meth., **797**(2015) 265.
- [5] T. Oda, Dr thesis, Kyoto University, 2015.
- [6] M. Hino, *et al.*, to be published in JNST

# CO1-3 The Correlation between Microstructural Evolution and Mechanical Property Changes in Neutron-irradiated Vanadium Alloys

K. Fukumoto, T. Onitsuka, K. Tone<sup>1</sup> and Q. Xu<sup>2</sup>

RINE, Univ. of Fukui

<sup>1</sup> Graduate school of Eng., Univ. of Fukui

<sup>2</sup> Research Reactor Institute, Kyoto University

**INTRODUCTION:** Vanadium alloys are candidate materials for fusion reactor blanket structural materials, but the knowledge about the mechanical properties at high temperatures during neutron irradiation is limited and there are uncertainties that may have influenced the results such as the interstitial impurity content of specimens. Recently, material irradiation technology in a liquid metal environment was developed and irradiation experiments in various liquid metal environments can be performed for vanadium alloys. Environmental effects and irradiation effects for mechanical properties should be distinguished independently in order to understand the essential behavior of vanadium alloys during irradiation for fusion reactor application. The objective of this study is to investigate the mechanical properties and microstructural changes of the vanadium alloys, V-4Cr-4Ti alloys during neutron irradiation. In this study, tensile test and microstructural observation were carried out for V-4Cr-4Ti alloys.

**EXPERIMENTS:** The majority of test specimens for this study were prepared from V-4Cr-4Ti alloys. The tensile specimens had nominal gauge dimensions of 0.25mm(t) x 1.2mm(w) x 5mm(l). Before irradiation, all specimens were annealed in vacuum at 1000°C for 2hrs. The specimens were irradiated in Joyo in the temperature range from 450°C to 650 °C with total neutron dose from 0.47 to 2.1 x 10<sup>26</sup> n/m<sup>2</sup>. In the previous study, the ratio of damage level, displacement per atom (dpa) to neutron dose in pure vanadium in Joyo MK-II was 2.5 x 10<sup>-26</sup> dpa/Φ<sub>tot</sub>. The amounts of estimated damage level ranged from 1.2 to 5.3 dpa. Tensile tests were conducted at room temperature and 400°C with various strain rate ranged from 6.7x10<sup>-4</sup> to 10<sup>-2</sup> to obtain the information of strain rate sensitivity at high temperature. SEM observation for fractography after tensile test was carried out in KUR, Kyoto University.

**RESULTS:** Tensile tests for V-4Cr-4Ti alloys were carried out at RT and 400 °C at strain rates between 6.7x10<sup>-4</sup> and 6.7x10<sup>-1</sup>/s. The strain-rate dependence was determined for the lower yield stress σ<sub>LYS</sub>. From the gen-

eral relationship between flow stress and strain rate, the strain rate sensitivity (SRS) parameter is defined as follows;

$$m = \frac{1}{\sigma} \frac{d\sigma}{d \ln \dot{\epsilon}} \quad (1)$$

When the flow stress  $\sigma$  rises with the increase of strain rate  $\dot{\epsilon}$ , i.e.,  $m > 0$ , slip deformation is a thermally activated process. When  $m < 0$ , a barrier strength of obstacle against dislocation slip motion is weakened and leads to reduction of the flow stress, because increasing the strain rate decreases time available for solute diffusion to dislocations. Values of the SRS for the lower yield stress were determined for each irradiation condition and test temperature from a logarithmic fit to the lower yield strength data. Figure 1 shows the SRS of lower yield stress dependence on the test temperature for the irradiated V-4Cr-4Ti in this study and the previous data for V-4Cr-4Ti (US-832665) irradiated in HFBR [1]. The data of SRS,  $m$  in this study shows significantly positive value and larger than the  $m$  values of previous data for US V-4Cr-4Ti alloy irradiated in HFBR. The interaction between interstitial impurities and defect clusters/dislocation is affected by the irradiation damage process after neutron irradiation at 400 °C. Therefore, the dynamic strain aging should be only thermal activation process between impurity and mobile dislocation, and independent of irradiation damage process.

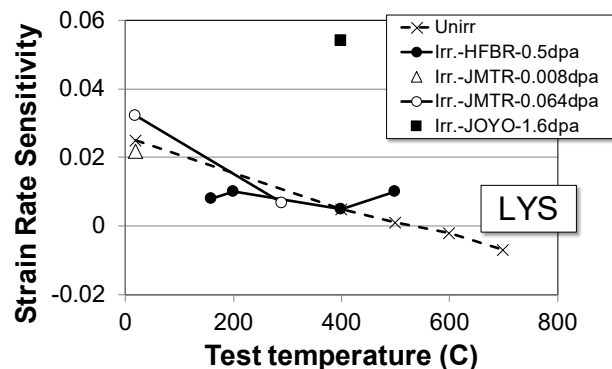


Figure 1 : The strain rate sensitivity (SRS) of lower yield stress dependence on the test temperature for the irradiated V-4Cr-4Ti alloy in this study and the previous data for V-4Cr-4Ti irradiated in HFBR [1].

Reference

[1] A. F. Rowcliffe, S. J. Zinkle and D. T. Hoelzer. J. Nucl. Mater., 283-287 (2000) 508-512

## CO1-4 Preliminary Study of Radiation Resistivity of *Bacillus subtilis natto*

Y. Yanagisawa, T. Chatake<sup>1</sup>, T. Saito<sup>1</sup>, T. Ohsugi<sup>2</sup>,  
H. Sumi<sup>2</sup>

Faculty of Pharmaceutical Sciences, Chiba Institute of  
Science

<sup>1</sup>Research Reactor Institute, Kyoto University

<sup>2</sup>Department of Life Science, Kurashiki University of Science and the Arts

**INTRODUCTION:** *Bacillus subtilis natto* (BSN) is one of famous bacteria in Japan, because Japanese traditional food 'natto' is made of soybeans by fermentation using BSN. Since BSN produces biologically active substances: nattokinase [1], water-soluble vitamin K [2] etc, the detailed mechanism of BSN growth would provide useful information for improvement of quality and quantity of the production of this nutritional food.

The growth of BSN is entirely different from *Escherichia coli* (*E. coli*), which is the most popular bacterium in the field of bacteriology. *E. coli* increase by only simple cell division, and when their population reach the limit, cell division is suppressed. On the other hand, BSN transform themselves to spores like seeds of plants, under their excess pupation. The spores have high resistance to various severe conditions such as starvation, heat, cold, dry, chemical reagents (fungicides). Of course, they have high radiation resistance [3].

The aim of this project is to investigate radiation resistivity of BSN not in its spore state but in its growth state. Generally, the radioresistance of *Bacillus subtilis* is believed to be derived from the formation of spores (sporulation). It would be true, but vegetative cells of BSN might have different property of radioresistance from other bacteria, too.

In our previous study, radioresistance of vegetative cells of *E. coli* was investigated in detail. We tried to establish experimental procedure of the assessment of the radioresistance of vegetative cells of BSN, in the same manner as that of *E. coli*. Here is the first preliminary report of this experiment.

**EXPERIMENTS:** First, cell cloning was carried out using *Bacillus subtilis natto* Miyagino. The obtained clone was confirmed by the fibrin plate method that assesses the fibrinolysis activity of nattokinase, which is abundantly produced in BSN. Prior to irradiation experiments, the growth curve of BSN in LB medium was determined. Glycerol stock (40  $\mu$ L) of the BSN clone was inoculated in 4 mL LB liquid medium in a test tube, and then pre-incubated at 42 °C with the shaking at 1,200 rpm for 16–20 hours. Pre-cultured medium (40  $\mu$ L) was inoculated in 4 mL LB liquid medium, and incubated with the same condition as the pre-incubation. Optical density at 600 nm ( $OD_{600}$ ) was monitored for 8 hours during the incubation.

Irradiation experiment was carried out at the Co-60 Gamma-ray Irradiation Facility of Kyoto University Research Reactor Institute. Incubated medium (500  $\mu$ L) with

$OD_{600}$  of 0.536 was sealed in a 1.5 mL plastic tube. Five samples were prepared, and irradiated with gamma rays at a dose of 0, 50, 100, 200, and 400 Gy at a dose rate of 24 Gy/min. Temperature of the experimental room was 15 °C. After the irradiation, each liquid medium was diluted by LB medium, and plated on standard method agar "Nissui". Colony formation units were counted after 8 hour incubation at 42 °C.

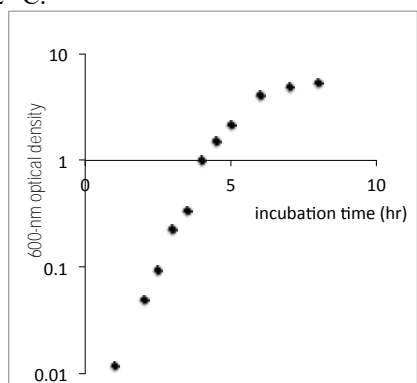


Fig. 1. Growth curve of BSN in LB medium.

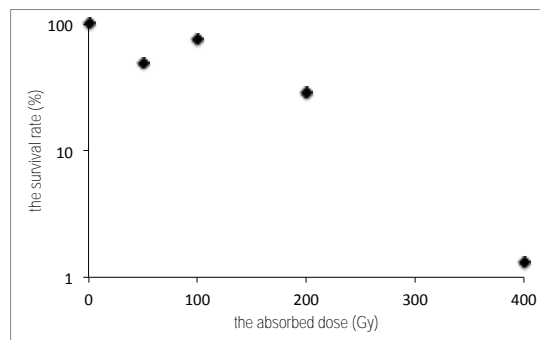


Fig. 2. Cell survival curve of BSN.

**RESULTS:** As shown in Fig. 1, the growth of BSN is in an exponential phase for 1–4 hours from the inoculation. The corresponding  $OD_{600}$  are 0.01–0.98. In this phase, sporulation is thought to rarely occur. The optimum condition for irradiation experiment is estimate to be  $OD_{600}$  = 0.2–0.8 (3–3.5 hours incubation).

Fig. 2 shows our preliminary result of the radioresistance of vegetative cells of BSN in this project.  $D_{10}$  value (10% survival dose) was about 250 Gy. The present result suggests that vegetative cells of BSN do not have so high radioresistance as spore of BSN. On the other hand, we found a few different features in the cell survival curve from that of *E. coli*.

In order to discuss the radioresistance of BSN in detail, improvement of our experimental procedure and repeated irradiation experiments are in progress.

### REFERENCES:

- [1] H. Sumi *et al.*, *Experientia*. **42** (1987) 1110–1111.
- [2] H. Sumi, Y. Yanagisawa, N. Kishimoto, *Nippon Noeikagaku Kaishi* **73** (1999) 599–604.
- [3] P. Setlow, *J. Appl. Microbiol.* **101** (2006) 514–525.

## CO2-1 High-Precision Mass Analysis of RI Sample for Cross-Section Measurements

S. Nakamura, Y. Shibahara<sup>1</sup>, A. Uehara<sup>1</sup>, T. Fujii<sup>2</sup>,  
A. Kimura, B. Hales and O. Iwamoto

Japan Atomic Energy Agency

<sup>1</sup>Kyoto University Research Reactor Institute

<sup>2</sup>Osaka University

**INTRODUCTION:** The ImPACT project[1] aims to realize a "large reduction of and exploitation of resources in high-level nuclear waste by nuclear transmutation", by using an accelerator to accomplish nuclear transmutation of long-lived fission products (LLFPs). To perform accelerator-based nuclear transmutation effectively, it is necessary to acquire reaction cross-section data for radionuclides across a wide spectrum of incident particle energies. This project targets the major LLFPs: <sup>107</sup>Pd, <sup>93</sup>Zr, <sup>135</sup>Cs, <sup>126</sup>Sn, and <sup>79</sup>Se, as well as incidentally the medium-lived fission product <sup>137</sup>Cs. We targeted the <sup>135</sup>Cs because of its long half-life ( $2.3 \times 10^6$  yr[2]). However, it is impossible to obtain a pure <sup>135</sup>Cs sample because it is not supplied by available vendors. This is also why the quantity of data is so scarce [3, 4]. Isotope separation of <sup>135</sup>Cs and <sup>137</sup>Cs is difficult, and therefore <sup>135</sup>Cs is included as an impurity in available <sup>137</sup>Cs samples. The isotope abundance of <sup>135</sup>Cs and <sup>137</sup>Cs in a standard <sup>137</sup>Cs source has been measured by mass spectrometry. Then, the amount of <sup>135</sup>Cs can be obtained from yields of 662 keV decay gamma-rays of <sup>137</sup>Cs and the isotope abundance. It is also necessary to suppress contamination of the mass spectrometer from radioactive <sup>137</sup>Cs and <sup>135</sup>Cs. It is necessary to perform highly precise analysis for an extremely small amount of sample. Therefore, this research aims to apply mass spectrometry to a very small amount of radioisotope sample, and to confirm its effectiveness.

**EXPERIMENTS:** A standard solution of <sup>137</sup>Cs (370kBq) was obtained through the Japan Radioisotope Association. An appropriate amount of the <sup>137</sup>Cs solution was dispensed, and then converted to nitrate by a chemical processing. The mass spectrometer TRITON was used for this analysis, which was made by Thermo Fisher Scientific. A small amount of the chemically processed solution, about 10Bq, was pipetted onto a Re filament with a TaO activator, and then dried. Three filaments with applied Cs solution were prepared. The filaments were attached onto the ion source of the mass spectrometer.

**RESULTS AND DISCUSSION:** Figure 1 shows the resulting mass spectrum of the standard <sup>137</sup>Cs sample. From the yields of the mass spectrum, the obtained <sup>135</sup>Cs/<sup>137</sup>Cs isotope ratio was  $0.868 \pm 0.004$  ( $\pm 2\sigma$ ). Before the chemical processing, false peaks of about 1% were observed as the part of red line, which would

come from sources other than Cs or molecular ion. The false peaks appear at Cs masses plus 0.1u. On the other hand, it is known that peaks from Ba appear on the almost same mass. Since the false peaks decayed faster than Cs peaks with the elapse of time, it is supposed that the false peaks were due to some kind of chemical impurities. In the case of the chemically processed sample, false peaks did not appear as shown with the black line in Fig.1. From this, it is thought that false peaks were due to some kind of chemical impurities in the Cs sample because the false peaks became extinct after chemical processing. The results of the isotope ratios in both cases were in agreement with each other within the limits of errors.

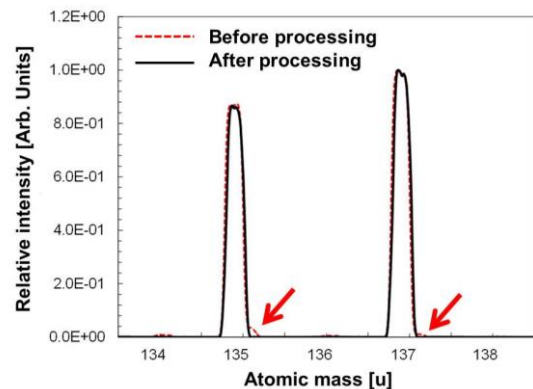


Fig. 1 Measured mass spectrum of <sup>137</sup>Cs sample

**CONCLUSION:** This work successfully measured the isotope ratio of <sup>135</sup>Cs and <sup>137</sup>Cs with an accuracy of 0.5% using a standard solution of <sup>137</sup>Cs. This technique makes it possible to analyze a very small amount (picogram order) of radioactive sample. When the Kyoto University Reactor is operated again in near future, neutron capture cross-section measurements of <sup>135</sup>Cs shall be performed by activation method with the <sup>137</sup>Cs solution analyzed in this work.

### Acknowledgement

The authors would like to thank the staff of Kyoto University Research Reactor Institute for their support.

This research was funded by ImPACT Program of Council for Science, Technology and Innovation (Cabinet Office, Government of Japan).

### REFERENCES:

- [1] <http://www.jst.go.jp/impact/index.html>
- [2] R.B. Firestone *et al.*, Table of Isotopes, 8th ed. Update, John Wiley and Sons, New York, (1998).
- [3] V.A. Anufriev *et al.*, Soviet Atomic Energy, **63**, 851(1988).
- [4] T. Katoh *et al.*, J.Nucl.Sci.Technol., **34**, 431(1997).

## CO2-2 Measurement of Doppler Effect by Small Accelerator Neutron Source (1)

T. Sano, J. Hori, Y. Takahashi, K. Nakajima, H. Unesaki

Research Reactor Institute, Kyoto University

**INTRODUCTION:** In order to reduce TRU, the research and technology development entitled as “TRU burning fast reactor cycle using uranium-free TRU metal fuel” have been started Japan at October 2014 [1]. The feature of the fast reactor is high content TRU and Zr without uranium in the fuel alloy so that additional TRU is not produced. On the other hand, uranium-free TRU metallic fuel leads to the reduction of the Doppler reactivity. Thus, the utilization of fuel alloy such as Mo and Nb instead of Zr is considered as one of the countermeasures [2]. As the Doppler effects depend on the magnitude of self-shielding at the resonances, it is important to verify the Doppler effects at each resonance of the fuel alloy (Mo or Nb) materials to evaluate the feasibility of the uranium-free TRU metallic fuel. However, the differential experiment of the Doppler effects for Mo and Nb has not been carried out so far. Therefore, we have initiated the measurement of the Doppler effects for Mo sample by Time-of-flight (TOF) method with the KURRI-LINAC pulsed neutron source.

**EXPERIMENTS:** We measured the Doppler effects of Mo sample with the KURRI-LINAC pulsed-neutron source. In the experiment, neutron capture rates in Mo sample at 300 K and 600 K were obtained by prompt gamma-ray measurement with the TOF method. The Mo sample was placed in the center of a heating device at a distance of 10 m from the Ta target. The surface temperature of the sample was observed by thermoelectric couple and controlled to be constant during the irradiation by a glass-heater. Two kinds of natural molybdenum samples with different thickness of 0.5 mm<sup>t</sup> and 3.0 mm<sup>t</sup> were prepared to identify the neutron self-shielding effects for each resonance. Those were metallic plates of 2.0×2.0 cm<sup>2</sup>. The measurements with thick and thin Mo samples, the graphite sample with 3.0 mm in thickness, and no sample (blank run) at 300 K and 600 K were carried out.

**RESULTS:** The measured TOF spectra with 0.5 mm<sup>t</sup> and 3.0 mm<sup>t</sup> Mo samples at 300K are shown in Fig. 1. The main resonances of Mo-95, Mo-96, Mo-97 and

Mo-98 were clearly observed in the energy range from 10 eV to 1 keV. For further analysis, counting statistics observed in TOF spectrum were improved by rebinning the data into the JSF70 group structure [5] corresponding to the lethargy width of 0.25. Comparison of the rebinned TOF spectra for the 3.0 mm<sup>t</sup> sample at 300 K and 600 K is shown in Fig. 1. The Doppler capture rate ratio defined as the capture rate at 600 K divided by it at 300 K was obtained for each energy group. The Doppler capture rate ratio were  $1.3 \pm 0.7\%$  at 44.9 eV,  $8.0 \pm 0.7\%$  at 70.9 eV,  $1.0 \pm 0.7\%$  at 131.4 eV and  $6.5 \pm 3.0\%$  at 358.6 eV resonances.

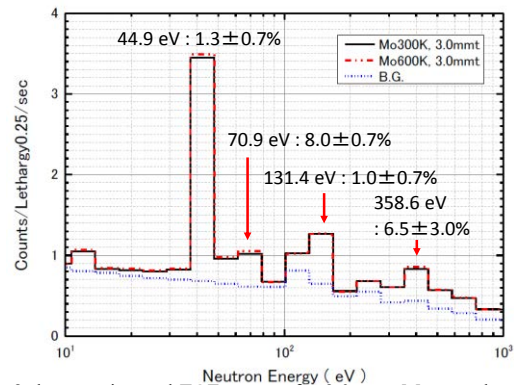


Fig. 2 the experimental TOF spectra for 3.0 mm<sup>t</sup> Mo sample at 300 K and 600 K

This study is being performed under the contract with the Ministry of Education, Culture, Sports, Science and Technology of Japan (MEXT) in the framework of MEXT’s Nuclear System Research and Development Program.

### REFERENCES:

- [1] K. Arie, et. al., Proc. of Global 2015, Sep. 20-24, Paris, France, Paper 5096, (2015).
- [2] K. Arie, et. al., Proc. of ICAPP 2014, Charlotte, USA, April 6-9, (2014).
- [3] Y. Nagaya et. al., JAERI1348, Japan Atomic Energy Research Institute, (2005).
- [4] K. Shibata, et. al., J. Nucl. Sci. Technol. 48(1), 1-30 (2011).
- [5] M.Nakagawa, K. Tsuchihashi, JAERI 1294 (1984)

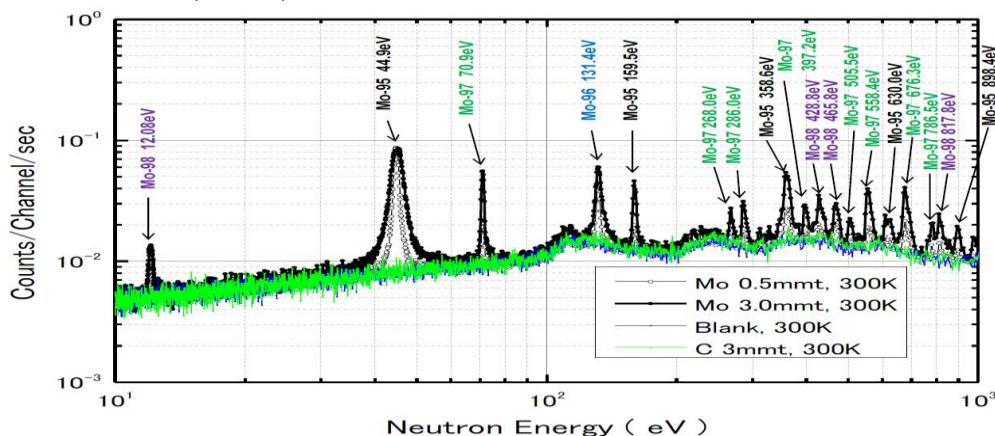


Fig. 1 The measured TOF spectra with Mo samples, graphite sample and no sample

## CO2-3 Development of Neutron Detectors for Precise Measurement of Epi-thermal Neutrons

T. Matsumoto, A. Masuda, H. Harano, H. Tomita<sup>1</sup>, Y. Ichinose<sup>1</sup>, K. Uema<sup>1</sup>, T. Iguchi<sup>1</sup>, K. Watanabe<sup>1</sup>, A. Uritani<sup>1</sup> and J. Hori<sup>2</sup>

*National Metrology Institute of Japan, National Institute of Advanced Industrial Science and Technology*

<sup>1</sup>*Department of Engineering, Nagoya University*

<sup>2</sup>*Research Reactor Institute, Kyoto University*

**INTRODUCTION:** Evaluation of neutron fluence and neutron dose equivalent for the epi-thermal neutron region is very important in work places with neutron sources or nuclear fuels as well as irradiation fields in a boron neutron capture therapy (BNCT). It is not easy to determine precisely the neutron fluence for the epi-thermal neutrons in an irradiation field because of large uncertainty of reaction cross sections in the epi-thermal region. In the present study, we have developed neutron detectors for absolute measurement of epi-thermal neutrons, high intensity epi-thermal neutrons in a BNCT field and an imaging detector for a hidden material.

**EXPERIMENTS:** A collimated neutron beam was obtained by the photo-neutron reaction using a water-cooled tantalum target at the KURRI Linac [1]. We experimentally evaluated characteristics of the epi-thermal neutron detector for absolute measurement, the high intensity epi-thermal neutron detector and the imaging detector.

(1) Epi-thermal neutron detector for absolute measurement

The epi-thermal neutron detector for absolute measurement is composed of a  ${}^6\text{Li}^{\text{nat}}\text{Gd}^{10}\text{B}_3\text{O}_9:\text{Ce}^+$  (LGB) scintillation detector and two BGO scintillation detectors. In our previous experiments, we used an NaI(Tl) scintillation detector instead of the BGO scintillation detectors. However, the NaI(Tl) scintillator has large sensitivity to neutrons as a comparison with the BGO scintillator. The 50 mm-diameter and 5-mm thick LGB scintillator was set at the center of the beam line. The 50.8 mm-diameter and 50.8 mm thick BGO scintillators were located on both sides of the LGB scintillator and out of neutron beam. When the LGB scintillator detects neutrons by the  ${}^{10}\text{B}(\text{n},\gamma\alpha)$  reaction, 478 keV monoenergetic gamma rays are produced and subsequently detected with the BGO scintillators. Moreover, the absolute neutron fluence is determined by measuring gamma rays from the  ${}^{10}\text{B}(\text{n},\gamma\alpha)$  reaction with the BGO scintillators in setting a 1-cm thick  ${}^{10}\text{B}_4\text{C}$  total absorption sample in front of the LGB scintillator.

Number of alpha particles and gamma rays produced by the  ${}^{10}\text{B}(\text{n},\gamma)$  reaction in the LGB scintillator are absolutely determined by the coincidence measurements. Pulse height spectra of the LGB and BGO scintillators from the  ${}^{10}\text{B}(\text{n},\gamma)$  reaction were obtained in the coincidence measurements. However, the evaluation of the background due to scattered neutrons was not sufficient. In future, we will improve the measurement process based on the present experimental results.

(2) High intensity epi-thermal neutron detector

The high intensity epi-thermal neutron detector is important in the BNCT. The detector is simply composed of a  ${}^6\text{Li}$ -glass scintillator and a  ${}^7\text{Li}$ -glass scintillator and photomultipliers (PMTs). Current from an anode output of the PMT is detected by a current integrator. The  ${}^7\text{Li}$ -glass scintillator is used to subtract the gamma ray contribution detected by the  ${}^6\text{Li}$ -glass scintillator. We experimentally evaluated the difference between the neutron detection efficiencies of the  ${}^6\text{Li}$ -glass and  ${}^7\text{Li}$ -glass scintillators using the Linac neutron source. Finally, we successfully obtained the relation between the thermal neutron flux and output current using the neutron detection efficiencies in the thermal neutron standard field of the National Institute of Advanced Industrial Science and Technology. In future, we will perform the high flux neutron irradiation using the KUR.

(3) Imaging detector

The imaging detector is used to search hidden materials such as nuclear materials and radioactive sources. The imaging detector is composed of multi-pixel type CdTe detectors. The imaging detector detects prompt gamma rays produced by the neutron capture reaction in the hidden materials or gamma rays from a hidden radioactive source. After that, the imaging detector determines a position of the hidden material or the hidden radioactive source. Characteristics of the detector were evaluated using gamma rays from the neutron capture reactions of  ${}^{10}\text{B}$  and  ${}^{197}\text{Au}$ . We will continue the experiments in order to verify potential of the practical realization using the TOF method.

**REFERENCE:**

[1] K. Kobayashi et al., Annu. Rep. Res. Reactor Inst. Kyoto Univ. 22, 142 (1989).

This work was supported by JSPS KAKENHI(JP16K21679, JP16K09030).

## CO2-4 Research and Development for Accuracy Improvement of Neutron Nuclear Data on Long-lived Radioactive Nuclei at KURRI-Linac

J. Hori, T. Sano, Y. Takahashi and H. Yashima<sup>1</sup>

Research Reactor Institute, Kyoto University

**INTRODUCTION:** There are strong requests for reducing the uncertainty of neutron capture cross section data of minor actinides (MAs) to estimate the transmutation rate of those long-lived radioactive nuclei in the innovative reactor system. In recent years, intense pulsed spallation neutron sources became available to remarkably improve the precision of neutron TOF data. However, there are discrepancies out of a range of tolerance between current experimental results. It is understood that the unrecognized systematic errors make a difference. In order to recognize and reduce the systematic errors, the project entitled as “Research and development for Accuracy Improvement of neutron nuclear data on Minor Actinides (AIMAC)” has been started [1]. In this project, we aim at obtaining the resonance parameters precisely of MAs by combining the neutron capture  $\gamma$ -ray measurement to transmission neutron measurement at KURRI-Linac. Neptunium-237 is one of the most important MAs with a long half-life. In this year, neutron total cross section and capture cross section of  $^{237}\text{Np}$  were measured and resonance analysis was also performed.

**EXPERIMENTS:** The total and capture cross section measurements have been performed by the neutron time-of-flight (TOF) method using the 46-MeV electron linear accelerator at the Research Reactor Institute, Kyoto University (KURRI-LINAC). Transmitted neutrons were detected by a 6 mm thick GS20  $^6\text{Li}$ -glass scintillator. Neptunium oxide powder of 1.13 g packed in an aluminum disk container of 30mm in diameter and 0.4 mm thick wall, which was placed at a distance of 10.15 m from the photo-neutron source. An aluminum disk container without the neptunium oxide powder was also used as a dummy case. The linac was operated with an electron energy of about 30 MeV, an averaged beam current of 17  $\mu\text{A}$ , a repetition rate of 50 Hz, a pulse width of 0.1  $\mu\text{s}$ . Neutron capture gamma rays from the sample were measured with a  $4\pi$  bismuth germinate (BGO) scintillation detectors composed of 12 BGO cylindrical crystals having 2 inch. in diameter and 2 inch. in length. A capture sample was set in the center of the detector. Three samples of  $^{237}\text{Np}$  with different thickness were used; the activities of the samples were 26, 5.2 and 1 MBq, respectively. The incident neutron flux shape was measured with a  $^{10}\text{B}$  sample.

**RESULTS:** Preliminary result of total cross section of  $^{237}\text{Np}$  is shown in Fig. 1. The resonance analysis of the deduced cross section values were performed with the

SAMMY code [ 2] in the energy range from  $10^{-2}$  to 80 eV. The resonance parameters of the 0.49-eV resonance were modified to reproduce the present results. The neutron capture yields for the samples with different thickness were also obtained as shown in Fig. 2. The neutron self-shielding and multiple-scattering effect in the sample depends on the resonance parameter. Therefore, the data were used for the cross-check of resonance parameters.

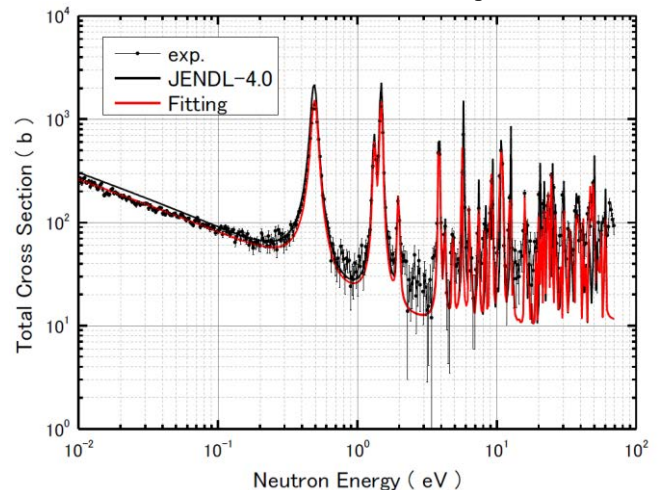


Fig. 1 Preliminary results of neutron total cross section of  $^{237}\text{Np}$

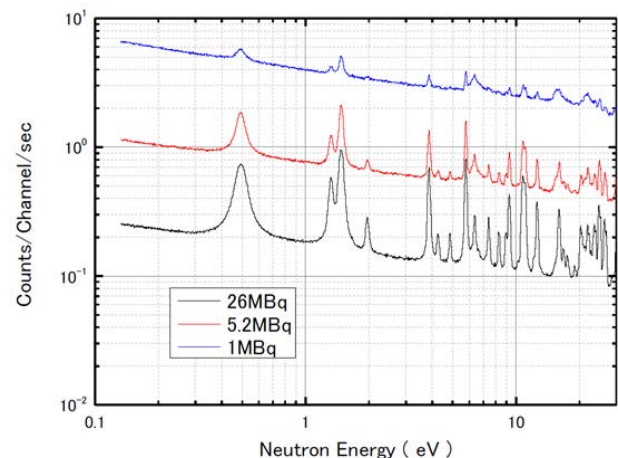


Fig. 2 Capture yields for three  $^{237}\text{Np}$  samples measured by the BGO spectrometer

Present study includes the result of “Research and Development for accuracy improvement of neutron nuclear data on minor actinides” entrusted to the Japan Atomic Energy Agency by the Ministry of Education, Culture, Sports, Science and Technology of Japan (MEXT).

### REFERENCES:

- [1]H. Harada *et al.*, EPJ Web of Conferences **93**, 06001 (2015).
- [2]N. W. Larson, ORNL/TM-9179/R6, Oak Ridge National Laboratory, 1998.

T. Awano and T. Takahashi<sup>1</sup>

*Faculty of Engineering, Tohoku Gakuin University  
<sup>1</sup>Research Reactor Institute, Kyoto University*

**INTRODUCTION:** We have observed millimeter wave absorption bands of AgI-superionic conductive glasses in sub-terahertz region. We also observed these absorption bands in CuI-superionic conductive glasses[1-3]. These bands seem to be due to collective motion of the conductive ions because their frequencies are lower than those estimated from the ionic masses. However, the dynamics of the collective movement of ions is not clear yet.

Ionic liquids(ILs) are molten salts even at room temperature because of large and anisotropic radius of composing anions and cations. It is interesting to compare ionic motion in the ILs with those in superionic conductor for making clear the effect of glass network structure onto the collective movement of ions.

Recently, we have observed sub-terahertz absorption bands of ILs[4-6]. These bands seem to be due to ionic movement because of their temperature dependence. That is to say, the absorption bands disappear at low temperatures at which the IL is solid. However, the thermal change of absorption spectra of these ILs were in various way. This difference seems to be due to the difference of the process of their phase transition to the solid states (crystal or glass).

In this study we have measured millimeter wave absorption spectra of 33 ILs to make clear the ionic movement from the temperature change of absorption spectra.

**EXPERIMENTS:** A fixed amount of ionic liquids (Tokyo Chemical Industry Co., Ltd.) were spread into filter paper. Transmission spectra of single and double papers with ionic liquids were measured at room temperature and low temperatures. Absorption spectra were obtained by subtraction of them. To confirmation, measurements were repeated two or three times for each IL. Molecular dynamics simulation is executed by Gromacs 5.0.

**RESULTS:** Four types of the spectral change occurred at temperature above melting point or glass transition temperature[7]. The intensities of the absorption bands in the ILs which are crystal in the solid state showed rapid decrease at their melting points[4,5]. On the other hand, those in ILs which are vitreous in the solid state weakened and shifted gradually. Some others showed complicated change. The other type showed no absorption band in this spectral range. Figures 1.a-d show typical spectra of these four types. Origin of these difference is not clear yet. To investigate these variety of spectra, molecular dynamics simulation is underway.

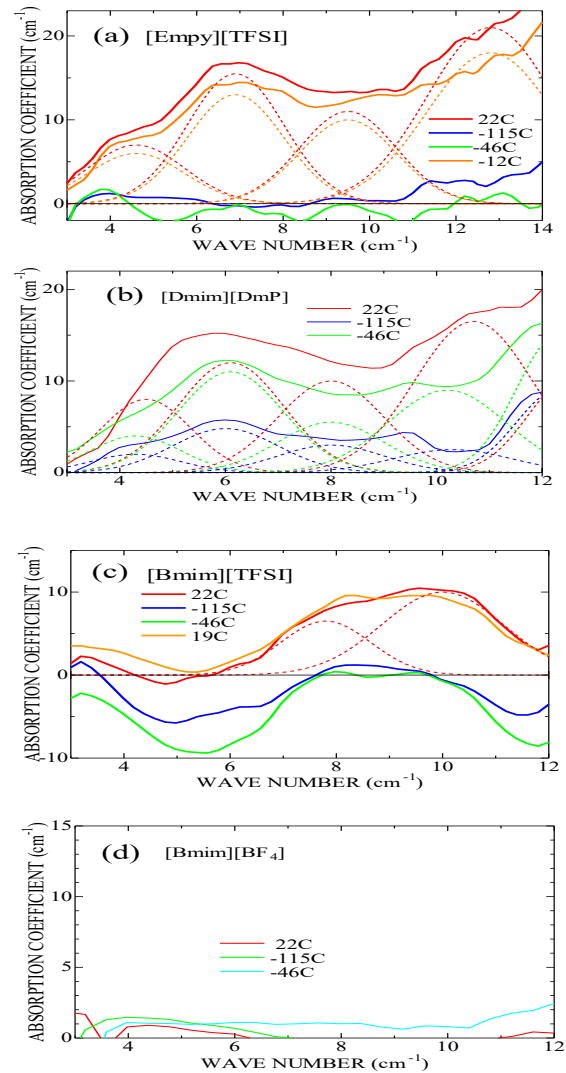


Fig. 1. Typical temperature dependence of absorption increment spectra of ionic liquids. The baseline is the absorption spectrum at 88 K.

#### REFERENCES:

- [1] T. Awano and T. Takahashi, *J. Phys. Conf.*, **148** (2009) 012040/1-4.
- [2] T. Awano and T. Takahashi, *J. Phys. Soc. Jpn.* **79** Suppl. A (2010) 118-121.
- [3] T. Awano and T. Takahashi, *Proceedings of the 13<sup>th</sup> Asian Conference on Solid State Ionics*, (2012) 569-576.
- [4] T. Awano and T. Takahashi, *KURRI Progress Report 2014*, CO4-2.
- [5] T. Awano, A. Shikoda and T. Takahashi, *20<sup>th</sup> International Conference on Solid State Ionics*, (2015) D2.02.
- [6] T. Awano and T. Takahashi, *KURRI Progress Report 2015*, CO4-1.
- [7] T. Awano, A. Shikoda and T. Takahashi, *21<sup>th</sup> International Conference on Solid State Ionics*, (2017) IV-6 P.

F.Hori, H.Nakanishi, A.Tokai, M.Tanaka, S.Toda, M.Tani,  
A.Iwase, K.Okitsu, Y.Mizukoshi<sup>1</sup> and Q.Xu<sup>2</sup>

*Dept. of Mater. Sci., Osaka Prefecture University*

<sup>1</sup>*Institute of Materials Research, Tohoku University*

<sup>2</sup>*Research Reactor Institute, Kyoto University*

**INTRODUCTION:** Metallic nanoparticles have some specific properties, which are not appeared in bulk materials such as catalytic activities, magnetic properties, electro conductivity and light absorption. These properties depend on its size, shape, structure, chemical composition and so on. They have many possibilities to applied for various industrial fields. However, it is not easy to fabricate multi elemental alloy nanoparticles with controlling their size, shape and structure. Generally, many kinds of metal nanoparticles commercially are synthesized by using chemical reaction method, which is not necessarily in water solution. Recent years, some reports show that it is possible to fabricate various metal nanoparticles under irradiation reduction fields such as ultrasonic, solution plasma, electron beam, ion beam and gamma-ray irradiation. So far, we have tried and reported that synthesis of shape and size controlled Au, Ag, Pd, Pt, Cu and their complex nanoparticles under irradiation reduction fields. On the other hand, we have developed a one-step gamma-ray irradiation method to synthesize nanocomposites composed of graphene and Pt nanoparticles from aqueous solution containing graphene and Pt ions in water [1]. In this study, we have tried to synthesize nanocomposites composed of graphene (Gp) and Pd nanoparticles (NPs) in aqueous solution by gamma-ray irradiation, electron beam irradiation.

**EXPERIMENTS:** Aqueous solutions with a given concentration of Pd(II) ( $\text{PdCl}_2 \cdot 2\text{NaCl} \cdot 3\text{H}_2\text{O}$ ) and 2-propanol. Graphenepowder (6 - 8 nm thick x 5  $\mu\text{m}$  wide) was added into this water solution. The solution was argon gas purged and sealed into polystyrene vessels. After dispersion by an ultrasonic cleaning bath, they were irradiated at about 300 K with  $\gamma$ -rays from <sup>60</sup>Co radio active source at gamma irradiation facility in KURRI, Kyoto University. The total dose was fixed to 10 kGy with dose rate of 13.6 kGy/h. After irradiation, the products were separated by centrifugation, washed with water and dried by freeze-drying. UV-vis absorption spectra were measured and all products were

observed by conventional TEM. Infrared spectra and Raman spectra (RS) of the prepared samples were collected by a Fourier-transform infrared spectro-photometer (FT-IR) and a Raman spectrophotometer.

### RESULTS:

Pd NPs supported on Gp (Pd/Gp) were formed in one-pot aqueous solution containing Gp and Pd(II) complex ions by gamma-ray or electron beam irradiation. As shown in figure 1, it was confirmed that gamma-ray and electron beam irradiation provided carbonyl groups (C=O) on Gp and Pd NPs formed from the radiolytic reduction of Pd(II) complex ions were supported on the carbonyl modified Gp. Although there is no fundamental difference in the reaction generated by gamma-ray and electron beam irradiation, but the size of Pd NPs of Pd/G was differed greatly between them. Furthermore, Pd NPs supported on nitrogen-doped Gp (Pd/N-Gp) were prepared by the same condition of gamma-ray and electron beam irradiation. The size of the Pd NPs of Pd/N-Gp was smaller than that of Pd/G because of the increased number of adsorption sites of Pd NPs.

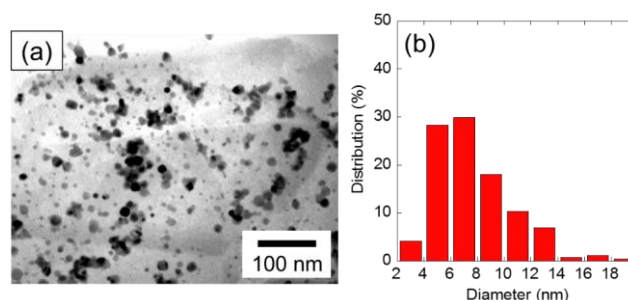


Fig. 1 TEM image and size distribution of Pd-NPs supported on graphene synthesized under gamma-ray irradiation field.

### Acknowledgement

This work was supported by JSPS KAKENHI Grant-in-Aid for Scientific Research (A)-15H02342.

### Reference

- [1] A.Tokai, K.Okitsu, F.Hori, Y.Mizukoshi, A.Iwase, Rad. Phys. Chem. 123, (2016) 68-72

## CO4-3 Electron Irradiation Induced Damage Structure in Intermetallic Alloys

F. Hori, Y. Ueno, Y. Sumikura, K. Kobayashi, A. Iwase, K. Ohsawa<sup>1</sup>, Q. Xu<sup>2</sup> and N. Abe<sup>2</sup>

*Dept. of Mater. Sci., Osaka Prefecture University*

<sup>1</sup>*Res. Inst. of Appl. Mech., Kyushu University*

<sup>2</sup>*Res. Reactor Inst., Kyoto University*

**INTRODUCTION:** Fe-Al compound alloys have good properties such as specific strength to weight ratio, oxidation resistance and strength in elevated temperature. It is well known that intermetallic compound alloys possibly include more than two types of vacancies basically, that is A-vacancy and B-vacancy in A-B compound alloy. Thermally equilibrium defects and chemically deviated structural defects in these compound alloys are very complicated. However, the amount of defect and the defect structure affects the various characteristic features, such as strength and electronic conductivity and so on. Moreover, first principle calculation shows that different number of hydrogen atoms can be trapped by Al- or Fe-vacancy in B2 type Fe-Al alloy. On the other hand, we have reported that vacancies introduced by electron irradiation strongly depend on electron energy because of their different threshold energy of displacement for each elemental atom. Then we supposed that radiation induced vacancy type defects can be controlled by changing the energy of electron irradiation. In this study, we have performed electron irradiation for Fe-Al alloys followed by hydrogen charging by electrochemical method and H<sup>+</sup> ion implantation. After irradiation and hydrogen charging into Fe-Al alloys, Thermal desorption spectrometry (TDS) and positron annihilation measurements were carried out.

**EXPERIMENTS:** Fe-48%Al alloy specimens with B2 structure were prepared by arc melting method. Sliced samples with the thickness of 0.5 mm were annealed at 973 K for 120 h followed by air-quenched in vacuum. These specimens were irradiated with 2 MeV electron to the fluence of  $1 \times 10^{17}$  and  $1 \times 10^{18}$  /cm<sup>2</sup> at JAEA-Takasaka and with 9 MeV electron to the fluence of  $5 \times 10^{17}$  and  $3 \times 10^{18}$  /cm<sup>2</sup> at KURRI, Kyoto University. In both cases, irradiations were carried out at about 330 K controlled by

water flow system. After electron irradiation, hydrogen atoms were cathodically charged in the sulfuric acid aqueous solution including NH<sub>4</sub>SCN as an additive. Also 1.5 MeV-H<sup>+</sup> irradiation with the fluence of  $1 \times 10^{16}$  ions/cm<sup>2</sup> have performed for these alloys at National Institute for Quantum and Radiological Science and Technology. After and before irradiation, samples were examined by X-ray diffraction, positron annihilation lifetime, coincidence Doppler broadening measurements and TDS. The positron lifetime spectra were analyzed by using POSITRONFIT program.

**RESULTS:** After electro-chemical charging and hydrogen implantation into Fe-Al alloys, some peaks observed in TDS spectra representing emission of decomposed hydrogen bounded by defects and grain boundary (Fig.1). It found that hydrogen released temperature for electron irradiated sample followed by hydrogen charging is slightly higher than that for hydrogen charged sample without irradiation. This result reveals that the introduced hydrogen atoms might be trapped by vacancy. On the other hand, positron annihilation Doppler broadening S parameter decreases after hydrogen charging or H<sup>+</sup> irradiation showing that implanted hydrogen is trapped by vacancy. This result is consistent with the results of TDS.

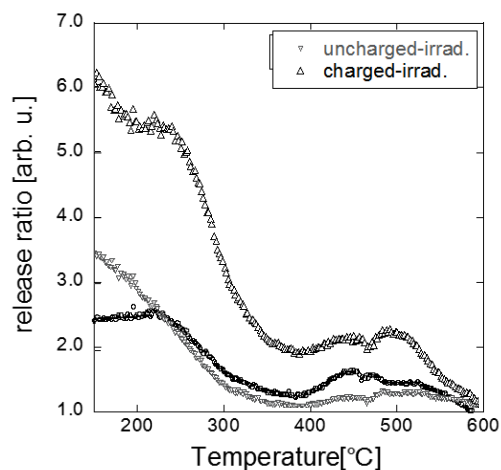


Fig. 1 Hydrogen emission behavior of before and after irradiated Fe-Al alloys.

### Acknowledgement

This work was supported by JSPS KAKENHI Grant-in-Aid for Scientific Research (B)-26289365.

## CO4-4 Observation of Transient Damage States in Materials under Ion Irradiation

H. Tsuchida<sup>1,2</sup>, H. Minagawa<sup>2</sup>, S. Nakanishi<sup>2</sup> and Q. Xu<sup>3</sup>

<sup>1</sup>Quantum Science and Engineering Center, Kyoto University

<sup>2</sup>Department of Nuclear Engineering, Kyoto University

<sup>3</sup>Research Reactor Institute, Kyoto University

**INTRODUCTION:** The effects of energetic-particle irradiation on metallic materials have been extensively studied in nuclear and radiation materials science. Ion irradiation induces crystal lattice disorder following various dynamic relaxation processes including defect recombination and aggregation. During irradiation, damage evolution proceeds by the reciprocal processes of defect production and relaxation, and then reaches a certain equilibrium damage state. To date, experimental and computer simulation studies have focused on an understanding of a transient damage state under irradiation, and a new model calculation relevant to dynamic annealing has recently been reported [1].

To understand transient damage states in materials under ion irradiation, we performed in situ X-ray diffraction (XRD) study of lattice expansion associated with deformation of a thin Al foil under MeV-energy heavy-ion irradiation [2]. The change in the lattice parameter during irradiation and its ion-beam flux dependence were analyzed. We investigated the effect of defect production on lattice expansion. Moreover, with the correlation between lattice expansion and displacement damage, we considered a model for lattice expansion originating from the accumulation of Frenkel defects. From the model, we obtained the relationship between the relative change in lattice parameter and the value of displacement per atom (dpa) rate. A comparison of the results from model calculations and experiments shows that the dpa rate calculated from the model, which takes account of athermal defect-recombination, is strongly correlated with the change on lattice parameter. This result suggests that the concentration of surviving defects under irradiation diminishes because of spontaneous recombination of defect produced.

**EXPERIMENTS:** A high-purity well-annealed aluminum foil with a thickness of 3  $\mu\text{m}$  was used as a target specimen. The free-standing target foil was irradiated with three different projectiles: specifically 2.5-MeV C, 3.0-MeV O and 4.3-MeV Si ions. We performed in situ X-ray diffraction (XRD) analysis of the target specimen under ion irradiation, and measured diffraction peak from Al (200) plane before, during and after ion irradiation.

**RESULTS:** During ion irradiation, the diffraction peak position was sifted to a lower diffraction angle compared with that measured before irradiation, indicating an expansion of lattice. The relative change in lattice parameter,  $\Delta a/a = (a_{\text{during}} - a_0)/a_0$ , increases as the beam flux increases,

where  $a_0$  and  $a_{\text{during}}$  are the lattice constant observed before and during irradiation, respectively. Fig. 1 shows the dependence of dpa rate on the relative change in the lattice parameter. The dpa rate is given as  $\sigma_d^{\text{arc}} \times \phi$ , where  $\sigma_d^{\text{arc}}$  is the displacement damage cross section estimated using the athermal recombination-correlated (*arc*) model [3], and  $\phi$  is the beam flux. The *arc* model was developed to estimate the damage cross sections taking account of athermal defect-recombination. This enables the determination of the surviving fraction or the recombination fraction of defects produced during irradiation. The result indicates that the magnitude of the lattice expansion is correlated with the *arc*-dpa rate. Thus, the present in situ XRD experiment affords a new method to investigate transient damage states in materials under ion irradiation.

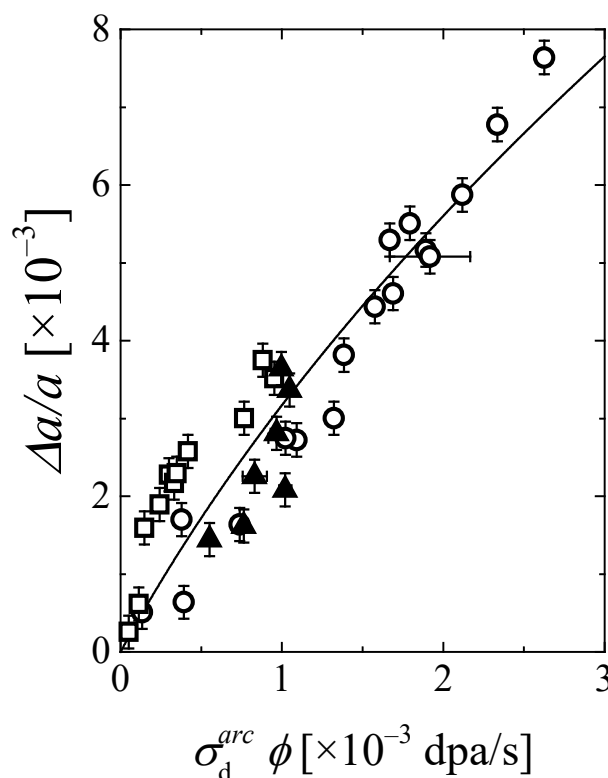


Fig. 1. Dependence of the relative change of the lattice parameter on the dpa rate. Symbols denote the experimental data:  $\square$  for 2.5-MeV C ions,  $\blacktriangle$  for 3.0-MeV O ions, and  $\circ$  for 4.3-MeV Si ions. Solid curve denotes a result of fitting the data.

### REFERENCES:

- [1] X.M. Bai *et al.*, Science, **327** (2010) 1631-1634.
- [2] M. Minagawa *et al.*, Nucl. Instr. and Meth. B, **372** (2016) 38-43.
- [3] K. Nordlund *et al.*, Nucl. Sci. NEA/NSC/DOC (2015) 9.

## CO4-5 Trapping of Hydrogen Isotopes at Vacancy-Type Defects in Tungsten

Y. Hatano, K. Yumizuru<sup>1</sup>, T. Toyama<sup>2</sup> and Q. Xu<sup>3</sup>

Hydrogen Isotope Research Center, Organization for Promotion of Research, University of Toyama

<sup>1</sup>Graduate School of Science and Engineering for Education, University of Toyama

<sup>2</sup>Institute for Materials Research, Tohoku University

<sup>3</sup>Research Reactor Institute, Kyoto University

**INTRODUCTION:** Retention of hydrogen isotopes especially tritium in plasma facing materials is one of the most important issues in safety assessment of fusion reactors. It has been shown that neutron irradiation causes significant increase in deuterium (D) retention in W, a leading candidate of plasma-facing material, due to trapping effects of radiation-induced defects [1]. Detailed understanding of trapping mechanisms is necessary for the mitigation of this undesirable irradiation effects.

To examine defect-hydrogen isotope interactions in W, the authors irradiated samples of polycrystalline W with high energy electrons to  $10^{-3}$  dpa to induce Frenkel pairs uniformly throughout the bulk [2]. Then the irradiated samples were annealed at 573 K under vacuum or D<sub>2</sub> gas atmosphere, and clustering of vacancy-type defects and D trapping were examined using positron annihilation spectroscopy (PAS) and thermal desorption spectroscopy (TDS) [2]. Significant increase in positron lifetime accompanied with increase in D retention was observed after electron irradiation and subsequent annealing due to formation of vacancies and their clustering. In addition, positron lifetime for D-charged samples was shorter than that for D-free samples annealed in vacuum. This difference was ascribed to the presence of electrons of D atoms in vacancies.

In this year, detailed coincidence Doppler broadening (CDB) measurements were performed for better understanding of D trapping at vacancy clusters. Samples irradiated to lower dose were also examined to clarify the threshold damage level at which the irradiation effects on hydrogen isotope retention starts to appear.

**EXPERIMENTS:** Disk samples of W were irradiated with 8.5 MeV electrons to  $\sim 1 \times 10^{-3}$  dpa at LINAC at Kyoto University Research Reactor Institute (KURRI). The irradiated samples were shipped to International Research Center for Nuclear Materials Science, Institute for Materials Research (IMR-Oarai), Tohoku University. A part of samples were sealed into quartz capsules under vacuum or D<sub>2</sub> gas atmosphere (0.1 MPa) and heated at 573 K for 100 h. Then CDB measurements were performed using <sup>22</sup>Na positron source.

Several W samples were irradiated with 5.5 MeV electrons at LINAC at KURRI to  $\sim 5 \times 10^{-4}$  dpa. Positron lifetime and D retention after exposure to D plasma at 450 K were measured.

**RESULTS AND DISCUSSION:** Fig. 1 shows ratio

curves of CDB spectra obtained by normalizing each CDB spectrum to that of well-annealed W sample. The electron irradiation and subsequent annealing in vacuum resulted in clear increase in the ratio values in the low momentum region and decrease in the high momentum region. This change indicates increase in the probability of positron annihilation with conduction electrons due to formation and clustering of vacancies. The presence of D in the samples led to further increase in the ratio values in the low momentum region and decrease in the high momentum region. The remarkable influence of D is explained by annihilation of positrons with valence electrons of D atoms in vacancies. In other words, the observed change in the ratio curve is one of the direct evidences of D trapping at vacancies.

The positron life time for W samples irradiated to  $\sim 5 \times 10^{-4}$  dpa was  $117.9 \pm 0.4$  ps. This value is comparable with that for non-irradiated W (118 ps). No clear effects on D retention was observed. It was therefore concluded that irradiation effects on hydrogen isotope retention becomes significant at  $\sim 10^{-3}$  dpa.

CDB measurements were performed under the framework of Joint Research of IMR-Oarai.

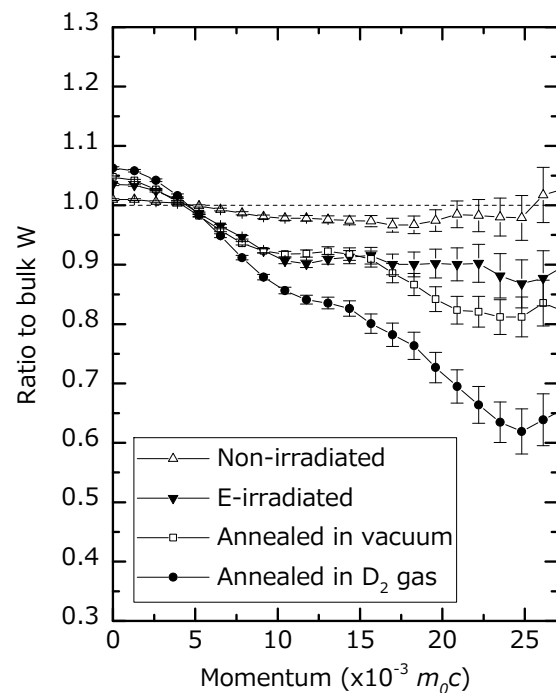


Fig. 1 Ratio curves of CDB spectra of non-irradiated W and those after electron irradiation and subsequent annealing at 573 K under vacuum or D<sub>2</sub> gas atmosphere (0.1 MPa). The curves were obtained by normalizing each CDB spectrum to that of well-annealed W samples.

### REFERENCES:

- [1] Y. Hatano *et al.*, J. Nucl. Mater., **438** (2013) S114–S119 and Nucl. Fusion **53** (2013) 07300
- [2] Y. Hatano *et al.*, KURRI Progress Report 2015, 81

Y. Gotoh, T. Morito, M. Nagao<sup>1</sup>, N. Sato<sup>2</sup>, M. Akiyoshi<sup>3</sup>, and I. Takagi

*Graduate School of Engineering, Kyoto University*

<sup>1</sup>*National Institute of Advanced Industrial Science and Technology, AIST*

<sup>2</sup>*Research Reactor Institute, Kyoto University*

<sup>3</sup>*Radiation Research Center, Osaka Prefecture University*

**INTRODUCTION:** We have been investigating radiation tolerance of the components of a compact image sensor based on field emitter array (FEA) and photoconductor [1,2]. The purpose of the development is to realize a compact image sensor that can be used for the nuclear decommissioning process for Fukushima Daiichi nuclear power plant. By the last year, we have irradiated gamma-ray to the FEAs and cadmium telluride-based photo-diodes to check the robustness of these devices. As a result, the properties of these devices were not deteriorated with the  $\gamma$ -ray irradiation until the adsorbed dose reached 1.2 MGy [1]. Now the research phase is moved to the next stage where *in situ* observation of the device performance under  $\gamma$ -ray irradiation. Last year, we have made the first preliminary experiments of the *in situ* observation [3]. However, the method of the measurements has not yet been established. In this study, we have performed a similar experiments, but irradiating the FEA sample from oblique direction.

**EXPERIMENTAL SETUP:** The measurements of the current-voltage characteristics were made in a small vacuum vessel that was evacuated before the irradiation experiments. The vacuum vessel was connected with a separate vacuum pumping system via a 1/4" stainless steel tube. The vessel itself did not possessed a pumping system. Therefore, the vessel was once evacuated by a vacuum system connected to the vessel, and the vessel was then encapsulated to be irradiated by  $\gamma$ -rays.

**EXPERIMENTAL PROCEDURE:** The FEAs were fabricated at National Institute of Advanced Industrial Science and Technology. Since the FEAs possessed three electrodes of emitter, gate and focus, the current that flowed these electrodes were monitored with a source-measure units. In the previous measurement, irradiation of  $\gamma$ -ray was performed from the normal direction of the FEA surface. In the present study, irradiation was performed from the side to observe the effect of the  $\gamma$ -ray incidence. The measurements were done at two different distances from the  $\gamma$ -ray source: 22 cm and 40 cm.

**RESULTS:** Figure 1 shows the current-voltage characteristics of the emitter, gate, and focus electrodes under  $\gamma$ -ray irradiation, measured at 22 cm distant from the  $\gamma$ -ray source. When the emitter was biased to -5 V, the

emitter current of about -4 nA was observed. While the gate and focus currents were about 1.5 nA and sum of these currents approximately coincides the value of the emitter current. The electric resistance was calculated to be about 1 G $\Omega$ , which was approximately the same value obtained in the previous measurement. The data acquired at the distance of 40 cm showed similar values.

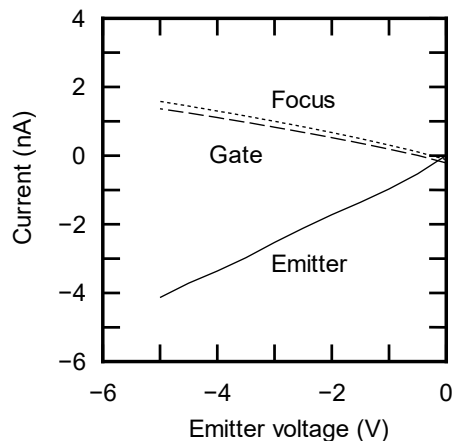


Fig. 1. Current-voltage characteristics of the emitter, gate, and focus electrodes under the  $\gamma$ -ray irradiation.

**DISCUSSION:** In the FEA, the emitter was common and the upper electrode was either the gate or the focus electrode. The ratio of the areas corresponding to the gate and the focus is not unity, it was somewhat strange to have similar currents between the gate and the focus. One possible reason for this would be the effect of the leads from the feedthrough to the device. Shielding the lead may be necessary.

**SUMMARY:** The current-voltage characteristics of FEAs under the  $\gamma$ -ray irradiation were measured. The emitter current was larger than the gate and the focus electrodes. Detailed analysis of these currents are now underway.

**ACKNOWLEDGMENTS:** A part of this study was supported by Japan Society for Promotion of Science through a Grant-in-Aid for Scientific Research No. 16H04631.

**REFERENCES:**

- [1] Y. Gotoh *et al.*, Tech. Dig. of the 29<sup>th</sup> International Vacuum Nanoelectronics Conference, IVNC2016, Vancouver, July 8-10, 2016, p. 20.
- [2] T. Okamoto *et al.*, Physica Status Solidi (c) **13** (2016) 635.
- [3] Y. Gotoh *et al.*, KURRI Progress Report 2015 (2016) p. 73.

## CO4-7 Study of the Properties of Water and the Physiological Activation Phenomena by using High-Intensity Pulsed Coherent Radiation

S. Okuda, Y. Tanaka, Y. Kida and T. Takahashi<sup>1</sup>

Graduate School of Engineering, Osaka Prefecture University

<sup>1</sup>Research Reactor Institute, Kyoto University

**INTRODUCTION:** The coherent transition radiation (CTR) from electron bunches of a linear accelerator (linac) has continuous spectra in a submillimeter to millimeter wavelength range corresponding to the terahertz (THz) frequency range. It is a picosecond pulsed light and hence, has extremely high peak-intensities compared with the other THz light sources. The light source system using the CTR from the electron beams of the 45 MeV L-band electron linac was established at Kyoto University Research Reactor Institute (KURRI) [1-3]. This CTR light source developed has been applied to absorption spectroscopy. Recently, the possibility of any nonlinear effects was found in the measurement of the absorption spectroscopy at KURRI.

The important application of the light source is the investigation of the biological effects of the CTR. The main purpose of the present work is the investigation of the biological effects of the high-intensity pulsed CTR.

**EXPERIMENTAL METHOD:** The electron linac at KURRI was used in the experiments. In most experiments the beam energy, macropulse length and the repetition rate are 42 MeV, 47 ns and 60 Hz, respectively. The experimental configurations for the absorption spectroscopy are schematically shown in Fig. 1. The output CTR light from a light source chamber was transported out from the accelerator room. The spectrum of the light after passing through the sample was measured with a Martin-Puplett type interferometer and a liquid-He-cooled silicon bolometer. The wavenumber resolution was 0.1  $\text{cm}^{-1}$ . The incident light was divided to two parts with the same light intensity in the interferometer. In this system the absorption spectroscopy and the irradiation were carried out at the same time.

In the absorption spectroscopy the sample was located on the light path between the interferometer and the detector. The thickness of the liquid sample was about 100  $\mu\text{m}$ , which was sandwiched with two anhydrous quartz plates 3 mm thick. The light was focused at a light collimator 8 mm $\phi$  in diameter located before the sample. The details of the methods for the measurements are described in ref. 2 and 3. The liquid samples used in the experiments were water, aqueous solutions of NaCl for the investigation of the basic behaviors of the absorbed light in the analysis of the biological effects by the irradiation of CTR.

In the irradiation experiments of the CTR several kinds of bacillus, cell and microorganism were used. After the irradiation the physiological activation phenomena were investigated. The new system for observing the sample

during the CTR irradiation experiments is under preparation.

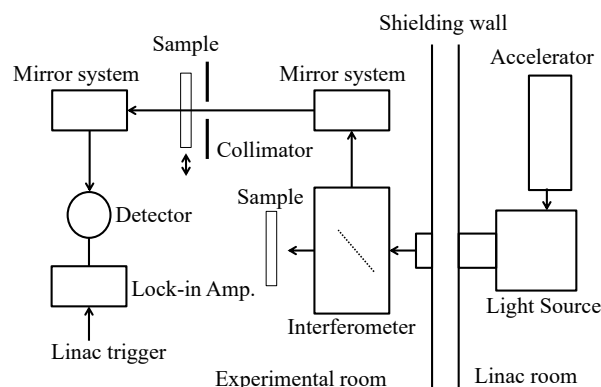


Fig. 1. Schematic diagram showing the configurations for absorption spectroscopy and irradiation experiments using the CTR

**RESULTS AND DISCUSSION:** The characteristics of the CTR light source were investigated, and the electron beam conditions and the experimental configurations were optimized. The light spectrum was sufficiently stable during the measurements within  $\pm 2-3\%$  in a wavenumber range of 4-13  $\text{cm}^{-1}$ . The spectrum had a peak at a wavenumber of about 7  $\text{cm}^{-1}$ . If a band-pass light filter or a grating-type monochromator is used in order to avoid the influence of the main part of the spectrum around the peak the wavenumber range would be expanded to 2-35  $\text{cm}^{-1}$ , which is determined by the specification of the detector. The intensity of light was estimated to be about  $10^{-7}$  W/0.1%b.w. and was found to be sufficiently high even if it becomes  $10^{-6}$  of the initial one after transmission through the sample due to absorption. The micropulse length of the CTR which corresponds to that of the electron beam from the linac was evaluated by the interferogram to be about 3 ps. Such a relatively short pulse length is due to the special bunching process in the optimized operational conditions of the linac. These results indicate that the peak light intensity in the micropulse is about  $10^4$  W. While the averaged CTR power is sufficiently low to induce thermal effects, the comparatively high peak power might cause any nonlinear effects.

In the irradiation experiments of CTR to investigate the biological effects the experimental conditions have been optimized. Preliminary results have been obtained by the CTR irradiation so far.

### REFERENCES:

- [1] T. Takahashi et al., Rev. Sci. Instrum. **69** (1998) 3770.
- [2] S. Okuda and T. Takahashi, Infrared Phys. Technol. **51** (2008) 410.
- [3] S. Okuda and T. Takahashi, J. Jpn. Soc. Infrared Science & Technology **25** (2016) 49 (in Japanese).

T. Takahashi

Research Reactor Institute, Kyoto University

**INTRODUCTION:** In recent years various types of coherent radiation emitted from a short bunch of relativistic electrons have attracted a considerable attention as a bright light source in the THz-wave and millimeter wave regions for the spectroscopic purpose. Coherent transition radiation (CTR), which is emitted from a boundary between two media, is one of such a coherent light source. CTR is usually utilized as a non-polarized light source, because the electric vector of transition radiation (TR) emitted from a metallic screen is axially symmetric with respect to the trajectory of an electron beam. In my previous reports [1] the circularly polarized CTR using a pair of wire-grid radiators with the different polarization has been developed with a new idea. The significant point of my new technique is the use of linearly polarized CTR with the wire-grid radiator. With this technique the polarization degree is able to be controlled precisely. Circularly polarized light has been useful in the circular dichroism spectroscopy. In this report spectra of some kinds of amino acid have been measured using linearly polarized CTR.

**EXPERIMENTAL PROCEDURES:** The experiment was performed at the coherent radiation beamline [2] at the L-band linac of the Research Reactor Institute, Kyoto University. The energy, the width of the macro pulse, and the repetition rate of the electron beam were 42 MeV, 47 ns, and 60 Hz, respectively. The average current of the electron beam was 2.3  $\mu$ A. The spectrum of CTR was measured by a Martin-Puplett type interferometer and a liquid-helium-cooled Si bolometer. The schematic diagram of the experiment was shown in Fig.1.

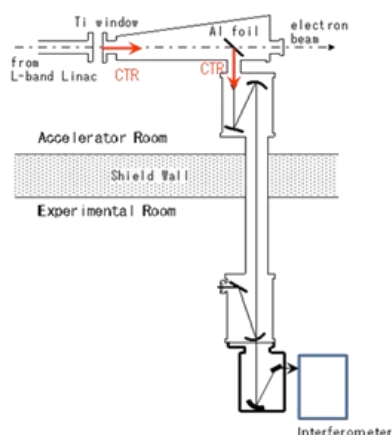


Fig. 1 The schematic diagram of the experiment.

**RESULTS:** Measured spectra of some kinds of amino acid, e.g., Phenylalanine,  $\alpha$ -Alanine, and Tryptophan, are shown in Figs. 2. Difference between L and D forms has been observed. The identification of observed absorption is now in progress.

**REFERENCES:**

- [1] T. Takahashi, *et al.*, KURRI-PR 2015 CO4-7.
- [2] T. Takahashi *et al.*, *Rev. Sci. Instrum.* **69** (1998) 3770.

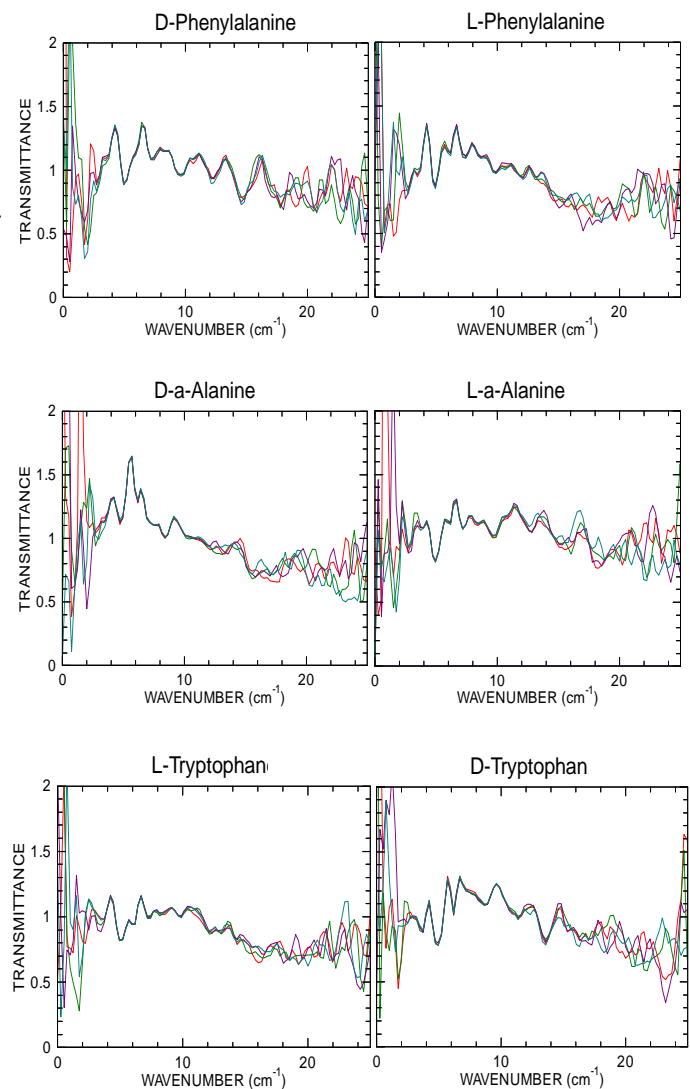


Fig. 2 Spectra of some kinds of amino acid.

## CO4-9 Complex Structure of Ions Coordinated with Hydrophilic Polymer. 17. Inner Precipitation of Inorganic Salt as Fillers and Their Dissolution.

A. Kawaguchi and Y. Morimoto

Research Reactor Institute, Kyoto University

**INTRODUCTION:** We have reported interacted structures between iodine (polyiodide ions,  $I_n^{m-}$ ,  $m, n$ : integer,  $n \neq 1$ ) and polymers.[1] Even if polyiodide ions are prepared as solutes in aqueous solution, they can be diffused into various polymeric matrix, both to hydrophilic polymers and to hydrophobic ones through easy operation at room temperature. Such preparation is expected to introduce novel functionality and wide applications to polymeric materials with easy operation.[2]

On the other hand, results applied with "inner precipitation" can not be easily controlled in some cases. As one reason, it is due to spontaneous ionic diffusion from outer solution of free transfer of ions into polymeric environment with restriction on ionic diffusion and due to inner ionic diffusion under hierarchic structure of polymers and uncertainty of polyiodide ions. Under such complication and diversity, posterior ionic diffusion represented as "secondary doping" of  $Ag^+$  ion or other metallic ions is expected to indicate different scheme of ionic diffusion or their reaction different from ones in solution.

And, for precipitation or production of AgI, which is hardly soluble inorganic salt in water, it also shows unusual behavior against independent ordinary powder of the salt.

**EXPERIMENTS:** Sample preparation for hydrophilic polymer (PA6, polyamide-6, Nylon<sup>TM</sup>-6, TORAY) and hydrophobic matrix ("SEBS"-elastomer, ARON-KASEI Co.Ltd.) was mentioned before.[3,4]

"Rayfan #1401" in thickness of 0.1mm was used as non-doped PA6. A strip cut from a PA6 sheet were stretched (x3-4) and was annealed at 210°C in vacuum. This strip was doped with  $I_2$ -KI(aq) (0.2N) at 5°C for more than 5days and this process (iodine-doping) was terminated by rinsing with water. After drying in vacuum at R.T.(25°C) for 3 weeks, the sample was immersed in  $AgNO_3$ (aq) (2M) at R.T. for more than 24hrs.

As hydrophobic materials as matrix, commercial "SEBS"-elastomer, AR-770C and AR-830C were used as hydrophobic matrixes, which are composed of both polystyrene (hard segment) and polyethylene-polybutylene co-polymer (soft segment). Iodine doping for these hydrophobic matrixes was achieved with  $I_2$ -KI(aq)/3.0N (for 22 hrs., at R.T.) and secondary doping of  $Ag^+$  ion was done with  $AgNO_3$ (aq)/0.25M (for 30min., at R.T.).

**RESULTS:** Iodine ( $I_2$ ) is insoluble to water. Therefore, for preparation of aqueous solution of  $I_3^-$ , which is the smallest polyiodide ion, mono-iodide ion ( $I^-$ ) is required

for polyiodide ions to solve in aqueous solution. On the other hand, prior existence of  $I^-$  ion produces precipitation of silver iodide (AgI) salt on posterior addition of  $Ag^+$  ion. ( $Ag^+ + I^- \rightarrow AgI \downarrow$ ) In the case of aqueous solution of polyiodide ion or "(1st iodine-doped" hydrophilic polymers (for example,  $I_2$ -KI(aq) or "iodine-doped" PA6 or "iodine-doped" PVA, etc.), posterior addition of  $Ag^+$  ion forms precipitation of AgI nano-grains; inner diffusion of  $Ag^+$  ion ("secondary doping") into "iodine doped" hydrophilic polymers can realize "as-shaped" hybrid composite where fillers of inorganic salt grains are dispersed in hydrophilic matrixes.[5]

However, while independent AgI grains are stable at room temperature and show very low solubility in water, AgI precipitates dispersed in polymeric matrixes which are prepared as "as-shaped" composite are not always stable nor unchanged. Inner precipitation of AgI grains in PA6 matrix also shows activity to swelling; dissolution of the "hardly soluble" salt by water swelling is observed in SANS profiles.[6] And even for as hydrophobic matrix, such as "SEBS"-elastomer, inner dispersion of  $Ag^+$  ion and dissolution of AgI or polyiodide ions are also observed.[7] Generally, there is tendency that excessive "secondary doping" induces dissolution of AgI precipitates.

It is one evidence to indicate that  $Ag^+$  ion can be posteriorly diffused into hydrophobic matrixes from aqueous solution, and that inner precipitation of AgI which temporarily formed in the matrixes can be easily dissolved or released with advance of "secondary doping". On considering application or functionality on surface of polymeric materials applied with "iodine-doping", suggested as metallic plating for example, such antinomic process should be also considered.

### REFERENCES:

- [1] A. Kawaguchi, *Polymer*, **35**, 3797-3798. (1994)
- [2] patent. JPN-5444559 (2014).
- [3] A. Kawaguchi, *et.al.*, KURRI Prog. Rep. 2010, 218-218. (2011)
- [4] A. Kawaguchi, *et.al.*, KURRI Prog. Rep. 2014, 114-114. (2015)
- [5] A. Kawaguchi, *et.al.*, *Polym. Prep. Jpn.*, **56**, 769-769. (2007)
- [6] A. Kawaguchi, *et.al.*, KURRI Prog. Rep. 2002, 20-20. (2003)
- [7] A. Kawaguchi, *Polym. Prep. Jpn.*, **60**, 630-630. (2011)

K. Tokunaga, M. Matsuyama<sup>1</sup>, K. Araki, M. Hasegawa, K. Nakamura and Q. Xu<sup>2</sup>

*Research Institute for Applied Mechanics, Kyushu University*

<sup>1</sup>*Hydrogen Isotope Research Center, University of Toyama*

<sup>2</sup>*Research Reactor Institute, Kyoto University*

**INTRODUCTION:** It is of importance to clarify phenomena of implantation, retention, diffusion and permeation of tritium on surface of the armor materials of the first wall/blanket and the divertor on fusion device from a viewpoint of precise control of fuel particles, reduction of tritium inventory and safe waste management of materials contaminated with tritium (T). Refractory metals such as tungsten (W) is potential candidate for an armor of the first wall and the divertor plate of the fusion reactor because of its low erosion yield and good thermal properties. The armor material will be subjected to heavy thermal loads in the steady state or transient mode combined with high energy neutron irradiation that will cause serious material degradation. In addition, high energy runaway electrons would bombard the armor materials along the equatorial plane in fusion device. It is considered that these cause radiation damage and enhance tritium retention. In the present works, T exposure experiments have been carried out on W samples which were irradiated by high energy electrons using LINAC in KURRI of Research Reactor Institute, Kyoto University to investigate effects of high energy electrons irradiation and microstructure on tritium retention of W. In this fiscal year, pure W and recrystallized W were irradiated by high energy electron beam. After that, positron annihilation experiment was carried out to identify the radiation defect. In addition, tritium exposure experiments have been carried out using a tritium (T) exposure device.

**EXPERIMENTS:** W samples used were ITER grade W (IG-W) and recrystallized W. In the case of IG-W, one was W sample (ITER grade W(1)) which the surface were manufactured to be oriented parallel to the rolling surface and rolling direction. The other W sample (ITER grade W(3)) which the surface were manufactured to be oriented perpendicular to the rolling surface and rolling direction. On the other hand, heat treatment was performed at 1800 °C for 1h at high vacuum to recrystallize IG-W. The sizes of W samples were 10mm x 10mm x 1mm. The surface of the both samples were polished to be mirrored. High energy electrons irradiation has been carried out using LINAC in KURRI of Research Reactor Institute, Kyoto University. An energy of electron irradiated was 10 MeV and DPA was  $2.8 \times 10^{-3}$ . Temperature during the irradiation was measured by thermocouples which was contacted with a backside of the W samples. After the electron beam irradiation, positron annihilation

experiment was carried out. In addition, T exposure experiments have been carried out using a T exposure device in University of Toyama. Pressure of the T gas was 1.3 kPa and T exposure was kept for 4 h. T concentration in the gas was about 5 %. Temperatures of pre-heating and T exposures were 100 °C. After the exposure to T gas, T amount retained in surface layers of the sample was evaluated by  $\beta$ -ray-induced X-ray spectrometry (BIXS) and imaging plate (IP) measurements.

**RESULTS:** As shown in Fig. 1, there is little difference between results from W(1) and W(3). On the other hand, after the recrystallization, lifetime from defect ( $\tau_2$ ) increased and intensity of  $I_2$  decreased. This result indicates that defects of the small number with large clusters were formed by the recrystallization. The electron irradiation made life time of  $\tau_2$  small. In addition, intensity of  $I_2$  increased. These indicate that small defects were induced and concentration of the defects increased both of pure W and recrystallized W by the electron irradiation. T exposure experiments have been carried out and impact on the electron beam irradiation of T retention is under investigation.

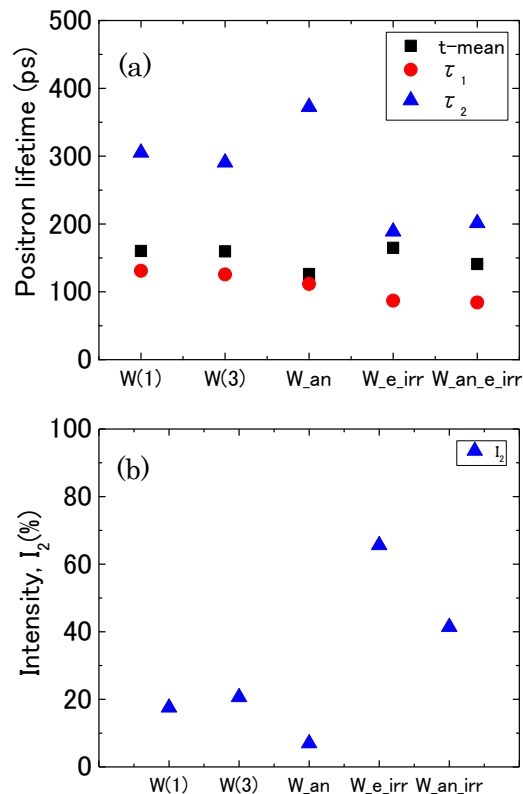


Fig. 1. Positron life time(a) and intensity of  $I_2$  (b). W\_an is the sample which was recrystallized. W\_e\_irr and W\_an\_e\_irr are electron irradiated samples of pure W and recrystallized W, respectively.

## CO4-11 Presence of Diluted High-valence Fe and Sn Ions in Layered Rock-salt Structure

M. Tabuchi and Y. Kobayashi<sup>1</sup>

National Institute of Advanced Industrial Science and Technology (AIST)

<sup>1</sup>Research Reactor Institute, Kyoto University

**INTRODUCTION:** Although the Fe ion in iron oxides has 2+ and/or 3+ states, tetravalent and pentavalent Fe ion can be stabilized in Perovskite structure. Tabuchi et al. found tetravalent Fe ion in  $\text{LiFeO}_2\text{-Li}_2\text{MnO}_3$  solid solution with layered rock-salt structure ( $R\text{-}3m$ ) at 15 years ago [1] using  $^{57}\text{Fe}$  Mössbauer spectroscopy. He detect also pentavalent Fe ion in the solid solution below 10K [2]. Through long-term efforts to brush-up synthetic method, this material is now attractive one as high-capacity positive electrode material [3, 4].

In this work,  $0.2\text{LiFeO}_2\text{-}0.8\text{Li}_2\text{MnO}_3$  solid solution was selected using different synthetic procedure. We succeeded to find hexavalent iron by low-temperature  $^{57}\text{Fe}$  Mössbauer measurements. Although the hexavalent iron can be stabilized at only tetrahedral site, X-ray Rietveld analysis was done.

**EXPERIMENTS:** The  $0.2\text{LiFeO}_2\text{-}0.8\text{Li}_2\text{MnO}_3$  sample was prepared by coprecipitation-calcination method.  $\text{Fe}(\text{NO}_3)_3 \cdot 9\text{H}_2\text{O}$  and  $\text{MnCl}_2 \cdot 4\text{H}_2\text{O}$  reagents dissolved with distilled water. The Fe-Mn aq. soln. (Fe:Mn molar ratio=2:8) was dripped into NaOH solution at 20 °C for 2-3 h. The Fe-Mn coprecipitate was oxidized by bubbling with oxygen for 2 days. After washing and filtration, aged Fe-Mn coprecipitate was dispersed into LiOH soln. ( $\text{Li}/(\text{Fe}+\text{Mn})=2.00$ ). The slurry was dried at 50 °C for 2 days and then the dried mixture was pulverized for calcination. The mixture was firstly calcined at 500°C for 20h under  $\text{O}_2$  flow and then fired at 700 or 750 °C for 20h in  $\text{O}_2$  or  $\text{N}_2$  flow. All products were washed with distilled water, filtered and dried at 100 °C for above characterization.

**RESULTS:** Fig. 1 shows  $^{57}\text{Fe}$  Mössbauer spectra at 3 K for two samples calcined at different temperature in  $\text{O}_2$  flow. The spectra were analyzed by same fitting model: three sextets and one symmetric doublet with different isomer shifts (IS). A sextet with the largest internal field ( $H_i=45\text{-}46$  T) is assigned as high-spin trivalent iron because of its IS value (+0.42-+0.43 mm/s). Other two sextets have almost the same IS value (+0.20-+0.21 mm/s) and different  $H_i$  values (12 and 22T). These parameters indicated that tetravalent irons with two kinds of local structure existed. The origin is still unknown. Surprisingly, the IS value for the doublet (IS=-0.73 mm/s) was quite small, which can be assigned as hexavalent iron like  $\text{BaFeO}_4$ . To the best of our knowledge, this is the first time to detect hexavalent Fe in complex oxides. Since the hexavalent iron can be stabilized at tetrahedral site, careful X-ray Rietveld analysis was performed.

The analysis showed that transition metals existed not only typical four octahedral 4g, 2b, 2c and 4h sites but

also tetrahedral 8j one (5-7 % in occupancy) in monoclinic layered rock-salt structure ( $C2/m$ ). As shown in Fig. 2, the  $M_{8j}\text{O}_4$  tetrahedron adjacent to  $M_{4g}\text{O}_6$  octahedron was highly distorted; they consisted of three short  $M_{8j}\text{-O}$  distances and one long  $M_{8j}\text{-O}$  one. In addition to the above analysis, low-temperature XRD data have to be taken, because the hexavalent iron cannot be detected at 300 K.

After finishing the above analysis, Sn doped samples will be prepared, because tin doped sample is attractive to improve the electrochemical cycle performance.

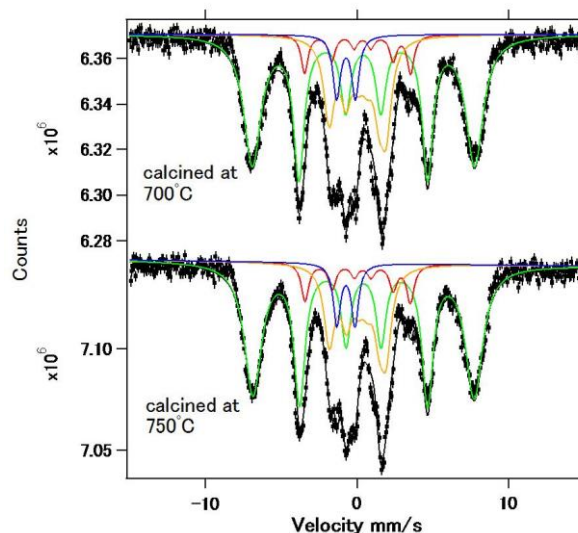


Fig. 1  $^{57}\text{Fe}$  Mössbauer spectra at 3 K for two samples calcined at 700 (upper) or 750 °C (lower part) in  $\text{O}_2$  flow.

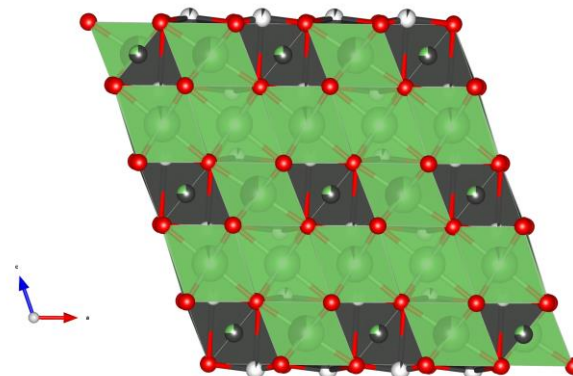


Fig. 2 Applied cation distribution model for X-ray Rietveld analysis. Gray circles correspond to cation on tetrahedral 8j site.

### REFERENCES:

- [1] M. Tabuchi *et al.*, J. Electrochem. Soc., **149** (2002) A509-A524.
- [2] M. Tabuchi *et al.*, J. Appl. Phys., **104** (2008) 043909-1-10.
- [3] M. Tabuchi *et al.*, J. Power Sources, **318** (2016) 18-25.
- [4] M. Tabuchi *et al.*, J. Power Sources, **195** (2010) 834-844.

## CO5-1 Evaluation of Radioactive Cesium Behavior in Natsui River Basin, Fukushima

K. Sato<sup>1</sup>, M. Ikegami<sup>2</sup>, M. Morisada<sup>3</sup>

<sup>1</sup>College of Science and Engineering, Ritsumeikan University

<sup>2</sup>Research Reactor Institute, Kyoto University

<sup>3</sup>Graduate School of Science and Engineering, Ritsumeikan University

### INTRODUCTION:

Most of radioactive cesium (<sup>137</sup>Cs) released by the nuclear accident in 2011 remains in the basin soil, but a part of it has flowed out into the water environment and accumulate in the bottom sediment or moves to further downstream such as bay and sea. For example, in Dam Lake, it was confirmed that about 90% of the <sup>137</sup>Cs which have been flowed from its watershed is accumulated<sup>1)</sup>. It is concerned that <sup>137</sup>Cs remaining in various places such as lake bottom sediments we have an impact on our life through elderution phenomena and bioaccumulation.

In this study, on-site sampling and analysis of samples obtained there were conducted at the Natsui River Basin in Fukushima for the purpose of estimating and predicting <sup>137</sup>Cs concentration and its dynamics in the dam lake. We focus on the particle origin (originated from internal production and derived from river SS) in the dam lake, and report the findings obtained on the <sup>137</sup>Cs concentration and its dynamics.

### SURVEY and EXPERIMENT METHODS:

The area surveyed in this study is the Natsui river basin (750km<sup>2</sup>) in Fukushima, and lake water was collected especially at the Kodama dam located in the middle stream, the Kodama river water that flow into the Kodama dam and the Natsui river water as main stream. At the Kodama dam, bottom sediment and surface water were collected at a point 40m (water depth 55m) upstream from the dam body, and also river water was collected at Kodama and Natsui river. At each site, 1-5 tons of environmental water was locally concentrated by a pore size of 38-250 μm sieves. The recovered particles and sediment samples were brought back to the laboratory and have been freeze-dried. The amount of particles recovered in this survey (on-site concentration) was 50-400 mg dry weight per each point.

For environmental water (30-100L), solid-liquid separation was first carried out by 1μm pore size of GFF. The residue on the GFF was used as a suspended sample, and <sup>137</sup>Cs in the filtrate (30 L) was selectively concentrated with Empore<sup>TM</sup> Rad-disc made by 3M Inc. <sup>137</sup>Cs was analyzed by Ge semiconductor detector (mainly GX 4018, Canberra), CN ratio of particles was analyzed CN coder (NC-22F, Sumitomo Chemical), stable carbon isotope ratio of particles, δ<sup>13</sup>C, was analyzed by mass spectrometer (DELTA V Advantage).

### RESULTS and DISCUSSIONS:

Fig.1 shows the <sup>137</sup>Cs concentrations of 38-250μm parti-

cles at Kodama dam and Kodama river, and the dam sediment in the July and November 2016. The CN ratios of them are also shown in the figure. Particles on the surface water of the dam were estimated to be derived from internal production (i.e., plankton) based on their particle size and CN ratio. <sup>137</sup>Cs concentrations of particles in surface water at the dam were 3-6 times lower than those of the inflowing Kodama river. This fact means that the suspended <sup>137</sup>Cs concentration assumed to be derived from internal production tends to be lower than that derived from outside river. The <sup>137</sup>Cs concentration of the dam sediment was also slightly lower than the SS of the inflowing river, then it was speculated that it was also influenced by particles originating from internal production also from the CN ratio. The ratio, which is corresponding to BCF, of the <sup>137</sup>Cs concentration in the planktonic and dissolved matter at the surface water was estimated as 1.3-3.6 (×10<sup>5</sup> L / kg).

Fig.2 shows the analytical results of distribution coefficient K<sub>d</sub> and δ<sup>13</sup>C of the SS in Kodama dam surface water and Natsui river water. The K<sub>d</sub> was indicated the value obtained by dividing the suspended <sup>137</sup>Cs (Bq/kg-SS) by the dissolved <sup>137</sup>Cs (Bq/L). In many cases at normal stage conditions especially, the K<sub>d</sub> value of dam surface water tended to be smaller than that of river water.

As the results, focusing on the difference of particle origin by δC, seasonal fluctuation was confirmed in dam surface water, unlike river water. Because seasonal variation of δ<sup>13</sup>C in phytoplankton has been reported<sup>2)</sup>, it was indicating that SS of dam surface water was affected by internal production. Since BCF of plankton was lower than the K<sub>d</sub> value of river water, it was suggested that the K<sub>d</sub> value is reduced due to the influence of internal production.

From the results of this study, it was found that the dam lake at the flood stage condition was greatly influenced by the inflowing river. On the other hand, at the normal stage conditions the influence of the origin due to the internal production was larger than that by inflowing of river water, then the influence have been also reflected in dam sediment.

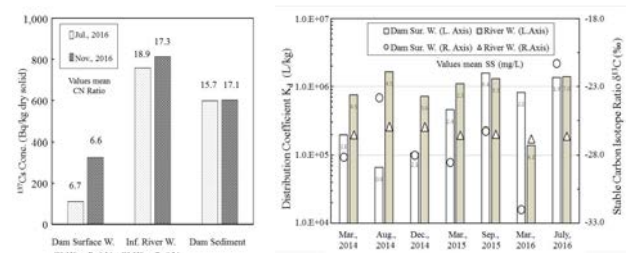


Fig.1: <sup>137</sup>Cs concentration of suspended matter in Kodama dam lake and its influent river (Left figure above)

Fig.2: Partition coefficients and stable carbon isotope ratios of dam surface water and Natsui river water (Right figure above)

### REFERENCES:

- [1] Kitamura *et al.* (2014) *Anthropocene.*, 5, 22-31.
- [2] Yamada *et al.* (1998) *Jpn. J. Limno.*, 59, 409-427.

N. Ito, A. Mizohata, R. Okumura<sup>1</sup> and Y. Iinuma<sup>1</sup>

Radiation Research Center, Osaka Prefecture University,

<sup>1</sup>Research Reactor Institute, Kyoto University

Bromine which is a halogen atom with symbol Br and atomic number 35 naturally exist mainly in the sea water (65mg/L) and industrially used mainly as a organic compounds used for fire-resistant sheet. These consumed compounds are finally burned in the incinerator and exhausted as a gaseous matter. Gaseous bromine can be easily changed to the atmospheric aerosols with its high boiling point (332K). Because of its poison properties the concentration levels and size distribution of bromine in the atmospheric aerosols must be investigated. Here we show the result of observations in bromine in the atmospheric aerosols at Sakai, 2012. Also we show the size distribution of Chlorine as a same halogen atoms to compare the differences of properties owing to the boiling point (239K Cl).

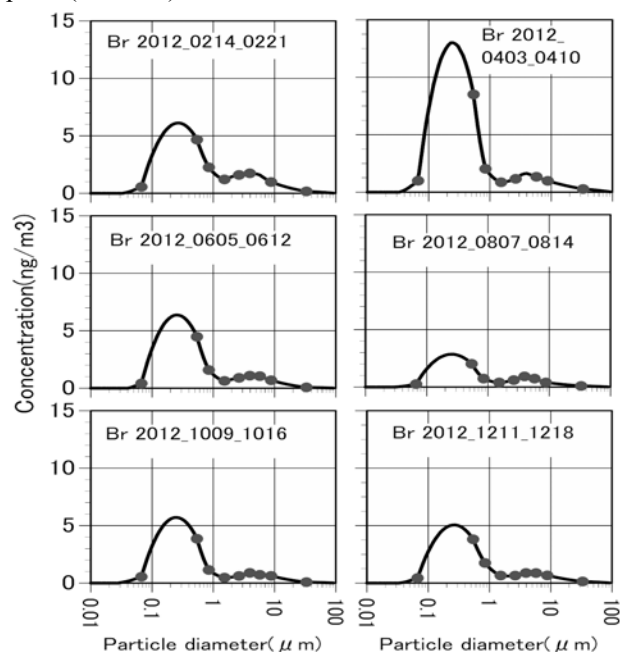


Fig. 1 Size distribution of Bromine observed at Saka, 2012

The atmospheric aerosols were collected on 6 periods (Feb.12-14, Apr.03-10, Jun.05-12, Aug.07-14, Oct.09-16, Dec.11-18) in 2012. The aerosols were collected on a polyethylene sheet attached with 9 stages by the ranges (>11μm, 7.0-11.0μm, 4.7-7.0μm, 3.3-4.7μm, 2.1-3.3μm, 1.1-2.1μm, 0.65-1.1μm, 0.43-0.65μm, <0.43μm) using Andersen Sampler. Bromine and Chlorine in these samples were analyzed by Neutron Activation Analysis using Kyoto University Reactor.

We have got the size distribution profile of Bromine which have high concentration in fine (<1μm) particles that were products from gaseous bromine and short coarse (>1μm) concentrations mainly come from sea salt particle (Fig.1). The peaks in fine range can be found

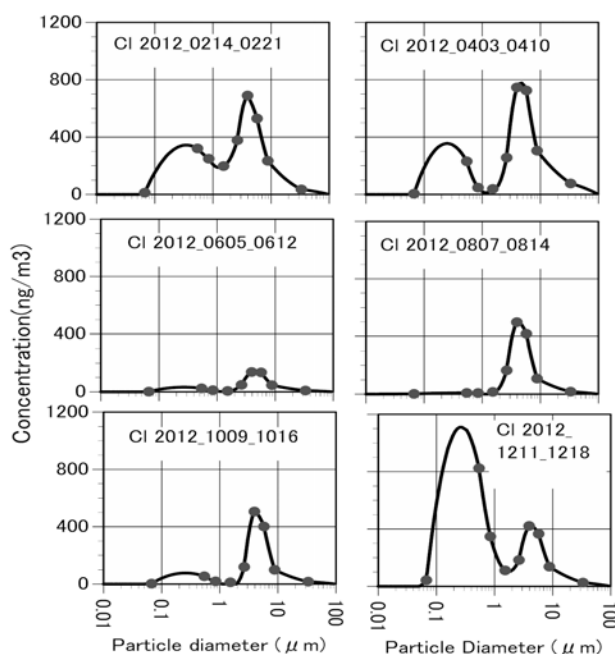


Fig. 2 Size distribution of Chlorine observed at Saka, 2012

around 0.2μm and concentration is changed from 1.2 to 4.3 (ng/m<sup>3</sup>). Peaks in fine range for Chlorine can be found as a smaller than that in coarse range except winter period (1211-1218) (Fig.2).

Concentrations in (C) and fine (F) ranges and ratio to Na are listed on Table1. Ratios to Na in the coarse for both of Bromine and Chlorine are small for that of sea salt, extremely lowest in summer (0807-0814). This decrease suggest the halogen loss by the temperature effect.

**Table1 Concentrations of Bromine and Chlorine in coarse range (C, >2.1μm) and fine range (F <2.1μm), ratio to Sodium (Br/Na, Cl/Na) in coarse range (Br/Na=6.2x10<sup>-3</sup>, Cl/Na=1.8 in sea water)**

Period in 2012	Concentration (ng/m <sup>3</sup> )				Ratio to Na in coarse range	
	Br		Cl		Br x10 <sup>-3</sup>	Cl
0214-0221	1.1	2.9	250	170	6.8	1.5
0403-0410	1.1	4.3	290	44	3.8	0.99
0605-0612	0.57	2.0	42	11	5.0	0.47
0807-0814	0.49	1.2	110	18	2.8	0.58
1009-1016	0.46	2.4	91	20	3.2	0.64
1211-1218	0.6	2.1	140	230	5.9	1.3

N. Hasebe, K. Miura<sup>1</sup>, M. Ogata<sup>1</sup> and R. Hayasaka<sup>1</sup>

*Institute of Nature and Environmental Technology, Kanazawa University*

<sup>1</sup>*Graduate School of Natural Science and Technology, Kanazawa University*

**INTRODUCTION:** Luminescence dating observes the natural accumulated radiation damage caused by radioisotopes such as U and Th as the form of glow after stimulation by heating or lightening. Thermally stimulated luminescence from calcite shows strong red emission. When thermoluminescence characteristics of calcites are examined using natural occurring calcite, their response to the various radiations depends on minor chemistry (Fe, Mg, Mn and Sr). In this study, calcites with controlled impurity concentrations were synthesized and analyzed to evaluate relationship between multiple impurity concentration and thermoluminescence properties quantitatively, together with natural calcites.

**EXPERIMENTS:** Calcite were synthesized from sodium carbonate (>99.8wt%) and calcium chloride (>95 wt%). Iron (II) chloride (>99.0-102.0 wt%), magnesium chloride (>98.0wt%), and manganese chloride (>99.0- wt%) were added at different levels to produce calcites with different amount of impurity. Chemical composition of resultant calcite were measured by LA-ICP-MS. Gamma irradiation was carried out at the <sup>60</sup>Co gamma irradiation facility at Kyoto University Research Reactor. Alpha and beta ray irradiations were carried out with disc-type <sup>241</sup>Am and <sup>90</sup>Sr source, respectively. Given doses by Gamma and beta irradiation were estimated by quartz irradiated together with synthesized calcite. A given dose by alpha irradiation was estimated by alpha track counting. Then luminescence emission from calcite was measured by the luminescence reader MOSL-22, and dose was estimated by the external x-ray source, whose dose rate is calibrated as 0.1 Gy/sec with quartz. This measured dose on calcite was compared to the given dose on quartz, and the ratio (calcite/quartz) was calculated for each irradiation (gamma, beta). Results on alpha irradiation will be reported later.

**RESULTS:** Calcite/quartz ratios in dose estimate by luminescence were different among samples. Gamma and beta efficiencies are 0.115-0.398 and 0.122-0.481, respectively, and it indicates that equivalent doses of calcite samples were underestimated with X-ray calibrated using quartz. The gamma and beta efficiencies may be inversely proportional to Mg+Mn+Fe and (Mg+Mn+Fe)/Fe, respectively (Fig1&2). These may be caused by differences in the common substitution elements of calcite and quartz, as well as the interactions

between medium with different atomic numbers and various radiation energies. The contribution of photoelectric effect increases with increasing impurity (Mg, Mn and Fe) concentration for radiation of 0.059MeV (tungsten target X-ray), thus gamma efficiency may decrease with increasing total impurity concentrations (Mg+Mn+Fe). Beta efficiencies must be considered together with the CL emission. Fe, which works as quencher in CL, may keep radiation energy from beta ray instead of transmitting to activator, thus accumulated dose of calcite may increase with increasing Fe concentration; therefore, beta efficiency may depend on (Mg+Mn+Fe)/Fe.

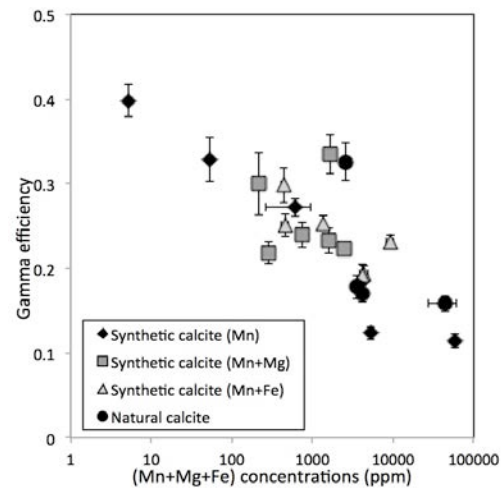


Fig. 1. Gamma efficiency as a function of (Mg+Mn+Fe).

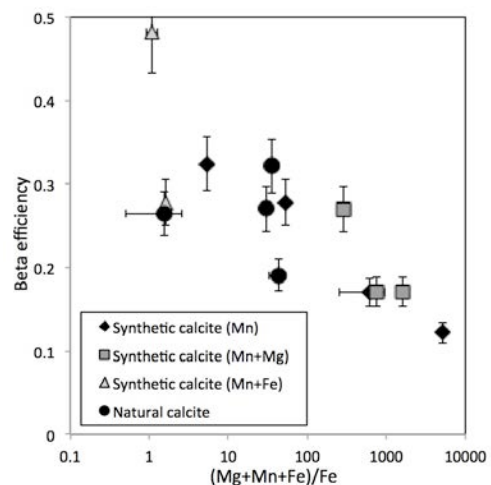


Fig. 2. Beta efficiency as a function of (Mg+Mn+Fe)/Fe.

## CO5-4 Application of Neutron Activation Analysis to Micro Gram Scale of Solid Samples

S. Sekimoto, N. Shirai<sup>1</sup> and M. Ebihara<sup>1</sup>

Research Reactor Institute, Kyoto University

<sup>1</sup> Graduate School of Science, Tokyo Metropolitan University

**INTRODUCTION:** Instrumental neutron activation analysis (INAA) is often used in cosmochemistry, where meteorites are the objects for INAA. Chondritic meteorites (chondrites) and iron meteorites contain relatively high contents of Co and Ir compared with those in the earth crust. As Co and Ir have high sensitivity in INAA, they can be good markers for the identification of such extraterrestrial materials. In NAA of chondrites, a few tens mg of specimen is commonly used. For such a case, a few hundred  $\mu\text{g kg}^{-1}$  of Ir and a few hundred  $\text{mg kg}^{-1}$  of Co can be reliably determined. When an extremely small size (e.g., micro gram) of samples such as micrometeorites recovered on the Earth surface and tiny particles returned from extraterrestrial asteroids are to be analyzed by INAA, the conventional INAA procedure used for a few tens mg is not suitable. For such tiny samples, neutron irradiation with high neutron flux and long irradiation time (namely, high neutron dose) is required. Recently we have presented the INAA procedure for micro gram scale of solid samples [1]. In this report, one typical example for the application of the proposed procedure is shown with limited scientific discussion.

**RESULTS:** Instrumental NAA results of the magnetic spherule are summarized in Table 1, where elemental concentrations are also given.

**Table 1** Elemental contents in magnetic spherule analyzed by INAA in this study

	Content	Concentration
Sm	< 0.4 pg	< 0.06 $\text{mg kg}^{-1}$
La	< 1.6 pg	< 0.24 $\text{mg kg}^{-1}$
Sc	< 1.8 pg	< 0.27 $\text{mg kg}^{-1}$
Fe	$3.90 \pm 0.05 \mu\text{g}$	$601 \pm 8 \text{ g kg}^{-1}$
Na	$0.406 \pm 0.008 \text{ ng}$	$62.5 \pm 1.3 \text{ mg kg}^{-1}$
Co	$20.4 \pm 0.2 \text{ ng}$	$3140 \pm 40 \text{ mg kg}^{-1}$
Cr	$1.06 \pm 0.06 \text{ ng}$	$164 \pm 9 \text{ mg kg}^{-1}$
Ni	$328 \pm 4 \text{ ng}$	$50 \pm 1 \text{ g kg}^{-1}$
Au	$0.59 \pm 0.05 \text{ pg}$	$0.091 \pm 0.007 \text{ mg kg}^{-1}$
Zn	< 0.98 ng	< 0.1 $\text{g kg}^{-1}$
Ir	$16.3 \pm 0.4 \text{ pg}$	$2.51 \pm 0.06 \text{ mg kg}^{-1}$

The magnetic spherule analyzed is characterized by high concentrations of iron ( $601 \text{ g kg}^{-1}$ ) and nickel ( $50 \text{ g kg}^{-1}$ ). These two elements comprise 65% of the bulk mass. Its Ir concentration ( $2.51 \text{ mg kg}^{-1}$ ) also is extremely high compared with terrestrial samples. Apparently, this spherule is extraterrestrial in origin. Such spherules are called cos-

mic spherules and often picked up from the deep sea sediment [2].

Elemental abundances of this spherule are illustrated in Fig. 1, where abundances are normalized to CI chondrite values [3]. Data for the other magnetic spherules from our previous work [4] are also indicated for comparison. Based on the elemental composition, magnetic spherules can be classified into two groups: one group have high CI-normalized abundances of Ir, Co, Ni and Fe (siderophile elements), and low abundances of Cr and Sc (lithophile elements), whereas another group have unfractionated CI-normalized abundances of both siderophile and lithophile elements. The magnetic spherule analyzed in this study apparently belongs to the former group. There has not been reported for Sc values for this group. It now becomes obvious that Sc is even lower than Cr in their CI-normalized abundances.

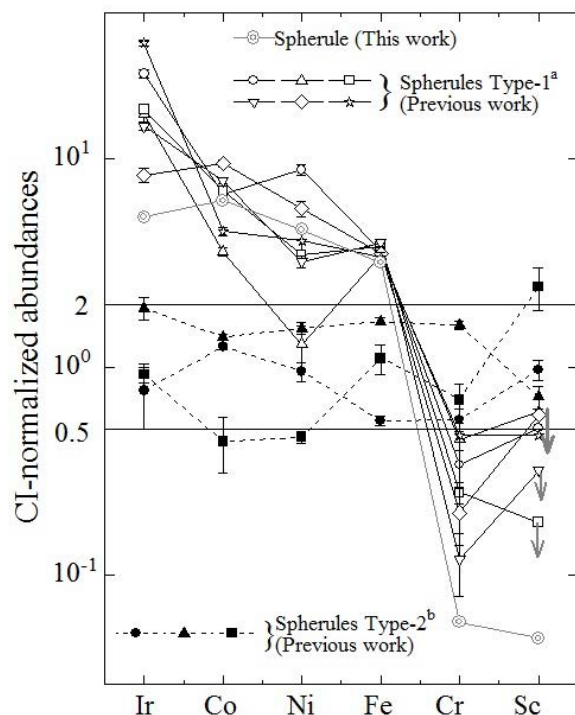


**Fig. 1** CI-normalized abundances of Ir, Co, Ni, Fe, Cr and Sc in cosmic spherules

### REFERENCES:

- [1] S. Sekimoto *et al.*, J Radioanal Nucl Chem, **307** (2016) 1757-1764.
- [2] J. Murray & A.F. Renard (1891) Report on Deep-Sea Deposits based on the specimens collected during the voyage of H.M.S. Challenger in the years 1872 to 1876, Neill and Company, Edinburgh
- [3] E. Anders & N. Grevesse, Geochim Cosmochim Acta, **53** (1989) 197-214.
- [4] S. Sekimoto *et al.*, J Radioanal Nucl Chem, **278** (2008) 319-322.

H. Hashizume, A. Uehara<sup>1</sup>, S. Fukutani<sup>1</sup>, K. Fujii and T. Ando

National Institute for Materials Science

<sup>1</sup>Research Reactor Institute, Kyoto University

**INTRODUCTION:** Oxides like MgO and CaO react with water ( $H_2O$ ) very easily and hydroxides such as  $Mg(OH)_2$ , and  $Ca(OH)_2$  are formed. The reaction (e.g. hydration) between the oxide and water is very quick, the reaction also happens in the air. For that, CaO is used as a desiccant. The oxide will be able to be reacted with tritium water, easily. Tritium is a radioisotope and has been increasing by the nuclear testing and utility of nuclear power. In Japan, the accident of Fukushima the 1st atomic power station had released many kinds of radioisotopes and we are still removing the material with radioisotopes and there are some radioisotopes that the removal is difficult. Tritium is one of them. Tritium was a radioisotope of hydrogen. The characteristics of tritium are almost the same as hydrogen. In water, tritium water behaves almost similar to water. The boiling temperature and the decomposition of the electrolysis of tritium water are slightly different from those of water. If the extreme care should not be taken to remove tritium, it is very difficult to remove tritium water from water by the boiling temperature and decomposition of the electrolysis. We investigate that the hydroxide prefers tritium ion to proton, or proton to tritium ion, when the hydroxide is formed from the oxide and water including tritium water [1].

**EXPERIMENTS:** We used MgO (light) to be on the market. Since CaO reacts with water very easily, it was very difficult to prepare the treatment.  $Ca(OH)_2$  can react  $CO_2$  or carbonic acid, easily, and OH and OT of calcium hydrate removed to water again. We did not use CaO. For the reaction of MgO and tritium in water, we prepare the glass bottles with  $10\text{ cm}^3$  of water including tritium water and 1, 1.5 or 2g of MgO. The bottles were left for 1 to 24 h. On the other hand, glass bottles were stirred by the shaker for 1 to 24 h. After our purpose time, suspension was filtered by 0.45 or 0.2  $\mu\text{m}$  of a disposable filter. For the measurement of concentration of tritium,  $0.1\text{ cm}^3$  of supernatant was mixed by  $20\text{ cm}^3$  of the liquid scintillator. The mixture solution was measured by a scintillation detector (Packard, Liquid Scintillation Analyzer).

**RESULTS:** Figure 1 shows the removal of tritium from water including tritium water by MgO to the variation of time. In the case of Fig. 1 (a), the bottles were not shaken but left on the table. In the reaction with MgO, tritium would be caught to  $Mg(OH)_2$  formed. The concentration of tritium was smaller than the initial water. For leaving on the table, the surface of MgO reacts with water and  $Mg(OH)_2$  would hardly removes from the surface. In Fig. 1 (a), the reaction of MgO and

water would be quick and the removal might be high. The removal would be stable or decreasing after 5 h. MgO would not react with water on the surface. When the bottles were stirred (Fig.1, b), the removal shows slightly negative slope to the time. After the reaction, the concentration of tritium would increase in supernatant, because MgO preferred the reaction of proton to that of tritium and  $H_2O$  would decrease slightly in supernatant. Most MgO reacts with water ( $H_2O$ ) and  $Mg(OH)_2$  is formed. MgO is a cubic structure and  $Mg(OH)_2$  is a hexagonal structure.  $Mg(OH)_2$  would be removed from MgO surface because the particles were collided by the stirring. Water would be contacted with a fresh surface of MgO. In Fig. (b), the removal is almost around zero within 5 h after shaking. We can not find out the selection of tritium or proton of MgO. The removal would be negative, gradually in a long shaking time. In both Fig. 1 (a) and (b), the equilibrium reaction would not be achieved. We would investing the difference between Fig. 1 (a) and (b).

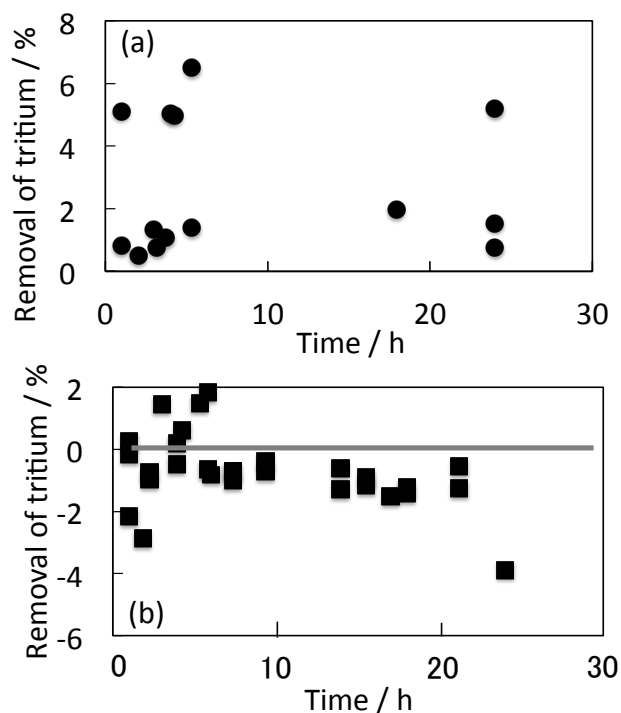


Fig. 1 Removal of tritium to the variation of time when the bottles were left (a), and the bottles were shaken (b). The gray line in (b) shows zero. The removal (%) was calculated by  $R=(C_0-C)/C_0 \cdot W \cdot 100$ , where R is removal,  $C_0$  is the count of the initial water including tritium water, C is the count of supernatant after the contact with MgO and W is the weight of MgO.

#### REFERENCE:

[1] H. Hashizume et al. Shutugan Bango Tokugan 2016-135839, Japanese Patent Office(2016).

# CO5-6 Chemical Variations of Miller Range 091010 (CV) Collected in the Ice at Miller Range, Antarctica

N. Shirai, S. Sekimoto<sup>1</sup> and M. Ebihara

Department of Chemistry, Tokyo Metropolitan University  
<sup>1</sup>Research Reactor Institute, Kyoto University

**INTRODUCTION:** Most of meteorites are currently collected from cold and hot deserts. As these meteorites may have resided on the Earth's surface, they have experienced variable degrees of terrestrial weathering. Terrestrial weathering obscures petrographic and chemical features, leading to misclassification and misunderstanding of geochemistry and cosmochemistry of these meteorites. In addition, misinterpretations probably result from sampling effect [1]. A large data set for carbonaceous chondrites was obtained by using 250-350 mg of sample [2]. It was reported that this amount of sample is not enough to obtain representative chemical compositions [1]. Therefore, we examine how sampling problem affects chemical classification by using Miller Range (MIL) 091010 (CV) which was collected in the ice at Miller Range, Antarctica.

**EXPERIMENTS:** Five different aliquots were taken from MIL 091010. These five samples were analyzed by INAA and IPAA at the Kyoto University Research Reactor Institute. For INAA, samples were irradiated two times with different irradiation periods which are adjusted for the half-lives of the nuclides usable for determining elemental abundances. For IPAA, electrons are accelerated by the linear accelerator to 20 MeV, with an electron current of 120  $\mu$ A. The samples were irradiated for 30 hrs. For comparative method, JB-1 was used as reference standard.

**RESULTS AND DISCUSSION:** Twenty nine elements could be determined by using INAA and IPAA. Sodium, Mg, K, Ca, Sc, Ti, Cr, Mn, Co and Ni were determined by both INAA and IPAA. Our data obtained by these two methods are in excellent agreement with each other. Heterogeneity of chemical compositions is significantly higher (less than 10% for Mg, Cr, Mn and Fe; more than 20% for other elements) than the previous study [2]. Carbonaceous chondrites are grouped into main eight groups (CI, CM, CO, CV, CK, CR, CH and CB) and C-ungrouped derived from diverse asteroids according to petrological, mineralogical, chemical and oxygen isotopic features. This meteorite was grouped into CV based on petrological and mineralogical studies [3]. It has been shown by Goodrich and Delaney [4] that carbonaceous chondrites can be easily distinguished from each other in Fe/Mn and Fe/Mg ratios. Figure 1 compared Fe/Mn and Fe/Mg ratios of carbonaceous chondrites. As seen in Fig. 1, our five samples have Fe/Mn and Fe/Mg ratios similar to those for CV and CK chondrites. It was reported that there are no clearly resolvable differences between CV and CK chondrites [5]. Carbonaceous chondrites can be

also distinguished from each group based on volatile elements abundances relative to refractory elements abundances. Figure 2 shows Al/Mn and Zn/Mn ratios of our five samples. Most samples do not fall in the ranges of CV and CK chondrites. It was observed that variations of Al/Mn ratios among the five samples are significantly higher than those of Zn/Mn ratios. The sample mass of about 0.6 g is not large enough to obtain the representative chemical compositions. Aluminum is cosmochemically grouped into refractory elements, while Mn is grouped into moderately volatile elements. In CV chondrites, a major host phase for Al is considered to be Ca-Al-rich inclusion (CAI). Therefore, observed large variations of Al/Zn ratio are attributed to the heterogeneous distribution of CAIs. The two samples (11,04 and 11,07) have higher refractory element abundances than those for the other three samples.

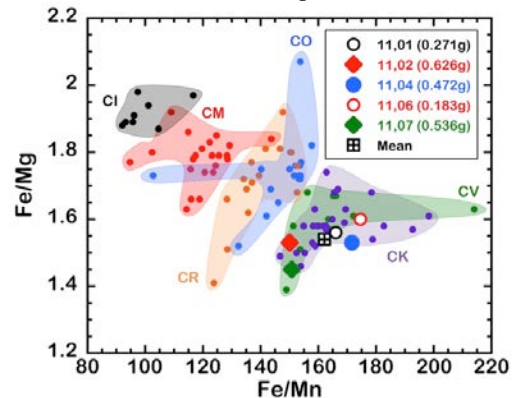


Figure 1. Fe/Mn vs. Fe/Mg diagrams for carbonaceous chondrites.

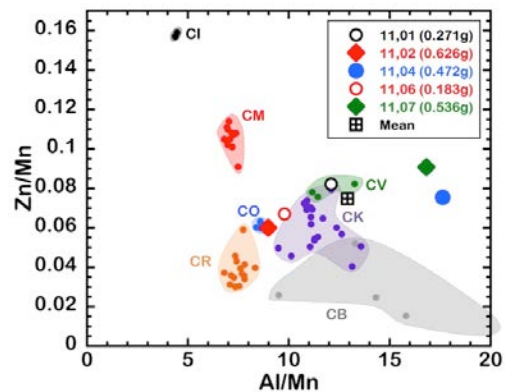


Figure 2. Al/Mn vs. Zn/Mn diagrams for carbonaceous chondrites.

## REFERENCES:

- [1] J. R. Hass and L. A. Haskin, *Meteoritics*, **26** (1991) 13-26.
- [2] G. W. Kallemeyn and J. T. Wasson, *GCA*, **45** (1981) 1217-1230.
- [3] Antarctic Meteorite Newsletter 33 (2), September 2010.
- [4] C. A. Goodrich and J. S. Delaney *GCA*, **64** (2000) 149-160.
- [5] J. T. Wasson et al. *GCA*, **108** (2013) 45-62.

## CO6-1 Design and Synthesis of Boron-containing Compounds for Effective Accumulation in Tumor Tissues and Detection by Boron Magnetic Resonance Imaging

S. Aoki<sup>1</sup>, T. Tanaka<sup>1</sup>, Y. Hisamatsu<sup>1</sup>, Y. Sawamoto<sup>1</sup>, Rikita Araki<sup>2</sup>, Takaomi Saido<sup>3</sup>, T. Suzuki<sup>4</sup>, K. Horie<sup>4</sup>, Ryo Abe<sup>4</sup>, S. Masunaga<sup>5</sup>, N. Kondo<sup>5</sup>, Y. Sakurai<sup>5</sup>, and K. Ono<sup>5</sup>

<sup>1</sup>Faculty of Pharmaceutical Sciences, Tokyo University of Science

<sup>2</sup> Bruker Biospin K. K.

<sup>3</sup>RIKEN Brain Science Institute

<sup>4</sup>Research Institute of Biomedical Sciences, Tokyo University of Science

<sup>5</sup>Research Reactor Institute, Kyoto University

**INTRODUCTION:** Boron neutron capture therapy (BNCT) is one of powerful therapies for local tumor control in the treatment of brain tumor, melanoma, and so on [1]. Our object in this work is to develop new methods for the tumor-specific accumulation of boron-containing compounds and the real-time detection of B concentrations in local tumor tissues. In this study, we have designed and synthesized new boron compounds appended with glucose moiety and metal chelators for BNCT and B NMR (nuclear magnetic resonance) or MRI (magnetic resonance imaging) [2].

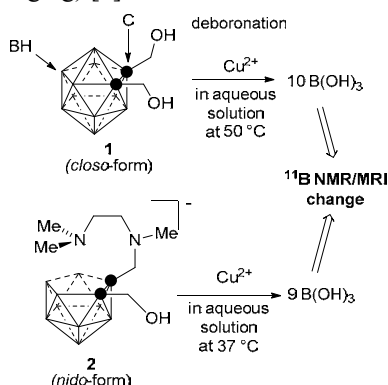


Fig 1. Deboronation reaction of carborane derivatives **1** and **2**, induced by Cu(II) in aqueous solutions.

### EXPERIMENTS and RESULTS:

#### <sup>11</sup>B NMR and MRI change of carborane derivatives by decomposition reaction promoted by copper(II).

Decomposition reaction of **1** and **2** was by <sup>11</sup>B NMR and MRI. Interestingly, the probe **2** undergoes faster decomposition than that of **1** at 37 °C and neutral pH, which was successfully detected on <sup>11</sup>B NMR and MRI [3,4].

#### Concise and versatile synthesis of natural product derivatives that possess B-cluster parts

Sulfoquinovosyl acylpropanediol (SQAP) has been reported to show a variety of biological activities, including accumulation in tumor cells and the inhibition of tumor cell growth. We developed a new concise and versatile synthesis of SQAP itself and derivatives bearing iodoaryl groups and boronclusters (**5**) starting from compound **3** via the selective acylation at C1 position of the intermediate **4** [5].

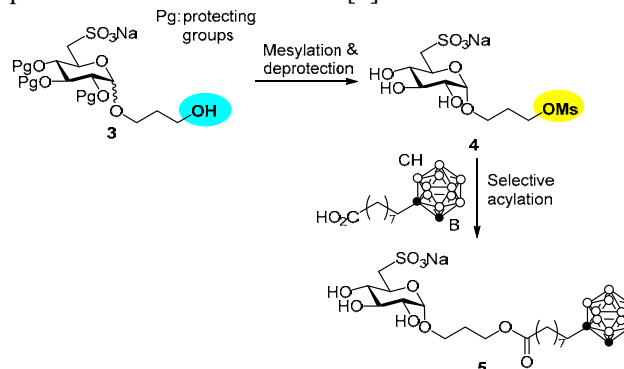


Fig 2. The synthetic route for preparing SQAP derivatives in this study

#### Design and synthesis of new carriers of boron-containing compounds.

The aforementioned results prompted us to design and synthesize new carrier compounds of B-containing compounds. It was found that uptake of the conjugate compounds of our new carriers and B-containing compounds is almost similar to boronylphenylalanine (BPA) (these structures are not shown in this paper, because they will be submitted to the patent in due course).

### REFERENCES:

- [1] a) R. F. Barth *et al.*, *Clin. Cancer Res.*, **11** (2005) 3987-4002. b) R. F. Barth *et al.* *Rad. Oncol.* **7** (2012) 146-166.
- [2] a) G. W. Kalbalka, *et al.* *J. Neuro-Oncol.* **33** (1997) 153-161. b) P. Bendel, *NMR in Biomed.* **18** (2005) 74-82.
- [3] T. Tanaka *et al.*, *Eur. J. Inorg. Chem.* 1819-1834 (2016).
- [4] T. Tanaka *et al.*, *Eur. J. Inorg. Chem.* 3330-3337 (2016).
- [5] T. Tanaka *et al.*, *Chem. Pharm. Bull.* **65**, 566-572 (2017).

K. Akamatsu, N. Shikazono and T. Saito<sup>1</sup>

*Irreparable DNA Damage Analysis Research Group,  
Quantum Beam Science Research Center, Japan Atomic  
Energy Agency (JAEA)*

<sup>1</sup>*Research Reactor Institute, Kyoto University*

### INTRODUCTION:

DNA lesions induced by ionizing radiation and chemicals can cause mutation and carcinogenesis. In particular, “clustered damage” site, that is a DNA region with multiple lesions within one or two helical turns, is believed to hardly be repaired. This damage is considered to be induced, *e.g.*, around high-LET ionizing radiation tracks. However, detail of the damage is not known. We have already developed a method for estimating degree of localization of abasic sites (APs) in DNA using Förster resonance energy transfer occurred between different fluorescence probes (“hetero-FRET”) using Alexa350 and Alexa488 [1]. The results showed that <sup>12</sup>C<sup>5+</sup> beam produced close APs within a track: the apparent distance calculated was approximately 17 base pairs [2]. This finding indicates that *direct radiation effect* of <sup>12</sup>C<sup>5+</sup> beam near the Bragg peak produces clustered DNA damage. We have recently applied the method to DNA in a cell-mimetic radical scavenging condition. However, there are some problems of the complex protocol and of the sensitivity due to the low extinction coefficient of Alexa350. We have, therefore, developed “homo-FRET” occurred between two or more Alexa488 molecules. We will obtain magnitude of FRET also from “fluorescence anisotropy” of homo-FRET between Alexa488 molecules. The new protocol using homo-FRET enables us to estimate DNA damage localization without any enzymes and improves sensitivity to detect a clustered damage.

### EXPERIMENTS:

#### ●Sample preparation and irradiation

The plasmid DNA digested by Sma I was used (linear form). The DNA was dissolved to be 0.1 g/L in 0.2 M Tris-HCl buffer (pH 7.5) which is a cell-mimetic condition in relation to radical scavenging capacity. Twenty microliters of the DNA solution was transferred to a microtube (0.5-mL size), and was irradiated with <sup>60</sup>Co  $\gamma$ -rays (LET:  $\sim$ 0.2 keV/ $\mu$ m; Kyoto University Research Reactor Institute: KURRI) as a standard radiation source. Moreover, the DNA solution was irradiated with carbon ion beam (LET:  $\sim$  90 keV/ $\mu$ m) at HIMAC (National Institute of Radiological Sciences, QST).

#### ●Preparation of fluorophore-labeled irradiated DNA and the FRET observation

The irradiated DNA (10  $\mu$ L in water) and 10  $\mu$ L of 100 mM Tris-HCl (pH 7.5) were mixed in a microtube. Two microliters of Alexa488/DMSO was added to the DNA solution and was incubated for 24 h at 35°C. The fluorophore-labeled DNA was purified by ethanol-precipitation followed by ultrafiltration. The fluores-

cence anisotropy was measured at 525 nm (ex. 470 nm).

The anisotropy,  $\langle r \rangle$ , is defined as follows:

$$\langle r \rangle = \frac{I_{VV} - G \cdot I_{VH}}{I_{VV} + 2G \cdot I_{VH}},$$

where  $I_{VV}$  is the fluorescence intensity when the excitation and emission polarizers are both vertically oriented.  $I_{VH}$  is one when the excitation/emission polarizers are vertically/horizontally oriented.  $G$  is the grating factor defined as  $I_{HV}/I_{HH}$ .

### RESULTS AND DISCUSSION:

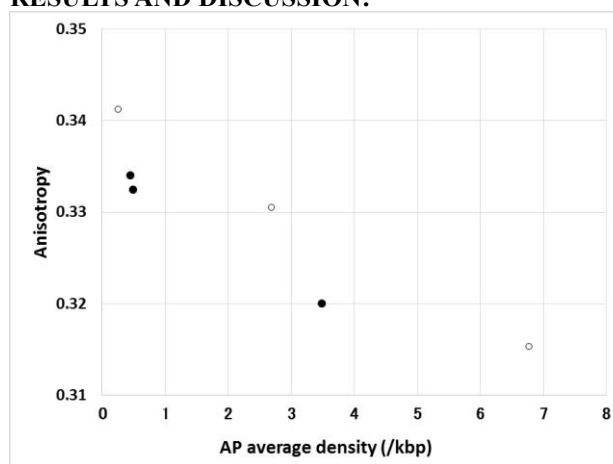


Fig. 1. Relationship between AP average density (the number of APs per kilo base pairs) and fluorescence anisotropy for <sup>60</sup>Co  $\gamma$ -rays (o) and carbon ion beam (HIMAC) (●).

In general, fluorescence anisotropy decreases with increasing FRET [3]. As shown in Fig.1, there was a little difference between the  $\gamma$ -ray data points and a theoretical curve based on exponential distribution. This finding suggest that APs produced by the  $\gamma$ -rays are likely to be localized compared to those randomly distributed. This tendency is similar to the hetero-FRET results as shown previously [2]. A radiation “spur” on or nearby DNA might sometimes produces clustered damage. On the other hand, the anisotropy curve (points) for carbon ion beam was slightly lower than that for the  $\gamma$ -rays, whereas that for carbon ion beam to dry DNA was much lower than these experiment to aqueous DNA (data not shown). This implies that clustered DNA damage mainly occurs by direct radiation effect.

### REFERENCES:

- [1] K. Akamatsu, N. Shikazono, *Anal. Biochem.* **433** (2013) 171-180.
- [2] K. Akamatsu, N. Shikazono, and T. Saito, *Radiat. Res.* **183** (2015) 105-113.
- [3] L. W. Runnels, and S. F. Scarlata, *Biophys. J.* **69** (1995) 1569.

T. Takata<sup>1,2</sup> and N. Fujii<sup>2</sup><sup>1</sup>Tokyo University of Pharmacy and Life Sciences<sup>2</sup>Research Reactor Institute, Kyoto University

**INTRODUCTION:** The passive chaperone lens  $\alpha$ -crystallin ( $\alpha$ -Crys), a small heat shock protein, is composed of two subunits ( $\sim 20$  kDa)  $\alpha$ A- and  $\alpha$ B-crystallin ( $\alpha$ A-Crys and  $\alpha$ B-Crys), which form a hetero-oligomeric and polydisperse complex with molecular mass of  $\sim 600$  kDa in the vertebrate lenses. Recent studies by LC/MS/MS analysis have shown that many aspartyl residues (Asp) in  $\alpha$ A-Crys inverted to isomers (L $\beta$ -Asp, D $\alpha$ -Asp, D $\beta$ -Asp) with age (1-2). However, it is not well understood whether Asp isomers in native polymeric  $\alpha$ A-Crys are different from those in dissociated  $\alpha$ A-Crys. In the present study, we examined to clarify the isomerized Asp in dissociated  $\alpha$ A-Crys, which may contribute to abnormal lens protein subunit-subunit interactions in aged lens.

**EXPERIMENTS:** Lens of four different ages (42, 54, 69 and 83 years old) were homogenized, centrifuged, and the soluble fraction was applied to size-exclusion chromatography (Fig. 1). The polymeric and monomeric  $\alpha$ A-Crys fractions were independently obtained, and then digested by trypsin. Each tryptic peptide was applied to mass spectrometry equipped with nano-scale liquid chromatography to extract each of  $\alpha$ A-Crys-derived peptides containing Asp isomers. The ratio of Asp isomers was determined by the comparison of peak area from four Asp isomer containing peptide.

### Exp 1: Asp in $\alpha$ A-crystallin monomeric state

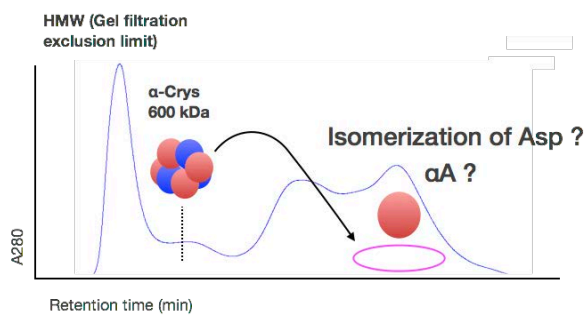


Fig. 1. Experiment design. This is typical size exclusion chromatograms from aged lens soluble fraction. The  $\alpha$ A-Crys hetero-oligomer was eluted at early time. The  $\alpha$ A-Crys monomeric fraction should be eluted at later in aged lens. Each fraction was measured by absorbance at 280 nm during chromatography, fractionated and applied for D/L analysis independently.

**RESULTS:**  $\alpha$ A-Crys was identified as a polymeric and monomeric state in the soluble fraction of aged lens. The isomerization of Asp 58, Asp 84 and Asp 151 of  $\alpha$ A-Crys were highly detectable in the monomeric fraction, but not those in the polymeric one. These results showed that the distribution of Asp isomers is different between the dissociated and aggregated states of  $\alpha$ -Crys in aged lens. Furthermore, The ratios of Asp isomers at the residues, 58, 84 and 151 in monomeric  $\alpha$ A-crystallin were age-dependent and similar to the previously reported ratio in  $\alpha$ A-crystallin from the water-insoluble fraction of aged lens (Fig. 2). Thereby, age-dependent Asp isomerization in  $\alpha$ -Crys is likely to contribute to the solubility of lens protein in aged lens. Age-dependent isomerization of Asp is also stress dependent. The more damage in lens, the more isomerization would be presented in lens Crys even in the same age. In future study, we will add various stresses into lens Crys such as UV,  $\gamma$ -ray and neutron beam to cause oxidative damage, and quantitated isomerization. From current study, our conclusion is that the isomerization of Asp as well as many other modifications would reduce the normal subunit-subunit interaction of  $\alpha$ -Crys with aging, resulting in senile cataract formation.

### Age-dependent isomerization of Asp 58 in monomeric $\alpha$ A-crystallin

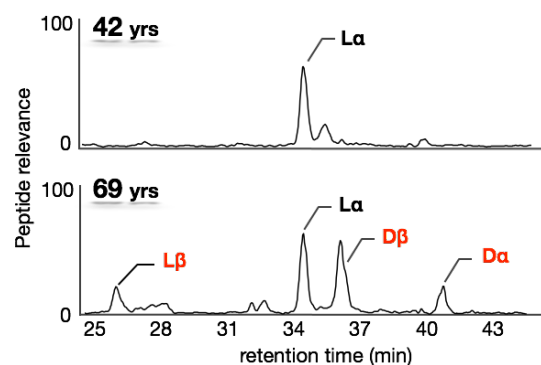


Fig. 2. Age-dependent isomerization of Asp 58 in  $\alpha$ AT6 from the monomeric crystallin fraction. The isolated monomeric fraction was further digested by trypsin and applied for LC-MS/MS analysis. Top panel; 42-year-old lens monomeric crystallin fractions. Bottom panel; 69-year-old lens monomeric crystallin fractions.

### REFERENCES:

- [1] N. Fujii *et al.*, J Biol Chem. **287** (2012) 39992-40002.
- [2] H. Sakaue, *et al.*, Biochimica et biophysica acta. **1854** (2015), 1-9.

## CO6-4 LC-MS/MS Analysis of Post-translational Modifications of Lens Protein in Patients with Retinitis Pigmentosa

Y. Ikeda, I. Kim<sup>1</sup>, S. Nakatake, Y. Murakami and N. Fujii<sup>1</sup>

*Department of Ophthalmology, Graduate School Medical Sciences, Kyushu University*

<sup>1</sup>*Research Reactor Institute, Kyoto University*

**INTRODUCTION:** Retinitis pigmentosa (RP) is a group of inherited retinal degeneration diseases resulting from photoreceptor cell death and are frequently associated with cataract. We previously showed that chronic inflammation plays a role in the pathology of RP and could pose a risk of the development of cataract formation. The aim of this study was to identify the post-translational modifications that occur in lens protein of RP patients during inflammatory process.

**EXPERIMENTS:** Lens samples were collected during cataract surgery. This study was approved by the Institutional Review Board of Kyushu University Hospital (Fukuoka, Japan) and was conducted in accord with the tenets of the Declaration of Helsinki on Biomedical Research Involving Human Subjects. Informed Consent for the research was obtained from all patients. Sample preparation was performed as described in our previous study [1]. Samples were homogenized in 50 mM sodium phosphate buffer (pH 7.4), 150 mM NaCl, 1 mM phenylmethylsulfonyl fluoride (PMSF), 1 mM EDTA by ultrasonication and fractionated into water-soluble (WS) and water-insoluble (WI) fractions by centrifugation at  $12,000 \times g$  for 20 min at 4 °C. The WI proteins were dissolved in 8 M urea, and the urea concentration was

then diluted to less than 1 M in the same buffer before the enzymatic digestion. The WS proteins were digested with trypsin for 17 h at 37 °C in 50 mM sodium phosphate buffer (pH 7.4), 150 mM NaCl at an enzyme-to-substrate ratio of 1:50 (mol/mol). The WI proteins were digested with trypsin for 17 h at 37 °C in 50 mM sodium phosphate buffer (pH 7.4), 150 mM NaCl, 1 M urea, 1 mM CaCl<sub>2</sub> at an enzyme-to-substrate ratio of 1:50 (mol/mol). A nano-flow HPLC system was used for liquid chromatography (LC). Mass spectrometry (MS) was performed on an ion trap system. Peptides (500 ng) resulting from digestion with trypsin were separated by nano-flow HPLC using a C18 column (L-column, 0.1 × 150 mm) with a linear gradient of 5%–60% acetonitrile in the presence of 0.1% formic acid at a flow rate of 0.5 µL/min over 120 min and analyzed by Proteome Discoverer 1.0 software. MS analysis was carried out by alternating between full MS and MS/MS scans. The MS/MS scan used the collision-induced dissociation (CID) mode with dynamic exclusion function.

**RESULTS:** Post-translational modifications including oxidation and deamidation was detected in several lens proteins, such as  $\alpha$ - and  $\beta$ -crystallins in patients with RP.

### REFERENCE:

[1] Kim I, *et al.* Site specific oxidation of amino acid residues in rat lens  $\gamma$ -crystallin induced by low-dose  $\gamma$ -irradiation. *Biochem Biophys Res Commun.* **466** (2015) 622-628.

## CO6-5 Purification, Crystallization, and X-ray Diffraction Study of Lysozyme in D<sub>2</sub>O and H<sub>2</sub>O Solution.

T. Chatake, S. Fujiwara<sup>1</sup>, I. Tanaka<sup>2</sup>

Research Reactor Institute, Kyoto University

<sup>1</sup>Quantum Beam Science Research Directorate, National Institutes for Quantum and Radiological Science and Technology

<sup>2</sup>Faculty of Engineering, Ibaraki University

**INTRODUCTION:** Neutron scattering length of hydrogen (H) and its isotope deuterium (D) are remarkably different, and such isotope effect is widely utilized in neutron experiments. In particular, the contrast analysis between deuterated and non-deuterated sample is the main method in small angle neutron scattering (SANS) for biology, because H content of biomacromolecule is about half of all atoms in the molecule. In SANS, deuteration is used for labeling arbitrarily a part of macromolecular complex, simultaneously it decrease background noise of neutron scattering. In previous studies, we developed deuterium/hydrogen (D/H) contrast technique for neutron protein crystallography (NPC) [1]. This technique has great advantages in determining and evaluating hydrogen atoms, especially, it is very powerful for visualizing water molecules (D<sub>2</sub>O/H<sub>2</sub>O) surrounding proteins. The hydration structure is very important for folding and function of protein. In order to compare hydration structures of various kinds of proteins, we are crystallizing the proteins and carried out preliminary diffraction studies using X-ray.

Here, we report purification, crystallization, and X-ray diffraction study of lysozyme in D<sub>2</sub>O and H<sub>2</sub>O solution.

**EXPERIMENTS:** Hen egg white lysozyme (Sigma Aldrich) was purified prior to crystallization. 100 mg lysozyme powder was solved in 3 mL of 50 mM sodium acetate (NaAc) buffer (pH5.0). The lysozyme solution was 0.22 μm-filtered, and then applied on GE Hiscreen CatopSP Impres ion-exchange column (CV:4.7 mL), lysozyme was eluted by graduation from 0 M to 1 M NaCl in the 50 mM NaAc buffer (pH 5.0). The eluted lysozyme solution was dialyzed against 50 mM NaAc buffer (pH 4.5) overnight, and then concentrated to be 40 mg/mL by centrifuge concentration.

Crystallization for preliminary X-ray diffraction experiment was carried out sitting drop vapor diffusion method. Reservoir solutions contained 0.8, 1.0, or 1.2 M NaCl in the NaAc buffer (pH4.5). Each droplet was prepared by mixing 20 μL of 40 mg/mL lysozyme solution and 20 μL of reservoir solution. Crystallization plates were stored at 20 °C. The same crystallization was performed using D<sub>2</sub>O solution, in which deuteration was carried out the repeats of buffer exchange from H<sub>2</sub>O buffer to D<sub>2</sub>O buff-

er.

Preliminary X-ray diffraction experiments were carried out at beamline NW12 of the synchrotron facility in Photon Factory. Deuterated and non-deuterated crystals were sealed in glass capillaries with each buffer, respectively, and synchrotron experiments were carried out at room temperature (300K). X-ray diffraction images were collected by the helical scanning method in order to avoid serious radiation damage on the crystals. 200 oscillation images were taken with  $\Delta\omega = 1^\circ$  and  $t = 1$  sec. Since considerable numbers of low-resolution diffractions were saturated on the detector, two data sets were taken for each of D<sub>2</sub>O- and H<sub>2</sub>O-crystals with and without attenuator. Diffraction spots on the images were indexed, integrated, and merged by the program HKL2000.

**RESULTS:** After two weeks one or few large crystals emerged in droplets with the reservoir solution of 0.8 or 1.0 M NaCl. The side-length of these crystals were at least larger than 0.7 mm, and sometimes larger than 1.0 mm. In the present study, purification process seems to improve crystal size of lysozyme.

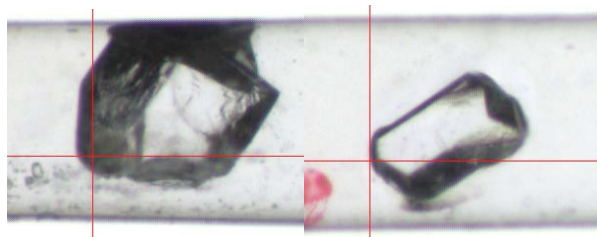


Fig. 1. Lysozyme crystal used for X-ray experiments. H<sub>2</sub>O-crystal (right) and D<sub>2</sub>O-crystal (left) was sealed in a capillary with a diameter of ~ 1 mm.

Both crystals belong to the same space group  $P4_32_12$ , with the similar cell dimensions ( $a=b=79.2$  Å,  $c=38.0$  Å for H<sub>2</sub>O crystal,  $a=b=79.2$  Å,  $c=37.9$  Å for the D<sub>2</sub>O crystal), suggesting the isomorphousness between the two crystals. For the H<sub>2</sub>O crystal, 1.35 Å X-ray data could be obtained with the completeness and  $R_{\text{merge}}$  of 99.9% and 6.9%, respectively. Meanwhile, for the D<sub>2</sub>O crystal, 1.45 Å X-ray data could be obtained (completeness and  $R_{\text{merge}}$  were 99.8% and 6.90%). In order to compare the two crystal structures, structure determinations are in progress.

### REFERENCE:

[1] T. Chatake and S. Fujiwara, Acta Crystallogra. D72 (2016) 71-82.

T. Takahashi and N. Miyoshi<sup>1</sup>

*Research Reactor Institute, Kyoto University*

<sup>1</sup> *National University of Kyoto Institute of Technology*

**INTRODUCTION:** The accelerator-based radiation source in the millimeter and terahertz wave region has very attractive feature for the spectroscopy. Coherent transition radiation (CTR), which has been emitted from the short bunches of electrons at the KURRI-LINAC, has been used to observe the transmittance spectra of a sectioned tissue of raw brain tumor C6 model as a collaborate study in the research reactor institute, Kyoto university. The absorption spectra in the sub-terahertz region had been not so clear for the raw tumor tissue although Ashworth-PC. *et al.* [1] had reported for the excised human breast cancer by a terahertz pulsed spectroscopy observed at 320 GHz, which was estimated a longer relaxation time component of the induced electricity for water molecules [2-3] in the raw tumor tissue for three years at the linear analysis.

We also estimated what kind of water molecules become dominant in the viable and necrotic cancer regions by the different measurement method as an aim of 2D mapping study.

**EXPERIMENTS:** (1) Instrument of Near-field in tera-hertz region: The experiment was performed at the coherent radiation beamline [4] at the 40-MeV L-band linac of the Research Reactor Institute, Kyoto University. The THz-wave source was CTR emitted from an aluminum foil with 15- $\mu\text{m}$  thickness. The radiation was detected by a liquid helium cooled Si bolometer. The conical cone with an aperture 260  $\mu\text{m}$  in diameter was used as the illumination probe and its F-number was 2.5. The spectrum of CTR was measured by a Martin-Puplett type interferometer.

(2) Sample preparation: A cryo-sectioned (thickness=100  $\mu\text{m}$ ) tissue was prepared from the raw C6 glial tumor model using a Cryo-section (C) Maker (Leica) and was sealed sandwich-type with polyvinylidene chloride (PVDC) film (thickness=10  $\mu\text{m}$ ), under freezing condition (-20 C) before the measurements. The rest large block of the tumor tissue was fixed with 10% formaldehyde for 1 week and was made of paraffin block to slice of 50  $\mu\text{m}$  film sample (P) with PVDC film.

**RESULTS:** The absorbance of the raw tissue at 16  $\text{cm}^{-1}$  was larger than 0.1 comparing the paraffin sample which was decreased of water contents by formaldehyde effect as shown in Figs. 1 and 2. Especially, the water contents were distributed in the necrotic area (white area in

cryo-section). On the other hand, the absorbance at 19  $\text{cm}^{-1}$  was distributed also in the necrotic area of the tumor tissues which looks like paraffin contents (lipid). In conclusion, lipid and water contents were distributed in the necrotic area of tumor tissue by this sub-THz LINAC beam analysis. It was found the absorbance at 16 and 19  $\text{cm}^{-1}$  were belonged as the water and lipid components, respectively in tumor tissue. The condition of water components should be more cleared in future, a cluster model of the water molecules and the other absorbance in this sub-THz region.

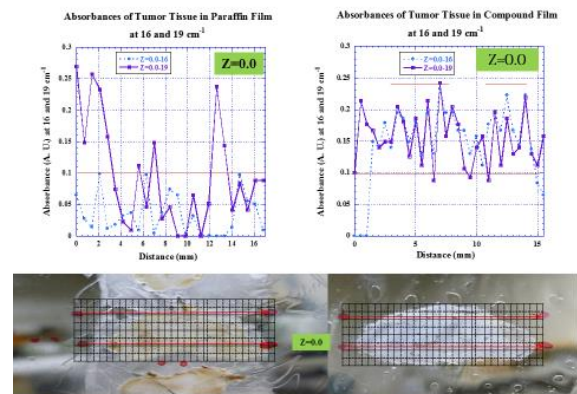


Fig. 1 Linear analysis of Cryo (C) and Paraffin (P)-sectioned samples.

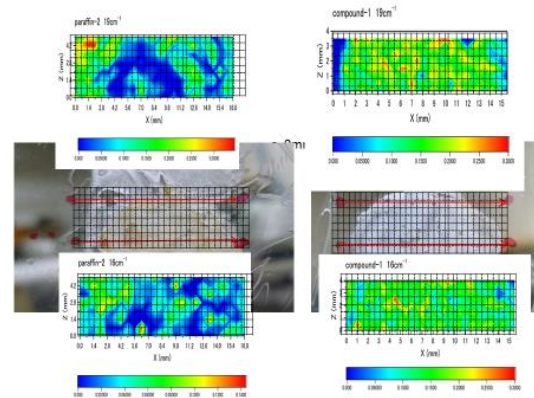


Fig. 2 2D-Mapping Images of Cryo- and Paraffin-sectioned samples at 16 and 19  $\text{cm}^{-1}$ , respectively.

### REFERENCES:

- [1] Phillip C. Ashworth, *et al.*, *Optics Express*, **17(14)**: 12444-12454 (2009).
- [2] Toshiko Fukasawa, *et al.*, *Phys. Rev. Lett.*, **95**: 197802 (2005).
- [3] Hiroyuki Yada, *et al.*, *Chem. Phys. Lett.*, **464**: 166-170 (2008).
- [4] T. Takahashi, *et al.*, *Rev. Sci. Instrum.* **69** (1998) 3770.

## CO6-7 The Study for Development and Application of Tissue Equivalent Neutron Dosimeter

M. Oita, T. Kamomae<sup>1</sup>, T. Takada<sup>2</sup> and K. Sakurai<sup>2</sup>

Graduate School of Health Sciences, Okayama University

<sup>1</sup> Graduate School of Medicine, Department of Radiology, Nagoya University

<sup>2</sup> Research Reactor Institute, Kyoto University

**INTRODUCTION:** Recent years, the clinical application of boron neutron capture therapy (BNCT) has been expected to make significant contributions to treatment for intractable cancer such as glioblastoma multiforme and melanoma. In BNCT, the boron (n, $\alpha$ )-reaction of the isotope  $^{10}\text{B}$  has a high cross section toward thermal neutrons, and the produced alpha and lithium particles have a short range on the micrometer scale. However, the neutron spectrum always spans a broad energy range, which results in different dose components and biological effects in tissue. Therefore, there are some difficulties of neutron dosimetry in clinical practice.

A radiochromic film (RCF) is one of the most useful devices for the QA of radiotherapy equipment. The advantages of RCFs are their high spatial resolution, small energy dependence, tissue equivalence, and self-development without processing in a darkroom<sup>1</sup>. A reflective-type RCF, e.g., GAFCHROMIC® EBT3, has been developed for qualitative dosimetry such as stereotactic irradiation (STI) and intensity modulated radiotherapy (IMRT)<sup>2,3</sup>. In this work, the authors investigated the response of reflective-type RCF for neutron beam as a tissue equivalent dosimeter.

**EXPERIMENTS:** A reflective-type RCF, GAFCHROMIC® EBT3 (Ashland Inc., Wayne, NJ, USA) using an Americium-Beryllium ( $^{241}\text{Am}$ -Be) neutron source (74 GBq,  $5 \times 10^6$  neutrons.s<sup>-1</sup>) with a cylindrical design (20 mm diameter by 30 mm long) made of the corrosion-resistant alloy was evaluated in this study. The RCFs were handled by the recommendation outlined in the American Association of Physicists in Medicine Task Group No. 55 report<sup>1</sup>.

For irradiation,  $6.0 \times 6.0$  cm<sup>2</sup> pieces of the RCF were placed at 1 cm, 4 cm, and 7 cm from just beneath the source with slit window along one direction, and with behind 1 mm acrylic plate along opposite direction in air (Fig.1). The RCF pieces were irradiated 180 min by the source, respectively.

**RESULTS:** Fig.1 shows the geometry of irradiation of RCFs by the  $^{241}\text{Am}$ -Be neutron source. Fig.2 shows the change of pixel values of RCFs irradiated by the  $^{241}\text{Am}$ -Be neutron source. There was significance difference of pixel values of irradiated RCFs by the neutron

source. The change of pixel value of RCF piece between 1 cm and 4 cm was 1811, while the value with the acrylic plate was attenuated by 1513. The dose in former converted by X-ray calibration of the RCF in the air were 36.2 cGy. Similarly, the dose of using a NaI scintillation survey meter was 15.3 cGy. Besides neutrons, the RCFs were exposed to gamma rays coming from events taking place in the source itself and the surrounding moderator. Further analysis was needed of the response of RCFs with neutron spectrum and contributions of gamma rays using Monte Carlo simulation. However, the results suggested that the dosimetry using RCFs is important for a better knowledge of fast neutron flux distribution with the  $^{241}\text{Am}$ -Be source. Moreover, it would be feasible for BNCT dosimetry in medical application.

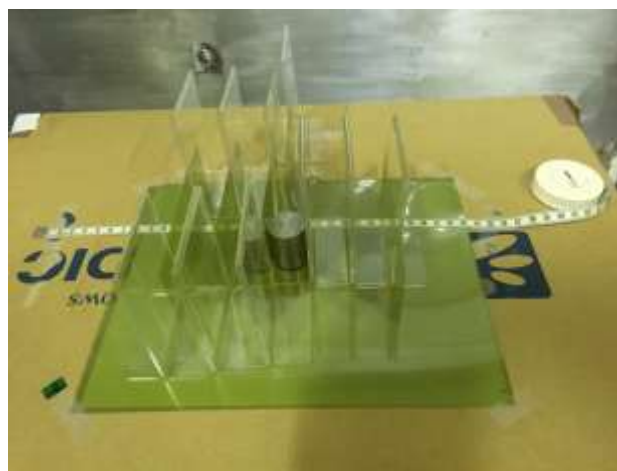


Fig. 1. The geometry of irradiation of RCFs by the  $^{241}\text{Am}$ -Be neutron source.

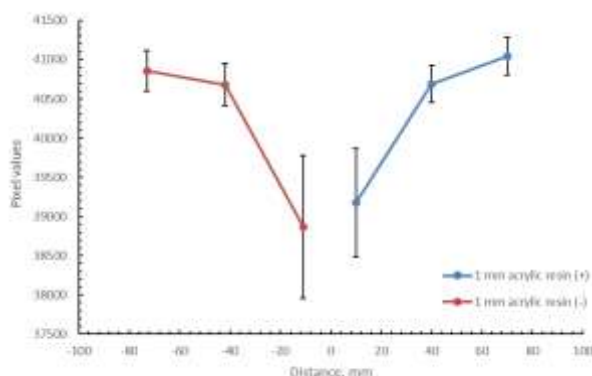


Fig. 2. The change of pixel values of the RCFs irradiated by the  $^{241}\text{Am}$ -Be neutron source.

### REFERENCES:

- [1] Niroomand-Rad, Azam, *et al.* Medical physics **25** (1998), 2093-2115.
- [2] Borca, Valeria Casanova, *et al.* Journal of applied clinical medical physics **14** (2013).
- [3] Fiandra, Christian, *et al.* Medical physics **40** (2013).

## Gadolinium accumulation using Gd-DTPA-incorporated Calcium Phosphate Nanoparticles for Gd-neutron capture therapy

N. Dewi<sup>1,5</sup>, P. Mi<sup>2,3</sup>, H. Yanagie<sup>1,4,5</sup>, Y. Sakurai<sup>4</sup>, H. Cabral<sup>2</sup>, N. Nishiyama<sup>3</sup>, K. Kataoka<sup>2,6</sup>, Y. Sakurai<sup>7</sup>, H. Tanaka<sup>7</sup>, M. Suzuki<sup>7</sup>, S. Masunaga<sup>7</sup>, K. Ono<sup>7</sup>, Minoru Ono<sup>4,8</sup>, Jun Nakajima<sup>4,9</sup>, and H. Takahashi<sup>1,4</sup>

<sup>1</sup>Dept of Nuclear Engineering & Management, Univ of Tokyo, <sup>2</sup>Bioengineering Dept, Univ of Tokyo, <sup>3</sup>Polymer chemistry division, Chemical Resource Laboratory, Tokyo Institute of Technology, <sup>4</sup>Cooperative Unit of Medicine & Engineering, Univ of Tokyo Hospital, <sup>5</sup>Dept of Innovative Cancer Therapeutics, Meiji Pharmaceutical University, <sup>6</sup>Materials Engineering Dept, The University of Tokyo, <sup>7</sup>Research Reactor Institute, Kyoto University, <sup>8</sup>Dept of Cardiac Surgery, The University of Tokyo Hospital, <sup>9</sup>Dept of Thoracic Surgery, The University of Tokyo Hospital

**INTRODUCTION:** Gadolinium-157 has been getting attention as an attractive agent for neutron capture therapy (NCT) because of its high thermal neutron cross section (255 000 barns), which is the highest among all stable elements. However, gadolinium neutron capture reaction (Gd-NCR) results in release of gamma rays, which reduce the localization effect of the treatment, increasing the possible additional effect if Gd-157 is accumulated to a bulk tumor cluster [1].

We synthesized Gd-DTPA-incorporated Calcium Phosphate (Gd-DTPA/CaP) nanoparticles with two-step preparation method by self-assembly poly(ethylene glycol)-b-poly(aspartic acid) block copolymer, Gd-DTPA, and CaP in aqueous solution, followed with hydrothermal treatment. Evaluation of possible apoptosis by detecting the DNA fragmentation following GdNCT treatment has shown that the number of cells killed after treatment was observed to be similar for single and multiple injection groups of Gd-DTPA/CaP nanoparticles, while non-treated group shows normal histology with clear cytoplasm and nucleus [3].

In this work, we evaluated the tumor accumulation of Gd atoms for single and multiple injections using Gd-DTPA/CaP nanoparticles.

**EXPERIMENTS:** We carried out the biodistribution experiments of in vivo quantitative analysis, each for single and multiple injections of Gd-DTPA/CaP nanoparticles. To confirm the pharmacokinetics of Gd-DTPA/CaP nanomicelles for 0.2 mL single injection, tumor, blood, and other organ samples were harvested at 12 and 24 hr following nanoparticles administration. Three times injections of Gd-DTPA/CaP nanomicelles with 10 hr interval were then carried out in order to achieve higher gadolinium accumulation in tumor site. Samples from both experiments were analyzed using ICP-MS.

**RESULTS:** Quantitative analysis from ICP-MS measurement results of gadolinium accumulation in tumor and several mice organs were shown in Table 1. We could achieve the tumor-to-blood (T/B) ratio of around 2.4 at 24 hr after Gd-DTPA/CaP nanoparticles injection.

**Table 1. Gd accumulation in tumor and several organs of tumor bearing mice after single injection of Gd-DTPA/CaP nanoparticles**

	Gd concentration ( $\mu\text{g/g}$ or $\text{mL}$ )	
	12hr	24hr
Tumor	5.85 $\pm$ 0.64	8.03 $\pm$ 0.82
Blood	14.55 $\pm$ 0.50	3.29 $\pm$ 0.40
Liver	10.71 $\pm$ 0.17	16.71 $\pm$ 0.60
Spleen	7.08 $\pm$ 0.41	10.03 $\pm$ 0.30
Kidney	2.66 $\pm$ 0.24	2.13 $\pm$ 0.06
Brain	0.16 $\pm$ 0.01	0.04 $\pm$ 0.01

Higher gadolinium accumulation in tumor site was successfully achieved for multiple injections of Gd-DTPA/CaP nanoparticles as shown in Figure 1. Gadolinium concentration reached the amount of more than three times higher compared to those at 10 hr after the first injection. Significant increase in gadolinium concentration in blood plasma was also observed at 30hr after first injection. This result indicates the prolonged blood circulation of Gd-DTPA/CaP nanoparticles.

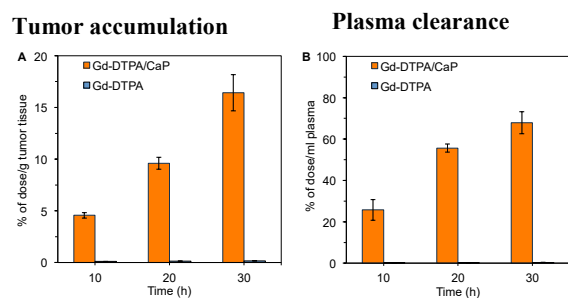


**Figure 1. Gadolinium biodistribution for multiple injections. Higher gadolinium accumulation in tumor site was achieved significantly after three times injection. More than 60% of injected dose of gadolinium was still observed in plasma indicating the prolonged blood circulation of Gd-DTPA/CaP nanoparticles.**

### REFERENCES:

- [1] Dewi N et al., Biomed & Pharmacother (2013) **67**:451-7.
- [2] Mi P, et al.: [ACS Nano](#) (2015) **23**;9(6):5913-21.
- [3] Dewi N et al., J Can.Res.Clin.Oncol. (2016) **142**(4):767-75.

## CO7-2 A Fundamental Experiment for the Measure Against the Activation of the Irradiation-room Concrete at BNCT Facility (III)

T. Takata, Y. Sakurai, K. Kimura<sup>1</sup>, H. Tanaka, K. Takamiya

Research Reactor Institute, Kyoto University  
<sup>1</sup>Fujita Corporation

**INTRODUCTION:** At present time, the research and development of accelerator-based neutron sources for boron neutron capture therapy (BNCT) are underway by several research groups around the world, with Cyclotron-based BNCT Epi-thermal Neutron Source (C-BENS) in the lead [1]. In near future, BNCT using the accelerator-based neutron sources may be carried out at several places in the world. Compared to irradiation facilities for X-ray and charged-particle radiation therapy, the neutron yield is much larger at BNCT facility. Thus, the activation of concrete, which is a main structure material of the irradiation facility, becomes an issue from the viewpoints of radiation exposure of medical workers, the decommissioning of the facility, etc.. This research is intended to perform the characteristic estimation of the materials for activation reduction and to confirm its usability at BNCT facility. In 2016, characteristic estimation of a neutron shielding material covering concrete wall surfaces was performed by using an Am-Be neutron source in the same manner in 2014 and 2015 [2], because Kyoto University Reactor (KUR) was not operated.

**METHODS:** A characteristic estimation was performed for the resin-based shielding materials containing B<sub>4</sub>C with different particle sizes. The small-size particles were used in the sample A, in which the B<sub>4</sub>C can be considered to be distributed homogeneously in the resin. On the other hands, the particles with a submillimeter diameter were used in the sample B, in which the B<sub>4</sub>C was localized in the particles and thus considered to be distributed sparsely in the resin. These samples were prepared to have the almost same B<sub>4</sub>C concentration level as a whole volume average. Four resin sheets of 10-cm side, 10-cm long and 4-mm thickness were stacked on the concrete surface. The shielding performance against the Am-Be neutron source was estimated by activation method of indium foils placed between the stacked resin layers. The characteristic for fast neutron shielding was estimated by the change in the  $^{115}\text{In}(n,n')^{115\text{m}}\text{In}$  reaction rate, and the characteristic for thermal neutron generation was estimated by the change in the  $^{115}\text{In}(n,\gamma)^{116\text{m}}\text{In}$  reaction rate.

**RESULTS:** Figures 1 and 2 show the reaction rates for the  $^{115}\text{In}(n,n')^{115\text{m}}\text{In}$  and  $^{115}\text{In}(n,\gamma)^{116\text{m}}\text{In}$  reactions, respectively, as a function of the neutron-shield thickness of the sample A and B. From the comparison of the changes in the  $^{115}\text{In}(n,n')^{115\text{m}}\text{In}$  reaction rate, the shielding ability for fast neutrons was found to be almost same between the sample A and B. From the comparison of the changes in the  $^{115}\text{In}(n,\gamma)^{116\text{m}}\text{In}$  reaction rate, the generation of ther-

mal neutrons was found to be slightly larger in the sample B compared to the sample A.

**CONCLUSION:** Toward the restart of KUR operation, the estimations for the important characteristics of the shielding materials as well as the low-activation concrete materials are planned, such as the shielding effect for neutrons and gamma rays, the generation of the secondary gamma rays, etc., using Heavy Water Neutron Irradiation Facility [3]. Also, the neutron activation analysis for these materials and its basic ingredients using Pneumatic Tubes is planned to estimate the activation characteristics from short to long time range.

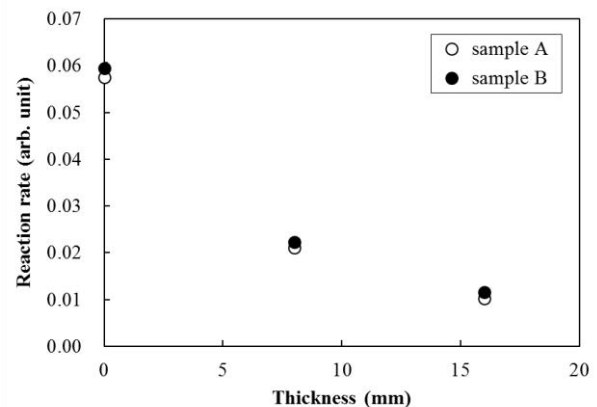


Fig. 1.  $^{115}\text{In}(n,n')^{115\text{m}}\text{In}$  reaction rate as a function of the shield thickness.

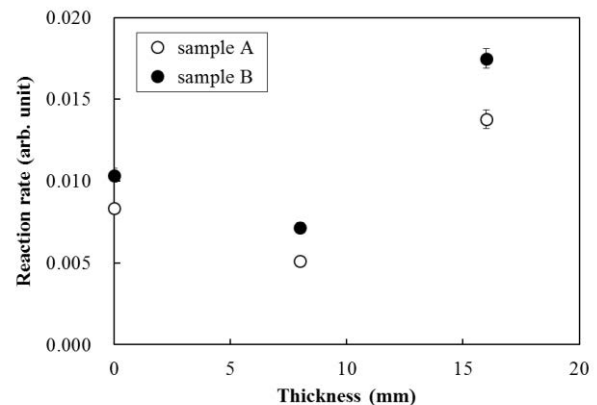


Fig. 2.  $^{115}\text{In}(n,\gamma)^{116\text{m}}\text{In}$  reaction rate as a function of the shield thickness.

### REFERENCES:

- [1] H. Tanaka *et al.*, Nucl. Instr. Meth. B **267** (2009) 1970-1977.
- [2] Y. Sakurai, T. Takata *et al.*, KURRI Progress Report 2015 (2016) 97.
- [3] Y. Sakurai *et al.*, Nucl. Instr. Meth. A **453** (2000) 569-596.

Y. Takahashi, L. Payne<sup>1</sup>, C. Hutton<sup>1</sup>, K. Takamiya, T. Saito, J. Hori, H. Unesaki, T. Scott<sup>1</sup>

*Research Reactor Institute, Kyoto University*  
<sup>1</sup>*Interface Analysis Centre, School of Physics, University of Bristol*

**INTRODUCTION:** Measurements of radiation dose rates in highly active environments, such as the Fukushima Daiichi Nuclear Power Plant or Sellafield in UK, is challenging due to the extreme environments encountered and restricted access. Therefore, novel radiation detector technology is required to address these challenges. One such example of a radiation detection material is diamond, as it is able to withstand and measure high radiation intensities, is chemically inert and formable into extremely small, sensitive detectors. These detectors generate small currents when exposed to radiation, and if the radiation levels are high enough this can be measured. Testing of such detectors is not possible in routine laboratories due to the requirement to have high active radiation sources in UK. However, through a new collaboration formed through Kyoto University-the University of Bristol bilateral symposia, UK researchers are accessible to the high active radiation source at Kyoto University Research Reactor Institute (KURRI). This report presents some preliminary results from radiation testing of diamond detectors developed by University of Bristol at Co-60 facility in KURRI.

**EXPERIMENTS:** Three diamond detectors as shown in Fig. 1 (S1, C1 and C2) were exposed to varying dose rates using a Co-60 irradiator irradiation facility at KURRI. This facility has a strong Co-60 source in a large irradiation room that allows exposure to a large range of dose rates from approximately 0.1 Gray/hour up to >4000 Gray/hour by the change of the irradiation position. The diamond detectors were located on the end of a 50 meter cable and controlled using custom built software that applies a 300 V bias voltage and records current data every 50 ms. For each dose rate a background was recorded for 30 seconds before and after the source was introduced, with 60 seconds of data collected while the diamond was exposed to the source. The mean and standard deviation of the current recorded was calculated for each dose rate and background measurement. A background subtraction, between the start background and measurement current, was performed to allow the current generated by irradiation to be plotted.

**RESULTS:** The response of the S1 detector to various dose rates from Co-60 are shown in Fig. 2 as an example, where the data point is a mean of 60 seconds of data and the error bars are one standard deviation to give an indication of detector stability. Detector S1 shows a stable and linear response, with an increasing dose rate being

proportional to an increase in current measured. This response would allow the use of this detector in civil nuclear applications as a reliable calibration factor can be derived. Following testing using the Co-60 facility, any detectors that show promise for use, such as S1, will be tested further using the other facilities present at KURRI. This will include exposure to different energy gamma radiation such as Cs-137, to establish if the incident gamma energy has any effect on detector response. Additionally, upon restart of the Kyoto University Research Reactor (KUR) and Kyoto University Critical Assembly (KUCA) the detector response in highly active gamma and neutron/gamma mixed fields can be investigated.



Fig. 1 Diamond detector (left: S1, right: C1,C2)

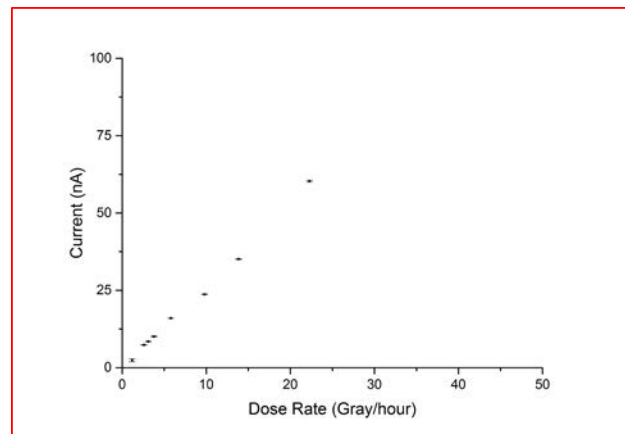
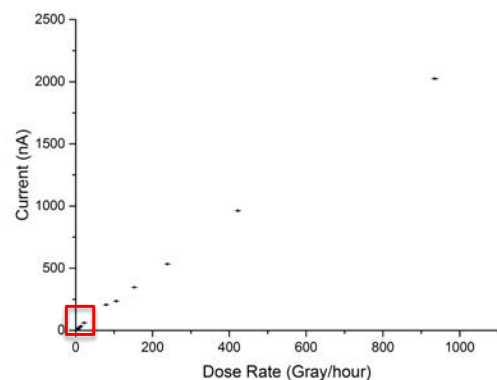


Fig. 2 Dose rate response of S1 detector

Y. Takahashi, J. Hori, T. Sano, D. Ito, H. Unesaki,  
K. Nakajima

*Research Reactor Institute, Kyoto University*

**INTRODUCTION:** A fast reactor system with trans-uranium fuels containing minor-actinide is expected to be effective for the incineration of high-level radioactive wastes. In order to realize the fast reactor system, integrity evaluation of the fuels with high activity is required for the safety operation. However, present techniques are considered to be difficult to apply the evaluation of the fuels with high radioactivity and high decay heat. In order to develop the related methodology adapted for the integrity evaluation, the N-DeMAIN (Development of Non-Destructive Methods Adapted for Integrity test of Next generation nuclear fuels) project has been started from October 2014. In the project, the neutron resonance transmission analysis is adapted for the identification and quantification of nuclides in the fuels by time-of-flight (TOF) measurement. In addition, the determination of temperature distribution in the fuels based on Doppler-effect and neutron imaging are conducted by the neutron resonance technique. To obtain accurate data by these methods, high quality neutron beam regarding neutron flux, time resolution and spatial resolution is required. The 46 MeV electron accelerator in Kyoto University Research Reactor Institute (KURRI-LINAC) will be used for the project because KURRI-LINAC is the only pulsed neutron facility where nuclear materials can be utilized in Japan. In order to satisfy the neutron beam quality required to successfully execute the experiments described above, the design of the neutron source, especially the moderator, reflector and collimator, should be improved and optimized. In this project, the neutron source system including moderator and reflector was newly developed as shown in Fig. 1 and the collimator in 12 m beam line was also re-arranged. The characteristic of the system was investigated experimentally.



Fig. 1 Newly developed neutron source system

**EXPERIMENTS:** A water-cooled photo-neutron target was set at the center of the neutron source system located in the target room. To enhance the neutron flux in thermal and epi-thermal regions, the size of the moderator of polyethylene was 5 cm thickness and 15 cm square. The measuring station at 12 m from the target on the 135 degree beam line was selected in this project. A lead shadow bar, 5 cm in diameter and 20 cm long, was placed on the neutron beam axis in front of the neutron source system to reduce intense gamma-flash from the target effectively. The collimators of polyethylene with 10% boron of 20 cm thickness were set at following positions; 15, 10, 5 cm in inner diameter at 3, 9, 12 m from the target, respectively. Neutron spectrum measurements were obtained from capture reaction rate of  $^{10}\text{B}$  (22 mm diameter, purity 96.98%) and dummy samples. A BGO scintillator (2 inch diameter and 2 inch long) was used for measuring total energy absorption gamma-rays. The conditions of the accelerator were as follows: average beam current was 14.5  $\mu\text{A}$ , frequency was 50 Hz and pulse width was 100 ns.

**RESULTS:** Measured neutron spectrum is shown in Fig. 2. The neutrons in a few keV energy regions could be measured owing to the reduction of gamma-flash influence. The thermal neutron flux of  $2.36 \times 10^2$  [ $\text{n}/\text{cm}^2/\mu\text{A}/\text{s}$ ] and the epi-thermal neutron flux of  $5.72 \times 10^2$  [ $\text{n}/\text{cm}^2/\mu\text{A}/\text{s}$ ] were obtained under this experimental condition. It was found we can obtain the maximum thermal neutron flux of  $4.72 \times 10^4$  [ $\text{n}/\text{cm}^2/\text{s}$ ] and the maximum epi-thermal neutron flux of  $1.14 \times 10^5$  [ $\text{n}/\text{cm}^2/\text{s}$ ] under 6 kW operation of KURRI-LINAC.

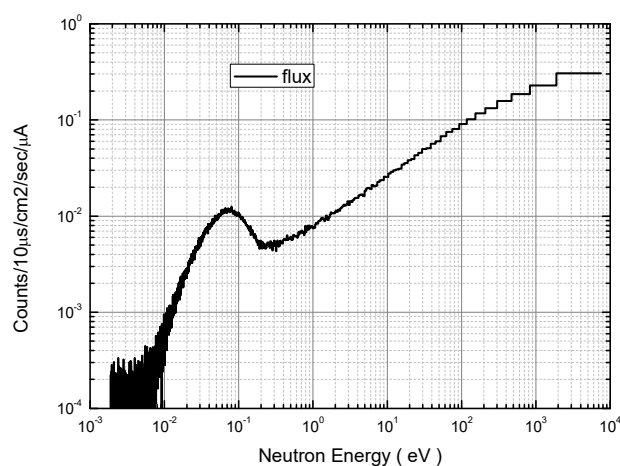


Fig. 2 Measured neutron spectrum

Present study includes the result of “Development of Non-Destructive Methods Adapted for Integrity test of Next generation nuclear fuels” entrusted to the Kyoto University by the Ministry of Education, Culture, Sports, Science and Technology of Japan (MEXT).

## CO9-1 Search for the Ultraviolet Photons Emitted from $^{229\text{m}}\text{Th}$ Samples Reacted with HF Gas

Y. Yasuda, Y. Kasamatsu, Y. Shigekawa, T. Ohtsuki<sup>1</sup>, K. Takamiya<sup>1</sup>, A. Shinohara

Graduate School of Science, Osaka University

<sup>1</sup>Research Reactor Institute, Kyoto University

**INTRODUCTION:** Thorium-229m lies in the extremely low energy level and the excitation energy was reported to be  $7.8 \pm 0.5$  eV [1]. The energy corresponds to vacuum ultraviolet photon ( $\lambda=160$  nm). Because of the low energy, it is expected that  $^{229\text{m}}\text{Th}$  decays by internal conversion or gamma-ray transition depending on its chemical condition. Recently, it was reported that the  $^{229\text{m}}\text{Th}$  neutral atom decays by internal conversion with a half-life of 7  $\mu\text{s}$ , and that the  $^{229\text{m}}\text{Th}^{2+}$  ion in the isolated system decays with a half-life of longer than 60 s [2, 3]. It suggests that  $^{229\text{m}}\text{Th}^{2+}$  ion may decay by gamma-ray transition (photon emission). However, the photons from  $^{229\text{m}}\text{Th}$  have never been observed. To observe the photons, in this study we performed following experiments: First, we prepared  $^{229\text{m}}\text{Th}$  as recoil products (high valence  $^{229\text{m}}\text{Th}$  ions). Subsequently,  $^{229\text{m}}\text{Th}$  ions were directly reacted with hydrogen fluoride gas. Since the lowest binding energy of the outermost electron in  $\text{ThF}_4$  is 8.3 eV [4] which is larger than the  $^{229\text{m}}\text{Th}$  excitation energy, 7.8 eV, it is expected that  $^{229\text{m}}\text{Th}$  is not able to decay by internal conversion. Finally, the photon detection was performed for the sample.

**EXPERIMENTS:** To obtain  $^{229\text{m}}\text{Th}$  ions as recoil products, we prepared thin  $^{233}\text{U}$  sample by electrodeposition. A 10  $\mu\text{L}$  aliquot of the  $^{233}\text{U}$  solution in 0.1 M  $\text{HNO}_3$  (24  $\mu\text{g}/\mu\text{L}$  of  $^{233}\text{U}$ ) and 10 mL of isopropanol were placed into the 30-mm diameter electrodeposition cell. Using a Pt wire as the anode,  $^{233}\text{U}$  was electrodeposited on a Pt foil (0.02 mm thickness) with a current of 17 mA. The electrodeposition yield was determined by alpha spectroscopy to be 54% corresponding to  $17.8 \pm 0.3$   $\mu\text{g}/\text{cm}^2$  of  $^{233}\text{U}$  in thickness. The  $^{233}\text{U}$  sample was set in the Collection Apparatus for Recoil Products (CARP) [5]. In collecting  $^{229\text{m}}\text{Th}$  ions, He gas or He/HF mixture gas were guided into the CARP and the required voltage was applied to guide  $^{229\text{m}}\text{Th}$  ions onto the copper plate. After  $^{229\text{m}}\text{Th}$  was collected for several hours to 1 day, photon detection was performed. To detect the photons, we used the photomultiplier tube (PMT, HAMAMATSU R6836), which detects 4-10 eV photons. The PMT was cooled to about 10°C and set in vacuum.

**RESULTS:** In the result of photon detection for the  $^{229\text{m}}\text{Th}$  samples collected in He gas, weak decaying photon counts were observed as shown in Fig.1 (a). This time variation can be fitted with the decaying curve of two half-life components,  $^{212}\text{Pb}$  and  $^{213}\text{Bi}$ . However, this count rate was lower than the expected value (2 cps) for  $^{229\text{m}}\text{Th}$ , and therefore we tried to detect the photons emit-

ted from the  $^{229\text{m}}\text{Th}$  sample reacted with HF gas. In this case, decaying photons were also observed as shown in Fig.1 (b). However, the count rate of photon emitted from this sample was almost the same as that from the sample collected in He gas. This fact indicates that these photons mainly originated from daughter nuclides such as  $^{213}\text{Bi}$ ,  $^{209}\text{Tl}$ ,  $^{212}\text{Bi}$ , and  $^{208}\text{Tl}$ . Thorium-229m might not be reacted sufficiently. To reduce the photons induced by daughter nuclides, we will use the electrodeposited sample of newly purified  $^{233}\text{U}$ .

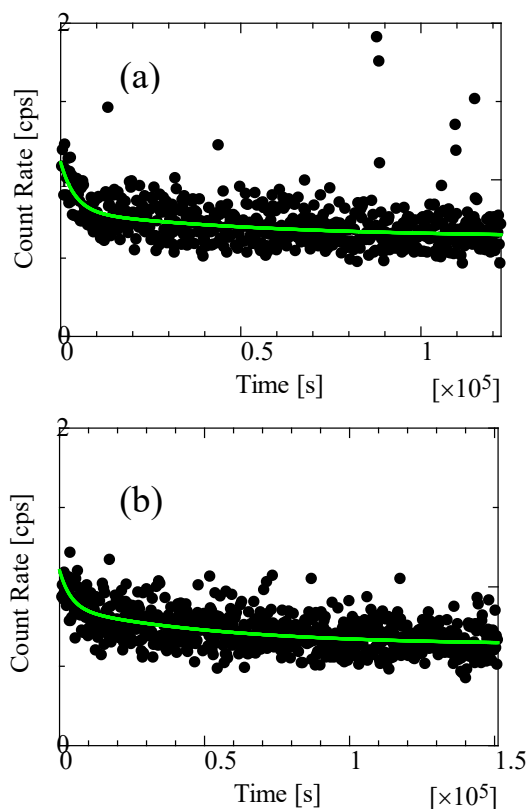


Fig. 1. The photon counts for the  $^{229\text{m}}\text{Th}$  samples. Solid curves describe the fitted curves containing two decaying components. Fig.1 (a) shows the counts for  $^{229\text{m}}\text{Th}$  sample prepared in He gas for about 15 h and (b) shows that reacted with HF gas for about 25 h.

### REFERENCES:

- [1] B. R. Beck *et al.*, LLNL-PROC-415170(2009).
- [2] L. von der Wense *et al.*, Nature **533** (2016) 47-51.
- [3] B. Seiferle *et al.*, Phys. Rev. Lett. **118** (2017) 042501.
- [4] N. Trautmann, J. Alloys Compd. **213/214** (1994) 28.
- [5] Y. Shigekawa *et al.*, Rev. Sci. Instrum. **87**(2016) 053508.

## CO9-2 Stability of Triphosphine Trioxide Extractant against $\gamma$ -Ray Irradiation in $\text{HNO}_3$

M. Nogami, E. Tamaru, S. Maeda and N. Sato<sup>1</sup>

Faculty of Science and Engineering, Kindai University  
<sup>1</sup>Research Reactor Institute, Kyoto University

**INTRODUCTION:** We have been paying attention to one of triphosphine trioxides, 1,1,3,5,5-pentaphenyl-1,3,5-triphosphapentane trioxide (PPTPT : Fig. 1) for a potential versatile extractant [1,2]. The most distinguished nature of PPTPT would be its unusual high selectivity to U(VI) in  $\text{HNO}_3$  of very low concentrations [3]. Another expected nature of PPTPT is higher chemical stability in acid media. In principle, phosphine oxides do not undergo acid hydrolysis unlike compounds not containing phosphorus such as diamides, and ester phosphates such as tri-*n*-butylphosphate (TBP). In addition, PPTPT has no ether bonds which are known to decrease the stability of extractants in acid media[4], although they have been sometimes included in chemical structures of extractants to increase extraction properties. Based on the above, radiation stability of PPTPT was investigated mainly from the identification of degradation products in this study.

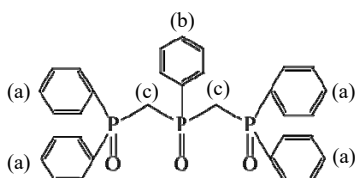


Fig. 1. Chemical structure of PPTPT.

**EXPERIMENTS:** For  $\gamma$ -ray irradiation to PPTPT, the samples were prepared by mixing PPTPT of white crystal with  $\text{H}_2\text{O}$ , 3 and 9 mol/dm<sup>3</sup> (= M)  $\text{HNO}_3$ , respectively. The mixture was put in a Pyrex tube and irradiated by the <sup>60</sup>Co source at ca. 3.7 kGy/h up to 1.6 MGy at room temperature under ambient atmosphere. Irradiated samples were analyzed by <sup>1</sup>H and <sup>13</sup>C NMR.

**RESULTS:** PPTPT irradiated in  $\text{H}_2\text{O}$  showed powdered state. While, those irradiated in 3 and 9 M  $\text{HNO}_3$  turned into brown viscose oil. <sup>1</sup>H NMR spectra of neat PPTPT and that irradiated in 9 M  $\text{HNO}_3$  are shown in Fig. 2. It can be seen that the signal at ca. 1.5 ppm which is

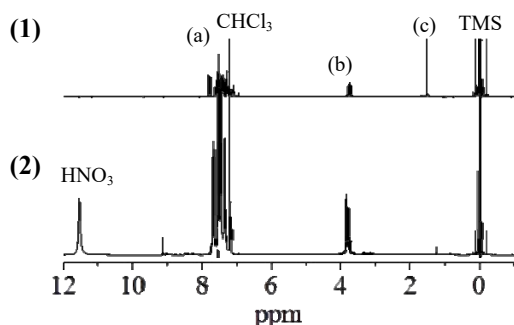


Fig. 2. <sup>1</sup>H NMR of PPTPT : (1) neat, (2) irradiated in 9 M  $\text{HNO}_3$  (solvent :  $\text{CDCl}_3$ ).

attributed to the hydrogen atoms at (c) in Fig. 1 is significantly decreased after irradiation. This suggests that the bond cleavage occurred between phosphorus and methylene carbon.

For comparison, PPTPT was treated with 9 M  $\text{HNO}_3$  containing 10 mM Nd(III) or Fe(III), or 3 %  $\text{H}_2\text{O}_2$  at boiling temperature for 6 h. It was also treated similarly with conc.  $\text{HNO}_3$ . Under these conditions, little structure changes were observed for <sup>1</sup>H NMR spectra. This would indicate high chemical stability of PPTPT in  $\text{HNO}_3$  media. On the other hand, <sup>1</sup>H NMR analysis for PPTPT treated with aqua regia at room temperature for 1 day suggests the similar bond cleavage to the irradiated PPTPT. Further <sup>1</sup>H and <sup>13</sup>C NMR analyses for PPTPT treated with aqua regia suggest that formic acid and two kinds of phenylphosphoric acid were generated as the degraded compounds (Fig. 3). Large portion of formic acid might be decomposed to CO and  $\text{H}_2\text{O}$ . Such a pathway of degradation was similar to some extent to that of octylphenyl-*N,N'*-diisobutylcarbamoylmethyl phosphine oxide (CMPO), a conventional bidentate phosphine oxide extractant, by  $\gamma$ -ray irradiation [5].

So far, the detailed pathway of degradation for irradiated PPTPT is not confirmed. However, it is expected that the pathway is close to that shown in Fig. 3.

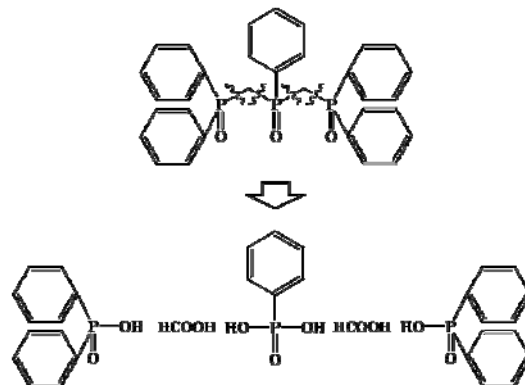


Fig. 3. Expected structure change in PPTPT by treatment with aqua regia.

### REFERENCES:

- [1] M. Nogami *et al.*, Energy Procedia, **71** (2015) 123-129.
- [2] K. Hashimoto, *et al.*, Abst. ASNFC 2015, Tokyo, Japan, 2B-24 (2015).
- [3] M. Nogami, *et al.*, J. Radioanal. Nucl. Chem., **284** (2010) 195-199.
- [4] C. Madic, *et al.*, Nuclear science and technology, Final report, EUR19149, European Commission, 44 (2000).
- [5] J. N. Mathur, *et al.*, Sep. Sci. Technol., **33** (1998) 2179-2196.

# CO10-1 Possibility of Suppression of Cs Elution from Incineration Fly Ash by Adding Soil

M. Yoneda, Y. Shimada, M. Matsui, A. Taruoka, Y. Yoshiyama, T. Kometani, D. Setoguchi, S. Fukutani<sup>1</sup> and M. Ikegami<sup>1</sup>

Faculty of Engineering, Kyoto University  
<sup>1</sup>Research Reactor Institute, Kyoto University

**INTRODUCTION:** The procedure to the final disposal of the waste polluted with radioactive Cs in Fukushima is far from well established. In carrying out a middle storage of the polluted waste and its final disposal, it is necessary that behaviors of radioactive Cs in the wastes are clarified and a realistic method is suggested to prevent leakage of radioactive Cs to the environment in future to establish the safe disposal method of the waste. This study examines the effectiveness of the method to mix the soil which had strong adsorption ability of the Cs with incineration fly ash as elution suppression measures.

**EXPERIMENTS:** At first, behavior of stable Cs-133 of the concentration of 500µg/kg and radioactive Cs-134 of the concentration of 125,000Bq/kg (2.6ng/kg) is compared when they are added to heat treated forest soil as a decontamination waste. Here, heat treated forest soil means that the soil is heated for 30min at 500 degree Celsius by muffle kiln. Soil of experiment forest of Iwate University is used, because it is thought to be similar to forest soil in Fukushima. Then, the elution rate to water of Cs from the mixture of a simulated incineration fly ash and heated or unheated forest soil is examined by the method of elution test of Soil Contamination Countermeasure Law considering the quantity of K as a competitive adsorption element contained in the mixture. Table 1 shows the components of the simulated fly ash. Stable Cs-133 is used if there is no clear difference in the elution rate from soil between Cs-133 and Cs-134.

Table 1. Components of simulated incineration fly ash.

fly ash A		fly ash B	
component	ratio (%)	component	ratio (%)
activated C	3.0	activated C	3.0
KCl	10.0	KCl	4.0
SiO <sub>2</sub>	86.8	NaCl	4.0
metals	0.2	CaCl <sub>2</sub> ·2H <sub>2</sub> O	2.0
		SiO <sub>2</sub>	29.0
		Al <sub>2</sub> O <sub>3</sub>	29.0
		CaCO <sub>3</sub>	29.0

**RESULTS:** Although the concentration of Cs-133 and Cs-134 are 5 order of the magnitude different, there was no clear difference between in the elution rate of Cs-133 and in that of Cs-134 from heated soil. The elution rate of Cs from heated forest soil was less than 1%. However,

the drop of the elution rate from incineration ash by adding heated or unheated forest soil was not so effective as we expected. Fig.1 shows the elution rate of Cs from the mixture of the simulated fly ash and heated or unheated forest soil. It was necessary to mix the soil of the quantity of a little less than 10 times of fly ash to drop the elution rate to around several percent. When the soil and fly ash was mixed, the concentration of [K<sup>+</sup>] (meq/mL) in the solution of the elution test would be approximately estimated by the contents of element K of the simulated fly ash, if the content of K was much bigger than the cation exchange capacity (CEC) of the soil in each mixture. We found that we could estimate the elution rate of Cs by the equation (1) based on Langmuir type competition adsorption theory when we mixed soil and fly ash.

$$\text{elution rate (\%)} = 100 / (1 + 0.05 / [K^+]) \quad (1)$$

When quantity of K in the mixture of soil and fly ash is larger enough than quantity of CEC, [K<sup>+</sup>] can be approximately estimated as total K minus CEC of the mixture solved in the solution. It was possible to estimate each observed Cs elution rate with around 10% of errors by the equation (1). Therefore, it means that it is necessary to suppress [K<sup>+</sup>] less than 0.5 x 10<sup>-3</sup> (meq/mL), or the contents of Cs in each mixture less than around 0.5 x 10<sup>-2</sup> mmol/g to control each elution rate of Cs less than 1%. In addition, it was expected that the behavior of Cs in the mixture would be greatly change if the contents of Cs exceeded the contents of frayed edge site where Cs is preferentially sorbed. Because the amount of frayed edge site of the soil used in this study was around 0.0002 (meq/g), behavior of Cs in the soil would not be different if the amount of Cs added to the soil is less than 27mg/kg. It was also found that when the amount of Cs was more than the amount of frayed edge site, the elution rate could be estimated based on the competition adsorption theory of the Freundlich type, though the effect of the difference of soil parameters was great.

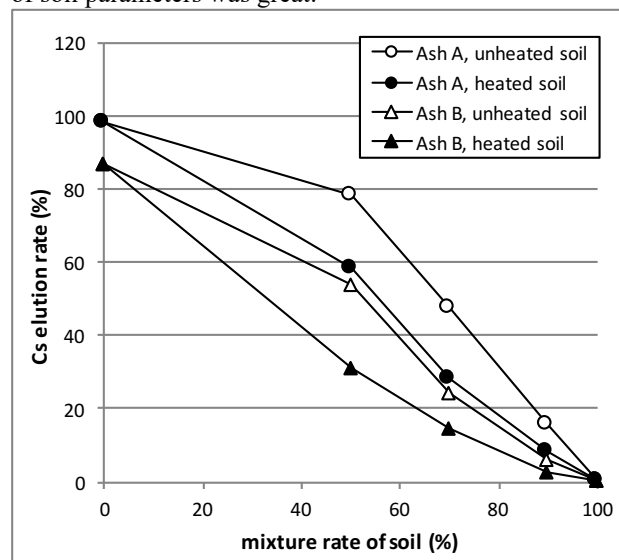


Fig. 1. Elution rate of Cs from mixture of simulated incineration fly ash and soil.

M. Takagaki, K. Uno and S. Masunaga<sup>1</sup>

*Leuis Pasteur Center of Medical Research*  
<sup>1</sup>*Research Reactor Institute, Kyoto University*

At the end of March 2017, after the seventh year of the earthquake disaster, governmental order for evacuation was mostly terminated except for Nagadoro where radiation levels are still high. The radiation level in the living zone of Iitate village has decreased to less than 0.3  $\mu\text{Sv/hr}$  and it is about 1  $\mu\text{Sv/hr}$  even when going to worship deep in the mountain of Yamazumi shrine that worships the local mountain gods (Figure 1). The form of life style of villagers is varied, after the evacuation order for them is terminated. Villagers trying to return home in Iitate immediately will be less than 20%. Most of them are elderly people with little risk of radiation damage, and it is difficult to regenerate the community. The only clinic that has restarted at Iitate manages the outpatient clinic only twice a week in the morning.



Figure 1. GPS-mapping of environmental radiation distribution on Google around the central Iitate. Radiation dose of almost all living areas are less than 0.3  $\mu\text{Sv/hr}$  (3.16, 2017).

#### 1. Nuclear bio-politics

Is there any justification of the scientific basis for the political evacuation direction against the disaster area? Unfortunately, it must be said that the scientific basis of regulation was lacking. Safety standards extrapolated from model experiments of radiation safety management and regulation standards in the field are considerably divergent. It can be said that it is rather a different concept. Experimental condition setting does not reflect the current situation in the field. Sciences (eg, radiobiology) were ineffective and impossible to regulate the field based on their experimental results. Nonetheless, the importance of scientific advice for political administration is recognized as an issue to be discussed more and more after 3.11 disaster (1). How can scientific advices [scientifically] reflect on political administration? Despite the necessity of politically neutral think tanks and scientific brains of politicians, etc. have been advocated, why did not they work in this 3.11 disaster? I believe that there was already a problem in the planning and establishment process of Japanese Basic Nuclear Energy Law (196th December 19th Act No. 186).

#### 2. Engine called law to drive bio-politics

Since there is a legal system of nuclear energy policy starting with the Basic Law of Nuclear Energy, bureaucrats can not "take a step" within the law, and will pro-

mote nuclear power politics endlessly along the law. It is difficult to change the bureaucratic mind for safety regulation unless the law will be changed (2). Bureaucrats are robots that run by law. Since nuclear power administration consists of inevitable incorporation of plutonium cycle from the beginning, abandoning nuclear reactors at the present time is a politically incompatible choice. In creating safety regulations, science that fills the gap between the scientific safety and the relief of victims should be established (for example, regulation anthropology). Many villagers can not return home safely even if evacuation regulation is terminated. It is not a simple matter of radiation dose in the field. It is a problem that there are significant estrangement between environmental safety and victim's feeling for relief.

Case study in which occupational prompt resuming was reliably connected to victim's relief: Mr. K was 54 years old (at the time of the disaster), a public officer, has worked with side jobs for Turkey bellflower, rice and honey, but after the disaster early retired from officer and evacuated temporarily, but immediately after July 2011 Later, leaving his family at refuge and seeking new farmland in the neighboring prefecture to start his life work as a house farmer mainly for Turkey bellflower. However, there was no administrative support in entrepreneurship in other prefectures, and in the situation that there was no subsidy payment immediately after the disaster, they were forced to start their own business without any administrative supports.

*「From the officers in Iitate village, I was treated as a traitor. But I got into this place with a strong mind that I could not live any more without resume of my life work. Initially I had difficulty with village ostracism, harassment etc. But I am now contributing to the rebuilding of the village for my success in business.」* Regional administration that does not support diaspora-like reconstruction in order to enclose villagers in the village, as a result, it can not escape from the driving force of the national nuclear power administration. On the other hand, is the unconscious resistance of the vulnerable people who are not bound by administrative districts and bricolages even farmlands might become a sustainable reconstruction power? (3). Many of the villagers were cultivation pioneers from 2 to 3 generations ancestors (Iitate Son-Shi, 1979), culture inherited from ancient times has become one of the bricolagic driving force through the network for their recovery. As seen in the Nanohana project (hybrid plant of radiation pollution and nature) in radiation contaminated environments in Fukushima, the driving force of reconstruction can be found even in the hybrid structure with pollution, so in order to fit Latour's scientific theory into a low-level radioactive environment, we should rethink the real nature and the progress of science in his theory.

#### References:

- (1) Takeo Arimoto, Yasushi Sato, Keiko Matsuo, Hiroyuki Yoshikawa.: Scientific Advice: Science, Technology, and Policy Making in the Twenty-First Century, University of Tokyo Press, 2016.(in Japanese)
- (2) Alan Hunt, Gary Wickham.: Foucault and the Law: Towards a Sociology of Law As Governance. Pluto Press, 1994.
- (3) Bruno Latour.: *Nous n'avons jamais été modernes.* La Decouverte, Paris, 1991.

# CO10-3 Characteristics Measurement in High Gamma Ray dose Environments for a Neutron Detector and Amplifier Used in an Active Neutron Method

M. Komeda, M. Maeda, H. Tobita, T. Saito<sup>1</sup>, H. Tanaka<sup>1</sup>

Japan Atomic Energy Agency

<sup>1</sup>Research Reactor Institute, Kyoto University

## INTRODUCTION:

We have been working on the development of a non-destructive assay (NDA) of nuclear materials by using the fast neutron direct interrogation (FNDI) method that is one of active neutron methods. Now we are proceeding with studies for NDA methods in high gamma ray dose environments, and then it is significant to investigate the influence of high gamma ray dose on a neutron detector. An amplifier of the neutron detector for the FNDI system requires fast pulse shaping to prevent counting loss. Furthermore, it is important to keep the base line stable in order to reduce the pile-up due to the high count rate. We have produced amplifiers with the double delay-line shaping function to satisfy the requirements. The purpose of this experiment is to evaluate the performance of the amplifiers under high dose-rate gamma ray environments. Note that the irradiation object in this experiment is not the amplifier but a neutron detector.

## EXPERIMENTS:

The experiment was carried out in the Co-60 gamma-ray irradiation facility. Figure 1 shows an amplifier, which is 18 cm in length, 4 cm in width and 3 cm in depth. The experimental setup is shown in Figure 2. We utilized He-3 neutron detector (proportional counter) that was 1 m in length and its pressure was 4 atm. The amplifier was mounted in close proximity to the detector. Lead blocks were set in front of the amplifier in order to reduce gamma rays. Since neutron signal from the detector was necessary, a neutron source (Cf-252) with polyethylene moderator was attached on the detector. The gamma ray dose-rate was varied from 1.3 Gy/h to 8.0 Gy/h by changing the distance between the gamma ray source and neutron source. We measured neutron counts at gamma ray irradiations.

## RESULTS:

Table 1 shows relative neutron counts compared to counts at 0 Gy/h. It was found that the ratio was reduced by 25 % at 2.0 Gy/h and 50 % at 4.0 Gy/h though the ratio at 1.3 Gy/h was almost constant. These results will give us important information to develop a new measurement system in high gamma ray dose environments. In the future, we will examine other neutron detectors for use in such severe environments. It may enable us to achieve further improvements.



Fig. 1 Amplifier for a neutron detector

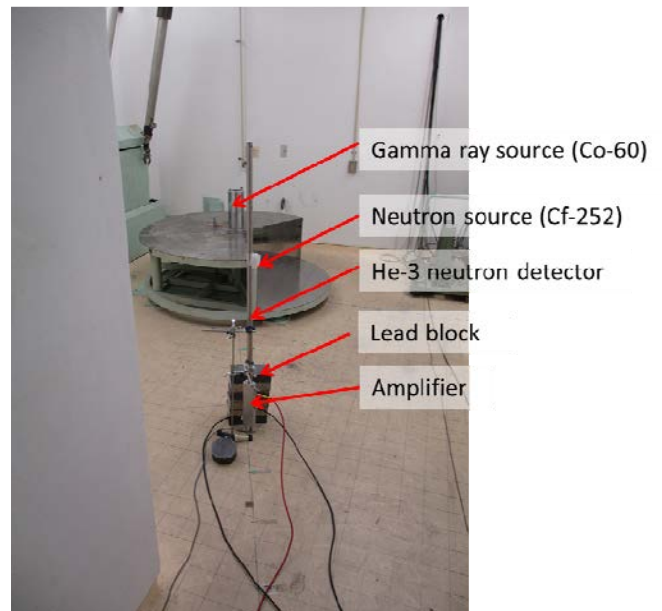


Fig. 2 The experimental setup

Table 1 Relative neutron counts

Gamma ray dose-rate (Gy/h)	1.3	2.0	4.0	8.0
Neutron counts	1.06	0.75	0.50	0.26

## CO12-1 Preliminary Experiments of Coherent Cherenkov Radiation Matched to the Circular Plane at KURRI-LINAC

N. Sei, T. Takahashi<sup>1</sup>

Research Institute for Measurement and Analytical Instrumentation, National Institute of Advanced Industrial Science and Technology

<sup>1</sup>Research Reactor Institute, Kyoto University

**INTRODUCTION:** The coherent Cherenkov radiation (CCR) is one of the intent light sources in the terahertz (THz) region. However, it is difficult to concentrate the CCR beam efficiently because the CCR propagates in a conical shape. Then, one of the author proposed a new method for matching the wave front of the CCR beam to the basal plane of a hollow conical dielectric by turning the apex of the hollow conical dielectric toward the incident electron beam [1]. When the angle between the generatrix and the rotation axis is half of the radiation angle of the CCR generated on the inner surface of the hollow conical dielectric, the CCR undergoes total reflection from the conical surface and the CCR phase is matched to the basal plane. We challenge to demonstrate the intent THz wave source using the CCR matched to a circular plane wave (CCR-MCP) at a linac at the Kyoto University Research Reactor Institute (KURRI-LINAC).

**EXPERIMENTS:** In order to generate the CCR-MCP beam, we use hollow conical dielectrics made of the high density polyethylene (HDPE). The refractive index and the absorption coefficient of the HDPE are 1.53 and  $0.02 \text{ cm}^{-1}$  at the wavelength of 1 mm. Because the absorption coefficient is low, an intent CCR beam can be expected to use the long hollow conical dielectric. Then, we prepared two hollow conical dielectrics with the lengths of 40 and 80 mm. The inner diameter of the hollow conical dielectrics was 10 mm. The angle between the generatrix and rotation axis was set to approximately  $25^\circ$ , which was a half of the Cherenkov angle for the HDPE. Figure 1 shows the photograph of the hollow conical dielectric used in the experiments. An aluminum collimator, whose length and inner diameter were 150 and 8 mm, was set in front of the hollow conical dielectric not to expose it to the electron beam. A kapton film with a thickness of  $50 \mu\text{m}$ , which was located at 0.4 m from the hollow conical dielectric downstream, was used to separate the CCR beam and the electron beam. Because coherent transition radiation was not generated at the kapton film, it could reduce the background in the THz region. The CCR beam was transported in the vacuum, and observed with a Martin-Puplett-type interferometer and a Si bolometer [2].

**RESULTS:** We performed experiments using an electron beam with the energy of 42 MeV at the KURRI-LINAC. The beam current passed the aluminum collimator was approximately 35 nA. Figure 2 shows interferograms measured with the Martin-Puplett-type inter-

ferometer. It is noted that satellite pulses appeared away from the zero pass difference (ZPD). The distance between the satellite pulse and the ZPD was proportional to the length of the hollow conical dielectric, and the proportionality coefficient was the refractive index of the HDPE. Therefore, these pulses were generated by the interference between the CCR beam and coherent diffraction radiation generating at the exit of the aluminum collimator. The intensity of the CCR beam can be measured by the increment of the base of the interferogram. The measured CCR intensity indicated that the absorption coefficient of the HDPE was  $0.02 \text{ cm}^{-1}$ . We plan to measure the two-dimensional spatial distribution of the CCR beam and to demonstrate the CCR beam to be the CCR-MCP.

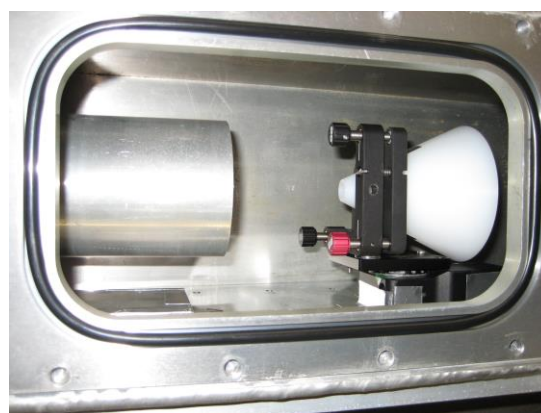


Fig. 1 Photograph of the hollow conical dielectric.

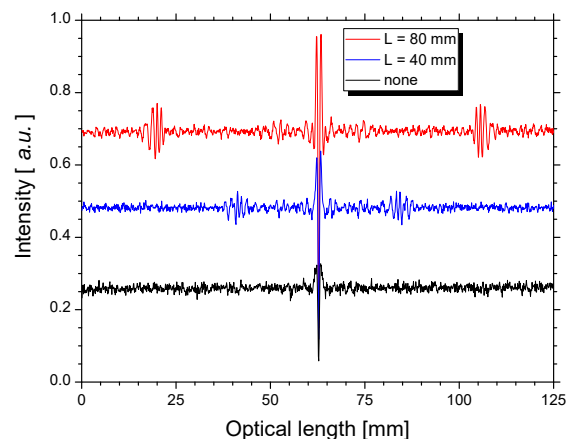


Fig. 2 Interferograms measured with the Martin-Puplett-type interferometer.

### REFERENCES:

- [1] N. Sei *et al.*, Phys. Lett A, **379** (2015) 2399-2404.
- [2] T. Takahashi and K. Takami, Infrared Phys. & Technol. **51** (2008) 363-366.

## CO12-2 Structural Analysis of Solid-Liquid Interface for Tribological Study by Means of Multi-Analytical Methods Involving Neutron Reflectometry

T. Hirayama, N. Akamatsu<sup>1</sup>, H. Hattori<sup>2</sup>, F. Takagi<sup>2</sup>, M. Hino<sup>3</sup>, N. Yamada<sup>4</sup>

*Dept. of Mechanical Eng., Doshisha University*

<sup>1</sup>*Dept. of Mechanical Eng., Graduate School of Doshisha University*

<sup>2</sup>*Idemitsu Kosan Co., Ltd.*

<sup>3</sup>*Research Reactor Institute, Kyoto University*

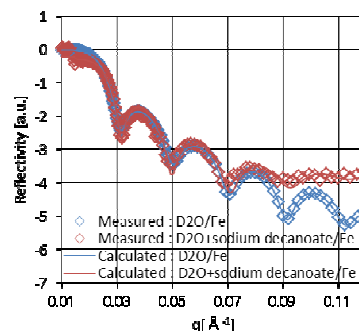
<sup>4</sup>*Institute of Materials Structure Science, KEK*

**INTRODUCTION:** In recent years, reduction of friction and wear in machines is one of the most important subjects from the viewpoint of global environmental issues, energy conservation and resource saving. Especially, the development of materials having excellent tribological properties is required to extend the life of machine parts by reducing friction loss. Particularly, under the boundary lubrication regime, oiliness additives and extreme pressure agents are used to reduce friction and wear.

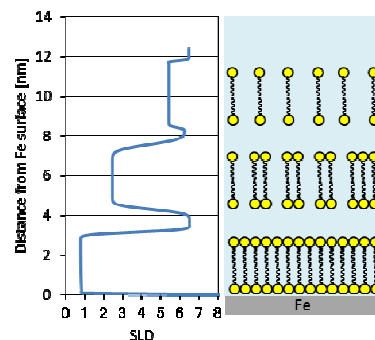
Sodium carboxylate is one of the most common additives for friction reduction and anticorrosion, for example. This report shows the structure of sodium carboxylate on the metal surface estimated by neutron reflectometry (NR) and its nanotribological properties measured by atomic force microscope (AFM) with a colloidal probe.

**EXPERIMENTAL RESULTS:** To investigate the structure of sodium decanoate as one of sodium carboxylates on Fe surface in water, NR experiment was conducted. The obtained reflectivity profiles and estimated structure are shown in Fig. 1. From the fitting operation, it was confirmed that the molecules of sodium decanoate formed multilayer structure shown in Fig. 1(b) when the concentration of sodium decanoate was comparatively large. On the other hand, when disodium sebacate was used as a target additive, the fitting operation for the NR profile presented the existence of higher-concentrated molecule layer on the Fe surface, but multilayer structure was not seen.

The friction forces measured by AFM with SiO<sub>2</sub> colloidal probe were shown in Fig. 2. We can see that the friction forces decreased when the additives were mixed into water. The friction force when the sodium decanoate was mixed into water was smaller than that when the disodium sebacate was used. The reason why was due to the formation of multilayer structure obtained by the sodium decanoate molecules. It was confirmed that the formation of multilayer structure of molecules brings large friction reduction, and we finally succeeded to make a correlation between the interfacial additive structure and the trend of friction force.

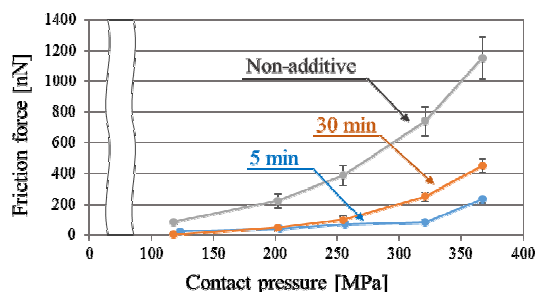


(a) NR profile

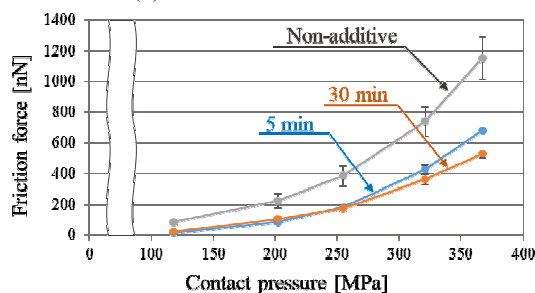


(b) Estimated structure

Fig. 1. NR experimental result of sodium decanoate on Fe surface in water



(a) With sodium decanoate



(b) With disodium sebacate

Fig. 2. Friction forces measured by AFM with SiO<sub>2</sub> colloidal probe in water

T. Iimoto, R. Hayashi, Y. Seki, A. Fujimoto, M. Ishida, T. Takahashi<sup>1</sup> and S. Takahashi<sup>1</sup>

*The University of Tokyo*

<sup>1</sup>*Research Reactor Institute, Kyoto University*

### INTRODUCTION:

Important research aspects can be found in the following keywords such as safety, security, hygiene and disaster prevention. Nuclear research reactor is one of representative facilities together with these keywords under their operation. It is effective to investigate the latest status on practical measures on these keywords in various facilities including nuclear research reactors, to compare each other among facilities, and to discuss more optimized ones for our positive safety management. Through this process, it is also essential to investigate the latest international and/or national regulations and the movement of revision of them. This total discussion contents and its fruit are directly useful for all relating laboratories.

### RESEARCH APPROACH:

General research approach is as follows.

- Measures of safety management during operation or standstill status of the real facilities would be investigated. This information would be used for our research discussion on the positive and more optimized safety management.
- It would not be a single year research, but maybe two to three years research for one theme.
- Information source of facilities would not be only KUR, KUCA or the other facilities in Kyoto University, but also the Kinki university research nuclear reactor or the facility of National Institute of Fusion Science, etc. This research is an active joint-research with these relating facilities and positive researchers on safety management.
- One of the distinctive features of this research is to involve office staffs as cooperators as well as researchers and technical staffs. In The University of Tokyo, most of the members in Division for Environment, Health and Safety are office staffs who knows real situation of safety management in laboratories very well.

Discussion target in FY of 2016 was determined as two items; “education framework, curriculum and textbooks for safety managers and users as well as relating officers to fill up the nuclear material controlling sheet for the use of small amount of U and Th” and “safety culture improvement in radiation

facilities” through our member discussion.

### EDUCATION FRAMEWORK FOR SMALL AMOUNT OF URANIUM AND THORIUM

Safety education for the users of small amounts of U and Th is not legally required. According to our survey in the universities in Japan, most of the universities use small amount of U and Th without education and/or training to staffs and students. However, since 2012, when new regulatory standards are applied, it has been required to establish an organizational structure, which ensures both user's technology securing and safety management for the use of U and Th. Currently, each university tries to establish a new system of education and has begun to examine the contents of education.

### LATEST SITUATION ON RADIATION SAFETY CULTURE IMPROVEMENT:

We started to gather the real activities information on the improvement of safety culture in international and domestic radiation or chemical facilities. Here are examples in The University of Tokyo.

- As a university headquarters, there is a mechanism to gather information on accidents and incidents occurring inside the university and to horizontally share the information. We are discussing countermeasures etc. for them at regular meetings.
- We publish a mail-magazine as a university headquarters and distribute it once a month for the purpose of making it easy for all members to understand the content of accidents or troubles occurring inside the university and the domestic trends related to it. It is also possible to browse back issues at the environmental safety portal website of the university.

Good practices will be listed up, and how to sustain and improve the motivation, skill and knowledge of the radiation safety officers will be the next target.

### NEXT RESEARCH TARGETS:

We started to discuss on various activities for improvement of safety culture in radiation facilities. Related international and/or domestic investigation and discussion should be continued next year.

We express our gratitude for their strong support and active discussion of Dr. K. Yasuda (Kyoto University), Dr. M. Takahashi, T. Saze (National Institute of Fusion Science) and Dr. H. Yamanishi (Kinki University) and others.

# CO12-4 Development of a Micro-cell MWPC for a Muon-electron Conversion Search Experiment, DeeMe

H. Natori, N. Abe<sup>1</sup>, M. Aoki<sup>2</sup>, Y. Furuya<sup>3</sup>, S. Mihara, F. Morimoto<sup>3</sup>, D. Nagao<sup>2</sup>, Y. Nakatsugawa, T. M. Nguyen<sup>2</sup>, H. Nishiguchi, Y. Seiya<sup>3</sup>, T. Takahashi<sup>1</sup>, Y. Takezaki<sup>3</sup>, N. Teshima<sup>3</sup>, K. Yamamoto<sup>3</sup>

High Energy Accelerator Research Organization (KEK)  
<sup>1</sup> Research Reactor Institute, Kyoto University  
<sup>2</sup> Department of Physics, Osaka University  
<sup>3</sup> Department of Physics, Osaka City University

**INTRODUCTION:** Discovery of Higgs boson filled the last piece of the Standard Model (SM) of elementary particle physics. The next coming issue is the physics beyond the SM (BSM). A discovery of mu-e conversion may be a clear clue to the BSM. DeeMe is going to search for mu-e conversion in J-PARC. The detector is required to tolerate to prompt burst pulses with an instantaneous hit rate of approximately 100GHz/mm<sup>2</sup> and width of 200ns and to detect electron signal with delay time of O( $\mu$  s) from the burst pulse. We have invented a new technique of dynamic gain control of wire chamber to avoid a long dead time by space charge effect.

**EXPERIMENTS:** Experimental setup is shown schematically in Fig. 1. Electron beam collimated to 18mm x 20mm penetrates a Multi-Wire Proportional Chamber (MWPC) and beam counters. Beam rate is tuned changing current of electron gun heater.

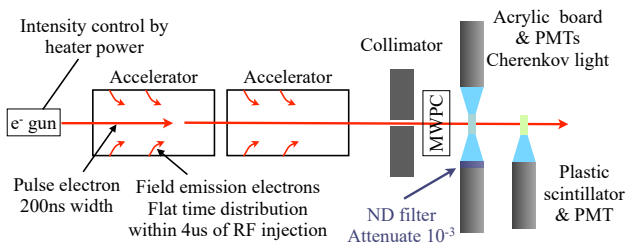


Fig. 1. Experimental setup

The pulsed electron beam with tuned beam rate generated from the beam gun emulates the prompt burst pulse. Delayed electron signals are emulated by field emission electrons. DC high voltage (HV) is applied to anode wires. MOSFET based switching module makes a pulsed HV to be applied to potential wires of the MWPC. During a main pulse comes, HV is applied to potential wires to make voltage difference between wires 0V. Soon after the main pulse passes the MWPC, potential wires are switched to ground level to make large voltage difference between anode-potential wires to detect delayed electrons. We developed this HV switching technique, which en-

ables sweeping electrons generated by a burst pulse without giving avalanche multiplication and enables the chamber to give avalanche multiplication for delayed signal electron without suffering gain reduction by space charge effect. This, on the other hand, induce large current on the cathode strip readouts by the rapidly changing voltage on the potential wires. Amplifier should cope with this input. Fig. 2 shows the circuit of our amplifier. We tuned the circuit elements not to make the amplifier saturated by the large current input. Pole zero cancellation circuit is implemented between 2-staged amplifiers to compensate slow tail by ion movement. We have manufactured the final version of the chamber and the amplifier. This experiment was planned to be a test of the final detector system under the condition equivalent to the final DeeMe condition.

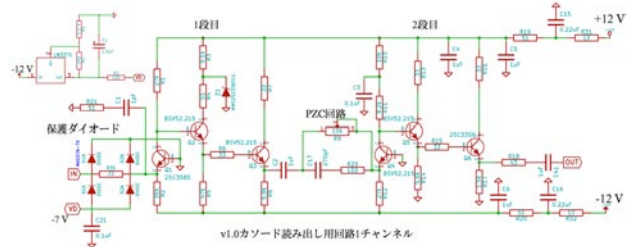


Fig. 2. Circuit diagram of the amplifier

**RESULTS:** The DeeMe MWPC with HV switching worked stably under the DeeMe final experiment compatible condition, electron pulse with instantaneous hit rate of 100GHz/mm<sup>2</sup>, width of 200ns and repetition of 25 Hz. Delayed electron from field emission electrons was observed by the MWPC without gain reduction by space charge effect. We also performed tuning of Pole-Zero Cancellation circuit in our amplifier. We could confirm our final chamber works well in the final experiment compatible condition.

## REFERENCES:

- [1] H. Natori, *et al.*, Prog Theor Exp Phys (2017) 2017 (2): 023C01.  
 “A fast high-voltage switching multiwire proportional chamber”

# CO12-5 Electron Beam Test of Avalanche Photodiode for Ganymede Laser Altimeter of Jovian Icy Satellite Explorer

M. Kobayashi, O. Okudaira, K. Ishibashi, M. Fujii<sup>1</sup>, T. Takahashi<sup>2</sup> and N. Abe<sup>2</sup>

*Planetary Exploration Research Center, Chiba Institute of Technology*

<sup>1</sup>*FAM science*

<sup>2</sup>*Research Reactor Institute, Kyoto University*

**INTRODUCTION:** The Ganymede Laser Altimeter (GALA) as part of the JUICE (Jovian Icy Satellite Explorer) payload is one of the instruments focusing on aspects related to the presence and characterizations of subsurface water oceans [1] [2]. For the first time the time-variability of the global figure of a moon due to tides exerted by Jupiter will be detected by altimetry measurements.

Japan team of GALA has a responsibility for back-end optics, optical sensor and analog electronics module of the receiver part of GALA instrument. We adopted an avalanche photo diode (hereafter APD) product manufactured by Excelitas Technologies, Montreal in Canada. Their APD product that are customized for space use have been adopted for many space missions due to its compactness and heritage in space.

The APD has also sensitivity to radiation that induces hole-electron pair in the depression layer. In space environment, the induced signal may affect light detection as background noise, called radiation noise. Jupiter has a strong magnetosphere and previous studies revealed energetic electrons are trapped in the magnetosphere and major component among the other ionizing radiation like proton and the other energetic ion. The APD will be shielded up against to the Jovian radiation environment however some of electrons can penetrate the shield into the APD. In this study, we used KURRI-LINAC as an electron beam source to emulate electrons irradiating the APD to investigate how energetic electron induces signals and interferes the returning laser pulse signal.

**EXPERIMENTS:** As device under test, we used a commercial APD module, LLAM-1060-R8BH of Excelitas Technologies, on which the flight APD module is based. The module is designed as commercial product but the sensor used in the module is one from a sensor chip lot selected as the flight lot. The APD sensor has a diameter of 0.8 mm and an enhanced sensitivity in infrared range, about 0.4 of quantum efficiency at 1064 nm. They commercially manufacture APD product particularly a hybrid module of APD which contains an APD sensor, a preamplifier, a thermo-electric controller and a temperature sensor in a package.

We performed twelve runs of the LINAC and electrons was accelerated to six different energies for irradiation to the DUT, 3, 5, 10, 20, 30 and 40 MeV. Irradiation angle is changed to be 0° (straight forward), 60° and 180° (backward). For a run with 40MeV, stainless steel plate

was set in the front of the DUT, simulating the structure of focal lane assembly in which multiple scatter of electron was expected to occur. The output signals of the amplifier were recorded with a digital oscilloscope.

**RESULTS:** The pulse shape of radiation induced noise might be similar to the stop pulse of GALA, the pulse width ranges 10 – 200 nsec. If radiation induced noise features such pulse shape as that, RFM (range Finder Module) may detect it as false detection.

In the test, the single short pulse per electron hit on the APD sensor has a rise time of 2 – 3 nsec and a fall time of 2 – 3 nsec for any energies and any incident angle of electrons. The DUT of LLAM-1060-R8BH has a system bandwidth of 200MHz, so the rise time and fall time are expected to be 1 – 2 nsec, while the results in this test show slower rise and fall times.

Fig. 1 shows examples of signal waveform of typical signal events from the test. In the figure, the signal height of 5 MeV and 0deg is almost same as one of 40MeV and 0deg, while the signal with 5MeV and 60deg has a higher signal height that the others. For 0deg irradiation, most events for typical 0deg incident (whatever its energy is) show short width, 2nsec for rise time and 2nsec for fall time. The slower rise and fall times than expected would be caused by signal delay in a cable connecting the APD module output to the oscilloscope for readout, the cable length was 50 cm. GALA APD has a system bandwidth of 100MHz, and the cable length between the APD module output and the following amplifier will be 15cm at maximum, therefore, radiation induced noise on GALA APD has similar pulse shape to the results of this test.

The pulse shape of radiation induced noise is typically similar to one of the start pulse of GALA laser, but not stop pulse (receiving from the Ganymede). The timing of real start pulse is known, so the false start pulse can be distinguished by timing.

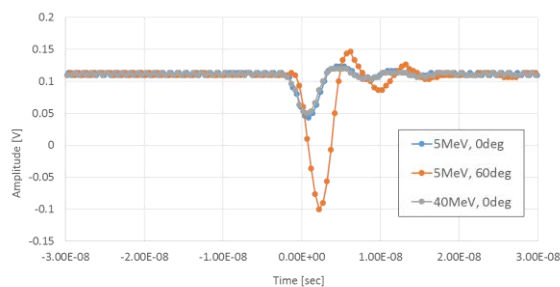


**Fig. 1. An example of output signal pulse from the APD.**

## REFERENCES:

- [1] Althaus, C. *et al.*, LPI Contribution No. 1980, id.4015, (2016).
- [2] Steinbrügge, G. *et al.*, Planet. Space Sci. 17, 184-191 (2015).

## CO12-6 Single Event Test using $^{252}\text{Cf}$ for On-board Computer used in Lean Satellite

H. Masui, H. Fukuda, S. Kawano, A. H. Kafi, M. Cho and K. Takamiya<sup>1</sup>

Laboratory of Spacecraft Environment Interaction Engineering, Kyushu Institute of Technology  
<sup>1</sup>Research Reactor Institute, Kyoto University

**INTRODUCTION:** Kyushu Institute of Technology (Kyutech) has been developing nano satellites since 2010. Kyutech are developing the suitable radiation test method for Lean satellite as nano/micro satellite. In the Lean satellite, it is more important to evaluate the reliability of the system than to evaluate the reliability of chips and parts. In other words, the implementation of the reliable reset system is important for the Lean satellite. In the radiation effect on the microprocessor, Single Event Latchup (SEL) is the most critical problem. The bas system such as on-board computer (OBC), electrical power system (EPS) and communication (COM) of Horyu-4[1] developed by Kyutech was tested in Kyoto University in 2015. However, the radiation effect on the mission part was not tested. In order to guarantee a long time mission, the radiation test on the mission part is essential. In FY2016, we conducted the checking reset system during mission part operating. In addition, Kyutech are developing cubesat as “BIRDS-1”[2]. BIRDS-1 has on-board computer almost similar to Horyu-4. The purpose of this test is to improve the stability of satellite system under the effects of radiation. This document reports the detail of testing and test results of Horyu-4.

**EXPERIMENTS:** Figure 1 shows the experimental setup. Circuit boards used in this test were Engineering Model for Horyu-4 and BIRDS-1. These boards have two H8 microprocessors (H8-1 and H8-2). The plastic package of microprocessors was removed so that the core of the microprocessors was directly exposed to  $^{252}\text{Cf}$  source. The circuit boards were set in a vacuum chamber. The pressure during the test was approximately 30 Pa. The voltage and current fed from the power supply were measured by a DAQ and oscilloscope and the operation of the microprocessors was verified by a PC with RS232 communication. An over-current protection (OCP) was implemented in the power line between each sub-system and EPS in the circuit boards. Once OCP detects over current due to SEL on the OBC, OCP sends a reset signal to EPS. To recover from the hang-up state of OBC by SEL, EPS automatically cuts the current from EPS to OBC. In this experiment,  $^{252}\text{Cf}$  source was mounted on XYZ stage. According to Horyu-4, we found that the satellite system operation becomes unstable during operating Attitude and Orbit Determination System (AODS) in preliminary test results. We specifically checked that the operation of the reset system when main mission, sub-system and AODS were operated. In the test,  $^{252}\text{Cf}$  source was moved above microprocessors and radiation was irradiated to two microprocessors after operating each system. We investigated whether the satel-

lite system can automatically be recovered or can be recovered by the reset command from the PC from the SEL state.

**RESULTS:** Table 1 shows the summary of test results for Horyu-4. Horyu-4 system could automatically recover from SEL state during operating main mission and AODS. However, the satellite system could not recover when SEL occurred during simultaneous operation of AODS and sub-system (camera etc.). In addition, the satellite could not recover when SEL occurred during operating some sub-systems. Therefore, it was found that simultaneous operation of the main mission and AODS for a long time is possible. On the other hand, we must take into account of the high possibility of SEL failure for simultaneous operation of AODS and sub-system.

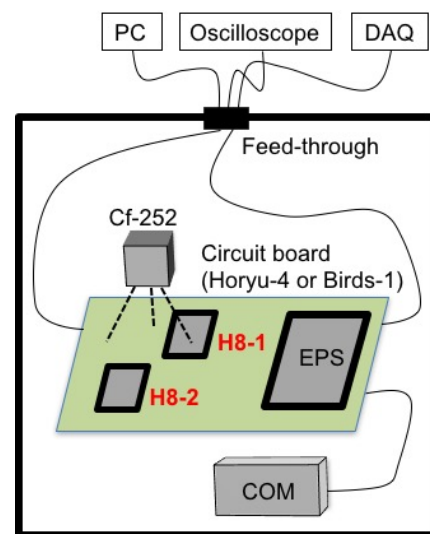


Fig. 1 Test setup of Horyu-4 and BIRDS-1

Table 1 Summary of Horyu-4 test results

	Operating part	H8-1	H8-2
1	Main mission	Pass	Pass
2	AODS	Pass	Pass
3	Main mission + AODS	Pass	Pass
4	AODS + Sub-system	Fail	Fail
5	Sub-system	Fail	Fail
6	Main mission + Sub-system	Fail	Fail

“Pass” means that satellite could recover from SEL state by automatically or command.

### REFERENCES:

- [1] T. Shimizu *et al.*, J. Spacecraft and Rockets. **54**, 2497-499 (2016).
- [2] G. Maeda *et al.*, 67<sup>th</sup> International Astronautical Congress IAC-16.B4.1.4 (2016).

**II. PUBLICATION LIST**  
**(APRIL 2016 – MARCH 2017)**

## 1. Slow Neutron Physics and Neutron Scattering

### Papers

Development of a large plano-elliptical neutron-focusing supermirror with metallic substrates  
Takeda Shin, Yamagata Yutaka, Yamada Norifumi L., Hino Masahiro, Hosobata Takuya, Guo Jiang, Morita Shinya, Oda Tatsuro, Furusaka Michihiro  
*Opt. Express* **12** (2016) 12478-12488.

Effect of Mg substitution on crystal structure and hydrogenation of Ce<sub>2</sub>Ni<sub>7</sub>-type Pr<sub>2</sub>Ni<sub>7</sub>  
K. Iwase, K. Mori, N. Terashita, S. Tashiro, T. Suzuki  
*J. Solid State Chem.* **247** (2017) 142-146.

Energy-resolved small-angle neutron scattering from steel  
Oba Yojiro, Morooka Satoshi, Ohishi Kazuki, Suzuki Jun-ichi, Takata Shin-ichi, Sato Nobuhiro, Inoue Rintaro, Tsuchiyama Toshihiro, Gilbert Elliot Paul, Sugiyama Masaaki  
*Journal of Applied Crystallography* **50**(2) (2016) 334-339.

Magnetic scattering in the simultaneous measurement of small-angle neutron scattering and Bragg edge transmission from steel  
Oba Yojiro, Morooka Satoshi, Ohishi Kazuki, Sato Nobuhiro, Inoue Rintaro, Adachi Nozomu, Suzuki Jun-ichi, Tsuchiyama Toshihiro, Gilbert Elliot Paul, Sugiyama Masaaki  
*Journal of Applied Crystallography* **49**(5) (2016) 1659-1664.

Neutron detection in the frame of spatial magnetic spin resonance  
Jericha Erwin, Bosina Joachim, Geltenbort Peter, Hino Masahiro, Mach Wilfried, Oda Tatsuro, Badurek Gerald  
*Nuclear Instruments and Methods in Physics Research Section A: Accelerators, Spectrometers, Detectors and Associated Equipment* **845** (2017) 552-555.

Pulsed neutron time-dependent intensity modulation for quasi-elastic neutron scattering spectroscopy  
Oda T. Hino M., Kitaguchi M., Geltenbort P., Kawabata Y.  
*Review of Scientific Instruments* **87**(10) (2016) 105124.

Real-time observations of lithium battery reactions – operando neutron diffraction analysis during practical operation  
S. Taminato, M. Yonemura, S. Shiotani, T. Kamiyama, S. Torii, M. Nagao, Y. Ishikawa, K. Mori, T. Fukunaga, Y. Onodera, T. Naka, M. Morishima, Y. Ukyo, D. S. Adipranoto, H. Arai, Y. Uchimoto, Z. Ogumi, K. Suzuki, M. Hirayama, R. Kanno  
*Scientific Reports* **6** (2016) 28843.

Structural origin of massive improvement in Li-ion conductivity on transition from (Li<sub>2</sub>S)<sub>5</sub>(GeS<sub>2</sub>)(P<sub>2</sub>S<sub>5</sub>) glass to Li<sub>10</sub>GeP<sub>2</sub>S<sub>12</sub> crystal  
Kazuhiro Mori, Takuya Kasai, Kenji Iwase, Fumika Fujisaki, Yohei Onodera, Toshiharu Fukunaga  
*Solid State Ionics* **301** (2017) 163-169.

Synthesis of PuNi<sub>3</sub>-type PrCo<sub>3</sub> and its hydrogen absorption-desorption property  
K. Iwase, K. Mori, S. Shimizu, S. Tashiro, T. Suzuki  
*Int. J. Hydrogen Energy* **41** (2016) 14788-14794.

### Proceedings

An effective deuterium exchange method for a neutron structure analysis by use of unfolding-refolding processes.  
A. Kita and Y. Morimoto  
*Int. Symp. Diffraction Structural Biology, Knoxville (Aug. 7-10, 2016)*

B-3 小型多目的中性子回折計建設の進捗状況  
小野寺陽平, 森一広, 吉野泰史, 佐藤節夫, 平賀晴弘, 岩瀬謙二, 塩野貴大, 松田浩平  
*京都大学原子炉実験所第51回学術講演会報文集 (1月26-27, 2017) 27. (in Japanese)*

J-PARC MLF BL06におけるTOF-MIEZE型スピンエコー分光法についての研究  
小田達郎, 日野正裕, 川端祐司, 遠藤仁, 山田悟史, 瀬戸秀紀  
*京都大学原子炉実験所第51回学術講演会報文集 (1月26-27, 2017) 40. (in Japanese)*

J-PARC/MLF BL06 中性子共鳴スピネコー分光器群(VIN ROSE)と中性子集光ミラー開発の現状 2  
日野正裕, 小田達郎, 吉永尚生, 金山雅哉, 川端祐司, 遠藤 仁, 山田悟史, 細島拓也, 武田 晋, 郭 江, 山形 豊,  
森田晋也, 古坂道弘, 瀬戸秀紀  
京都大学原子炉実験所第 51 回学術講演会報文集 (1 月 26-27, 2017)23. (in Japanese)

KUR B1 孔を利用した低速陽電子ビームライン輝度増強部の開発  
葛谷佳広, 大島永康, 木野村淳, 藪内 敦, 佐藤紘一, 徐 虬  
京都大学原子炉実験所第 51 回学術講演会報文集 (1 月 26-27, 2017)47. (in Japanese)

NC 制御加工装置による回転楕円体中性子ミラーの製作 II  
吉永尚生, 日野 正裕, 金山雅哉, 細島拓也, 山形 豊, 郭 江, 森田晋也, 武田 晋, 古坂道弘, 川端 祐司  
京都大学原子炉実験所第 51 回学術講演会報文集 (1 月 26-27, 2017)43. (in Japanese)

中性子散乱を利用したリチウムイオン電池研究の最前線  
森 一広  
京都大学原子炉実験所第 51 回学術講演会報文集 (1 月 26-27, 2017)54-56. (in Japanese)

## Reviews

J-PARC で見えたもの -大強度パルス中性子源の威力-  
瀬戸秀紀, 高木成幸, 海野昌喜, 森 一広  
化学 71 (2016) 70-71. (in Japanese)

入門講座中性子実験装置「J-PARC 編」(16)スピネコー分光器: J-PARC 中性子スピネコー分光器群  
(BL06 VIN ROSE)  
遠藤 仁, 日野正裕, 小田達郎  
日本中性子科学会誌 26 (2016) 104-108. (in Japanese)

## 2. Nuclear Physics and Nuclear Data

### Papers

Accuracy of Reactor Physics Parameters in Thorium-Loaded Accelerator-Driven System Experiments at Kyoto University Critical Assembly  
M. Yamanaka, C. H. Pyeon, T. Yagi and T. Misawa  
Nucl. Sci. Eng 183 (2016) 96-106.

Development of three-dimensional reactor analysis code system for accelerator-driven system, ADS3D and its application with subcriticality adjustment mechanism  
Sugawara Takanori, Nishihara Kenji, Iwamoto Hiroki, Oizumi Akito, Tsujimoto Kazufumi  
Journal of Nuclear Science and Technology 53(12) (2016) 2018-2027.

Fission fragments mass distributions of nuclei populated by the multinucleon transfer channels of the  $^{18}\text{O}+^{232}\text{Th}$  reaction Léguillon  
R., Nishio K., Hirose K., Makii H., Nishinaka I., Orlandi R., Tsukada K., Smallcombe J., Chiba S., Aritomo Y., Ohtsuki T., Tatsuzawa R., Takaki N., Tamura N., Goto S., Tsekhanovich I., Petrache C.M., Andreyev A.N.  
Physics Letters B 761 (2016) 125-130.

Liquid film dynamics of two-phase annular flow in square and tight lattice subchannels  
Daisuke Ito, Petros Papadopoulos and Horst-Michael Prasser  
Nuclear Engineering and Design 300 (2016) 467-474.

Measurements of gamma-ray emission probabilities of  $^{241}\text{Am}$ ,  $^{243}\text{Am}$  and  $^{239}\text{Np}$   
Terada Kazushi, Nakamura Shoji, Nakao Taro, Kimura Atsushi, Iwamoto Osamu, Harada Hideo, Takamiya Koichi, Hori Jun-ichi  
Journal of Nuclear Science and Technology 13(11) (2016) 1881-1888.

Medical applications of Cu, Zn, and S isotope effects  
Albarede Francis, Télouk Philippe, Balter Vincent, Bondanese Victor P., Albalat Emmanuelle, Oger Philippe, Bonaventura Paola, Miossec Pierre, Fujii Toshiyuki  
Metallomics 10 (2016) 1056-1070.

Monte Carlo Analysis of the Accelerator-Driven System at Kyoto University Research Reactor Institute  
W. K. Kim, H. C. Lee, C. H. Pyeon, H. C. Shin and D. J. Lee,  
Nucl. Eng. Technol. **48** (2016) 304-317.

## Proceedings

燃焼度確証時に利用可能な  $^{106}\text{Ru}/^{144}\text{Ce}$  放射能比の測定と燃焼解析  
佐藤駿介, 名内泰志, 早川岳人, 木村康彦, 須山賢也  
京都大学原子炉実験所第 5 回炉物理専門研究会 (RPW 2016) (11 月 30-12 月 1 日 2016) 54. (in Japanese)

ADS サイクルを用いた MA 低減と Pu-238 生成に関する研究  
小川 健斗, 千葉 豪  
京都大学原子炉実験所第 5 回炉物理専門研究会 (RPW 2016) (11 月 30 日-12 月 1 日 2016) 55. (in Japanese)

Investigation for sub-criticality adjustment mechanism of LBE cooled Accelerator-Driven System  
A. Oizumi, T. Sugawara, H. Iwamoto, K. Nishihara, K. Tsujimoto  
Proc. Third International Workshop on Technology and Components of Accelerator-Driven Systems (TCADS-3)  
Mito, Japan (Sep. 6-9, 2016)

Investigation of Nuclear Data of Minor Actinides in Variable Neutron Field for Accurate Determination of Thermal Neutron Capture Cross Section at KURRI  
Y. Takahashi, J. Hori, T. Sano, T. Yagi, H. Yashima, C. H. Pyeon, S. Nakamura and H. Harada  
Proc. Int. Conf. on the Physics of Reactors (PHYSOR2016) Sun Valley, Idaho, US (May 1-5, 2016) 1-5.

KUCA 固体減速架台における反応度評価の不確かさに関する研究  
伊藤誠人, 卞 哲浩, 三澤 毅  
京都大学原子炉実験所第 5 回炉物理専門研究会 (RPW 2016) (11 月 30 日-12 月 1 日 2016) 12. (in Japanese)

三次元多群燃料棒単位詳細炉心計算を再現する高速炉心計算の実現に向けた検討  
辻田浩介, 田淵将人, 巽 雅洋  
京都大学原子炉実験所第 5 回炉物理専門研究会 (RPW 2016) (11 月 30 日-12 月 1 日 2016) 25. (in Japanese)

中性子輸送計算に基づく検出確率を用いた未知放射線源の放射能強度推定  
菅谷信二, 遠藤知弘, 山本章夫  
京都大学原子炉実験所第 5 回炉物理専門研究会 (RPW 2016) (11 月 30 日-12 月 1 日 2016) 73. (in Japanese)

特異値分解とモード展開法を用いた Ringhals1 号機の炉雑音解析  
正部川英亨, 千葉 豪  
京都大学原子炉実験所第 5 回炉物理専門研究会 (RPW 2016) (11 月 30 日-12 月 1 日 2016) 38. (in Japanese)

軽水炉を用いた放射性毒性低減サイクルの検討  
和田怜志, 木村 礼, 松宮浩志, 櫻井俊吾, 吉岡研一, 平岩宏司  
京都大学原子炉実験所第 5 回炉物理専門研究会 (RPW 2016) (11 月 30 日-12 月 1 日 2016) 72. (in Japanese)

燃料メーカーにおける核データ不確かさ評価研究の位置付け  
山本賢治郎, 池原 正, 金 浩久, 山名哲平  
京都大学原子炉実験所第 5 回炉物理専門研究会 (RPW 2016) (11 月 30 日-12 月 1 日 2016) 23. (in Japanese)

## Reviews

ガンマ線スペクトル解析におけるピーク探査と面積計算実態と今後のスペクトル解析のあるべき姿  
青山道夫, 秋山正和, 浅井雅人, 阿部敬朗, 佐藤 泰, 高野直人, 高宮幸一, 濱島靖典, 武藤儀一, 山田隆志, 石津秀剛  
RADIOISOTOPES **65** (2016) 267-285. (in Japanese)

## 3. Reactor Physics and Reactor Engineering

### Papers

A Batch Size Decision Strategy by Checking Stability of Fission Source Distribution for Monte Carlo Eigenvalue Calculations  
S. H. Kim, M. Yamanaka, M. H. Woo, J. Y. Lee, C. H. Shin and C. H. Pyeon  
J. Nucl. Sci. Technol. **54** (2017) 301-311.

Analysis of KUCA Measurements by the Reactivity Monitoring M<sub>AP</sub>TA Method  
S. Dulla, S. S. Hoh, G. Marana, M. Nervo, P. Ravetto and C. H. Pyeon  
Ann. Nucl. Energy **101** (2017) 397-407.

Bubbly, Slug, and Annular Two-Phase Flow in Tight-Lattice Subchannels  
Prasser Horst-Michael, Bolesch Christian, Cramer Kerstin, Ito Daisuke, Papadopoulos Petros, Saxena Abhishek,  
Zboray Robert  
Nuclear Engineering and Technology **48(4)** (2016) 847-858.

Development of interfacial area concentration correlations for small and large bubbles in gas-liquid two-phase flows  
Shen Xiuzhong and Deng Baoqing  
International Journal of Multiphase Flow **87** (2016) 136-155.

Effective Delayed Neutron Fraction in Accelerator-Driven System Experiments with 100 MeV Protons at Kyoto  
University Critical Assembly  
M. Yamanaka, C. H. Pyeon, S. H. Kim, Y. Kitamura, H. Shiga and T. Misawa  
J. Nucl. Sci. Technol. **54** (2017) 293-300.

Monte Carlo Approach of Effective Delayed Neutron Fraction by k-ratio Method with External Neutron Source  
M. Yamanaka, C. H. Pyeon and T. Misawa  
Nucl. Sci. Eng. **184** (2016) 551-560.

New findings on neutron noise propagation properties in void containing water using neutron noise transport  
calculations  
T. Yamamoto, H. Sakamoto  
Progress in Nuclear Energy **90** (2016) 58-68.

Nuclear Date-Induced Uncertainty Qualification of Neutronics Parameters of Accelerator-Driven System  
G. Chiba, C. H. Pyeon, W. van Rooijen and T. Endo  
J. Nucl. Sci. Technol. **53** (2016) 1653-1661.

On-line Subcriticality Measurement using A Pulsed Spallation Neutron Source  
H. Iwamoto, K. Nishihara, T. Yagi and C. H. Pyeon  
J. Nucl. Sci. Technol. **54** (2017) 432-443.

Prediction of interfacial area transport in a coupled two-fluid model computation  
Schlegel Joshua P., Hibiki Takashi, Shen Xiuzhong, Appathurai Santosh, Subramani Hariprasad  
Journal of Nuclear Science and Technology **54** (2017) 58-73.

Proposal for selective isotope transmutation of long-lived fission products using quasi-monochromatic  $\gamma$ ray beams  
Hayakawa Takehito, Miyamoto Shuji, Hajima Ryoichi, Shizuma Toshiyuki, Amano Sho, Hashimoto Satoshi,  
Misawa Tsuyoshi  
Journal of Nuclear Science and Technology **53(12)** (2016) 2064-2071.

Sensitivity and Uncertainty Analyses of Lead Sample Reactivity Experiments at Kyoto University Critical Assembly  
C. H. Pyeon, A. Fujimoto, T. Sugawara, H. Iwamoto, K. Nishihara, Y. Takahashi, K. Nakajima and K. Tsujimoto  
Nuclear Science and Engineering **185** (2017) 460-472.

Uncertainty analysis of minor actinides transmutation in fast reactor cores  
Takeda Toshikazu, Fujimura Koji, Sano Tadafumi, Fouad Basma  
Annals of Nuclear Energy **101** (2017) 591-599.

気泡微細化沸騰における流れ場の PIV 計測  
伊藤大介, 刀塚 淳, 齊藤泰司  
日本機械学会論文集 B 編 (in Japanese) **83** (2017) 1-7. (in Japanese)

## Proceedings

A Preliminary Study on Applicability of Artificial Neural Network for Optimized Reflector Designs  
S. H. Kim, T. M. Vu and C. H. Pyeon  
Proc. 5th Int. Sympo. Innov. Nucl. Energy Systems (INES-5) Tokyo, Japan (Oct. 31- Nov.2, 2016) 1-6.

- Analysis and Interpretation of the KUCA ADS Benchmarks with Deterministic Analysis Codes  
W. F. G. van Rooijen, C. H. Pyeon, G. Chiba and T. Endo  
Proc. Int. Conf. on the Physics of Reactors (PHYSOR2016) Sun Valley, Idaho, US (May 1-5, 2016) 1-6.
- Benchmark Tests of Newly-Evaluated Data of  $^{235}\text{U}$  for CIELO Project using Integral Experiments of Uranium-Fueled FCA Assemblies  
Masahiro Fukushima, Yasunori Kitamura, Kenji Yokoyama, Osamu Iwamoto, Yasunobu Nagaya and Luiz Leal  
Proc. Int. Conf. on the Physics of Reactors (PHYSOR2016) Sun Valley, Idaho, US (May 1-5, 2016).
- Burn-up sensitivity analysis of minor actinide transmutation fast reactor  
T. Sano and T. Takeda  
Proc. Int. Conf. on the Physics of Reactors (PHYSOR2016) Sun Valley, Idaho, US (May 1-5, 2016) 684-693.
- Coupling Sjostrand and Feynman Methods in Prompt Neutron Decay Constant Analyses A. Talamo, Y. Gohar, F. Gabrielli, A. Rineiski and C. H. Pyeon  
Proc. Int. Conf. on the Physics of Reactors (PHYSOR2016) Sun Valley, Idaho, US (May 1-5, 2016) 1-6.
- Deterministic Analyses of the Phase-I Kinetic Experiments in the KUCA Subcritical A-core Configurations  
F. Gabrielli, A. Rineiski, A. Talamo, Y. Gohar and C. H. Pyeon  
Proc. Int. Conf. on the Physics of Reactors (PHYSOR2016) Sun Valley, Idaho, US (May 1-5, 2016) 1-6.
- Development of Hybrid Imaging Method for Multiphase Flow using X-ray and Neutrons  
Daisuke Ito and Yasushi Saito  
Proceedings of 11th International Topical Meeting on Nuclear Reactor Thermal Hydraulics, Operation and Safety Gyeongju, Korea (Oct.9-13, 2016).
- Estimation of interfacial area concentrations for two-group bubbles in gas-liquid two-phase flows  
X. Shen and B. Deng  
Proceeding of the 11th International Topical Meeting on Nuclear Reactor Thermal Hydraulics, Operation and Safety Gyeongju, Korea (Oct.9-13, 2016) N11P0136.
- Experimental Benchmarks on Accelerator-Driven System at Kyoto University Critical Assembly  
S. H. Kim, M. Yamanaka and C. H. Pyeon  
Proc. Workshop on Status on Accelerator Driven Systems Research and Technology Development (EuCARD2) CERN, Switzerland (Feb. 7-9, 2017) 1-5.
- Experimental Benchmarks on Subcriticality of Accelerator-Driven System with 100 MeV Protons at Kyoto University Critical Assembly  
C. H. Pyeon, M. Yamanaka and Y. Takahashi  
Proc. Int. Conf. on the Physics of Reactors (PHYSOR2016) Sun Valley, Idaho, US (May 1-5, 2016) 1-6.
- On Prediction Accuracy of Neutronics Parameters of Accelerator-Driven Sub-Critical System  
G. Chiba, W. F. G. van Rooijen, T. Endo and C. H. Pyeon  
Proc. Int. Conf. on Nucl. Data for Sci. Technol., (ND2016) Bruges, Belgium (Sep. 11-16, 2016) 1-6.
- Pulsed neutron imaging for non-destructive testing using simulated nuclear fuel samples  
Daisuke Ito, Tadafumi Sano, Jun-ichi Hori, Yoshiyuki Takahashi, Hiroyuki Hasemi, Takashi Kamiyama, Ken Nakajima  
Proceedings of 8th International Topical Meeting on Neutron Radiography Beijing (Sep. 4-8, 2016)
- Technique for bubble velocity vector in gas-liquid two-phase flow by using 4-sensor probe  
Saito Yasushi, Ariyoshi Gen and Ito Daisuke  
Proceedings of International Conference on Multiphase Flow 2016 Firenze, Italy (May 22-27, 2016).
- Turbulent characteristics in lead-bismuth flows flowing in poor and good wettability pipes  
Gen Ariyoshi, Daisuke Ito, Yasushi Saito and Kaichiro Mishima  
Proceedings of 24th International Conference on Nuclear Engineering Charlotte (Jun. 30, 2016).
- Turbulent structures in lead-bismuth flows measured by using intrusive probe methods  
Gen Ariyoshi, Daisuke Ito, Yasushi Saito and Kaichiro Mishima  
Proceedings of International Conference on Multiphase Flow 2016 Firenze, Italy (May 22, 2016).

Two-phase flow structure in a simulated debris bed

Milka Nava Daisuke Ito and Yasushi Saito

Proceedings of the 51st KURRI Scientific Meeting Kumatori, Japan (Jan. 26-27, 2017) 18.

Uncertainty Quantification of Spatial Correction Factor for Sjöstrand Method due to Cross-section Data

T. Kimura, T. Endo and A. Yamamoto

ANS 2016 winter meeting Las Vegas, NV USA (Nov. 6-10, 2016) 1081-1084.

Variance Reduction Factor Calculations for Neutronics Parameters of Accelerator-Driven System

G. Chiba, W. F. G. van Rooijen, T. Endo and C. H. Pyeon

Proc. Int. Conf. on the Physics of Reactors (PHYSOR2016) Sun Valley, Idaho, US (May 1-5, 2016) 1-6.

Visualization of solidification process in lead-bismuth eutectic

Daisuke Ito, Yasushi Saito, Hiroataka Sato, Takenao Shinohara

Proceedings of 8th International Topical Meeting on Neutron Radiography Beijing, China (Sep. 4-8, 2016).

$\alpha$  壊変反跳核  $^{229m}\text{Th}$  を捕集した試料からの真空紫外光測定

安田勇輝, 笠松良崇, 重河優大, 高宮幸一, 大槻 勤, 三頭聰明, 篠原 厚

京都大学原子炉実験所第 51 回学術講演会報文集 (1 月 26-27, 2017)41. (in Japanese)

トリウム燃料装荷による PWR 炉心特性への影響評価

小林千将, 竹田 敏, 北田孝典

京都大学原子炉実験所第 5 回炉物理専門研究会 (RPW 2016) (11 月 30 日-12 月 1 日 2016) 22. (in Japanese)

ナノ組織化した鉄鋼材料表面に形成する潤滑油膜観察に向けて

足立 望, 日野正裕, 大場洋次郎, 戸高義一

京都大学原子炉実験所第 51 回学術講演会報文集 (1 月 26-27, 2017)39. (in Japanese)

ロッドバンドル内気液二相流用界面積濃度輸送モデル

沈 秀中, 鄧 保慶

京都大学原子炉実験所第 51 回学術講演会報文集 (1 月 26-27, 2017)36. (in Japanese)

鉛ビスマス気液二相流に及ぼす壁面濡れ性の影響-プール体系におけるボイド率計測-

稲富良太, 有吉 玄, 伊藤大介, 齊藤泰司

京都大学原子炉実験所第 51 回学術講演会報文集 (1 月 26-27, 2017)16. (in Japanese)

鉛ビスマス凝固過程のパルス中性子イメージング

伊藤大介, 齊藤泰司, 佐藤博隆, 篠原武尚

京都大学原子炉実験所第 51 回学術講演会報文集 (1 月 26-27, 2017)15. (in Japanese)

小型分散電源用原子炉システムの開発 -月面・火星ミッションを想定した原子炉炉心の核熱設計-

木村 礼, 和田怜志, 吉田大志, 西岡佳朗, 兵藤義浩

京都大学原子炉実験所第 5 回炉物理専門研究会 (RPW 2016) (11 月 30 日-12 月 1 日 2016) 24. (in Japanese)

中性子照射模擬燃料デブリからの核種溶出挙動-試料調製

坂本峻一, 佐々木隆之, 小林大志, 秋山大輔, 桐島 陽, 佐藤修彰

京都大学原子炉実験所第 51 回学術講演会報文集 (1 月 26-27, 2017)22. (in Japanese)

長寿命超ウラン元素を燃焼可能な軽水炉 RBWR の開発

光安 岳

京都大学原子炉実験所第 5 回炉物理専門研究会 (RPW 2016) (11 月 30 日-12 月 1 日 2016) 53. (in Japanese)

Benchmarks of Subcriticality in Accelerator-Driven System at Kyoto University Critical Assembly

C. H. Pyeon, M. Yamanaka, S. H. Kim, T. M. Vu, T. Endo, W. F. G. van Rooijen and G. Chiba

Proc. Int. Conf. Mathematics & Computational Methods Applied to Nucl. Sci. & Eng. (M&C2017) Jeju, Korea (Apr. 16-20, 2017) 1-5.

Implementation of Fuel Depletion Sensitivity Calculation Capability into a Deterministic Reactor Physics Code System CBZ for Accelerator-Driven Sub-System Multi-Cycle Burnup Calculations

G. Chiba, W. F. G. van Rooijen, T. Endo and C. H. Pyeon

Proc. Int. Conf. Mathematics & Computational Methods Applied to Nucl. Sci. & Eng. (M&C2017) Jeju, Korea (Apr. 16-20, 2017) 1-8.

Nuclear Data-Induced Uncertainty Quantification of Neutron Multiplication Factor and Prompt Neutron Decay Constant for Pb-Bi loaded ADS Benchmark Problems at KUCA  
T. Endo, G. Chiba, W. F. G. van Rooijen, M. Yamanaka and C. H. Pyeon  
Proc. Int. Conf. Mathematics & Computational Methods Applied to Nucl. Sci. & Eng. (M&C2017)  
Jeju, Korea (Apr. 16-20, 2017) 1-8.

鉛ビスマス気液二相流におよぼす壁面濡れ性の影響- 強制対流体系におけるボイド率計測-  
有吉 玄, 稲富良太, 伊藤大介, 齊藤泰司, 三島嘉一郎  
京都大学原子炉実験所第 51 回学術講演会報文集 (1 月 26-27, 2017) 17. (in Japanese)

## Books

Thorium-Loaded Accelerator-Driven System Experiments in Kyoto University Research Reactor Institute, " Thorium Energy for the World  
C. H. Pyeon  
Springer 2016.

## 4. Material Science and Radiation Effects

### Papers

Attachment Behavior of Fission Products to Solution Aerosol  
Takamiya Koichi, Tanaka Toru, Nitta Shinnosuke, Itosu Satoshi, Sekimoto Shun, Oki Yuichi, Ohtsuki Tsutomu  
Journal of Radiation Protection and Research **41(4)** (2016) 350-353.

Automated Analysis of XANES: A Feasibility Study of Au Reference Compounds  
Chang S-Y, Molleta L B, Booth S G, Uehara A, Mosselmans J F W, Ignatyev K, Dryfe R A W, Schroeder S L M J. Phys.: Conf. Ser. **712** (2016) 12070.

Characteristics of Radiation-Resistant Real-Time Neutron Monitor for Accelerator-Based BNCT  
Nakamura Takemi, Sakasai Kaoru, Nakashima Hiroshi, Takamiya Koichi, Kumada Hiroaki  
Journal of Radiation Protection and Research **41(2)** (2016) 105-109.

Crystal-Site-Selective Spectrum of Fe<sub>3</sub>O<sub>4</sub> Obtained by Mössbauer Diffraction  
Nakamura Shin, Mitsui Takaya, Fujiwara Kosuke, Ikeda Naoshi, Kurokuzu Masayuki, Shimomura Susumu  
Journal of the Physical Society of Japan **86(2)** (2017) 23706.

Damage Behavior of REE-Doped W-Based Material Exposed to High-Flux Transient Heat Loads  
J. Shi, L.M. Luo, J.S. Lin, X. Zan, X.Y. Zhu, Q. Xu, Y.C. Wu  
Fusion Eng. Des. **113** (2016) 92-101.

Detection of Deuterium Sites in Tungsten by Thermal Desorption Spectroscopy and Positron Annihilation Spectroscopy  
K. Sato, R. Tamiya, Q. Xu, H. Tsuchida, T. Yoshiie  
Nucl. Mater. Energ **9** (2016) 554-559.

Dose dependence of irradiation hardening of neutron irradiated vanadium alloys by using temperature control rig in JMTR  
Fukumoto Ken-ichi, Onitsuka Takashi, Narui Minoru  
Nuclear Materials and Energy **9** (2016) 441-446.

Effect of Dislocations on Helium Retention in Deformed Pure Iron  
Y.H. Gong, X.Z. Cao, S.X. Jin, E.Y. Lu, Y.C. Hu, T. Zhu, P. Kuang, Q. Xu, B.Y. Wang  
J. Nucl. Mater. **482** (2016) 93-98.

Effect of Second-Phase Particles on the Properties of W-Based Materials under High-Heat Loading  
X.Y. Tan, P. Li, L.M. Luo, Q. Xu, K. Tokunaga, X. Zan, Y.C. Wu  
Nucl. Mater. Energ **9** (2016) 399-404.

Effects of Cr and W on defects evolution in irradiated F82H model alloys  
S.S. Huang, Q. Xu and T. Yoshiie  
Materials Letters **178** (2016) 272-275.

Effects of He, D Interaction on Thermal Desorption of He and D<sub>2</sub> and Microstructural Evolution in Pure Fe  
Q. Xu and J. Zhang  
J. Nucl. Mater. **479** (2016) 255-259.

Effects of microcrystallites on swelling behavior in chemically crosslinked poly (vinyl alcohol) gels  
Otsuka Emiko, Kudo Shuhei, Sugiyama Masaaki, Suzuki Atsushi  
Journal of Polymer Science Part B: Polymer Physics **2** (2016) 96-102.

Effects of Thermal Aging of Fe Ion-Irradiated Fe-0.6%Cu Alloy Investigated by Positron Annihilation  
Y.C. Hu, X.Z. Cao, P. Zhang, H. Tsuchida, Q. Xu, S.X. Jin, E.Y. Lu, Y.X. Li, R.S. Yu, B.Y. Wang, L. Wei  
Nucl. Sci. Tech. **28** (2017) 16.

Effects of zirconium element on the microstructure and deuterium retention of W-Zr/Sc<sub>2</sub>O<sub>3</sub> composites  
H.Y. Chen, L.M. Luo, J.B. Chen, X. Zan, X.Y. Zhu, Q. Xu, G.N. Luo, J.L. Chen, Y.C. Wu  
Scientific Reports **6** (2016) 32678.

Electrical resistivity measurement of Fe-0.6%Cu alloy irradiated by neutrons at 14-19 K  
Q. Xu, T. Yokotani, K. Sato, F. Hori  
J. Nucl. Mater. **481** (2016) 176-180.

Electron Irradiation-Induced Defects in Mo-Diluted FeCrNi Austenitic Alloy during Void Swelling Incubation  
B.Y. Wang, E.Y. Lu, C.X. Zhang, Q. Xu, S.X. Jin, P. Zhang and X.Z. Cao  
J. Phys. C **674** (2016) 12010.

Energy dispersive-EXAFS of Pd nucleation at a liquid/liquid interface  
Chang S-Y, Booth S G, Uehara A, Mosselmans J F W, Cibin G, Pham V-T, Nataf L, Dryfe R A W, Schroeder S L M  
J. Phys.: Conf. Ser. **712** (2016) 12058.

Ferrimagnetic Cage Framework in Ca<sub>12</sub>Fe<sub>10</sub>Si<sub>4</sub>O<sub>32</sub>Cl<sub>6</sub>  
Iimura Soshi, Tomota Yudai, Matsuishi Satoru, Masuda Ryo, Seto Makoto, Hiraka Haruhiro, Ikeda Kazutaka, Otomo Toshiya, Hosono Hideo  
Inorganic Chemistry **56(1)** (2017) 566-572.

Formation and destruction of physical crosslinks by mild treatments in chemically crosslinked poly(vinyl alcohol) gels  
Otsuka Emiko, Sugiyama Masaaki, Suzuki Atsushi  
Polymer Bulletin **7** (2016) 1215-1226.

High-Pressure-Hydrogen-Induced Spin Reconfiguration in GdFe<sub>2</sub> Observed by <sup>57</sup>Fe-Polarized Synchrotron Radiation Mössbauer Spectroscopy with Nuclear Bragg Monochromator  
Mitsui Takaya, Imai Yasuhiko, Hirao Naohisa, Matsuoka Takahiro, Nakamura Yumiko, Sakaki Kouji, Enoki Hiroto, Ishimatsu Naoki, Masuda Ryo, Seto Makoto  
Journal of the Physical Society of Japan **85(12)** (2016) 123707.

In vitro reconstitution and biochemical analyses of the Schizosaccharomyces pombe nucleosome  
Koyama Masako, Nagakura Wataru, Tanaka Hiroki, Kujirai Tomoya, Chikashige Yuji, Haraguchi Tokuko, Hiraoka Yasushi, Kurumizaka Hitoshi  
Biochemical and Biophysical Research Communications **482(4)** (2017) 896-901.

Investigation of Microstructure and Irradiation Behavior of W-Nb/Ti Composites Prepared by Spark Plasma Sintering  
J.B. Chen, L.M. Luo, M.L. Zhao, Q. Xu, X. Zan, Y.C. Wu,  
Fusion Eng. Des. **112** (2016) 349-354.

Irradiation Damage from Low-Dose High-Energy Protons on Mechanical Properties and Positron Annihilation Lifetimes of Fe-9Cr alloy  
Q. Xu, K. Fukumoto, Y. Ishi, Y. Kuriyama, T. Uesugi, K. Sato, Y. Mori, T. Yoshiie  
J. Nucl. Mater. **468** (2016) 260-263.

Laser Excited Novel Near-Infrared Photoluminescence Bands in Fast Neutron-Irradiated MgO·nAl<sub>2</sub>O<sub>3</sub>  
A.Z.M.S. Rahman, A.S.M.A. Haseeb, Q. Xu, J. Evslin, and M. Cinausero  
Radiat. Phys. Chem. **125** (2016) 122-126.

Local Fields at Nonmagnetic Impurity Sites in a Perovskite La<sub>0.7</sub>Ca<sub>0.3</sub>MnO<sub>3</sub>

W. Sato, S. Komatsuda, A. Osa, T. Sato and Y. Ohkubo

Hyperfine Interact. **237** (2016) 113.

Magnetic and spin transitions in wüstite: A synchrotron Mössbauer spectroscopic study

Maki Hamada, Seiji Kamada, Eiji Ohtani, Takaya Mitsui, Ryo Masuda, Tatsuya Sakamaki, Nanami Suzuki, Fumiya, Maeda and Masahide Akasaka

Physical Review B **93** (2016) 155165.

Measurement of neutron diffraction with compact neutron source RANS

Y. Ikeda, M. Takamura, A. Taketani, H. Sunaga, Y. Otake, H. Suzuki, M. Kumagai, Y. Oba, T. Hama

I Nuovo Cimento C **38** (2016) 177.

Microstructure and performance of rare earth element-strengthened plasma-facing tungsten material

L.M. Luo, J. Shi, J.S. Lin, X. Zan, X.Y. Zhu, Q. Xu, Y.C. Wu

Scientific Reports **6** (2016) 32701.

Nuclear Resonance Vibrational Spectroscopy and DFT study of Peroxo-Bridged Biferric Complexes: Structural Insight into Peroxo Intermediates of Binuclear Non-heme Iron Enzymes

Park Kiyong, Tsugawa Tomohiro, Furutachi Hideki, Kwak Yeonju, Liu Lei V., Wong Shaun D., Yoda Yoshitaka, Kobayashi Yasuhiro, Saito Makina, Kurokuzu Masayuki, Seto Makoto, Suzuki Masatatsu, Solomon Edward I.

Angewandte Chemie International Edition **4** (2016) 1294-1298.

Observation of Enhancement of the Morin Transition Temperature in Iridium-Doped  $\alpha$ -Fe<sub>2</sub>O<sub>3</sub> Thin Film by <sup>57</sup>Fe-Grazing Incidence Synchrotron Radiation Mössbauer Spectroscopy

Mitsui Takaya, Mibu Ko, Seto Makoto, Kurokuzu Masayuki, Pati Satya Prakash, Nozaki Tomohiro, Sahashi Masashi

Journal of the Physical Society of Japan **85**(6) (2016) 63601.

Observation of Flux Grown  $\alpha$ -Fe<sub>2</sub>O<sub>3</sub> Single Crystal at the Morin Transition by <sup>57</sup>Fe Synchrotron Radiation Mössbauer Diffraction

Takaya Mitsui, Shin Nakamura, Naoshi Ikeda, Kosuke Fujiwara, Ryo Masuda, Yasuhiro Kobayashi, and Makoto Seto

J. Phys. Soc. Jpn. **85** (2016) 54705.

One-step synthesis of graphene-Pt nanocomposites by gamma-ray irradiation

Tokai Akihiro, Okitsu Kenji, Hori Fuminobu, Mizukoshi Yoshiteru, Iwase Akihiro

Radiation Physics and Chemistry **123** (2016) 68-72.

Polymorphism of apyrimidinic DNA structures in the nucleosome

Osakabe Akihisa, Arimura Yasuhiro, Matsumoto Syota, Horikoshi Naoki, Sugawara Kaoru, Kurumizaka Hitoshi

Scientific Reports **7** (2017) 41783.

Properties of Lu<sub>2</sub>O<sub>3</sub> Doped Tungsten and Thermal Shock Performance

S. Wang, J. Zhang, L.M. Luo, X. Zan, Q. Xu, X.Y. Zhu, K. Tokunaga, Y.C. Wu

Powder Technology **301** (2016) 65-69.

Prospect for application of compact accelerator-based neutron source to neutron engineering diffraction

Ikeda Yoshimasa, Taketani Atsushi, Takamura Masato, Sunaga Hideyuki, Kumagai Masayoshi, Oba Yojiro, Otake Yoshie, Suzuki Hiroshi

Nuclear Instruments and Methods in Physics Research Section A: Accelerators, Spectrometers, Detectors and Associated Equipment **833** (2016) 61-67.

Radiation Synthesis of Binary Hydrogels with Thermoresponsive Pores

Sato Nobuhiro, Ueda Manabu, Matsuyama Tomochika, Sugiyama Masaaki

Transactions of the Materials Research Society of Japan **2** (2016) 127-130.

Retention and Thermal Desorption of Helium in Pure Tungsten

Q. Xu, J. Zhang, K. Maejima, N. Hirashita

Phil. Mag. Lett. **96** (2016) 477-481.

- Size Measurement of Radioactive Aerosol Particles in Intense Radiation Fields Using Wire Screens and Imaging Plates  
Oki Yuichi, Tanaka Toru, Takamiya Koichi, Osada Naoyuki, Nitta Shinnosuke, Ishi Yoshihiro, Uesugi Tomonori, Kuriyama Yasutoshi, Sakamoto Masaaki, Ohtsuki Tsutomu  
*Journal of Radiation Protection and Research* **41(3)** (2016) 216-221.
- Slow Dynamics in Glycerol: Collective de Gennes Narrowing and Independent Angstrom Motion  
Makina Saito, Yasuhiro Kobayashi, Ryo Masuda, Masayuki Kurokuzu, Shinji Kitao, Yoshitaka Yoda, Makoto Seto  
*Hyperfine Interact.* **237** (2016) 22.
- Structure of a Gold(III) Hydroxide and Determination of Its Solubility  
Kawamoto Daisuke, Ando Hiroaki, Ohashi Hironori, Kobayashi Yasuhiro, Honma Tetsuo, Ishida Tamao, Tokunaga Makoto, Okaue Yoshihiro, Utsunomiya Satoshi, Yokoyama Takushi  
*Bulletin of the Chemical Society of Japan* **11** (2017) 1385-1390.
- Study of Defects Introduced by 2 and 9 MeV Electron Irradiation in B2 Type Fe-Al Alloy  
Ueno Youhei, Iwase Akihiro, Ohsawa Kazuhito, Xu Qiu, Sato Koichi, Saitoh Yuichi, Horii Fuminobu  
*Defect and Diffusion Forum* **373** (2017) 126-129.
- Subcascade Formation Ratio in Neutron-Irradiated Stainless Steels  
T. Yoshiie, Y. Satoh, S.S. Huang, M. Horiki, K. Sato and Q. Xu  
*J. Phys. C* **674** (2016) 12002.
- Synchrotron Radiation Based Mössbauer Absorption Spectroscopy of Various Nuclides  
Ryo Masuda, Yasuhiro Kobayashi, Shinji Kitao, Masayuki Kurokuzu, Makina Saito, Yoshitaka Yoda, Takaya Mitsui and Makoto Seto  
*Hyperfine Interact.* **237** (2016) 43.
- Synchrotron Radiation Mössbauer Spectroscopy Using <sup>149</sup>Sm Nuclei  
Tsutsui Satoshi, Masuda Ryo, Kobayashi Yasuhiro, Yoda Yoshitaka, Mizuuchi Kota, Shimizu Yusei, Hidaka Hiroyuki, Yanagisawa Tatsuya, Amitsuka Hiroshi, Iga Fumitoshi, Seto Makoto  
*Journal of the Physical Society of Japan* **8** (2016) 83704.
- Synchrotron VUV-UV and Positron Lifetime Spectroscopy Study of Vacancy-Type Defects in Reactor Neutron-Irradiated MgO·nAl<sub>2</sub>O<sub>3</sub> (n=2)  
A.Z.M.S. Rahman, X.Z. Cao, B.Y. Wang, J. Evslin, Q. Xu and K. Atobe  
*Cogent Physics* **3** (2016) 1133481.
- Synchrotron-based Nickel Mössbauer Spectroscopy  
Gee Leland B., Lin Chun-Yi, Jenney Francis E., Adams Michael W. W., Yoda Yoshitaka, Masuda Ryo, Saito Makina, Kobayashi Yasuhiro, Tamasaku Kenji, Lerche Michael, Seto Makoto, Riordan Charles G., Ploskonka Ann, Power Philip P., Cramer Stephen P., Lauterbach Lars  
*Inorganic Chemistry* **14** (2016) 6866-6872.
- Testis-Specific Histone Variant H3t Gene Is Essential for Entry into Spermatogenesis  
Ueda Jun, Harada Akihito, Urahama Takashi, Machida Shinichi, Maehara Kazumitsu, Hada Masashi, Makino Yoshinori, Nogami Jumpei, Horikoshi Naoki, Osakabe Akihisa, Taguchi Hiroyuki, Tanaka Hiroki, Tachiwana Hiroaki, Yao Tatsuma, Yamada Minami, Iwamoto Takashi, Isotani Ayako, Ikawa Masahito, Tachibana Taro, Okada Yuki, Kimura Hiroshi, Ohkawa Yasuyuki, Kurumizaka Hitoshi, Yamagata Kazuo  
*Cell Reports* **18(3)** (2017) 593-600.
- The appearance of weak ferromagnetism of hexagonal stabilized ErFeO<sub>3</sub> thin film  
S. Jitsukawa, T. Nozue, H. Yokota, S. Nakamura, Y. Kobayashi, S. Kitao and M. Seto  
*Proceedings of ISAFE/CAPD/PFM 2016.* (2016)
- Thermal Stability of Nonmagnetic Cd and In Impurities in Fe<sub>3</sub>O<sub>4</sub>  
W. Sato, T. Ida, S. Komatsuda, T. Fujisawa, S. Takenaka, and Y. Ohkubo  
*J. Appl. Phys.* **120** (2016) 145104.
- Time-resolved positron annihilation study of relaxation dynamics of ion damage in fused quartz  
H. Tsuchida, S. Mizuno, H. Tsutsumi, A. Kinomura, R. Suzuki and A. Itoh  
*Materials Research Express* **3** (2016) 55201-55201.

Xeroderma pigmentosum group C protein interacts with histones: regulation by acetylated states of histone H3  
Kakumu Erina, Nakanishi Seiya, Shiratori Hiromi M., Kato Akari, Kobayashi Wataru, Machida Shinichi, Yasuda Takeshi, Adachi Naoko, Saito Naoaki, Ikura Tsuyoshi, Kurumizaka Hitoshi, Kimura Hiroshi, Yokoi Masayuki, Sakai Wataru, Sugasawa Kaoru  
Genes to Cells **22(3)** (2017) 310-327.

## Proceedings

Modification of the yellow luminescence in gamma-ray irradiated GaN bulk single crystal (Journal of Physics, IOP(UK))

Y. Torita, N. Nishikata, K. Kuriyama, K. Kushida, A. Kinomura and Q. Xu  
33rd International Conference on the Physics of Semiconductors Beijing, China (Jul. 31- Aug. 5, 2016).

Detection of re-emission positrons on metal surfaces during slow positron measurements

Kinomura A, Suzuki R, Ogawa H, Oshima N, O'Rourke B E, Yabuuchi A  
14th International Workshop on Slow Positron Beam Techniques & Applications Matsue, Japan (May. 22-27, 2016)  
012035-1 - 012035-4.

Evaluation of a positron-beam-pulsing system in KUR reactor-based positron beam facility

Yabuuchi A, Kinomura A, Kuzuya Y, Sato K, Xu Q, Oshima N, O'Rourke B E  
14th International Workshop on Slow Positron Beam Techniques & Applications Matsue, Japan (May. 22-27, 2016)  
12013-1 - 12013-4.

Evaluation of the optical performance of a brightness enhancement system developed for the KUR slow positron beamline

Kuzuya Yoshihiro, Oshima Nagayasu, Kinomura Atsushi, Yabuuchi Atsushi, Sato Koichi, Xu Qiu  
14th International Workshop on Slow Positron Beam Techniques & Applications Matsue, Japan (May. 22-27, 2017)  
012012-1 - 012012-4.

宝石評価に向けた光学的間接投影法

川口昭夫, 二宮洋文

京都大学原子炉実験所第 51 回学術講演会報文集 (1 月 26-27, 2017)26. (in Japanese)

KUR 低速陽電子ビームラインにおける陽電子消滅実験

藪内 敦

京都大学原子炉実験所専門研究会短寿命 RI を用いた核分光と核物性研究 III (12 月 20-21, 2016) 24-28.  
(in Japanese)

La<sub>0.7</sub>Ca<sub>0.3</sub>MnO<sub>3</sub>中に導入した不純物位置の超微細場測定

佐藤 渉, 小松田沙也加, 越知憲崇, 川田 知, 大久保嘉高

京都大学原子炉実験所専門研究会短寿命 RI を用いた核分光と核物性研究 III (12 月 20-21, 2016) 65-67.  
(in Japanese)

Reaction kinetic analysis of reactor surveillance data

T. Yoshiie, A. Kinomura, Y. Nagai

The 2016 Computer Simulation of Radiation Effects in S+D6olids (COSIRES) Loughborough, (Jun. 19-24, 2016)  
97-100.

Th 水酸化物固相の溶解度積に及ぼす温度影響の解釈

西川将吾, 小林大志, 佐々木隆之, 上原章寛

京都大学原子炉実験所第 51 回学術講演会報文集 (1 月 26-27, 2017)45. (in Japanese)

γ線照射還元法を用いた多元系金属ナノ微粒子の合成

戸田晋太郎, 田中元彬, 東海旭宏, 仲西穂高, 谷 真海, 興津健二, 水越克彰, 岩瀬彰宏, 阪本雅昭, 徐 虬, 堀 史説

京都大学原子炉実験所第 51 回学術講演会報文集 (1 月 26-27, 2017)30. (in Japanese)

ストロンチウム及びカルシウムの化学交換法における同位体分別研究 III

裕 隆太, 義本孝明, 佐久間洋一, 藤井俊行, 福谷 哲, 芝原雄司

京都大学原子炉実験所第 51 回学術講演会報文集 (1 月 26-27, 2017)46. (in Japanese)

リチウムイオン二次電池の放射光メスbauer一分光測定(Ni-61)

世木 隆

京都大学原子炉実験所 専門研究会短寿命 RI を用いた核分光と核物性研究 III (12 月 20-21, 2016) 75-80.  
(in Japanese)

酸化マグネシウムと含有トリチウム水の水酸化物化反応によるトリチウム分離の可能性

橋爪秀夫, 上原章寛, 福谷 哲, 藤井和子, 安藤寿浩

京都大学原子炉実験所第 51 回学術講演会報文集 (1 月 26-27, 2017)35. (in Japanese)

照射誘起結晶性回復の観測とモデリング

木野村 淳

京都大学原子炉実験所第 51 回学術講演会報文集 (1 月 26-27, 2017)51-53. (in Japanese)

多元素メスbauer一分光法の凝縮系研究への高度応用

瀬戸 誠, 北尾真司, 小林康浩, 齋藤真器名, 窪田卓見, 増田 亮, 黒葛真行, 神原陽一, 中村真一, 篠田圭司,

小島憲道, 横山拓史, 小寺政人, 山田幾也, 藤田晃司, 高橋正, 松下正史, 山本泰彦, 横田紘子

京都大学原子炉実験所第 51 回学術講演会報文集 (1 月 26-27, 2017)57-60. (in Japanese)

電子線照射 FeAl 金属間化合物中の空孔による水素捕獲

上野陽平, 岩瀬彰宏, 徐 虬, 佐藤紘一, 大澤一人, 河裾厚男, 前川雅樹, 齋藤勇一, 堀 史説

京都大学原子炉実験所第 51 回学術講演会報文集 (1 月 26-27, 2017)31. (in Japanese)

包接化合物を利用した親水性高分子と金属塩とのコンポジットの作製[V]~疎水性表面の改質~

川口昭夫

京都大学原子炉実験所第 51 回学術講演会報文集 (1 月 26-27, 2017)25. (in Japanese)

陽電子消滅法を用いた電子線照射した Fe-Cr 合金の相分離初期過程の検出

鬼塚貴志, 佐藤紘一, 徐 虬, 福元謙一

平成28年度日本金属学会・日本鉄鋼協会北陸信越支部連合講演会 金沢, 日本 (Dec.3, 2016) 56. (in Japanese)

## Books

全固体電池のイオン伝導性向上技術と材料,製造プロセスの開発,

第 11 章 第 8 節「中性子散乱法を用いた超イオン伝導体の中でのリチウムイオン伝導経路の観察」

森 一広

技術情報協会 2017 (in Japanese)

## Reviews

Crystal-Site-Specific Electronic States Measured Using Mössbauer Diffraction Method

Makoto Seto

JPSJ News and Comments **14** (2017) 2.

## Others

高強度コヒーレント放射の水および生物への作用に関する研究

奥田修一, 田中良晴, 木田侑, 高橋俊晴, S. Nam

大阪府立大学地域連携研究機構・放射線研究センター平成 27 年度放射線施設共同利用報告書 13 (2017).  
(in Japanese)

## 5. Geochemistry and Environmental Science

### Papers

$^{40}\text{Ar}$ - $^{39}\text{Ar}$  dating and tectonic implications of volcanic rocks recovered at IODP Hole U1342A and D on Bowers Ridge, Bering Sea

Sato Keiko, Kawabata Hiroshi, W. Scholl David, Hyodo Hironobu, Takahashi Kozo, Suzuki Katsuhiko, Kumagai Hidenori

Deep Sea Research Part II: Topical Studies in Oceanography **125-126** (2016) 214-226.

Accurate Determination of Chlorine, Bromine and Iodine in U.S. Geological Survey Geochemical Reference Materials by Radiochemical Neutron Activation Analysis  
Sekimoto Shun and Ebihara Mitsuru  
Geostandards and Geoanalytical Research **41(2)** (2016) 213-219.

Analysis of cesium isotope compositions in environmental samples by thermal ionization mass spectrometry-3  
Shibahara Yuji, Kubota Takumi, Fujii Toshiyuki, Fukutani Satoshi, Takamiya Koichi, Konno Mitsuyuki, Mizuno Satoshi, Yamana Hajimu  
Journal of Nuclear Science and Technology **54(2)** (2016) 158-166.

Exclusive attributes of undoped poly (ethylene terephthalate) for alpha particle detection  
Nakamura Hidehito, Sato Nobuhiro, Kitamura Hisashi, Maki Daisuke, Shirakawa Yoshiyuki, Takahashi Sentaro  
Radiation Measurements **92** (2016) 54-58.

Interaction of rare earth elements and components of the Horonobe deep groundwater  
Kirishima Akira, Kuno Atsushi, Amamiya Hiroshi, Kubota Takumi, Kimuro Shingo, Amano Yuki, Miyakawa Kazuya, Iwatsuki Teruki, Mizuno Takashi, Sasaki Takayuki, Sato Nobuaki  
Chemosphere **168** (2017) 798-806.

Origin of Spherule Samples Recovered from Antarctic Ice Sheet—Terrestrial or Extraterrestrial?  
Sekimoto Shun, Kobayashi Takayuki, Takamiya Koichi, Ebihara Mitsuru, Shibata Seiichi  
Nuclear Engineering and Technology **48(2)** (2016) 293-298.

Oxidation of Solid Phase and Ionic Strength Effect to the Cesium Adsorption on Pumice Tuff  
Rajib Mohammad, Kobayashi Taishi, Oguchi Chiaki T., Sasaki Takayuki  
Journal of Geoscience and Environment Protection **4** (2017) 64-73.

Risk Assessment of Neonatal Exposure to Low Frequency Noise Based on Balance in Mice  
Ohgami Nobutaka, Oshino Reina, Ninomiya Hiromasa, Li Xiang, Kato Masashi, Yajima Ichiro, Kato Masashi  
Frontiers in Behavioral Neuroscience **11** (2017) 20.

Separation and purification of <sup>99m</sup>Tc from <sup>99</sup>Mo produced by electron linear accelerator  
Sekimoto Shun, Tatenuma Katsuyoshi, Suzuki Yumi, Tsuguchi Akira, Tanaka Atsushi, Tadokoro Takahiro, Kani Yuko, Morikawa Yasumasa, Yamamoto Asaki, Ohtsuki Tsutomu  
Journal of Radioanalytical and Nuclear Chemistry **54(2)** (2017) 1361-1366.

Signatures of Multiple Mineralization Processes in the Archean Orogenic Gold Deposit of the Pampalo Mine, Hattu Schist Belt, Eastern Finland  
Molnár Ferenc, O' Brien Hugh, Lahaye Yann, Käpyaho Asko, Sorjonen-Ward Peter, Hyodo Hironobu, Sakellaris Grigorios  
Economic Geology **111(7)** (2016) 1659-1703.

Slab-derived halogens and noble gases illuminate closed system processes controlling volatile element transport into the mantle wedge  
Kobayashi Masahiro, Sumino Hirochika, Nagao Keisuke, Ishimaru Satoko, Arai Shoji, Yoshikawa Masako, Kawamoto Tatsuhiko, Kumagai Yoshitaka, Kobayashi Tetsuo, Burgess Ray, Ballentine Chris J.  
Earth and Planetary Science Letters **457** (2017) 106-116.

吸光光度法による溶融塩中の溶存イオンの定量と希土類磁石リサイクルプロセスへの応用  
関本英弘  
溶融塩および高温化学 **58(2)** (2016) 69-75. (in Japanese)

地下水中アンモニア除去へのアナモックスの適用—パイロット試験及び長期室内試験による検討  
藤川陽子, 平 大輔, 藤井隆夫, Phan Do Hung, 鈴木市郎, 古川憲治  
地下水・土壌汚染とその防止対策に関する研究集会講演論文集 **22** (2016) 94-96. (in Japanese)

## Proceedings

高レベル放射性廃棄物の多様化に向けた処分場中性子場解析システムの開発  
前田大輝, 大和田賢治, 相澤直人, 岩崎智彦  
京都大学原子炉実験所第5回炉物理専門研究会 (RPW 2016) (11月30日-12月1日 2016) 26. (in Japanese)

定説を越え,新たなプラスチックシンチレーション物質に関する研究とその応用

中村秀仁

京都大学原子炉実験所第 51 回学術講演会報文集 (1 月 26-27, 2017)7. (in Japanese)

日本とベトナムにおける環境問題の解決をめざす技術開発—放射性セシウムと砒素の除去

藤川陽子

京都大学原子炉実験所第 51 回学術講演会報文集 (1 月 26-27, 2017)9-13. (in Japanese)

福島原発事故による日本産フトミズ属 (Genus *Pheretima*) への放射性セシウムの移行と体内動態

田中草太, 足達太郎, 藤原慶子, 高橋知之, 高橋千太郎

京都大学原子炉実験所第 51 回学術講演会報文集 (1 月 26-27, 2017)28. (in Japanese)

Zr および Pd の産業利用の現状と環境動態:長寿命核分裂核種の再利用に伴う被ばく線量の評価の観点から

岩田佳代子, 田中草太, 高島直貴, 高橋知之, 高橋千太郎

京都大学原子炉実験所第 51 回学術講演会報文集 (1 月 26-27, 2017)29. (in Japanese)

放射能汚染検査装置の開発

奥村 良, 山田辰矢

京都大学原子炉実験所第 51 回学術講演会報文集 (1 月 26-27, 2017)32. (in Japanese)

溶液エアロゾルへの核分裂生成物の付着挙動における溶質の影響

西澤佑介, 高宮幸一, 関本 俊, 沖 雄一, 大槻 勤

京都大学原子炉実験所第 51 回学術講演会報文集 (1 月 26-27, 2017)33. (in Japanese)

福島で採取した放射性セシウムを含む微粒子の組成分析

西山雄大, 高宮幸一, 関本 俊, 沖 雄一, 大槻 勤

京都大学原子炉実験所第 51 回学術講演会報文集 (1 月 26-27, 2017)42. (in Japanese)

## 6. Life Science and Medical Science

### Papers

A Genetically Encoded Probe for Live-Cell Imaging of H4K20 Monomethylation

Sato Yuko, Kujirai Tomoya, Arai Ritsuko, Asakawa Haruhiko, Ohtsuki Chizuru, Horikoshi Naoki, Yamagata Kazuo, Ueda Jun, Nagase Takahiro, Haraguchi Tokuko, Hiraoka Yasushi, Kimura Akatsuki, Kurumizaka Hitoshi, Kimura Hiroshi

Journal of Molecular Biology **4828(20)** (2016) 3885-3902.

A polymerization-based method to construct a plasmid containing clustered DNA damage and a mismatch

Takahashi Momoko, Akamatsu Ken, Shikazono Naoya

Analytical Biochemistry **510** (2016) 129-135.

Abnormal Protein Aggregation Due to the Presence of D-Aspartyl Residues in Cataractous Lenses

Fujii Noriko, Fujii Norihiko, Sugiyama Masaaki

Transactions of the Materials Research Society of Japan **2** (2016) 131-134.

An Effective Deuterium Exchange Method for Neutron Crystal Structure Analysis with Unfolding–Refolding Processes

A. Kita and Y. Morimoto

Mol Biotechnol **58** (2016) 130-136.

Bioactive polysaccharide-based pH-sensitive polymers for cytoplasmic delivery of antigen and activation of antigen-specific immunity

Yuba Eiji, Yamaguchi Ayaka, Yoshizaki Yuta, Harada Atsushi, Kono Kenji

Biomaterials **120** (2017) 32-45.

Chromatin architecture may dictate the target site for DMC1, but not for RAD51, during homologous pairing

Kobayashi Wataru, Takaku Motoki, Machida Shinichi, Tachiwana Hiroaki, Machara Kazumitsu, Ohkawa Yasuyuki, Kurumizaka Hitoshi

Scientific Reports **6** (2016) 24228.

Cigarette smoke reversibly activates hypoxia-inducible factor 1 in a reactive oxygen species-dependent manner  
Daijo Hiroki, Hoshino Yuma, Kai Shinichi, Suzuki Kengo, Nishi Kenichiro, Matsuo Yoshiyuki, Harada Hiroshi,  
Hirota Kiichi  
Scientific Reports **6** (2016) 34424.

Crystal structures of heterotypic nucleosomes containing histones H2A.Z and H2A  
Horikoshi Naoki, Arimura Yasuhiro, Taguchi Hiroyuki, Kurumizaka Hitoshi  
Open Biology **6** (2016) 160127.

Design and Synthesis of Heteroleptic Cyclometalated Iridium(III) Complexes Containing Quinoline-type Ligands  
that Exhibit Dual Phosphorescence  
Sarvendra Kumar, Yosuke Hisamatsu, Yusuke Tamaki, Osamu Ishitani, and Shin Aoki  
Inorganic Chemistry **55** (2016) 3829.

Design and Synthesis of Tris-Heteroleptic Cyclometalated Iridium(III) Complexes Consisting of Three Different  
Nonsymmetric Ligands Based on Ligand-Selective Electrophilic Reactions via Interligand HOMO Hopping  
Phenomena  
Yosuke Hisamatsu, Sarvendra Kumar, Shin Aoki  
Inorganic Chemistry **56** (2017) 886.

Determination of dissolved natural thorium and uranium in Horonobe and Mizunami Underground Research  
Laboratory groundwater and its thermodynamic analysis  
T. Sasaki, T. Koukami, T. Kobayashi, A. Kirishima, H. Murakami, Y. Amano, T. Mizuno, T. Iwatsuki, H. Sasamoto,  
K. Miyakawa  
J. Nucl. Sci. Technol. **54(3)** (2017) 373-381.

Doxorubicin Delivery Using pH and Redox Dual-Responsive Hollow Nanocapsules with a Cationic Electrostatic  
Barrier  
Teranishi Ryoma, Matsuki Ryota, Yuba Eiji, Harada Atsushi, Kono Kenji  
Pharmaceutics **9(1)** (2016) 4.

Dual-stimuli responsive liposomes using pH- and temperature-sensitive polymers for controlled transdermal delivery  
Yamazaki Naoko, Sugimoto Takumi, Fukushima Mitsuhiro, Teranishi Ryoma, Kotaka Aki, Shinde Chiharu, Kumei  
Takayuki, Sumida Yasushi, Munekata Yuki, Maruyama Kei-ichi, Yuba Eiji, Harada Atsushi, Kono Kenji  
Polym. Chem. **9** (2017) 1507-1518.

Efficiency of radiation-induced base lesion excision and the order of enzymatic treatment  
Shiraishi Iyo, Shikazono Naoya, Suzuki Masao, Fujii Kentaro, Yokoya Akinari  
International Journal of Radiation Biology **93 (3)** (2017) 295-302.

Efficient Synthesis of Tris-Heteroleptic Iridium (III) Complexes Based on the Zn<sup>2+</sup>-Promoted Degradation of Tris-  
Cyclometalated Iridium (III) Complexes and Their Photophysical Properties  
Yuichi Tamura, Yosuke Hisamatsu, Sarvendra Kumar, Taiki Itoh, Kyouhei Sato, Reiko Kuroda, Shin Aoki,  
Inorganic Chemistry **56** (2017) 812.

Evaluation of Molecular Perturbation of a Deuterated Protein by Temperature Factor Refinement in X-Ray Structural  
Analysis of High- Resolution Diffraction Data  
Uemura Takuya, Kita Akiko, Yukio Morimoto  
J Biotechnol Biomater **6(2)** (2016) 1000223.

Exposure to diphtheria toxin during the juvenile period impairs both inner and outer hair cells in C57BL/6 mice  
Konishi Hiroyuki, Ohgami Nobutaka, Matsushita Aika, Kondo Yuki, Aoyama Yuki, Kobayashi Masaaki, Nagai Taku,  
Ugawa Shinya, Yamada Kiyofumi, Kato Masashi, Kiyama Hiroshi  
Neuroscience **351** (2017) 15-23.

FANCI-FANCD<sub>2</sub> stabilizes the RAD51-DNA complex by binding RAD51 and protects the 5' -DNA end  
Sato Koichi, Shimomuki Mayo, Katsuki Yoko, Takahashi Daisuke, Kobayashi Wataru, Ishiai Masamichi, Miyoshi  
Hiroyuki, Takata Minoru, Kurumizaka Hitoshi  
Nucleic Acids Research **44(22)** (2016) 10758-10771.

Ferulic Acid Suppresses Amyloid  $\beta$  Production in the Human Lens Epithelial Cell Stimulated with Hydrogen  
Peroxide  
Nagai Noriaki, Kotani Sachiyo, Mano Yu, Ueno Akina, Ito Yoshimasa, Kitaba Toshio, Takata Takumi, Fujii Noriko  
BioMed Research International **2017** (2017) 1-9.

H3K9me3 facilitates hypoxia-induced p53-dependent apoptosis through repression of APAK.  
Olcina MM, Leszczynska K, Senra JM, Isa N, Harada H, Hammond EM.  
*Oncogene* **35** (2016) 793-799.

Hypoxia-inducible factor 1 promotes chemoresistance of lung cancer by inducing carbonic anhydrase IX expression  
Sowa Terumasa, Menju Toshi, Chen-Yoshikawa Toyofumi F., Takahashi Koji, Nishikawa Shigeto, Nakanishi Takao, Shikuma Kei, Motoyama Hideki, Hijiya Kyoko, Aoyama Akihiro, Sato Toshihiko, Sonobe Makoto, Harada Hiroshi, Date Hiroshi  
*Cancer Medicine* **6** (2017) 288-297.

Identification and characterization of GmPDIL7, a soybean ER membrane-bound protein disulfide isomerase family protein  
Okuda Aya, Matsusaki Motonori, Masuda Taro, Urade Reiko  
*The FEBS Journal* **284(3)** (2016) 414-428.

Improved isolation procedure for shikonin from the root of the Chinese medicinal plant *Lithospermum erythrorhizon* and its solubilization with cyclodextrins  
H. Azuma, J. Li, R. Youda, T. Suzuki, K. Miyamoto, T. Taniguchi and T. Nagasaki  
*J. Appl. Res. Med. Arom Plants* **3(2)** (2016) 58-63.

Improvement of Peptide-Based Tumor Immunotherapy Using pH-Sensitive Fusogenic Polymer-Modified Liposomes  
Yoshizaki Yuta, Yuba Eiji, Komatsu Toshihiro, Uda Keiko, Harada Atsushi, Kono Kenji  
*Molecules* **21(10)** (2016) 1284.

Interaction between intrinsically disordered regions in transcription factors Sp1 and TAF4  
Hibino Emi, Inoue Rintaro, Sugiyama Masaaki, Kuwahara Jun, Matsuzaki Katsumi, Hoshino Masaru  
*Protein Science* **11** (2016) 2006-2017.

Isomeric replacement of a single aspartic acid induces a marked change in protein function: The Example of Ribonuclease A  
Sakaue H, Kinouchi T, Fujii N, Takumi T and Fujii N  
*ACS Omega* **2** (2017) 260-267.

Kinetics of the competitive reactions of isomerization and peptide bond cleavage at l- $\alpha$ - and d- $\beta$ -aspartyl residues in an  $\alpha$ A-crystallin fragment"  
Aki Kenzo and Okamura Emiko  
*Journal of Peptide Science* **23(1)** (2017) 28-37.

Limited effectiveness of household sand filters for removal of arsenic from well water in North Vietnam  
Ilmiawati C., Thang N. D., Iida M., Maeda M., Ohnuma S., Yajima I., Ohgami N., Oshino R., Al Hossain M. M. A., Ninomiya H., Kato M.  
*Journal of Water and Health* **14(6)** (2016) 1032-1040.

Manganese-mediated acceleration of age-related hearing loss in mice  
Ohgami Nobutaka, Yajima Ichiro, Iida Machiko, Li Xiang, Oshino Reina, Kumasaka Mayuko Y., Kato Masashi  
*Scientific Reports* **6** (2016) 36306.

Modulated expression levels of tyrosine kinases in spontaneously developed melanoma by single irradiation of non-thermal atmospheric pressure plasmas  
Kato M, Ninomiya H, Maeda M, Ilmiawati C, Al Hossain MM, Yoshinaga M, Ohgami N  
*Archives of Toxicology* **90(6)** (2016) 1523-1524.

New insight into the dynamical system of  $\alpha$ B-crystallin oligomers  
Inoue Rintaro, Takata Takumi, Fujii Norihiko, Ishii Kentaro, Uchiyama Susumu, Sato Nobuhiro, Oba Yojiro, Wood Kathleen, Kato Koichi, Fujii Noriko, Sugiyama Masaaki  
*Scientific Reports* **6** (2016) 29208.

One-shot LC-MS/MS analysis of post-translational modifications including oxidation and deamidation of rat lens  $\alpha$ - and  $\beta$ -crystallins induced by  $\gamma$ -irradiation  
I. Kim, T. Saito, N. Fujii, T. Kanamoto, and N. Fujii  
*Amino Acids* **48** (2016) 2855-2866.

Photoaffinity electrophoretic mobility shift assay using photoreactive DNA bearing 3-trifluoromethyl-3-phenyldiazirine in its phosphate backbone

Y. Sadakane and Y. Hatanaka  
Anal. Biochem. **506** (2016) 1-7.

Reply to the commentary "To Gorelenkova Miller and Mieyal (2015): Sulfhydryl-mediated redox signaling in inflammation: role in neurodegenerative diseases" by Mieyal JJ

Kato Masashi, Ninomiya Hiromasa, Maeda Masao, Ilmiawati Cimi, Al Hossain M M A., Yoshinaga Masafumi, Ohgami Nobutaka

Archives of Toxicology **90(6)** (2016) 1523-1524.

Sequence-directed nucleosome-depletion is sufficient to activate transcription from a yeast core promoter in vivo

Ichikawa Yuichi, Morohashi Nobuyuki, Tomita Nobuyuki, Mitchell Aaron P., Kurumizaka Hitoshi, Shimizu Mitsuhiko

Biochemical and Biophysical Research Communications **476(2)** (2016) 57-62.

Structural characterization of the circadian clock protein complex composed of KaiB and KaiC by inverse contrast-matching small-angle neutron scattering

Sugiyama Masaaki, Yagi Hirokazu, Ishii Kentaro, Porcar Lionel, Martel Anne, Oyama Katsuaki, Noda Masanori, Yunoki Yasuhiro, Murakami Reiko, Inoue Rintaro, Sato Nobuhiro, Oba Yojiro, Terauchi Kazuki, Uchiyama Susumu, Kato Koichi

Scientific Reports **6** (2016) 35567.

Structural insight into protein binding of boron tracedrug UTX-97 revealed by the co-crystal structure with lysozyme at 1.26 Å resolution

Y. Morimoto, H. Nagasawa, Y. Uto, T. Chatake and H. Hori

J. Pharm. Sci. **105** (2016) 2298-2301.

Structure and function of human histone H3.Y nucleosome

Kujirai Tomoya, Horikoshi Naoki, Sato Koichi, Maehara Kazumitsu, Machida Shinichi, Osakabe Akihisa, Kimura Hiroshi, Ohkawa Yasuyuki, Kurumizaka Hitoshi

Nucleic Acids Research **44(13)** (2016) 6127-6141.

Structure of the human DNA-repair protein RAD52 containing surface mutations

Saotome Mika, Saito Kengo, Onodera Keiichi, Kurumizaka Hitoshi, Kagawa Wataru

Acta Crystallographica Section F Structural Biology Communications **72(8)** (2016) 598-603.

Supramolecular Complexes Formed by the Self-Assembly of Hydrophobic Bis(Zn<sup>2+</sup>-cyclen) Complexes, Copper, and Di- or Trimide Units for Specific Hydrolysis of Phosphate Mono- and Diesters in Two-Phase Solvent Systems (Cyclen = 1,4,7,10-Tetraazacyclododecane)

Yosuke Hisamatsu, Yuya Miyazawa, Takeru Yoneda, Miki Miyachi, Mohd Zulkefeli, and Shin Aoki, Chemical and Pharmaceutical Bulletin **64(5)** (2016) 451-464.

The Flexible Ends of CENP-A Nucleosome Are Required for Mitotic Fidelity

Roulland Johan, Ouararhni Khalid, Naidenov Mladen, Ramos Lorrie, Shuaib Muhammad, Syed Sajad Hussain, Lone Imtiaz Nizar, Boopathi Ramachandran, Fontaine Emeline, Papai Gabor, Tachiwana Hiroaki, Gautier Thierry, Skoufias Dimitrios, Padmanabhan Kiran, Bednar Jan, Kurumizaka Hitoshi, Schultz Patrick, Angelov Dimitar, Hamiche Ali, Dimitrov Stefan

Molecular Cell **63(4)** (2016) 674-685.

VHL-deficient renal cancer cells gain resistance to mitochondria-activating apoptosis inducers by activating AKT through the IGF1R-PI3K pathway

Yamaguchi Ryuji, Harada Hiroshi, Hirota Kiichi

Tumor Biology **37(10)** (2016) 13295-13306.

リアルタイム PCR 法を用いた DNA 損傷の定量化とその放射線量評価法への応用

清水喜久雄, 中嶋隆登, 松尾陽一郎, 日高雄二, 佐藤典仁, 山本幸佳

日本放射線安全管理学会誌 **15(1)** (2016) 52-58. (in Japanese)

## Proceedings

Activation Mechanism of Cocoonase

Nagisa Tajima, Shigeru Shimamoto, Mitsuhiko Miyazawa and Yuji Hidaka

Proceedings of the 53rd Japanese Peptide Symposium Kyoto, Japan (Oct.26-28, 2016) 105-106.

Age-dependent isomerization and racemization at specific aspartyl residues in lens crystallins Analysis and biological relevance

Noriko Fujii, Takumi Takata, Norihiko Fujii and Hiroshi Sasaki

XXII Biennial Meeting of the International Society for Eye Research Tokyo. (Sep.25-29, 2016)

Age-related abnormal Asp isomers distribution in lens specific  $\alpha$ A-crystallin monomeric and polymeric state

Takumi Takata, Takashi Sato, Hiroshi Sasaki and Noriko Fujii

XXII Biennial Meeting of the International Society for Eye Research Tokyo. (Sep.25-29, 2016)

Age-related Asp isomerizations in dissociated alpha-crystallin from aged Lens

Takumi Takata, Noriko Fujii

ARVO2016 Annual meeting USA. (May 1-5, 2016)

Disulfide-Coupled Folding of Pro-Uroguanylin on Molecular Evolution

Kenta Mori, Kosuke Toyama, Shigeru Shimamoto, and Yuji Hidaka

Proceedings of the 53rd Japanese Peptide Symposium Kyoto, Japan (Oct. 26-28, 2016) 103-104.

Generator of Highly Concentrated Pure  $^{99m}\text{Tc}$  from Low Specific Activity  $^{99}\text{Mo}$  Produced by Reactor and/or Electron Linear Accelerator

K. Tatenuma, A. Tsuguchi, Y. Suzuki, K. Ishikawa, S. Sekimoto, and T. Ohtsuki

Proceedings of "Mo-99 2016 Topical Meeting on Molybdenum-99 Technological Development" St. Louis, Missouri, USA (Sep. 11-14, 2016)

Preparation of an Orexin Precursor Protein Using an E. coli Expression System by Acid Treatment

Natsumi Mitsuoka, Shigeru Shimamoto, and Yuji Hidaka

Proceedings of the 53rd Japanese Peptide Symposium Kyoto, Japan (Oct. 26-28, 2016) 221-222.

Rapid identification and quantification of amino acid isomers occurring in peptides under physiological conditions: a targeted proteomics approach.

Atsuhiko TOYAMA, Noriko FUJII, Toshiya MATSUBAR1, Jun WATANABE

HUPO 15th Annual World Congress (HUPO 2016) Taipei. (Sep. 18-22, 2016)

Regulation of the Disulfide-Coupled Folding of De Novo Designed Peptides by  $\alpha$ -Helix Formation

Saya Nishihara, Kosuke Toyama, Shigeru Shimamoto, and Yuji Hidaka

Proceedings of the 53rd Japanese Peptide Symposium Kyoto, Japan (Oct.26-28, 2016) 223-234.

$\gamma$ 線照射によるラット水晶体  $\alpha$ -及び  $\beta$ -クリスタリンの酸化,脱アミド化及び異性化等の翻訳後修飾の迅速 LC-MS/MS 分析

金 仁求, 齊藤 剛, 金本尚志, 藤井紀子

京都大学原子炉実験所第 51 回学術講演会報文集 (1 月 26-27, 2017) 19. (in Japanese)

サンゴ由来レクチン4糖複合体の結晶構造

喜田昭子, 神保充, 酒井隆一, 森本幸生, 武内良太, 田中浩士, 高橋孝志, 三木邦夫

京都大学原子炉実験所第 51 回学術講演会報文集 (1 月 26-27, 2017) 44. (in Japanese)

ヒト血清中の D-アミノ酸含有ペプチドの探索及び同定

Ha Seongmin, 藤井 紀子

京都大学原子炉実験所第 51 回学術講演会報文集 (1 月 26-27, 2017) 34. (in Japanese)

蛋白質の水和構造解明に向けた D/H コントラスト法の利用

茶竹俊行, 藤原 悟

京都大学原子炉実験所第 51 回学術講演会報文集 (1 月 26-27, 2017) 37. (in Japanese)

納豆菌由来 MK-7 の構造特性および納豆菌のガンマ線耐性の研究

柳澤泰任, 高根光紗, 足立達美, 茶竹俊行, 齊藤 剛, 井上倫太郎, 杉山正明, 松尾龍人, 藤原 悟, 大杉忠則, 須見洋行

京都大学原子炉実験所第 51 回学術講演会報文集 (1 月 26-27, 2017) 38. (in Japanese)

放射線照射や加齢による蛋白質損傷の化学的解明

藤井紀子, 木野内忠稔, 齊藤 剛, 高田 匠, 金 仁求, 定金 豊, 大神信孝, 安岐健三, 藤井智彦, 金本尚志

京都大学原子炉実験所第 51 回学術講演会報文集 (1 月 26-27, 2017) 1-6. (in Japanese)

## Books

D-Amino acid residues in proteins related to aging and age-related diseases and a new analysis of the isomers in proteins in D-Amino acids: Physiology, Metabolism, and Application  
Yoshimura T, Nishikawa T and Homma H. Noriko Fujii, Takumi Takata, Norihiko Fujii, Kenzo Aki and Hiroaki Sakaue  
Springer 2016.

Advances in Asymmetric Autocatalysis and Related Topics 1st Edition  
(6. The Importance Of The Idea Of „Parachirality” In Life Science)  
Editors: Gyula Palyi Robert Kurdi Claudia Zucchi  
(Chapter:6 Noriko Fujii, Norihiko Fujii, Takumi Takata and Hiroaki Sakaue)  
Elsevier 2017.

## Reviews

白内障の予防と治療を見据えた白内障クリスタリン中の異性体アミノ酸の迅速分析  
藤井紀子, 高田 匠, 藤井智彦, 金 仁求  
日本白内障学会誌 **28** (2016) 59-62. (in Japanese)

老化で生じる蛋白質中の D-アミノ酸とその分布  
藤井紀子  
科学と工業 **90** (2016) 315-321. (in Japanese)

老化,放射線による水晶体タンパク質中のアミノ酸一残基ごとの翻訳後修飾の解析  
藤井紀子, 金 仁求, 齊藤 剛, 高田 匠  
放射線生物研究 **52** (2017) 24-34. (in Japanese)

## 7. Neutron Capture Therapy

### Papers

A prospective multicenter single-arm clinical trial of bevacizumab for patients with surgically untreatable symptomatic brain radiation necrosis Furuse  
M, Nonoguchi N, Kuroiwa T, Miyamoto S, Arakawa Y, Shinoda J, Miwa K, Iuchi T, Tsuboi K, Houkin K, Terasaka S, Tabei Y, Nakamura H, Nagane M, Sugiyama K, Terasaki M, Abe T, Narita Y, Saito N, Mukasa A, Ogasawara K, Beppu T, Kumabe T, Nariiai T, Tsuyuguchi N, Nakatani E, Kurisu S, Nakagawa Y, Miyatake S.  
Neuro-Oncology Practice (2016) 1-9.

Boron neutron capture therapy for malignant brain tumors  
Miyatake S, Kawabata S, Hiramatsu R, Kuroiwa T, Suzuki M, Kondo N, Ono K  
Neurologia medico-chirurgica B (2016) 361-371.

Comparison of the pharmacokinetics between L-BPA and L-FBPA using the same administration dose and protocol: a validation study for the theranostic approach using [<sup>18</sup>F]-L-FBPA positron emission tomography in boron neutron capture therapy  
Watanabe Tsubasa, Hattori Yoshihide, Ohta Youichiro, Ishimura Miki, Nakagawa Yosuke, Sanada Yu, Tanaka Hiroki, Fukutani Satoshi, Masunaga Shin-ichiro, Hiraoka Masahiro, Ono Koji, Suzuki Minoru, Kirihata Mitsunori  
BMC Cancer **16(1)** (2016) 859.

Cytotoxicity of Tirapazamine (3-Amino-1,2,4-benzotriazine-1,4-dioxide)-Induced DNA Damage in Chicken DT40 Cells  
Moriwaki Takahito, Okamoto Saki, Sasanuma Hiroyuki, Nagasawa Hideko, Takeda Shunichi, Masunaga Shin-ichiro, Tano Keizo  
Chemical Research in Toxicology **30(2)** (2017) 699-704.

Design study of multi-imaging plate system for BNCT irradiation field at Kyoto university reactor  
Tanaka Kenichi, Sakurai Yoshinori, Kajimoto Tsuyoshi, Tanaka Hiroki, Takata Takushi, Endo Satoru  
Applied Radiation and Isotopes **115** (2016) 212-220.

Early clinical experience utilizing scintillator with optical fiber (SOF) detector in clinical boron neutron capture therapy: its issues and solutions

Ishikawa Masayori, Yamamoto Tetsuya, Matsumura Akira, Hiratsuka Junichi, Miyatake Shin-Ichi, Kato Itsuro, Sakurai Yoshinori, Kumada Hiroaki, Shrestha Shubhechha J., Ono Koji  
Radiation Oncology **11** (2016) 105.

Evaluation of a novel sodium borocaptate-containing unnatural amino acid as a boron delivery agent for neutron capture therapy of the F98 rat glioma

Futamura Gen, Kawabata Shinji, Nonoguchi Naosuke, Hiramatsu Ryo, Toho Taichiro, Tanaka Hiroki, Masunaga Shin-Ichiro, Hattori Yoshihide, Kirihata Mitsunori, Ono Koji, Kuroiwa Toshihiko, Miyatake Shin-Ichi  
Radiation Oncology **26** (2017) PMC5260095.

Hypoxia-inducible factor 1-mediated characteristic features of cancer cells for tumor radioresistance

Harada H  
Journal of Radiation Research **57(S1)** (2016) i99-i105.

In vivo evaluation of neutron capture therapy effectivity using calcium phosphate-based nanoparticles as Gd-DTPA delivery agent

Dewi N, Mi P, Yanagie H, Sakurai Y, Morishita Y, Yanagawa M, Nakagawa T, Shinohara A, Matsukawa T, Yokoyama K, Cabral H, Suzuki M, Sakurai Y, Tanaka H, Ono K, Nishiyama N, Kataoka K, Takahashi H.  
J Cancer Res Clin Oncol **142** (2016) 765-775.

LY6E: a conductor of malignant tumor growth through modulation of the PTEN/PI3K/Akt/HIF-1 axis

Yeom Chan Joo, Zeng Lihua, Goto Yoko, Morinibu Akiyo, Zhu Yuxi, Shinomiya Kazumi, Kobayashi Minoru, Itasaka Satoshi, Yoshimura Michio, Hur Cheol-Goo, Kakeya Hideaki, Hammond Ester M., Hiraoka Masahiro, Harada Hiroshi  
Oncotarget **7** (2016) 65837-65848.

Maleimide-functionalized closo-dodecaborate albumin conjugates (MID-AC): Unique ligation at cysteine and lysine residues enables efficient boron delivery to tumor for neutron capture therapy

Kikuchi Shunsuke, Kanoh Daisuke, Sato Shinichi, Sakurai Yoshinori, Suzuki Minoru, Nakamura Hiroyuki  
Journal of Controlled Release **237** (2016) 160-167.

Use of boron cluster-containing redox nanoparticles with ROS scavenging ability in boron neutron capture therapy to achieve high therapeutic efficiency and low adverse effects

Gao Zhenyu, Horiguchi Yukichi, Nakai Kei, Matsumura Akira, Suzuki Minoru, Ono Koji, Nagasaki Yukio  
Biomaterials **104** (2016) 201-212.

Visualization of Boronic Acid Containing Pharmaceuticals in Live Tumor Cells Using a Fluorescent Boronic Acid Sensor

Hattori Yoshihide, Ishimura Miki, Ohta Yoichiro, Takenaka Hiroshi, Kirihata Mitsunori  
ACS Sensors **12(1)** (2016) 1394-1397.

## Proceedings

BNCT 実用化に向けた橋渡し研究

鈴木 実, 高垣雅緒, 宮武伸一, 平塚純一, 櫻井英幸, 柳衛宏宣, 東 治人, 中村浩之, 谷森紳治, 安藤 徹, 藤本卓也, 長崎幸夫, 石川善恵, 山川延宏, 小松直樹, 田中憲一, 石川正純, 中村哲志, 林慎一郎  
京都大学原子炉実験所第 51 回学術講演会報文集 (1 月 26-27, 2017) 48-50. (in Japanese)

Progress in Reactor and Accelerator Based BNCT at Kyoto University Research Reactor Institute

Y. Sakurai  
Proceedings of Science (INPC2016) Adelaide, Australia (Sep.11-16, 2016).

局所腫瘍制御, 遠隔転移抑制, 及び癌幹細胞特性との関連性を加味する休止期腫瘍細胞の特性解析

増永慎一郎, 小野公二  
京都大学原子炉実験所第 51 回学術講演会報文集 (1 月 26-27, 2017) 14. (in Japanese)

## Books

Tumor Microenvironment and Hyperthermia. In "Hyperthermic Oncology from Bench to Bedside" PartII Basic Science in Whole Body

Masunaga S  
Springer 2016.

新版 放射線医科学-生体と放射線・電磁波・超音波  
鈴木 実  
医療科学社 2016. (in Japanese)

## Reviews

原発性悪性骨腫瘍に対するホウ素中性子捕捉療法(BNCT)(特集 悪性骨腫瘍の診断と治療の最前線)  
鈴木 実, 藤本卓也  
整形・災害外科 **59** (8) (2016) 1093-1100. (in Japanese)

治療生物学および放射線治療医的視点から見た中性子捕捉療法の特性  
増永慎一郎, 鈴木 実, 田野恵三, 真田悠生, 小野公二  
日本口腔腫瘍学会誌 **28** (2016) 134-147. (in Japanese)

ホウ素中性子捕捉療法(BNCT)と他の粒子線治療との違い  
宮武伸一, 川端信司, 不破信和  
日本臨牀 増刊号 **7** (71) (2016) 615-621. (in Japanese)

夢の細胞選択的粒子線治療 BNCT  
宮武伸一  
大阪医科大学雑誌 **75** (1・2) (2016) 12-15. (in Japanese)

ホウ素中性子捕捉療法(BNCT)の最新動向  
鈴木 実  
月刊インナービジョン **31** (2016) 55. (in Japanese)

## 8. Neutron Radiography and Radiation Application

### Papers

Lipid-membrane-incorporated arylboronate esters as agents for boron neutron capture therapy  
Ueda Masafumi, Ashizawa Kengo, Sugikawa Kouta, Koumoto Kazuya, Nagasaki Takeshi, Ikeda Atsushi  
Org. Biomol. Chem. **15** (2016) 1565-1569.

### Proceedings

Development of Portable SNMs Detection System Based on Threshold Energy Neutron Analysis"  
T. Misawa, Y. Kitamura, Y. Takahashi and K. Masuda,  
Proc of 2016 IEEE Nuclear Science Symposium & Medical Imaging Conference Strasbourg, France  
(Oct.29, 2016) N08-27.

Evaluation of void fraction around a tube in two-phase flow across horizontal tube bundle  
H. Murakawa, M. Baba, K. Sugimoto, N. Takenaka, D. Ito and Y. Saito  
9th International Conference on Multiphase Flow (ICMF-2016) Firenze, Italy (May 22-27, 2016) 433.

X線ラジオグラフィを用いた霜層密度分布の測定  
上地拓摩, 松本亮介, 影林和磨, 伊藤大介, 齊藤泰司  
2016年度日本冷凍空調学会年次大会 神戸, 日本 (2016年9月6-9日) E222-E222. (in Japanese)

## 9. TRU and Nuclear Chemistry

### Papers

Longgu (Fossilia Osis Mastodi) alters the profiles of organic and inorganic components in  
Keishikaryukotsuboreito  
Oguri Kazuki, Kawase Masaya, Harada Kazuo, Shimada-Takaura Kayoko, Takahashi Toshiharu, Takahashi  
Kyoko Journal of Natural Medicines **70**(3) 483-491. (2016)

## 10. Health Physics and Waste Management

### Papers

Radioactive contamination of arthropods from different trophic levels in hilly and mountainous areas after the Fukushima Daiichi nuclear power plant accident

Tanaka Sota, Hatakeyama Kaho, Takahashi Sentaro, Adati Tarô

Journal of Environmental Radioactivity **164** (2016) 104-112.

### Reviews

京大炉を用いた中性子放射化分析の例

関本 俊

日本応用物理学会 放射線分科会誌「放射線」**42** (2016) 11-14. (in Japanese)

### Others

A Simple Method for Sampling and Analysis of Particulate, Inorganic Gaseous and Organic Gaseous Halogens in the Atmosphere

Naofumi Akata, Hirofumi Tsukada, Tomoyuki Takahashi and Satoshi Fukutani

Radiation Environment and Medicine ISSN 2423-9097 (2016) 29-32.

## 11. Accelerator Physics

### Papers

Characterization techniques for fixed-field alternating gradient accelerators and beam studies using the KURRI 150 MeV proton FFAG

Sheehy S. L., Kelliher D. J., Machida S., Rogers C., Prior C. R., Volat L., Haj Tahar M., Ishi Y., Kuriyama Y., Sakamoto M., Uesugi T., Mori Y.

Progress of Theoretical and Experimental Physics **7** (2016) 073G01.

### Proceedings

Design study of niobium mushroom-shaped cavity for evaluating RF critical magnetic field of thin-Film superconductor

H. Oikawa, T. Higashiguchi, Y. Iwashita, M. Hino, H. Hayano, S. Kato, T. Kubo, T. Saeki

Proceedings of LINAC2016 East-Lansing, MI, USA (Sep.19, 2016) 372-376.

Non-destructive Texture Measurement of Steel Sheets with Compact Neutron Source “RANS”

Takamura M, Ikeda Y, Sunaga H, Taketani A, Otake Y, Suzuki H, Kumagai M, Hama T, Oba Y

Journal of Physics: Conference Series Bristol (Sep.19, 2016) 32047.

## 12. Others

### Papers

2014年長野県北部の地震の被害調査と震源のモデル化

池田隆明, 小長井一男, 釜江克宏, 佐藤京, 高瀬裕也

地震工学論文集 **35** I\_975-I\_983. (2016) (in Japanese)

3次元高密度強震アレイ観測記録に基づく硬質地盤の地震動空間変動特性と統計的モデル化

内田 治, 上林宏敏, 釜江克宏

日本地震工学会論文集 **88**\_42-8\_61. (2016) (in Japanese)

Conceptualizing maritime security for energy transportation security

Shoki Kosai and Hironobu Unesaki

Journal of Transportation Security **9(3)** (2016) 175-190.

Development of intense terahertz coherent synchrotron radiation at KU-FEL

Sei Norihiro, Zen Heishun, Ohgaki Hideaki

Nuclear Instruments and Methods in Physics Research Section A: Accelerators, Spectrometers, Detectors and Associated Equipment **832(1)** (2016) 208-213.

Dynamics of polybutadiene reinforced with unsaturated carboxylate studied by muon spin relaxation ( $\mu$ SR)  
Mashita Ryo, Kishimoto Hiroyuki, Inoue Rintaro, Koda Akihiro, Kadono Ryosuke, Kanaya Toshiji  
Polymer **105** (2016) 510-515.

Energy dependence with an Asian twist? Examining international energy relations in Southeast Asia  
Kamonphorn Kanchana, Benjamin C. McLellan, Hironobu Unesaki  
Energy Research & Social Science **21** (2016) 123-140.

Energy Security and Sustainability in Japan  
Jeffrey Kucharski and Hironobu Unesaki  
International Journal of Sustainable Future for Human Security **4(1)** (2016).

Frequency domain optical tomography using a Monte Carlo perturbation method  
T.Yamamoto and H.Sakamoto  
Optics Communications **364** (2016) 165-176.

Millijoule terahertz coherent transition radiation at LEBRA  
Sei Norihiro, Ogawa Hiroshi, Sakai Takeshi, Hayakawa Ken, Tanaka Toshinari, Hayakawa Yasushi, Nogami Kyoko  
Japanese Journal of Applied Physics **56(3)** (2017) 32401.

Phase transformation in Fe-Mn-C alloys by severe plastic deformation under high pressure  
Adachi Nozomu, Wu Ningning, Todaka Yoshikazu, Sato Hideyuki, Ueki Rintaro  
Materials Letters **185** (2016) 109-111.

Redox and Ligand Exchange during the Reaction of Tetrachloroaurate with Hexacyanoferrate(II) at a Liquid-Liquid Interface: Voltammetry and X-ray Absorption Fine-Structure Studies  
Uehara Akihiro, Chang Sin-Yuen, Booth Samuel G., Schroeder Sven L.M., Mosselmans J.Frederick W., Dryfe Robert A.W.  
Electrochimica Acta **190** (2016) 997-1006.

Screening of nanosatellite microprocessors using californium single-event latch-up test results  
Takahiro Tomioka, Yuta Okumura, Hirokazu Masui, Koichi Takamiya, Mengu Cho  
Acta Astronautica **126** (2016) 334-341.

ガンマ線スペクトル解析におけるピーク探索と面積計算実態と今後のスペクトル解析のあるべき姿  
青山道夫, 秋山正和, 浅井雅人, 阿部敬朗, 佐藤 泰, 高野直人, 高宮幸一, 濱島靖典, 武藤儀一, 山田隆志, 石津秀剛  
RADIOISOTOPES **65** (2016) 267-285. (in Japanese)

強震下の超高層集合住宅の挙動解明と今後の被害低減に向けた取り組み  
永野 正行, 肥田 剛典, 田沼 毅彦, 中村 充, 井川 望, 保井 美敏, 境 茂樹, 森下 真行, 北堀 隆司, 上林 宏敏  
日本地震工学会論文集 **5** (2016) 5\_2-5\_11. (in Japanese)

超高層 RC 造の長周期地震動による損傷度の簡易評価指標  
上林宏敏, 永野正行, 釜江克宏, 川辺秀憲  
日本地震工学会論文集 **5** (2016) 5\_33-5\_45. (in Japanese)

## Proceedings

Cu 線小角散乱装置の共同利用開始  
佐藤信浩, 大場洋次郎, 井上倫太郎, 杉山正明  
京都大学原子炉実験所第 51 回学術講演会報文集 (1 月 26-27, 2017)21. (in Japanese)

KUR-IBS を用いた研究展開  
日野正裕, 小田達郎, 足立 望, 大場洋次郎, 吉永尚生, 杉山正明, 川端祐司  
京都大学原子炉実験所第 51 回学術講演会報文集 (1 月 26-27, 2017)24. (in Japanese)

Mo 線源 X 線小角散乱装置の共同利用開始  
大場洋次郎, 佐藤信浩, 井上倫太郎, 杉山正明  
京都大学原子炉実験所第 51 回学術講演会報文集 (1 月 26-27, 2017)20. (in Japanese)

数十～数百 MeV イオンビーム照射場の利用環境開発 —医療・バイオから宇宙まで—  
高田卓志  
京都大学原子炉実験所第 51 回学術講演会報文集 (1 月 26-27, 2017) 8. (in Japanese)

輸送方程式をどのように数値的に解けるのか

Wilfred van Rooijen

京都大学原子炉実験所第 5 回炉物理専門研究会 (RPW 2016) (11 月 30 日-12 月 1 日 2016) 90. (in Japanese)

## Reviews

巻頭言 研究用原子炉の今後の問題点

川端祐司

波紋 **5** (2016) 71. (in Japanese)

固液界面とトライボロジー

平山朋子

ながれ **351** (2016) 297-300. (in Japanese)

電子加速器によるテラヘルツ波の発生

全 炳俊, 清 紀弘, 入澤明典, 加藤 政博

月刊 化学工業 **168** (3) (2017) 176-181. (in Japanese)

---

KURRI Progress Report 2016

Issued in July 2017

by the Research Reactor Institute, Kyoto University  
Kumatori-cho, Sennan-gun, Osaka 590-0494 Japan

Tel. +81-72-451-2300

Fax. +81-72-451-2600

In case that corrections are made, an errata will be provided  
in the following webpage:

<http://www.rri.kyoto-u.ac.jp/PUB/report/PR/ProgRep2016/ProgRep2016.html>

Publication Team

INO, Yuta  
INOUE, Rintaro (Subchief)  
ISHI, Yoshihiro  
IWASE, Tomohiro  
MORI, Kazuhiro (Chief)  
NAKAYAMA, Chiyoko  
SAITO, Takeshi  
SAKURAI, Yoshinori (Subchief)  
SANO, Hiroaki  
SEKIMOTO, Shun  
TSURUTA, Yachiyo  
YAMADA, Tatsuya  
YOKOTA, Kaori